МОСКОВСКИЙ ГОСУДАРСТВЕННЫЙ УНИВЕРСИТЕТ

имени М.В. ЛОМОНОСОВА

ФАКУЛЬТЕТ НАУК О МАТЕРИАЛАХ

На правах рукописи

Сюй Сеюй

Li-проводящий керамический электролит со структурой NASICON для твердотельных аккумуляторов

1.4.15 - Химия твердого тела

ДИССЕРТАЦИЯ

на соискание ученой степени

кандидата химических наук

Научные руководители:

д.х.н., чл.-корр. РАН Гудилин Евгений Алексеевич,

к.х.н. Капитанова Олеся Олеговна

Москва – 2024

M. V. Lomonosov Moscow State University

Faculty of Materials Science

Xu Xieyu

Li-conductive ceramic electrolyte with NASICON structure for solid-state batteries

1.4.15 - Solid state chemistry

PhD Thesis

for the degree of

candidate of chemical science

Scientific supervisors:

Corresponding member of RAS, Doctor of Chemical Sciences

Goodilin Evgeny Alekseevich

Doctor of Chemical Sciences Kapitanova Olesya Olegovna

Moscow - 2024

Table of contents

List of abbreviations and symbols

AGG — Abnormal grain growth

NGG — Normal grain growth

LIB — Lithium Ion Battery

SSE — Solid-state electrolyte

XRD — X-ray diffraction

SEM — Scanning electron microscopy

EDX — Energy-dispersive X-ray spectroscopy

PVD — Physical vapor deposition

CVD — Chemical vapor deposition

SPS — Spark plasma sintering

FAST — Field assisted sintering technique

UHS — Ultra-fast high-temperature sintering

TGA — Thermal gravimetric analysis

DSC — Differential scanning calorimetry

DLS — Dynamic light scattering

DIL — Dilatometry

EIS — Electrochemical impedance spectroscopy

SEI — Solid Electrolyte Interface

NASICON — Sodium super ionic conductor

NCM — Lithium nickel manganese cobalt oxides

LFP — Lithium iron phosphate

PVDF — Polyvinylidene fluoride

NMP — N-Methyl-2-pyrrolidone

DME — Dimethoxyethane

FEC — Fluoroethylene carbonate

LiTFSI — Lithium bis(trifluoromethanesulfonyl)imide

1. Abstract

The relevance of the work

The 2019 Nobel Prize in Chemistry for the creation of lithium-ion batteries was undoubtedly recognition of the great importance of electrochemical energy and solid-state chemistry as the most important areas of modern scientific and technological progress. In this regard, scientific research on the development of new materials for secondary power supplies is relevant and practically significant. One of the promising commercially available energy sources is lithium-ion batteries (LIB) due to their high specific energy density (240-270 Wh/kg) and power density (200-500 W/kg), long service life and stability during cycling. At the same time, a number of critical industrial, transportation, medical, telecommunications, information and engineering applications require achieving even higher performance. The possibility of significantly improving the main specific characteristics, as well as reducing costs, associated with the development of new electrode materials, as well as the use of new generations of materials based on solid-state electrolytes, which make it possible to achieve significant gains and improvements in specific energy, power and safety of devices today.

$Li_{1+x}Al_xTi_{2-x}(PO_4)_3$ phase family solid-state electrolyte with NASICON structure has high ionic conductivity (up to 10^{-3} S/cm for monocrystal) at room temperature, low cost due to the absence of rare and trace elements in the compound, chemical stability in air, a wide window of operating voltage (2.8-4.8V relative to Li^+/Li), high mechanical strength (elastic modulus ~ 150 GPa), no toxic, high thermal stability up to ~ 1300ºC. Methods for obtaining solid-state electrolytes based on LATP are divided into methods using solid state chemistry method, glass crystallization method, "soft chemistry" andchemical homogenization. Solid-state electrolyte ceramic samples have lower lithium-ion conductivity compared to the single crystal due to the negative contribution of grain boundaries and the presence of defects such as cracks and pores. Moreover, some types of defects in the ceramic electrolyte are sources of mechanical microstresses, which can lead to the formation of lithium protrusions during the electrochemical cycling of the battery and the risk of short circuit due to mechanical destruction of the electrolyte.

The relevance of the work is related to the development of new generations of materials for lithium-ion batteries with solid-state electrolytes, characterized by improved performance characteristics and safety. The feasibility of developing such materials is confirmed by the Decree of

the President of Russia on the establishment of the State Program of the Russian Federation "Energy Development" and corresponds to the priority direction of the development of science, technology and engineering in the Russian Federation: Energy efficiency, energy saving, nuclear energy.

Therefore, **the goal of the work** is the development of efficient approaches for obtaining ceramic solid-state electrolytes based on $Li_{1+x}Al_xTi_{2-x}(PO_4)_3$ phase composition with specified functional characteristics for solid-state secondary power supplies.

To achieve this goal, the following tasks were solved:

1. The use of numerical simulation by the phase field method, 2D and 3D visualization of the propagation process of dendritic structures of metallic lithium during battery charging to assess the complex of required physicochemical and morphological properties of the solid-state electrolyte.

2. Development of novel methods for the synthesis of powdered precursors for the fabrication of $Li_{1+x}Al_xTi_{2-x}(PO_4)_3$ phase solid-state electrolytes with improved characteristics.

3. Analysis of the influence of the background of obtaining precursors, molding features, temperature and time processing conditions on the sintering processes and the microstructure of $Li_{1+x}Al_xTi_{2-x}(PO_4)_3$ phase solid-state electrolyte samples.

4. Development of effective methods for the fabrication of high-density $Li_{1+x}Al_xTi_{2-x}(PO_4)_3$ ceramic materials with controllable geometric dimensions, granulometric composition and pore structure features for use as solid-state electrolytes.

5. Carrying out electrochemical testing and analysis of correlations of composition - structure - properties to select the most effective methods for creating solid-state electrolytes for secondary power supply; assembly and testing of prototypes of solid-state lithium batteries.

Objects:

1. $Li_{1+x}Al_xTi_{2-x}(PO_4)_3$ solid-state electrolyte powdered precursors obtained by the solid-state method, the molten salt quenching method and synthesis using polymerized matrices.

2. $Li_{1+x}Al_xTi_{2-x}(PO_4)_3$ ceramic materials with specified geometric dimensions, controlled granulometric composition, features of the pore structure depending on the morphology and

phase (crystalline/amorphous) composition of the powder precursors and the approach to their formation and sintering conditions.

The scientific novelty of the work

1. For the first time, with the help of the phase field simulation method, the initial stages and processes in the dynamics of the formation of lithium protrusions in the solid-state electrolyte were visualized depending on the grain size, their mechanical properties and pore morphology, which made it possible to predict the optimal properties of ceramics to reduce the negative consequences of the growth of dendritic structures of metallic lithium.

2. The synthesis was optimized using polymerized matrices, which made it possible to obtain $Li_{1.3}Al_{0.3}Ti_{1.7}(PO_4)_3$ phase particles with NASICON structure with a controlled average grain size in the range of 25-600 nm.

3. The optimal sintering conditions for $Li_{1+x}Al_xTi_{2-x}(PO_4)_3$ have been established for the first time, which make it possible to minimize the contribution of abnormal grain growth (AGG) and achieve effective compaction during heat treatment and achieve a relative density of $96.3\pm0.2\%$ and an elastic modulus of 125 ± 5 GPa.

4. For the first time, an approach has been proposed to improve the complex of functional properties of $Li_{1+x}Al_xTi_{2-x}(PO_4)_3$ phase solid-state electrolyte ceramics through the use of powdered precursors with a bimodal particle size distribution, as well as amorphous (glassy) components.

5. The relationship has been established between a number of parameters for obtaining ceramics and the electrochemical characteristics of the samples, in particular, ionic conductivity values up to $(8\pm0.2)\times10^{-4}$ S/cm have been achieved. It has been shown that the increase of relative density and ionic conductivity of ceramics led to a decrease in overvoltage values during the electrochemical deposition process of lithium, which makes it possible to obtain prototypes of lithium-ion secondary power supplies with improved characteristics.

The practical significance of the work

The results of the work are of great practical importance for the development and implementation of original approaches to obtain highly efficient lithium-conductive solid-state electrolyte for

secondary power supplies. In particular, it has been demonstrated that the transition to a bimodal size distribution in an ensemble of ~ 600 nm submicron $Li_{1.3}Al_{0.3}Ti_{1.7}(PO_4)_3$ particles with a fraction of 10 wt.% nano particles (~ 60 nm) makes it possible to obtain the ceramic solid-state electrolyte with improved values of relative density 96±1%, ionic conductivity $(5.9\pm0.2)\times10^{-4}$ S/cm and elastic modulus 119±9 GPa. A method for preparing the ceramic solid-state electrolyte using multi-component precursors based on crystal phase and the glass phase powders of $Li_{1.3}Al_{0.3}Ti_{1.7}(PO_4)_3$ has been proposed. The approach used makes it possible to avoid the process of abnormal grain growth during sintering process and, as a result, to improve the functional properties of the solid-state electrolyte, including increasing the ionic conductivity up to $(7.8\pm0.2)\times10^{-4}$ S/cm, relative density up to 95.1±0.3% and elastic modulus up to 120±8 GPa. The optimal weight ratio of the crystalline and glass phases was established as 95:5 in the frame of this study. Based on dilatometry data, a two-step sintering mode (570°C, 6h; 900°C, 6h) of composites based on $Li_{1.3}Al_{0.3}Ti_{1.7}(PO_4)_3$ was developed, which allows achieving maximum ionic conductivity values $(8\pm0.2)\times10^{-4}$ S/cm, relative density 96.3±0.2% and elastic modulus 125±5 GPa. Approaches have been developed to molding synthesized powders in the form of the solid-state electrolyte membrane with thickness down to 60 μm thick, which made it possible to assemble working prototypes of solid-state power supply with high performance characteristics.

The developed approaches to the production of such ceramic materials have a wide range of applications for use in electric vehicles, the aerospace industry, etc. In this regard, the results of the work may be in demand in the Russian companies GAZ, Roscosmos, Norilsk Nickel, Rosatom, as well as in foreign specialized companies.

Points for defense

1. Results of numerical modeling by the phase field method, 2D and 3D visualization of the propagation process of dendritic structures of metallic lithium and establishing optimal physic-chemical and morphological properties of the solid-state electrolyte to reduce the negative consequences of the lithium protrusions growth.

2. Results and techniques for the practical use of new methods for the synthesis of powdered precursors to obtain $Li_{1+x}Al_xTi_{2-x}(PO_4)_3$ solid-state electrolyte with improved characteristics.

3. Selection suggestions for the efficient routes of the precursors preparation, molding modes,

temperature-time processing conditions for obtaining $Li_{1+x}Al_xTi_{2-x}(PO_4)_3$ phase solid-state electrolyte samples with the optimized microstructure and high values of ionic conductivity.

4. Original methods for producing high-density $Li_{1+x}Al_xTi_{2-x}(PO_4)_3$ ceramic materials with controllable geometric dimensions, granulometric composition, specified parameters of the pore structure for use as solid-state electrolytes.

5. Correlations composition - structure - properties based on a large number of samples, which made it possible to propose the effective methods to fabricate solid-state electrolytes for secondary power supply.

6. Results of testing the electrochemical properties of solid-state electrolyte and prototypes of solid-state lithium batteries based on them.

Reliability of experimental results is confirmed by using an integrated approach depend on complementary physic-chemical methods, the reproducibility of the results obtained, as well as their agreement with literature data. To determine the phase composition and crystal structure - X-ray phase analysis (XRD), morphology - scanning electron microscopy (SEM), mechanical properties - nanoindentation and transport characteristics - impedance spectroscopy of the synthesized materials were used.

Main results of the PhD thesis work are presented in 5 Q1 scientific publications, indexed in the Web of Science, Scopus databases, and recommended for defense in the dissertation council of Moscow State University in the specialty 01.04.15 - Solid state chemistry.

Approbation of the work was presented at the following Russian and international conferences: XVIIIth conference of the European ceramic society (Lyon, France, 2023), XXXIII Mendeleev competition for chemistry students (Ivanovo, Russia, 2023), 65th All-Russian scientific conference in MIPT in honor of the 115th anniversary L.D. Landau (Moscow, Russia, 2023), International scientific conference of students, graduate students and young scientists "Lomonosov-2023" (Moscow, Russia, 2023).

Personal contribution of the author. The work of this PhD thesis is based on the results of

scientific research conducted directly by the author in the period from 2019 to 2023 in the division of Nanomaterials at Faculty of Materials Science of Lomonosov Moscow State University. The author analyzed the literature in detail, synthesized the samples and characterized them by various physic-chemical methods to establish the morphology, phase composition, relative density, ionic conductivity, elastic modulus and electrochemical characteristics. A mathematical model of solid-state electrolyte degradation was also developed, which the author carried out using Matlab and Comsol Multiphysics software. The results obtained were analyzed and interpreted in detail. Part of the instrumental studies was carried out in collaboration with senior researcher Evdokimov P.V. (TGA-DSC, dilatometry, SEM at Moscow State University), Dr. Liu YY. (SEM at MIPT), engineer Filippova T.V. (XRD at Moscow State University) and Ph.D. student Wang XY. (mechanical characteristics at Xi'an Jiaotong University in China).

Volume and structure of work

The PhD thesis consists of an abstract, literature review, experimental part, results and their discussion, conclusion, list of references and supporting information. The work is presented on 234 pages, contains 148 figures, 24 tables and 210 references to literary sources.

2. Literature review

The literature review consists of three parts. The first part introduces the development history of lithium battery, discusses the advantages, current issues and development direction of each component in lithium battery, and points out the future direction of the development from liquid electrolyte to solid-state electrolyte. The second part introduces the main types of solid-state electrolytes that have been explored so far and their corresponding advantages and obstacles, and introduces various parameters for evaluating the reliability of solid-state electrolytes. In the third section, the various synthesis and sintering approaches of the promising NASICON system solid-state electrolyte, as well as the characterization and developing strategies of solid-state electrolyte design to suppress lithium filament penetration are introduced.

2.1. The development history and working principle of lithium battery

2.1.1. History of lithium battery

Since the era of traditional farming, human beings have relied on natural energy such as wind and water to carry out various social activities to create and promote social progress and development. After the Industrial Revolution in the 18th century, the utilization of electric energy, nuclear energy and light energy greatly stimulated the development of high-tech science and technology, resulting in unprecedented economic productivity. With the rapid increase of the earth's population and the industrialization of developing countries, the demand for energy has reached an unprecedented level [1-2].

As the core support for energy development, energy storage technology is the key technology to promote the transformation of main energy from traditional energy sources such as fossil fuels to new renewable energy sources such as wind energy, solar energy, and geothermal energy. Among them, although the installed cost of electrochemical energy storage technology is high, its efficiency in energy storage and release is higher, so it has wider application prospects. It is important to note that in the field of "green" energy, chemical current sources (CPS) are necessary to equalize the load in electrical networks, regulate the frequency and provide consumers with renewable energy at times of power generation failures when using wind, solar or wave power plants [3].

Looking through all metal elements, lithium has the lightest molar mass (7 g/mol) and the lowest electrode potential (-3.04 V relative to standard hydrogen electrode), and theoretically has the largest energy density [3]. Therefore, lithium naturally attracts the attention of researchers in battery structure design. However, lithium metal is not compatible with water-based electrolytes, so the introduction of non-aqueous electrolytes becomes very critical.

The beginning of lithium-ion battery research began in 1962 with the proposal of non-aqueous electrolyte. Embedded compounds (fluorocarbon) were first introduced into lithium-ion battery design in 1970 [4]. In 1976, lithium-ion batteries composed of composite metal oxides appeared [5]. The success of these lithium-ion batteries made the research on lithium-ion battery systems enter a fiery peak at that time, and the scientific community began to gradually turn to the issue of improving the reversibility of battery reactions. In addition, Armand etc. found some molecules or ions that can be embedded in layered disulfides, and studied the reaction of alkali metals embedded in the graphite lattice [6]. At the same time, another the most significant problem in lithium batteries, lithium dendrites, began to emerge. During the experiment, the uneven surface of the lithium metal anode led to uneven lithium deposition rate and triggered the emergence of lithium dendrites.

These lithium dendrites continued to grow and eventually pierced the polymer separator, causing an internal short circuit, thus posing a greater safety hazard. At the same time, lithium dendrites also lead to the generation of "dead lithium", which greatly reduces the actual battery charge and discharge capacity. In 1983, the solid electrolyte interlayer (SEI) model was first proposed, which was proved to directly affect the cycling and reversible performance of lithium batteries [7].

Since then, the improvement of the interface properties between the electrode and the electrolyte has become the focus of research, but various improvement routes have no obvious effect. A series of explosions and fires caused by metal lithium anode secondary batteries in the 1980s and 1990s had an extremely bad impact on the field. The stagnation of industrialization and the withdrawal of funds directly led to most research institutions to stop the development of lithium metal anode batteries.

In those difficult years, the remaining researchers decided to abandon lithium metal and choose other intercalated compounds as anode, that is both anode and cathode use active materials that can de-intercalate lithium ions. However, there were still three issues to be overcome:

(1) Finding the suitable lithium intercalation material for the cathode;

(2) Finding the suitable lithium intercalation material for the anode;

(3) Finding the suitable liquid electrolyte that can maintain the stability of the interface layer during the charge-discharge process.

As early as 1980, Goodenough etc. proposed the possibility of lithium cobaltate and lithium nickelate being used in high voltage lithium-ion batteries, but it was generally believed that organic liquid electrolytes cannot maintain stability at high working voltage, so this work does not cause enough attention [8]. But after a few years, discovery and exploration of high voltage carbonate liquid electrolyte, which made lithium cobaltate, the preferred cathode material for Li-ion batteries commercially available. At the same time, Akira etc. applied for the first lithium-ion battery model patent with lithium cobaltate as the cathode and graphite material as the anode [9]. This patent was also adopted by Sony and produced the world's first commercial lithium-ion battery. Goodenough was awarded the Nobel Prize in Chemistry on October 9, 2019, for his work on lithium-ion batteries, along with M. Stanley Whittingham and Akira Yoshino. Since then, the research work of lithium-ion batteries has entered a period of rapid development, and has completely occupied the consumer electronics market in just a few decades. In the 21st century, CATL, ATL and BYD from China have made breakthroughs in the field of lithium iron phosphate and NCM cathodes after lots of technical research and development and accumulation, accounting for more than 60% of the installed capacity in the power battery field. With the development of the times, the safety problems of batteries have been raised again, and the idea of using solid electrolytes instead of liquid electrolytes has gradually become popular [10-11].

2.1.2. Working principle of lithium-ion battery

The charging and discharging process of lithium ions batteries is essentially the process of insertion and extraction of lithium ions. Lithium ions continuously reciprocate in the anode and cathode materials for the intercalation/deintercalation process, so they are vividly called "rocking chair batteries" [12].
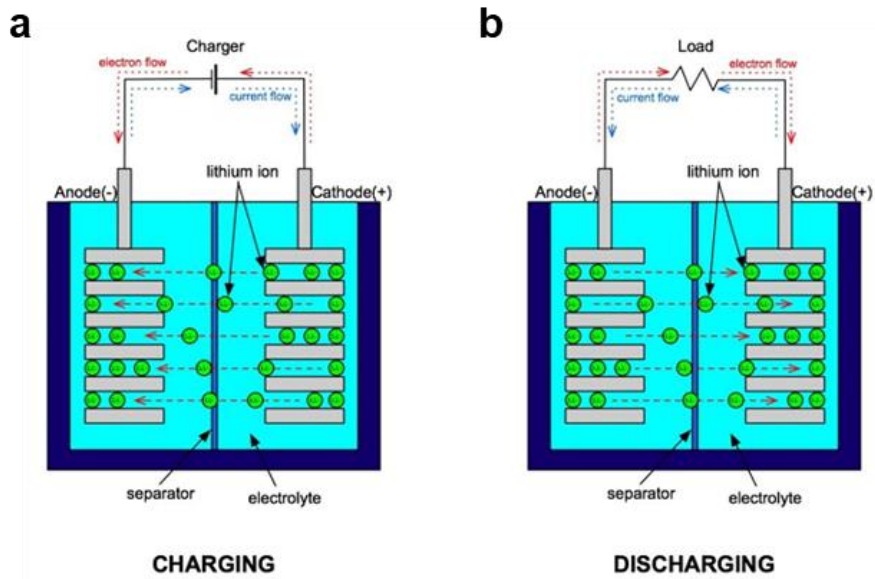
Figure. 2.1. Scheme of charge and discharge of the lithium-ion battery.

Redox processes in traditional commercial lithium cobalt oxide (cathode active material)/graphite (anode active material) battery are described below as an example:

Discharge process:

The cobalt element of the cathode is reduced, and the lithium intercalation reaction occurs:

$$Li_{1-x}CoO_2 + xLi^+ + xe^- \rightarrow LiCoO_2 \ (1)$$
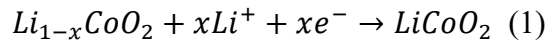
The graphite anode is oxidized, and the de-lithiation reaction occurs:

$$Li_xC_6 \rightarrow xLi^+ + C_6 + xe^- \ (2)$$

Total battery reaction is:

$$Li_{1-x}CoO_2 + Li_xC_6 \rightarrow C_6 + LiCoO_2 \ (3)$$
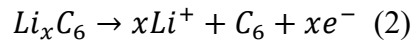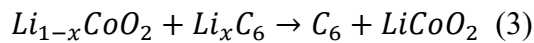
Charge process:

The cobalt element of the cathode is oxidized, and the de-lithiation reaction occurs:

$$LiCoO_2 \rightarrow Li_{1-x}CoO_2 + xLi^+ + xe^- \ (4)$$
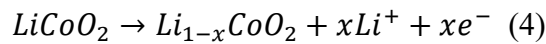
The graphite anode is reduced, and the lithium intercalation reaction occurs:

$$xLi^+ + C_6 + xe^- \rightarrow Li_xC_6 \ (5)$$

Total battery reaction is:

$$C_6 + LiCoO_2 \rightarrow Li_{1-x}CoO_2 + Li_xC_6 \ (6)$$
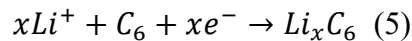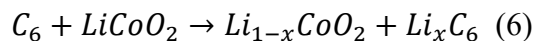
2.1.3. Research status of liquid electrolyte lithium battery

In order to ensure the smooth progress of the charging and discharging process, the basic components of the lithium battery are indispensable: the cathode, the anode, the electrolyte and the separator.

2.1.3.1. Cathode material

The cathode material accounts for about 40% of the lithium battery cost. In order to obtain high electrochemical performance, the cathode material needs to correspond several conditions [13]:

1. High discharge voltage (as large a voltage difference as possible from the anode material), which is beneficial to the design of high energy density batteries;

2. High electron and lithium-ion conductivity, which is the key factor for the efficient charge transport of the battery;

3. Ability to high intercalation capacity for lithium ions ensuring high specific capacity characteristics of the battery

4. High crystal structural stability, avoiding the structure collapses and deforms during the intercalation and deintercalation of lithium ions for high reversibility and long cycle life of the battery;

5. The simple cost-effective process for the preparation of cathode material;

At present, the research on cathode materials mainly focuses on lithium transition metal oxides, such as spinel oxide $LiMn_2O_4$ [14-15], layered metal oxide $LiCoO_2$ [16-17] or polyanionic oxide $LiFePO_4$ [18-19] et al. Each structure of the cathode material has its own unique advantages or values, so the methods for improving and modifying them are also very different. For example, $LiCoO_2$ as the most common cathode material, has excellent electrochemical properties, but its crystal structure is prone to change after multiple charge-discharge cycles. Surface modification of $LiCoO_2$ by doping Al_2O_3 or MgO can effectively improve the stability of the material and the cycle life of the battery [20-21]; For the $LiNi_{0.5}Mn_{0.5}O_2$ cathode material, although its overcharge resistance is good and the price is low, but its properties are greatly affected by temperature, especially the low temperature stability is poor. Use small amount of cobalt doping (from 5%) can improve the oxidation state electronic structure of oxygen and transition metal elements to improve its rate performance [22]; For the currently popular

LiFePO$_4$ material, the research mainly focuses on how to improve the electrical conductivity of materials, such as the use of conductive carbon materials for surface coating and element doping substitution when synthesis the materials [23-27].

2.1.3.2. Anode materials

In recent decades, even though more and more new anode material for lithium battery have been reported, but few of them can actually be commercialized. At present, the anode materials are still mainly natural graphite materials and artificial graphite materials. For the ideal anode material of lithium ions battery, it needs to meet [28]:

1. Low lithium intercalation potential, as close as possible to the redox potential of lithium metal;
2. High specific energy density per unit weight;
3. High electronic conductivity;
4. Low lithium-ion diffusion resistance inside the crystal structure;
5. Low cost and high lithiophilicity.

Similar to cathode materials, different structural properties of anode materials also endow the materials with different performance characteristics. Even if the crystal structure of the material is the same, different preparation and synthesis methods, doping processes, etc. will lead to different microstructures of the materials, resulting in large performance differences. For the most widely used graphite anode material at present, although it has high capacity (theoretical capacity is 372 mAh/g) and low lithium intercalation potential (< 0.01-0.2 V vs. Li/Li$^+$), it is prone to various side reactions with the normal organic liquid electrolyte (such as 1M LiPF$_6$ in EC). Therefore, the current commercial graphite anode material should be modified, such as surface coating or surface oxidation [29-30]. Cui et al. pretreated the graphite anode material with lithium sulfate on the surface, thicker solid electrolyte interface layer (SEI) formed on the electrode surface, thereby greatly improving the charge-discharge efficiency [31].

Silicon material (4200 mAh/g, < 0.4 V vs. Li/Li$^+$) is considered to be one of the most promising anode materials for lithium battery at present, but due to its large volumetric strain (up to 300%) during charging and discharging, it is easy to induce cause pulverization of the entire material, lithium ions will lose due to the SEI continually to crack, generate and consume, resulting in lower efficiency and

cycle stability. To solve this problem, the commonly used modification methods are designing porous structure, surface carbon coating, alloy composite and other techniques to improve its cycle stability [32-35].

2.1.3.3. Liquid electrolytes and additives

The liquid electrolyte can connect the anode and the cathode inside the battery, which has a great influence on the performance of lithium battery. To achieve high performance of lithium battery, the electrolyte should meet the following requirements [36]:

1. High ionic conductivity, $> 10^{-3}$ S/cm;
2. Wider electrochemical window range, which can ensure the stability when using high-voltage cathode or low-voltage anode materials;
3. Good compatibility with cathode, anode, electrode current collectors and separators, and will not cause chemical, thermochemical reactions damage to battery performance;
4. Environmentally friendly and high safety (nonflammable and nontoxic).

At present, the most common electrolyte is organic liquid electrolyte, which is mainly composed of lithium salt, organic solvent and additives. Compared with aqueous electrolytes, organic electrolytes have higher tolerable voltages. Although its electrochemical performance is excellent, its liquid properties make it still a big safety hazard in real application. For example, the endless explosion of mobile phones in recent years is caused by the short circuit of the cathode and anode inside the battery, and the thermal decomposition of the liquid electrolyte to generate gas. Therefore, the characteristic of the electrolyte plays an important role in ensuring the safety of lithium battery.

The role of electrolyte additives should not be ignored. For example, adding stabilizing additives can maintain the chemical and electrochemical stability of the electrolyte and improve the anti-decomposition ability of the electrolyte; adding flame retardant additives can improve the thermal stability of the electrolyte, which can greatly improve the safety performance of the battery under thermal-runaway conditions, prevent accidents as much as possible. Overall, the role of additives is to further improve the performance of the entire liquid electrolyte system, making it as close as possible to the requirements of the "ideal" electrolyte [37-38]. Till now the implementation of these kind of additives into the industry is inhibited by high price.

In addition, the in-depth understanding of the surface reaction mechanism between the electrolyte and the electrode, especially the formation and growth of the SEI layer, have a significant impact on the entire battery system.

2.1.3.4. Separator

The separator can protect from the direct contact between the cathode and anode and ensure the smooth migration of lithium ions. Therefore, the structural characteristics of the separator will directly affect the key performance of the battery. The next generation separator needs to have high compatibility with electrode materials in terms of mechanical properties and electrochemical stability. Specifically [39]:

1. Insulates electronic conductivity while ensuring high ionic conductivity;
2. High chemical and electrochemical stability;
3. High mechanical strength, bending resistance, folding resistance and puncture resistance under the condition of keeping the thickness as low as possible (< 25 μm to be compatible with commercial separator);
4. High thermal stability, small thermal shrinkage deformation.

Polyolefin-based film is currently the most widely used and most deeply researched lithium-ion separator material, such as polyethylene (PE) and polypropylene (PP), etc. Despite the widely crazing technology is mature and the cost is low, its poor thermal stability (shrinkage at temperature > 90°C) and liquid absorption limits its development in the field of high-power batteries or high-temperature batteries. At present, the modification of polyolefin-based separators mainly focuses on how to improve their lyophilic properties and high temperature resistance. Common modification methods such as surface coating with polymer resin, plasma irradiation grafting lyophilic monomers, etc. can significantly improve its lyophilic properties [40-42]. Although the liquid absorption performance can be significantly improved by the modification technology, the matrix structure is still polymer-based polyethylene in essence, and its thermal stability is poor and has not been significantly improved. Therefore, the organic-inorganic composite separator has become the focus of research. Organic-inorganic composite separators are often made of polyethylene separators or non-woven fabrics, and are prepared from inorganic ceramic particles with high thermal stability through different membrane-

forming methods, such as coating [43], electrospinning [44], molded and sintered at high temperature [45] and so on. The biggest problem of this type of composite separator is that the bonding force between the polymer and the ceramic particles is poor and easy to fall off. A common modification idea for this is to reasonably adjust the ratio of each component or optimize interfacial contact using advanced fabrication processes [46]. The focus of future research may be on the interface problem between the polymer and the ceramic particles and the optimization of the structure design, the research on the ion transport mechanism and kinetics in the composite separator is also beneficial to further improve the overall performance of the battery.

2.1.4. Chapter conclusion

On the whole, lithium batteries have a long history of development and play an important role in human production and life. The rapid development of science and technology and the huge changes in life patterns have put forward higher requirements for the performance of lithium batteries. Whether it is the material structure optimization of each component or the design of new battery assembly technology, it is ultimately hoped to achieve high safety, high energy density (> 400 Wh/kg) and high cycle stability (> 3000 cycles) of lithium batteries. Throughout the entire development process, solid-state lithium batteries are the promising candidate, and developing strategies of various components, including electrolyte, anode/electrolyte interface, and cathode design is the important roadmap to foster the practical application of the next generation batteries with improved performance and safety issues [47].
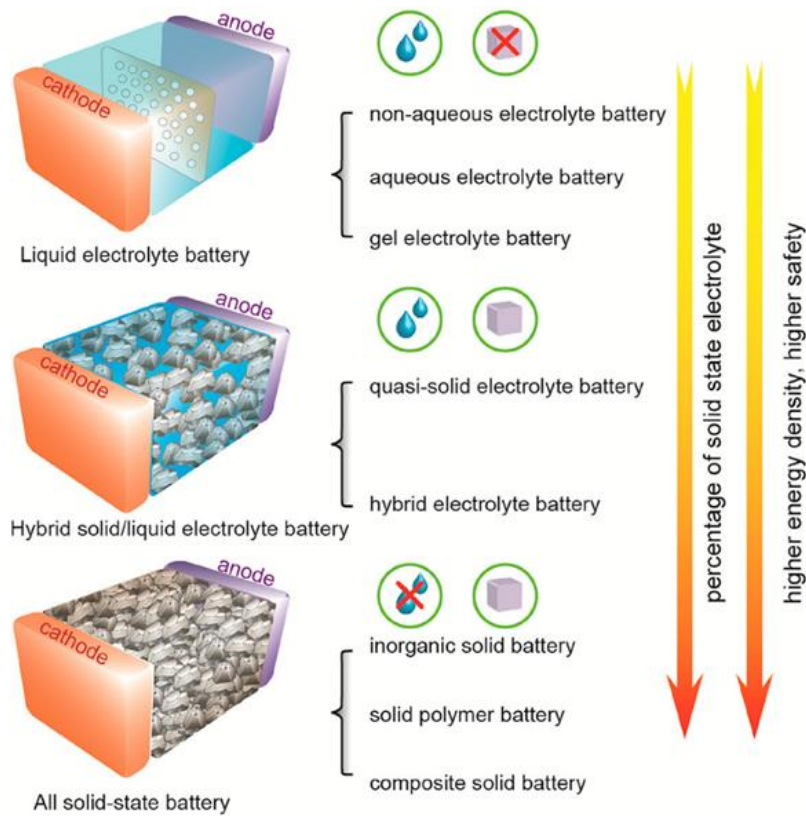
Figure. 2.2. Schematic illustration of the classifications of prevailing Li-ion batteries. Three types of batteries can be classified based on the amount of liquid and percentage of solid-state electrolyte (SSE) in the assembled batteries.

2.2. Transition from liquid to solid state electrolytes in lithium battery technology

2.2.1. The advantages of solid-state lithium battery

The best commercially available lithium-ion batteries (LIB) demonstrate specific energy ~ 250-270 Wh/kg. High speed development of portable electronics and electric vehicles requires improvement of specific battery characteristics and as a result, optimization of materials and cell design to achieve specific energy > 400 Wh/kg [48-50].
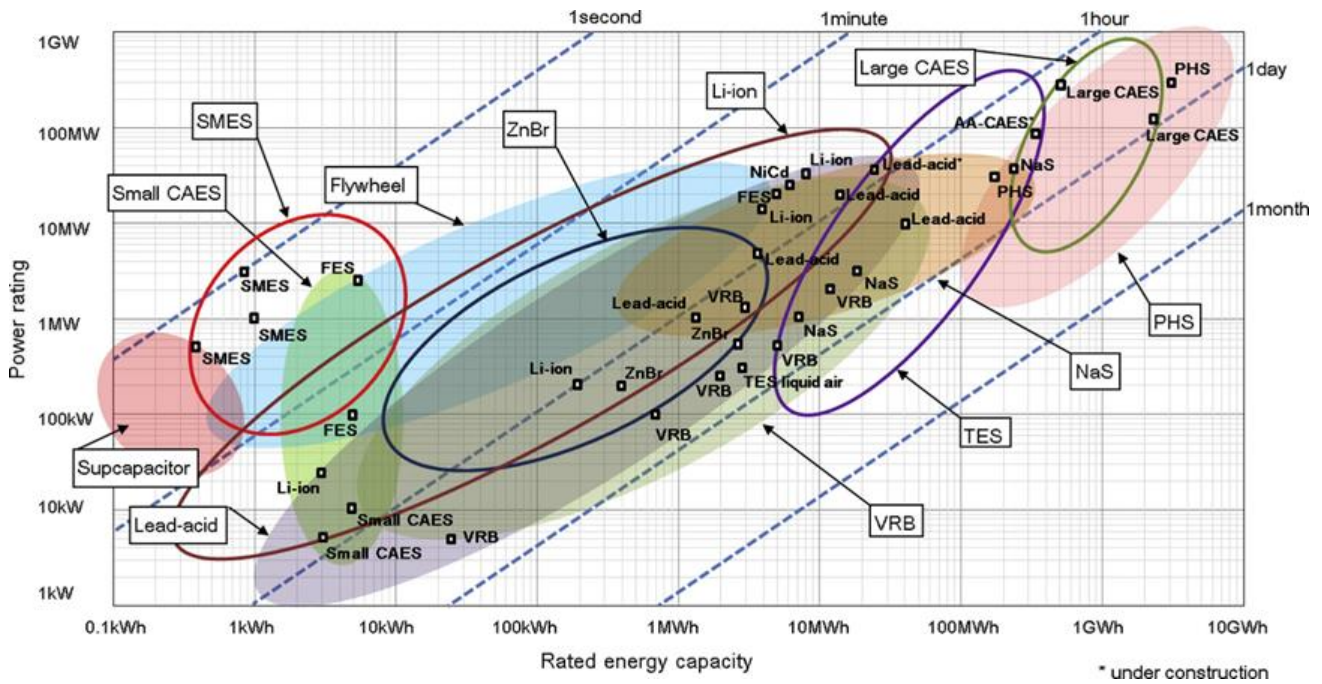
Figure. 2.3. Comparison of specific power and capacity for different types of batteries.
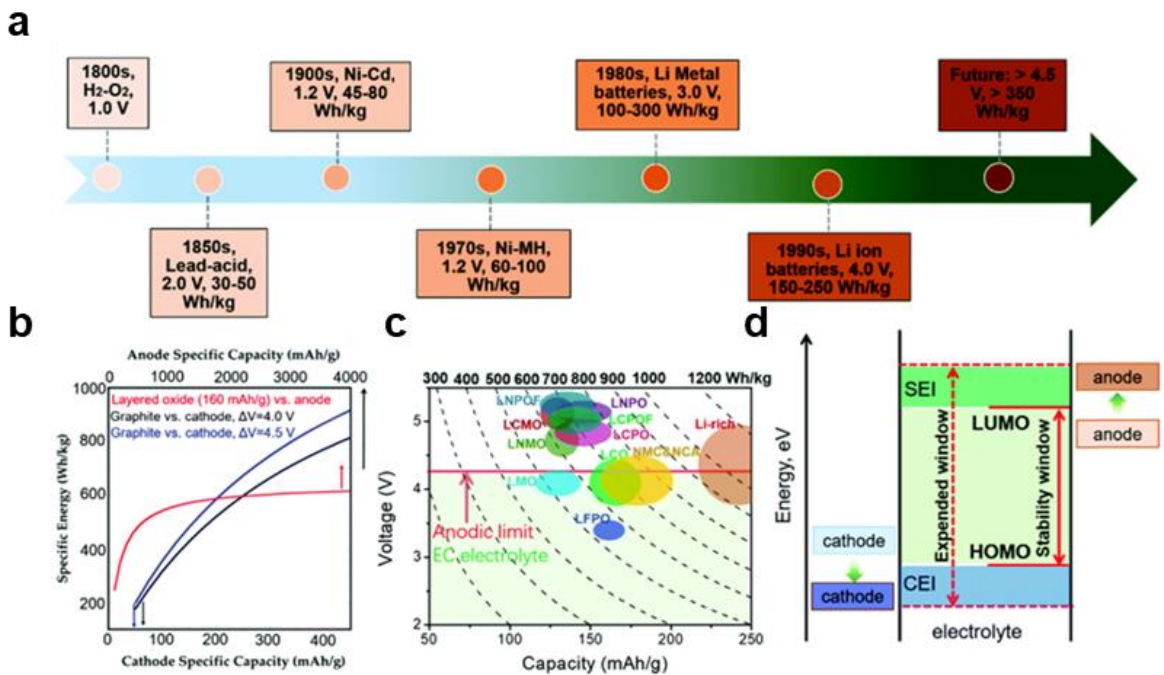
Figure. 2.4. (a) Milestones of reversible battery chemistries developed since 1800s until today. (b) Energy density variation of a battery by varying the capacity of cathode (dark and blue curve) and anode (red curve). The effect of voltage increase on the energy density is highlighted by the blue (4.5 V) and dark (4.0 V) curves. (c) The approximate reversible capacities and working voltage windows of the commercialized and intensively investigated intercalation cathode materials. The gravimetric energy density is calculated merely based on cathode materials. (d)

Schematic illustration of electrolyte working mechanisms in LIBs.

Thus, modern liquid electrolytes with high ionic conductivity (10^{-2}-10^{-3} S/cm) have a narrow potential stability window (< 4.0 V) and a low lithium-ion transfer number (~ 0.5-0.6). Also, organic electrolytes have a number of environmental disadvantages, such as toxicity and flammability. Moreover, they are not thermally stable at temperatures above 100ºC. One of the solutions to these obstacles is the use of solid-state electrolytes (SSE).

Compared with traditional lithium batteries, all components of solid-state batteries are solid, such as anode, cathode and electrolyte materials. In addition, the solid-state electrolyte not only play the role of conducting ions, but also can separate the anode and cathode as a separator. Therefore, the structure of the solid-state lithium battery is simpler, which can effectively save the preparation cost and widen the structural design direction of the irregular battery. In addition, solid-state lithium batteries have the following advantages:

1. High safety.

    The solid-state electrolyte is more stable in a wide temperature range (up to 500°C), generally non-volatile, non-flammable [47, 51]. Its implementation into battery doesn't require the cooling system of the battery pack in comparison with batteries with traditional organic liquid electrolytes.

2. High energy density.

    It is widely known that the performance of commercial lithium-ion batteries has basically reached the upper limit. It is necessary to develop high specific energy cathode materials and anode materials for next generation lithium batteries. For cathode materials, the development technical barriers are higher to break through the currently commonly used structural system; lithium metal anode has ultrahigh theoretical specific capacity (3860 mAh/g) and the lowest reduction potential (-3.04 V vs standard hydrogen electrode), however it was put aside by researchers due to battery safety accidents in the early years. In recent years due to its promising properties, the research on lithium metal anode has returned to the research focus. Of course, the biggest problem is the side reaction between lithium metal and the liquid electrolyte [52]. In addition, lithium dendrites are also an important reason to limit the development of lithium metal anode [53-55]. Excellent mechanical stability of solid-state

electrolytes to hinder the growth of lithium dendrites. From this point of view, solid-state lithium batteries can replace the currently available material systems to develop lithium batteries with better performance [56-57].

2.2.2. Major classifications of solid-state electrolyte

Ionic conductivity is a key property for solid-state electrolyte. However, for practical application in electrochemical energy storage and conversion systems, other basic properties are also important. The main properties required for solid-state electrolytes are: high ionic conductivity ($> 10^{-4}$ S/cm), high electronic resistance ($< 10^{-9}$ S/cm), high ionic selectivity, wide electrochemical stability range, good chemical compatibility with other components, excellent thermal stability, excellent mechanical properties, simple fabrication processes, low cost and environmental friendliness. Much progress has been made in improving the properties mentioned above, both with inorganic and organic (polymer) solid-state electrolyte materials.

2.2.2.1. Polymer-based solid-state electrolyte

The lithium conduction mechanism of polymer solid-state electrolytes is quite different from that of electrolytes. Lithium ions usually migrate in the amorphous region of polymers, including the ion migration formed by the local movement of lithium ions with the polymer molecular segments, and the ion migration formed by lithium ions within or between polymer chains. Therefore, reducing the glass transition temperature of the polymer, expanding the amorphous region (plasticizing), etc., are the main methods to optimize the performance of polymer-based solid-state electrolyte. Also, polymer-based solid-state electrolytes generally require the incorporation of lithium salts to obtain Li-ion conductivity.

The most promising polymer-based solid-state electrolytes are polyesters (a typical example is polyethylene oxide), polysiloxane, polycarbonates, polyacrylonitrile, polyvinylidene fluoride (and its copolymer with hexafluoropropylene), polymethyl methacrylate (plexiglass), and some polyionic liquids containing lithium salts and in the gel state (ionic gel). It is also worth noting that polymer-based solid-state electrolytes have a lower density, better physical contact with the electrode surface and easier to use technologically in comparison with ceramic solid-state electrolytes [58-60].
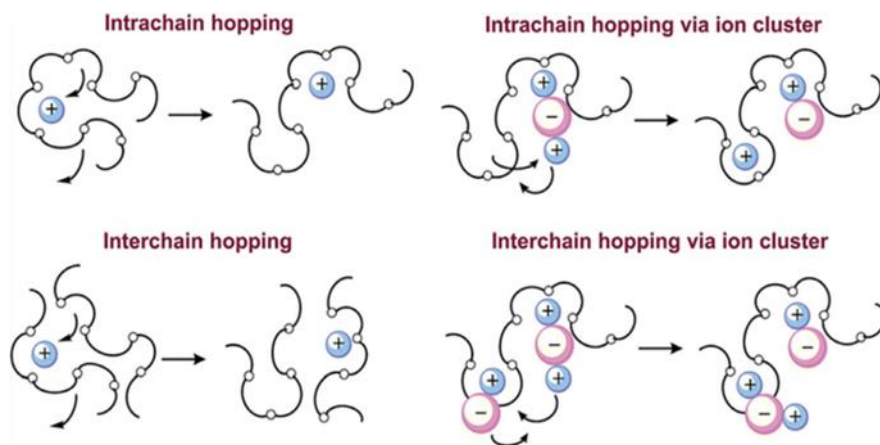
Figure. 2.5. Mechanism of ion transport in polymer-based solid-state electrolyte.

Polyethylene oxide (PEO) is the most well-studied polymer-based solid-state electrolyte [61]. Its dielectric constant is relatively high (amorphous state corresponds to a dielectric constant of 8), which can fully dissolve lithium salts; it has good physical contact properties with electrodes. However, at room temperature, the degree of crystallization is high and the ionic conductivity is low (10^{-8}-10^{-6} S/cm, the standard commercial liquid electrolyte as a reference is in the order of 10^{-3}-10^{-2} S/cm). Therefore, various treatment methods such as blending, block, grafting, adding plasticizers, adding fillers, etc. are needed to use. After effective treatment, the ionic conductivity of PEO SSE can reach the order of 10^{-4} S/cm at room temperature [62-63].
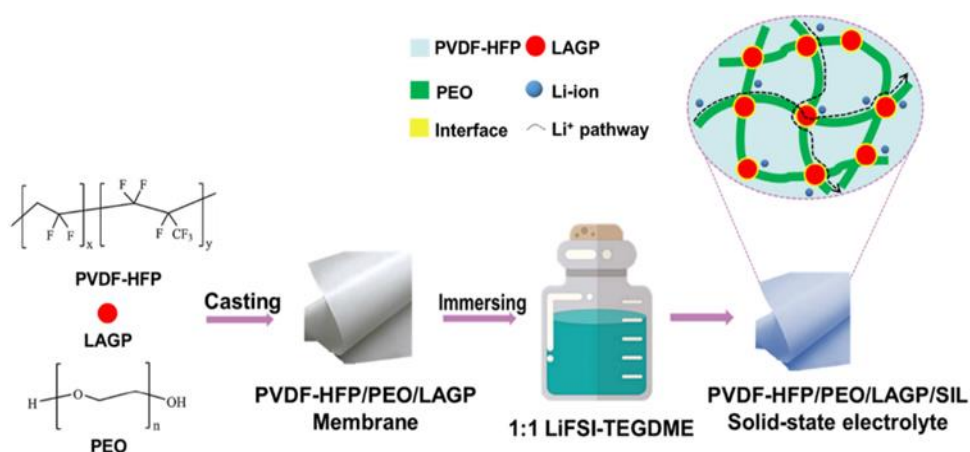
Figure. 2.6. The fabrication process of the hybrid (PVDF-HFP/PEO/LAGP/Ionic liquid) solid-state electrolyte.

Compared with polyethylene oxide, polysiloxane (PS) has better thermal stability (> 300-400°C), more flexible chain segment (determined by silicon-oxygen-silicon bond), lower glass transition temperature (~ -120°C) and stronger resistance to cathodic oxidation (> 4.2 V). However, its inherent

polarity is weak (dielectric constant 2.3-2.8), which makes the ability to dissolve lithium salts poor, which affects the conductivity of lithium ions. After grafting and block modification of polysiloxane (such as with polyethylene oxide block), its room temperature ionic conductivity can also reach the order of 10^{-4} S/cm [64].

Polycarbonate (PC) contains strongly polar carbonate groups, has high dielectric constant (2.8-3.8) and good segment flexibility, the room temperature ionic conductivity could achieve 10^{-5}-10^{-4} S/cm. However, it is difficult to manufacture on a large scale due to low stability. Therefore, it is difficult to become the first choice for polymer-based solid-state electrolytes [65].

In addition to being used as a binder for lithium battery electrode materials, polyvinylidene fluoride (PVDF) can also be used as a polymer-based solid-state electrolyte. PVDF and their copolymers (such as PVDF-HFP) have high dielectric constant (~ 8.4), good chemical stability (1.5-4.2 V) but low ionic conductivity ($< 10^{-6}$ S/cm), and their high crystallinity require effective modification for future application [66].

The purpose of filling the conventional polymer-based solid-state electrolyte matrix with inorganic fillers includes reducing crystallinity, forming Li-ion transport channels (at the interface between filler and matrix), and improving mechanical properties. Commonly used inorganic fillers include silicon dioxide, titanium dioxide, zirconium dioxide, barium titanate, and inorganic solid-state electrolyte powders, which can be either 0-dimensional materials (powders) or 1-dimensional materials (fibers). The uniform and stable dispersion of inorganic fillers in electrolytes and the exploration of suitable dosages are important subdivisions of polymer-based solid-state electrolyte scientific research, engineering and commercial applications [67].

2.2.2.2. Inorganic solid-state electrolyte

The lithium conduction mechanism of inorganic solid electrolytes is quite different from that of liquid electrolytes and polymer-based solid-state electrolytes. From the perspective of optimizing ionic conductivity, it is necessary to find inorganic solid-state electrolyte with suitable basic element composition and crystal structure, and analyze its lithium conduction mechanism (crystalline or amorphous state, grain lithium transport or grain boundary lithium transport, etc.). Inorganic solid-state electrolytes can be divided into oxides (perovskite, sodium superionic conductor, garnet,

amorphous LiPON, etc.), sulfide (crystalline lithium superionic conductor, amorphous sulfides, etc.), halides, etc. The lithium conduction mechanism of inorganic solid-state electrolytes is usually the transition of lithium ions between lattices framed by anions, so the defects and mismatches caused by appropriate element doping have a significant impact on the ionic conductivity. In addition to the bulk ionic conductivity, the interface contact between the electrode and the inorganic solid-state electrolyte is also very important [68-71].
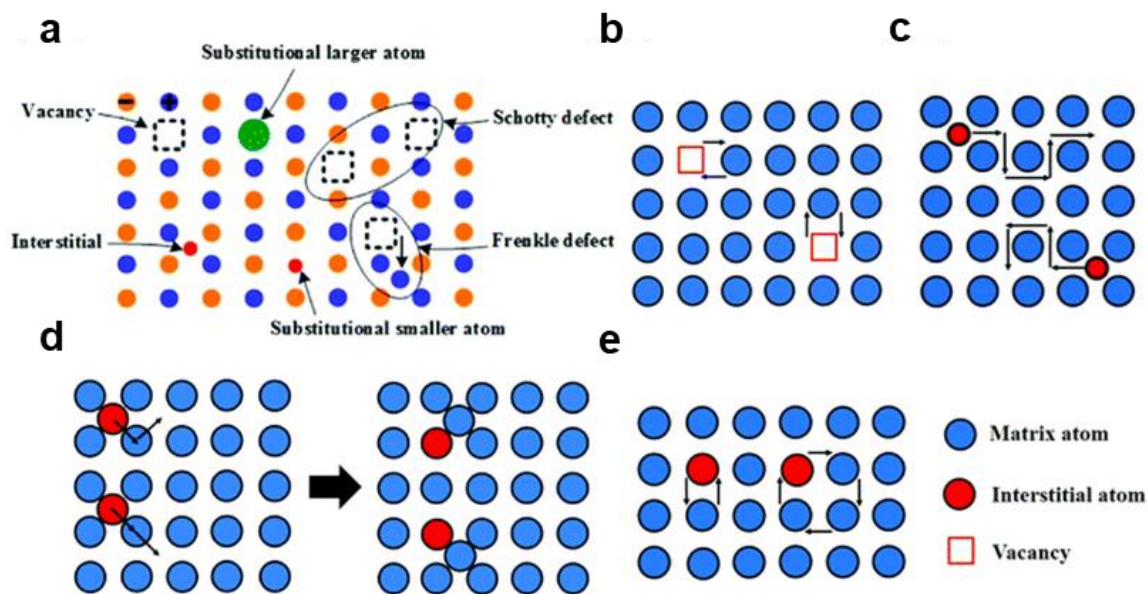
Figure. 2.7. Schematic diagram of various mechanisms of Li$^+$ transport in inorganic solid-state electrolyte. (a) Typical point defects, (b) Vacancy diffusion mechanism, (c) direct interstitial mechanism, (d) interstitial knock-off mechanism, and (e) direct exchange and ring mechanism.

2.2.2.2.1. NASICON solid-state electrolyte

NASICON type solid electrolyte, the full name of Sodium superionic conductor, is an important member of the inorganic solid-state electrolyte family. The general structural formula of NASICON-type solid electrolyte can be expressed as $AM_2(PO_4)_3$, where A= Li or Na, M= Ge, Ti, Zr, etc. Its basic skeleton structure is represented as $M_2P_3O_{12}$, that is, 2 MO_6 octahedrons and 3 PO_4 tetrahedra are connected to form a structural unit. In the framework structure, alkali metals occupy two structural sites, M1 and M2, and lithium ions are transported from M1 to M2 through the structural network formed by the MO_6 and PO_4 frameworks during transport [72-73]. The representative structure is

shown in Figure. 2.8.
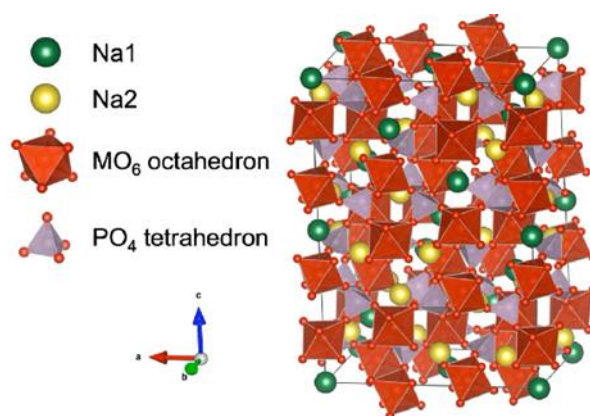
Figure. 2.8. Crystal structure of NASICON.

In addition, since adjacent MO_6 octahedra are separated by corner-sharing apex-connected PO_4, the electron orbital overlap and delocalization on the -M-O-M- transport chain is difficult to achieve, so the electronic conductivity of the NASICON structure is generally low ($< 10^{-6}$ S/cm). At the same time, the rigid skeleton structure of NASICON makes it more easily to change the structure by doping with multiple elements. In recent years, a series of other crystal structures derived from the parent crystal structure $LiTi_2(PO_4)_3$ or $LiGe_2(PO_4)_3$ have also become the focus of research. For example, partial replacement of Ti^{4+} or Ge^{4+} with heterovalent doping elements such as Al^{3+}, Ga^{3+}, Fe^{3+}, etc., has gradually developed into a unique NASICON structure category with high ionic conductivity into 2 orders of magnitude from 10^{-6}-10^{-4} S/cm [73-74].

2.2.2.2.2. Garnet solid-state electrolyte

The general crystal structure of the garnet-type solid electrolyte can be expressed as $A_3B_2(XO_4)_3$, where A, B, and X are 8-coordination, 6-coordination, and 4-coordination structures, respectively (Figure. 2.9) [75-77].
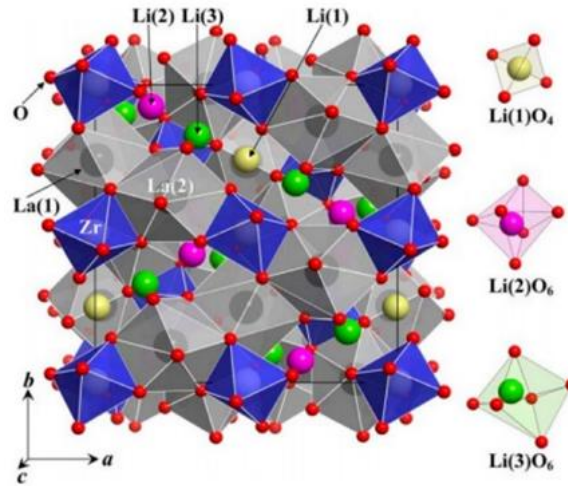
Figure. 2.9. Crystal structure of garnet solid-state electrolyte LLZO ($Li_7La_3Zr_2O_{12}$).

In 2003, Thangadurai et al. reported for the first time a garnet-structured solid-state electrolyte $Li_5La_3M_2O_{12}$(LLMO) (M= Nb, Ta) with an ionic conductivity of about 10^{-6} S/cm at room temperature. To increase the concentration of lithium ions, heterovalent doping of this structure was studied, which significantly improved the ionic conductivity. Thus, according to the change of lithium content in each structural unit, garnet-structured solid-state electrolyte can be divided into Li-3 series, $Li_3Ln_3Te_2O_{12}$ (Ln= Y, Pr, Nd, etc.), Li-5 series, $Li_5La_3M_3O_{12}$ (M= Nb, Ta, Sn, etc.), Li-6 series, $Li_6ALa_2M_2O_{12}$ (A= Ca, Sr, Ba, etc., M= Nb, Ta, etc.), Li-7 series, $Li_7La_3M_2O_{12}$ (M= Zr, Sn, Hf, etc.).

The ionic conductivity of garnet-type solid electrolytes is determined by several factors, including Li-ion concentration, Li-ion coordination environment, grain structure and grain boundary structure. For example, high Li-ion concentration is beneficial to improve the ionic conductivity, so the ionic conductivity gradually increases from Li-3 to Li-7 series; the lithium ion in the tetrahedral center (Li-3 series) has a weak Li-ion transport ability, and the lithium ion in the octahedral center (Li-5 to Li-7 series) has a strong Li-ion transport ability, so the number of lithium ions occupying the octahedral center directly affects the final Li-ion conductivity. In addition, there are two substructures in the Li-7 series, the cubic phase $Li_7La_3M_2O_{12}$ (M= Zr, Sn, Hf, etc.), and the arrangement of Li-ion is relatively disordered; The tetragonal phase $Li_7La_3M_2O_{12}$ (M= Zr, Sn, Hf, etc.), and the Li-ions are arranged in an orderly manner. Generally, the conductivity of cubic phase is 1-2 orders of magnitude higher than that of tetragonal phase, so it is often necessary to try various methods to stabilize the cubic phase. When Al^{3+} is doped, it generally enters the tetrahedral center, so doping Al^{3+} is an effective method to stabilize the cubic phase. In addition, the co-doping of Al^{3+} and Mg^{2+} is beneficial to improve the

environmental stability of the material, resulting in a significant reduction in the interfacial resistance with the Li anode. After elements doping modification, the ionic conductivity of the garnet solid-state electrolyte system can reach 10^{-4}-10^{-3} S/cm at room temperature [75, 78-79].

2.2.2.2.3. LISICON solid-state electrolyte

LISCON (lithium superionic conductor) type solid-state electrolyte has γ-Li_3PO_4 structure. The original LISCON solid state electrolyte, $Li_{14}ZnGe_4O_{16}$ was first reported by Hong et al., with 10^{-7} S/cm ionic conductivity at room temperature and 0.125 S/cm at 300°C.

In the $Li_{14}ZnGe_4O_{16}$, Ge, Zn, and Li occupy tetrahedral sites, and excess Li occupies octahedral interstitial sites, and the octahedron is coplanarly connected to the adjacent tetrahedron. A three-dimensional Li-ion transport channel can be formed inside the basic framework structure $[Li_{11}ZnGe_4O_{16}]^{3-}$, which is more favorable for Li-ion transport when there are vacancies in the center of the octahedron. Since all LISCON solid-state electrolytes have the same γ-Li_3PO_4 structure, various derivative structures can be formed by changing the chemical composition. The most typical example, $Li_{14}ZnGe_4O_{16}$ can be regarded as the solid solution of Li_4GeO_4 and Zn_2GeO_4. When Li_4XO_4 (X= Si, Ge, Ti, etc.) and Li_3YO_4 (Y= P, As, V, etc.) are combined, other series of LISCON solid-state electrolytes can be formed, which can be expressed as $Li_{3+x}X_xY_{1-x}O_4$. In this series, $Li_{3.5}Si_{0.5}P_{0.5}O_4$ has relatively high ionic conductivity up to 3×10^{-6} S/cm at room temperature [80-82].

However, the ionic conductivity of these materials at room temperature is really low (less than 10^{-6} S/cm). Replaced oxygen with sulfur and zinc with phosphorus, and obtained Li_4GeS_4-Li_3PS_4 (LGPS) based materials have been studied in the literatures. LGPS solid-state electrolyte and their derivatives have very high room temperature ionic conductivities, and $Li_{10}GeP_2S_{12}$ even reaches the order of 10^{-2} S/cm, which is the closest solid-state electrolyte system to commercial production today. However, the poor stability of LGPS due to hydrolysis in the air, passivation of the cathode, and continuous side reactions to the lithium anode limit its practical application [83].
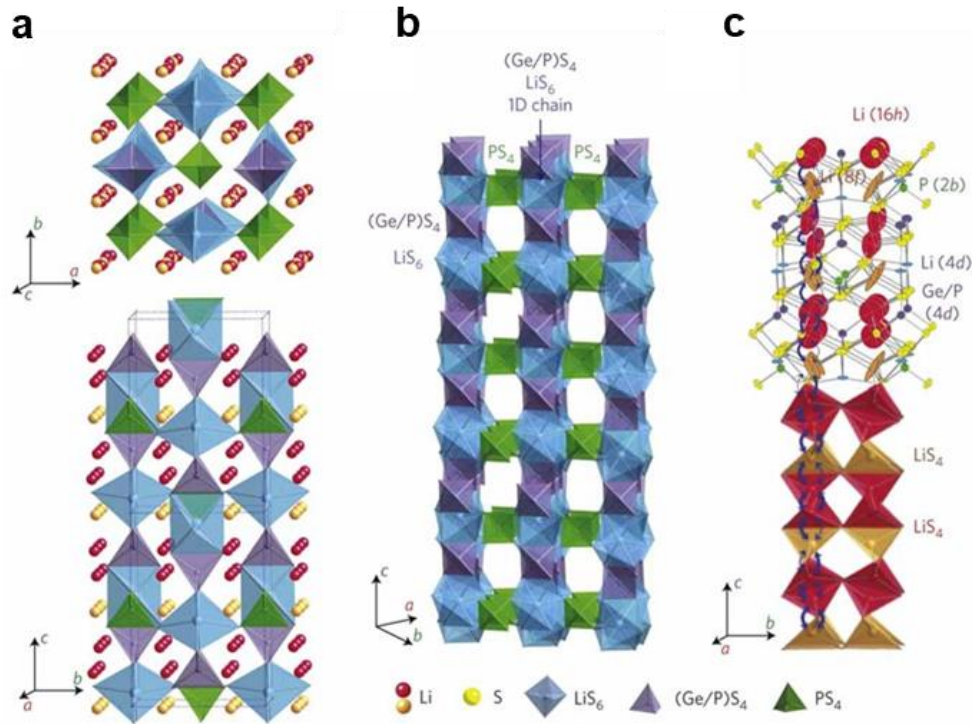
Figure. 2.10. (a) Crystal structure of LISCON. Red and yellow highlight Li^+ involved in ionic conduction; (b) Crystal structure of $Li_{10}GeP_2S_{12}$; (c) Conduction pathways of Li-ions.

The ionic conductivity of Argyrodite-structured solid-state electrolyte Li_7PS_6 is low, but the ionic conductivity is greatly improved to 10^{-2} S/cm after optimizing the composition to $Li_7P_3S_{11}$. After replacing part of sulfur with halogen to form Li_6PS_5X (X is a halogen ion, especially chlorine has the best effect, followed by bromine) solid-state electrolyte, the defects in the material system increase, and the ionic conductivity can be improved to 10^{-3} S/cm. After silicon, germanium and other elements replace part of phosphorus (at the same time, due to the consideration of ion size, halogen iodine with a large radius is used to match it), the ionic conductivity will be improved to a certain extent, such as $Li_{9.54}Si_{1.74}P_{1.44}S_{11.7}Cl_{0.3}$ could also reach 10^{-3} S/cm level. However, the sensitivity to water and oxygen and the narrow operating voltage range also limited the application of this type of solid-state electrolyte [84].
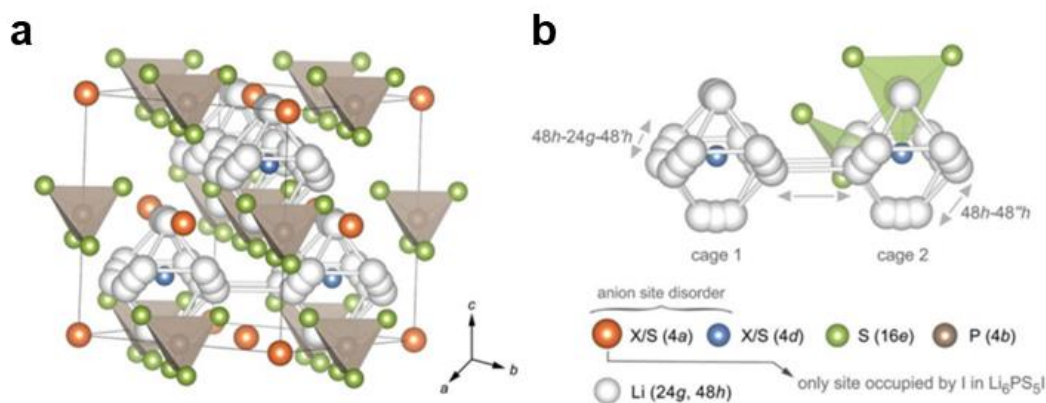
Figure. 2.11. (a) Crystal structure of Li_6PS_5X (X= Cl, Br, I). (b) Polyhedral containing Li^+, through which Li-ions are transported.

2.2.2.2.4. Perovskite solid-state electrolyte

The general structure of perovskite solid-state electrolyte is ABO_3. Schematic representation of crystal structure is shown in Figure. 2.12. The perovskite electrolyte can be represented as a framework formed by BO_6 octahedra, and the A-site exists in the center of 12 O atoms composed of 8 BO_6 octahedra.
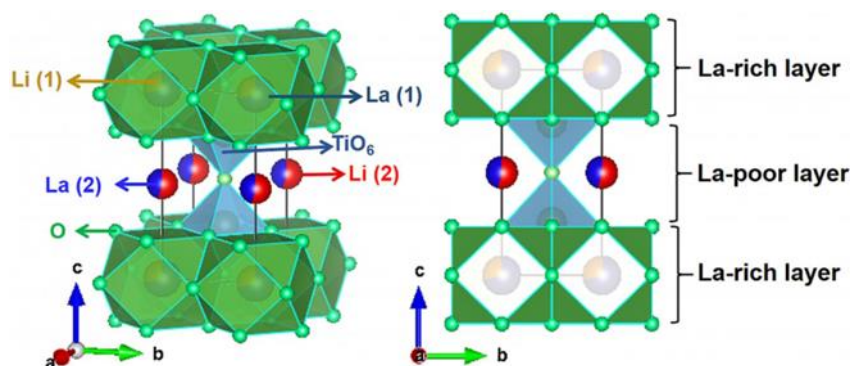
Figure. 2.12. Schematic representation of the perovskite structure LLTO solid-state electrolyte.

The perovskite structure has a high tolerance to the valence state and radius of A-site and B-site elements, so diversified and multifunctional perovskite functional materials can be developed. Brous etc. synthesized the perovskite-structured $Li_{0.5}La_{0.5}TiO_3$ (LLTO) for the first time by co-substituting the alkaline ions at the A-site with trivalent rare La^{3+} and monovalent alkaline cations (Li^+, Na^+, K^+). Inaguma etc. synthesized $Li_{3x}La_{2/3-x}\square_{1/3-2x}TiO_3$ ($\square$ is vacancy) series of solid electrolytes by regulating the substitution content of lithium ions, and the bulk ionic conductivity at room temperature up to 10^{-4}-10^{-3} S/cm, thus attracting extensive attention to $Li_{3x}La_{2/3-x}TiO_3$. Due to the asymmetric distribution

of La atoms, alternating formation of La-rich and La-poor layers, the perovskite structure electrolyte comparison is influenced by the lattice unit cell parameters and the relative Li-ion concentration. For Li-poor orthorhombic LLTO, high La-site occupancy and low vacancy lead to hindered Li-ion transportation; while Li-rich tetragonal LLTO often has higher ionic conductivity. When the occupancy of La element in Li-rich LLTO is low, the activation energy of Li-ions migration on the [001] direction is significantly reduced, resulting in a three-dimensional Li-ion transport channel. Meanwhile, the temperature-variable ionic conductivity data demonstrate that under high temperature conditions, the lattice distortion inside the crystal may change the Li-ion transport channel from two-dimensional to three-dimensional, and finally increase its overall Li-ion ionic conductivity [85-87].

2.2.2.3. Other typical solid-state electrolytes

In addition to solid-state electrolytes with typical structures, various new solid-state electrolytes have also received extensive attention.

The general structure of the anti-perovskite solid-state electrolyte can be expressed as Li_3OX. Due to the abundant lithium content in its general chemical formula, the anti-perovskite Li_3OX is also called lithium-rich anti-perovskite (LiRAP), large amount of lithium ions guarantees high ionic mobility, which facilitates high ionic conductivity. Since the perovskite or anti-perovskite structure has a large tolerance to the atomic radius and valence, the properties of solid electrolytes can be changed by manipulating the chemical composition, such as $Li_2(OH)_{0.9}F_{0.1}Cl$ with the room temperature conductivity up to 10^{-3}-10^{-2} S/cm, and it also has wide electrochemical stability window range. It is reported that the sintering preparation process and the intrinsic structure of the material are the key factors affecting the Li-ion ionic conductivity, indicating the changes in the microstructure, such as vacancy formation, local distortion., the local order-disorder transition will have a huge impact on the final ionic conductivity [88-90].
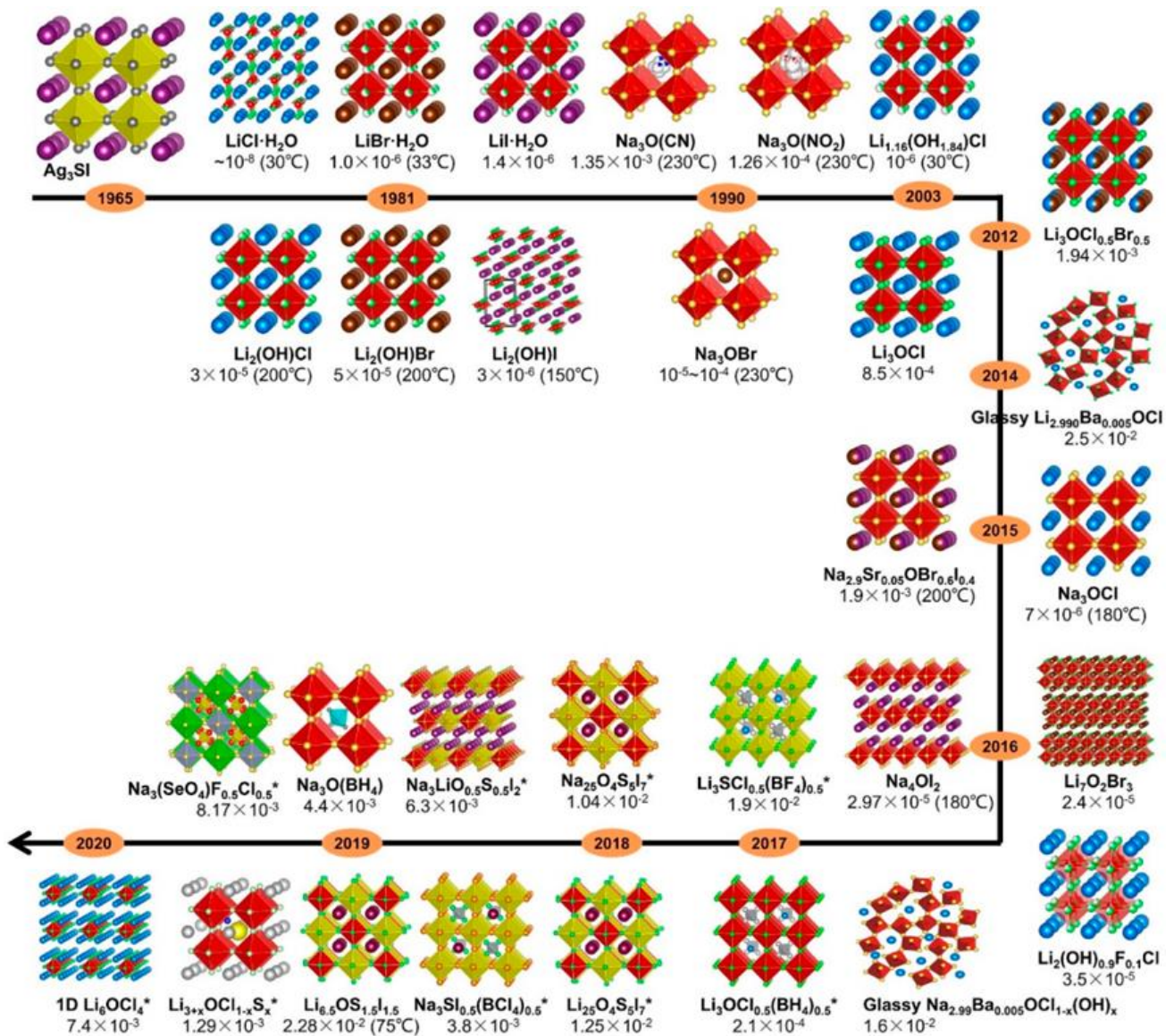
Figure. 2.13. Development of Li$^+$/Na$^+$ conducive anti-perovskite solid-state electrolytes versus year.

Another typical solid-state electrolyte, LiPON is also the focus of research and plays a crucial role in thin-film batteries. LiPON can be prepared by magnetron sputtering Li$_3$PO$_4$ target in N$_2$ atmosphere. Recently, some literatures have showed Li$_{3.6}$PO$_{3.4}$N$_{0.6}$ solid-state electrolyte by mechanical synthesis method, and its room temperature conductivity can reach 3.0×10^{-7} S/cm [91-94]. Since the thickness of the prepared solid-state electrolyte film is only few hundred nanometers, its low ionic conductivity is not a major problem. Thin-film batteries based on LiPON solid state electrolytes have been commercialized in some special fields, such as miniature medical devices or microelectronic components. However, it is precisely because the small size of the thin-film battery will limit its capacity that the application in the field of energy storage or power vehicles with high energy density

is still a problem. Nonetheless, the compatibility of LiPON solid state electrolyte with Li metal anode and the interfacial stability with most high-voltage cathodes materials make it an ideal buffer interlayer that can be used in all-solid-state batteries together with other solid-state electrolyte.

The binary sulfide system $Li_2S-M_xS_y$ is another important amorphous sulfide electrolyte, and its ionic conductivity can generally be as high as $10^{-4}-10^{-3}$ S/cm. Compared with oxide amorphous solid-state electrolytes, sulfide systems often have higher ionic conductivity due to their easily polarizable property and weaker interaction between S atoms and Li atoms. In addition, its higher mechanical softness and lower interfacial resistance make amorphous sulfide electrolytes more promising for planned production and use in the field of all-solid-state batteries system [95-97].

2.2.3. Comparison between different solid-state electrolytes

2.2.3.1. Comparison of ionic conductivity

After analyzing the basic performance characteristics of solid-state electrolytes, we compared and analyzed the key indicators of solid-state electrolytes that affect the process of industrialization. Some sulfide solid-state electrolytes are comparable to liquid electrolytes in terms of bulk ionic conductivity. However, if the bulk phase, grain boundary and electrolyte/electrode interface impedance are considered comprehensively. The overall impedance of solid-state electrolytes is 2-3 orders of magnitude greater than that of liquid electrolytes [47, 98].
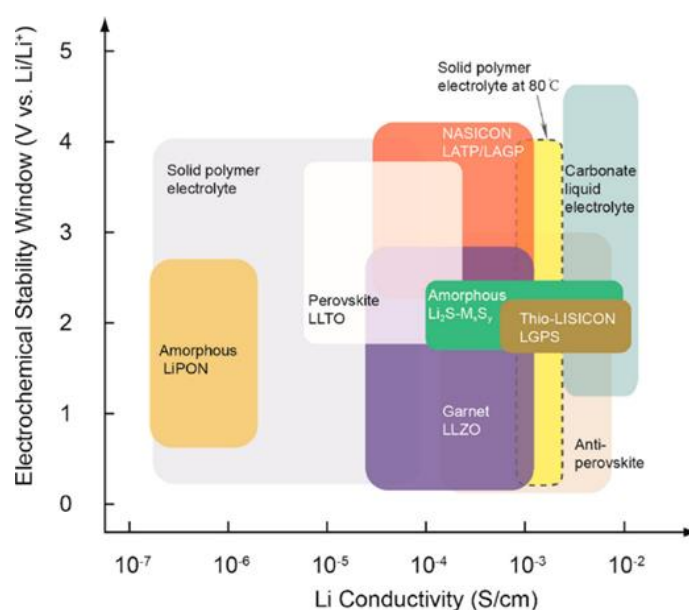
Figure. 2.14. Ionic conductivity of the main solid-state electrolyte system.

2.2.3.2. Chemical and electrochemical stability

In terms of chemical stability, the intrinsic electrochemical windows of most solid-state electrolytes are not satisfactory, or they are easily oxidized by high-voltage cathode, or easily reduced by lithium metal anode, or both.
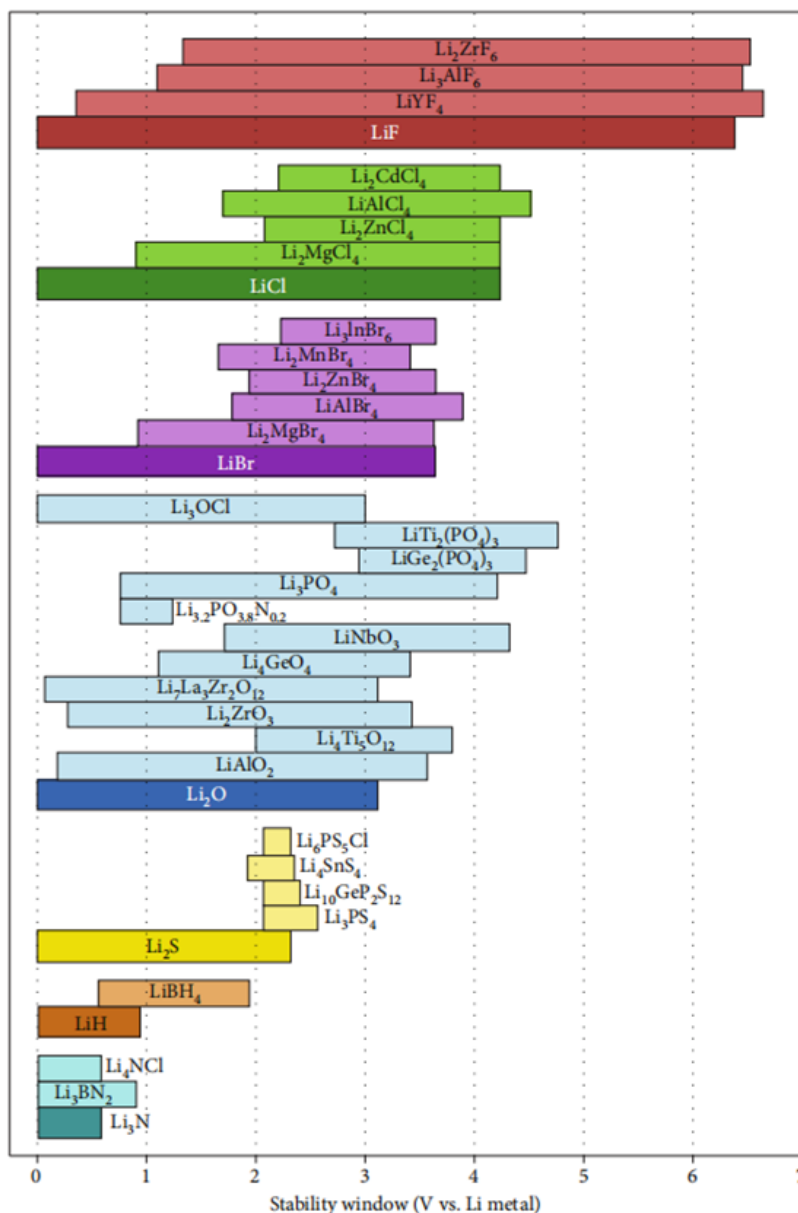
Figure. 2.15. Comparison of electrochemical stability windows of different solid-state electrolytes.

After considering the kinetic stability, the practical electrochemical window of the solid-state electrolyte is broadened to a certain extent (the formation of lithium ion conductive and electronically insulating nanolayers on the surface of the cathode and anode can correspond to kinetic stability);

Solid-state electrolytes corresponding to strong central ions, and solid-state electrolytes in which metals corresponding to central ions can be alloyed with lithium are generally not resistant to reduction by lithium metal. Most polymer solid-state electrolytes are passivated to lithium metal but unstable at high voltage, and some systems such as polynitrile are stable at high voltage but unstable to lithium metal anode [100-101].
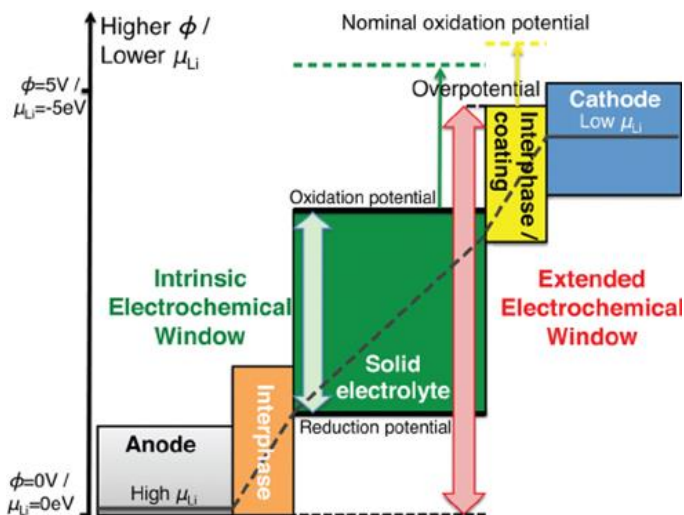
Figure. 2.16. Schematic illustration of the method for expanding the electrochemical window of solid-state electrolytes.

The thermal stability of solid-state electrolytes is better than that of liquid electrolytes, especially oxide systems. Excellent thermal stability also improves overall battery safety [47, 102].
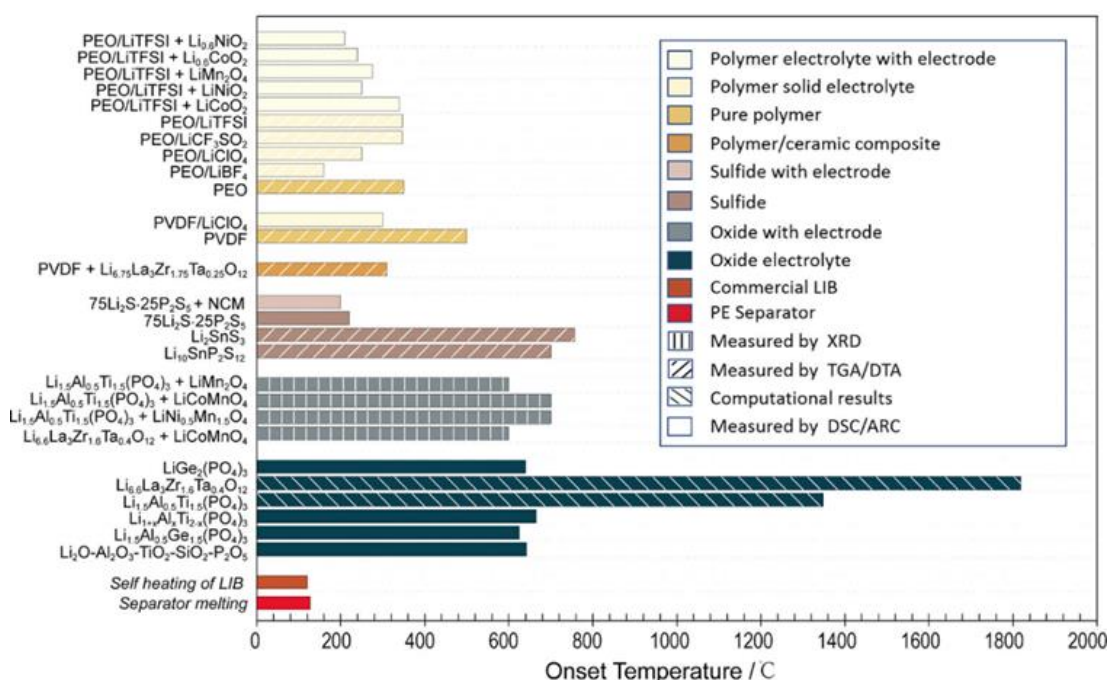
Figure. 2.17. Comparison of onset temperature of exothermal behaviors for different solid-state electrolytes.

The physical contact ability between the polymer-based solid-state electrolyte and the electrode is good, and the overall contact ability of the inorganic solid electrolyte is average. On the cathode side, commonly used solutions include oxide sintering, sulfide high pressure, etc.; on the anode side, solutions include surface-modified solid-state electrolytes, etc. In addition, lithium dendrites may still be generated on the anode side during battery cycling, which imposes requirements on the hardness, thickness, density, and current density of the solid-state electrolyte to varying degrees. At the same time, considering the reduction resistance of the solid-state electrolyte, the physical contact ability with lithium, the electrochemical stability during cycling, and the generation and development of lithium dendrites, the corresponding scientific exploration is still ongoing.

2.2.3.3. Mechanical stability

Although the electrochemical characteristic of solid-state electrolytes is the main aspect of materials development, the mechanical properties are also an important factor for their practical application. During the charge-discharge process of the battery, along with the insertion and de-insertion of Li-ions, the electrode material usually undergoes volume changes. Based on the characteristics of solid-state electrolytes, volumetric changes in electrode materials can lead to stress changes during electrochemical cycling, leading to potential mechanical instability and resulting mechanical failure.

There are mainly two reasons for the volume change of electrode materials, volume change based on stoichiometry (the effect of insertion and de-insertion of Li-ions on the lattice constant) and volume change based on phase transition. A typical example is the common $Li_xMn_2O_4$ cathode material. The data in the references show that the volume change of this cathode material mainly has three stages:

1. When x<0.7, with the insertion of Li-ions, the lattice parameters (c) are almost unchanged.
2. When 0.7<x<1.0, with the insertion of Li-ions, the lattice parameters (c) have increased (~ 1.2%)
3. When 1.0<x, with the insertion of Li-ions, the electrode material undergoes a transformation from a cubic phase to a tetragonal phase, resulting in a significant lattice parameter change (c)

(~ 12.3%), equivalent to a volume change of about ~ 6.5%.

It is in marked contrast to the $Li_4Ti_5O_{12}$ anode material, which exhibits a maximum volume change of about ~ 0.3% during cycling. Based on common sense, since the internal size and space of the assembled battery are fixed, the volume change of the electrode material is a direct manifestation of the stress load (from Mpa to GPa level) on the solid-state electrolyte during cycling. Therefore, solid-state electrolytes should have certain mechanical properties.

Table. 2.1. Brief collection of mechanical properties of solid-state electrolytes.

Electrolyte	Compound	Test method	Elastic modulus (GPa)	Hardness	Fracture toughness (MPa·m$^{0.5}$)
Sulfide	$Li_2S-P_2S_5$	RUS	18-25	-	-
	$Li_2S-P_2S_5$	Indentation	~18	-	0.23±0.04
LISICON	$Li_{10}GeP_2S_{12}$	Sim	37	-	-
LiPON	$Li_xPO_yN_z$	Nano	77	3.9	-
NASICON	$Li_{1.3}Al_{0.3}Ti_{1.7}(PO_4)_3$	Strain-stress	81-115	7.1	1.1
	$LiTi_2(PO_4)_3$	Sim	143.7	-	-
Garnet	$Li_7La_3Zr_2O_{12}$	Nano	124-163	9.0-11.8	-
	$Li_7La_3Zr_2O_{12}$	Indentation	-	6.8-9.9	0.60-0.82
	$Li_7La_3Zr_2O_{12}$	Nano	145.6±7.3	8.5±0.4	0.99±0.05
	$Li_{6.24}La_3Zr_2Al_{0.24}O_{11.98}$	RUS	149.8±0.4	6.3±0.3	-
	$Li_{6.19}La_3Zr_2Al_{0.27}O_{12}$	Nano	135-140	4.3-9.1	1-1.3
	$Li_{6.24}La_3Zr_2Al_{0.24}O_{11.98}$	Indentation	-	-	0.86-1.63
	$Li_{6.17}La_3Zr_2Al_{0.28}O_3$	Sim	146-163	-	-
Perovskite	$Li_{0.33}La_{0.57}TiO_3$	RUS	186-200	-	0.89-1.34
	$Li_{0.33}La_{0.57}TiO_3$	Indentation	200±3	9.5±0.7	1±0.04
	$Li_{0.33}La_{0.57}TiO_3$	RUS	223	-	-
	$Li_{0.33}La_{0.57}TiO_3$	RUS	143-203	8.1-9.5	1.15-1.24
	$Li_{0.5}La_{0.5}TiO_3$	Sim	233.9-262.5	-	-

RUS: resonant ultrasound spectroscopy; Nano: nano-indentation; Stress-Strain: slope of stress-strain curve; Sim: simulation;

According to the Monroe's linear elasticity theory the shear modulus of the electrolyte needs to be two times higher than the Li metal, which is related to the elastic modulus. For the ceramic materials

used as solid-state electrolyte, hardness and fracture toughness are also key properties for application, as they describe the ability of the material to resist penetration of the lithium dendrites and the fracture. In addition, as the ceramics that are brittle possess an inherent scatter in fracture stresses, the fracture reliability analysis is important for ceramic electrolytes to understand the brittleness property. Thus, the mechanical properties, like elastic modulus, hardness and fracture toughness, of the electrolyte materials are essential to be investigated for further battery cell design. Some investigations on the mechanical properties other than the electro-chemical properties of the electrolytes have been reported, as listed in Table. 2.1. In addition, the comprehensive mechanical properties of solid-state electrolytes are also affected by a series of external factors, such as the relative density after sintering, the second phase, and the relative grain size, etc. This is also a problem that should be explored in detail before the practical application of solid-state electrolytes [103].

2.2.4. The effect of scale on the transfer of lithium ions
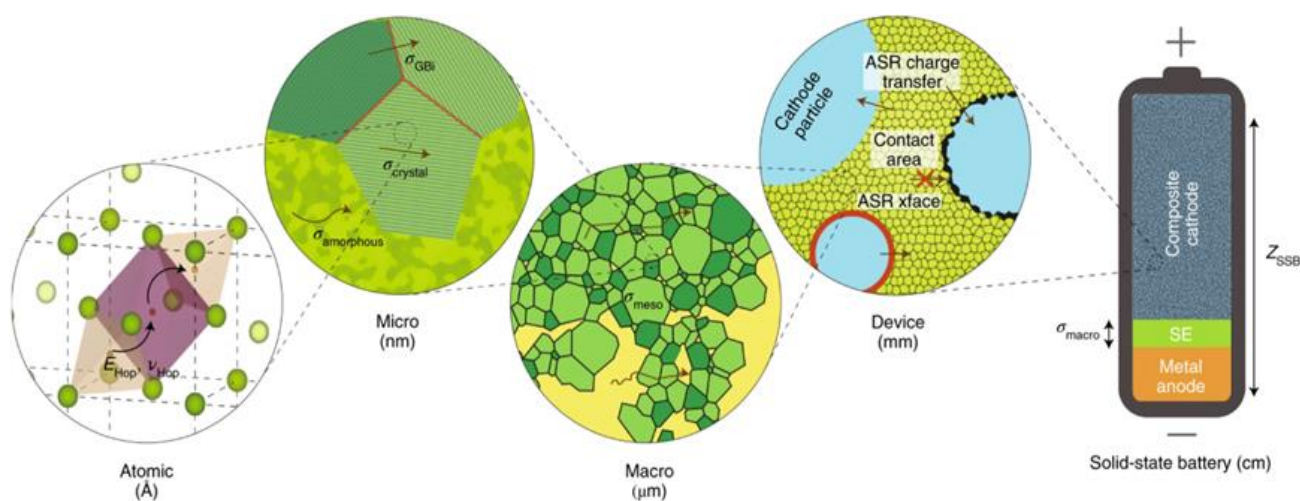
Figure. 2.18. Multiscale ion transport and major associated techniques.

The migration of Li-ions in solid-state batteries is a multiscale process, encompassing multiple scales from the atomic to the device scale [70, 99].

1. Atomic scale

   At the atomic scale, ions diffuse through solids along specific migration paths. These sites and their energies are mainly determined by the local ionic coordination environment. In crystalline compounds, these sites are usually octahedral or tetrahedral sites. The mobility of

ions in the material is therefore related to the sites defined by the anionic framework and the interconnections between sites. This is the underlying route for regulating the bulk ionic conductivity of solid-state electrolytes by chemical doping.

2. Nano, Micro and Mesoscopic scales

Compositional and structural inhomogeneities at the nano- and micro-scale often determine macroscopic ionic conductivity, whether beneficial or detrimental. For example, the grain boundaries are significantly different in structure and chemical composition from bulk grains. Grain boundaries are generally believed to increase the resistance for ions migration. Therefore, the ionic conductivity of materials can be increased by adjusting the concentration of grain boundaries. Glass-ceramic ionic conductors originate from the controlled crystallization process of the amorphous phase. In some solid-state electrolytes, the glass-ceramic phase can stabilize some metastable crystal structures and increase their ionic conductivity by several orders of magnitude, such as $Li_7P_3S_{11}$. Recent studies have shown that ion conductors previously thought to be amorphous may be nano-crystallites embedded in an amorphous matrix, such as Li_3PS_4. These nanocrystalline materials also may enhance ion transport through surface conduction mechanisms.

Another source of impedance in solid-state batteries is insufficient physical contact between electrodes and electrolytes. There must be intimate contact between the polycrystalline material and the solid particles in the composite electrode to ensure efficient ion transport. The existence of holes and voids means tortuous paths of ion transport and non-uniform current density. These factors cause an observe increase in impedance at the macroscopic scale. Therefore, the densification of polycrystalline solid-state electrolytes is very important, but the mechanical properties and processing properties of the materials are also should be considered.

3. Macro scale

The ionic conductivity of solid-state electrolytes is usually obtained by measuring impedance spectroscopy on macroscopic samples (electrolyte tablets etc.). Impedance spectroscopy is sensitive to structural features at all scales previously mentioned and can show total ionic conductivity. Point contacts, grain boundaries, amorphous phases, pores, voids, cracks and impurity parts can be resolved by fitting the total spectrum, but the fitting of the

impedance spectrum is usually based on empirical assumptions based on the observed capacitance.

4. Device scale

The impedance of the device includes not only the impedance of the material, but also the impedance of the interface phase that may be formed. Macroscopically high ionic conductivity solid-state electrolytes and high-performance electrodes do not necessarily combine to produce high-performance solid-state batteries. The solid-state electrolyte may decompose upon contact with the electrode material, creating an ion-blocked interlayer. So, for composite electrodes system, special 3D structural engineering must be performed to ensure adequate contact between the solid-state electrolyte and the electrode, at the same time, appropriate pressure is also an indispensable factor.

2.2.5. Chapter conclusion

In the table, we once again summarize the advantages and disadvantages of various mainstream solid-state electrolytes [104].

Table. 2.2. Summary of solid-state electrolyte materials for lithium battery.

Type	Materials	Conductivity $(S\,cm^{-1})$	Advantages	Disadvantages
Oxide	Perovskite $Li_{3.3}La_{0.56}TiO_3$, NASICON $LiTi_2(PO_4)_3$, LISICON $Li_{14}Zn(GeO_4)_4$ and garnet $Li_7La_3Zr_2O_{12}$	$10^{-5}-10^{-3}$	• High chemical and electrochemical stability • High mechanical strength • High electrochemical oxidation voltage	• Non-flexible • Expensive large-scale production
Sulfide	$Li_2S-P_2S_5$, $Li_2S-P_2S_5-MS_x$	$10^{-7}-10^{-3}$	• High conductivity • Good mechanical strength and mechanical flexibility • Low grain-boundary resistance	• Low oxidation stability • Sensitive to moisture • Poor compatibility with cathode materials
Hydride	$LiBH_4$, $LiBH_4-LiX$ (X = Cl, Br or I), $LiBH_4-LiNH_2$, $LiNH_2$, Li_3AlH_6 and Li_2NH	$10^{-7}-10^{-4}$	• Low grain-boundary resistance • Stable with lithium metal • Good mechanical strength and mechanical flexibility	• Sensitive to moisture • Poor compatibility with cathode materials
Halide	LiI, spinel Li_2ZnI_4 and anti-perovskite Li_3OCl	$10^{-8}-10^{-5}$	• Stable with lithium metal • Good mechanical strength and mechanical flexibility	• Sensitive to moisture • Low oxidation voltage • Low conductivity
Borate or phosphate	$Li_2B_4O_7$, Li_3PO_4 and $Li_2O-B_2O_3-P_2O_5$	$10^{-7}-10^{-6}$	• Facile manufacturing process • Good manufacturing reproducibility • Good durability	• Relatively low conductivity
Thin film	LiPON	10^{-6}	• Stable with lithium metal • Stable with cathode materials	• Expensive large-scale production
Polymer	PEO	10^{-4} (65–78 °C)	• Stable with lithium metal • Flexible • Easy to produce a large-area membrane • Low shear modulus	• Limited thermal stability • Low oxidation voltage (<4 V)

The NASICON solid-state electrolyte, based on its high ionic conductivity (higher than 10^{-4} S/cm) at room temperature, low cost (no rare elements), stable in air and water, and wide electrochemical window (2.8-4.8V vs Li/Li$^+$), makes it as one of the important options for large-scale commercialization solid-state electrolyte batteries. Therefore, follow chapter is devoted to discusses the current literature about the synthesis, sintering, characterization and electrochemical testing of solid-state electrolytes based on the NASICON system.

2.3. Preparation of $Li_{1+x}Al_xTi_{2-x}(PO_4)_3$ conductive solid-state electrolyte ceramic with NASICON structure

Approaches to the preparation of $Li_{1+x}Al_xTi_{2-x}(PO_4)_3$ solid-state electrolytes can be divided into solid state and wet-chemical methods. Solid methods include solid state reaction, melt-quenching and vacuum deposition. Wet methods include sol-gel, co-precipitation and self-assembly (through dissolution or evaporation). After that, ordinary sintering in muffle furnace or fast sintering can be used

to densify the solid-state electrolyte tablets or membrane prepared by the pressing method, casting method and spraying method, then obtain a solid-state electrolyte ceramic with certain ionic conductivity, density and mechanical strength.

2.3.1. Synthesis of precursor powders

2.3.1.1. Solid method

2.3.1.1.1. Solid-state reaction method

The general flow of the method is as follows: precursors are mixed and milled by wet ball milling method, followed by calcination and sintering at high temperatures (700-1200°C) and long holding times (~10 hours). The resulting samples usually have a highly crystalline structure, large grains (>5~10 μm), fewer grain boundaries, high ionic conductivity (bulk ionic conductivity >10^{-3} S/cm, total ionic conductivity >10^{-4} S/cm) and high relative density. However, the loss of lithium during prolonged heat treatment and the formation of side phases are the main disadvantages of this approach, which affect the Li-ion conductivity. Sintering parameters, such as temperature and time, affect the phase, relative density, and ionic conductivity and mechanical properties of the final product [105-106].

2.3.1.1.2. Melt-quenching method

The conventional melt-quenching method usually requires heating the inorganic salt mixture to a molten state at high temperatures (>1250-1450°C), and then quenching it onto a pre-heated metal plate (~ 500°C). Crushing the glass and reheating amorphous glass again for crystallization. In the synthesis of solid-state electrolytes by this method, the density, ionic conductivity, and phase purity are affected by three main factors: the composition of precursors, sintering methods, and temperatures [107-109].
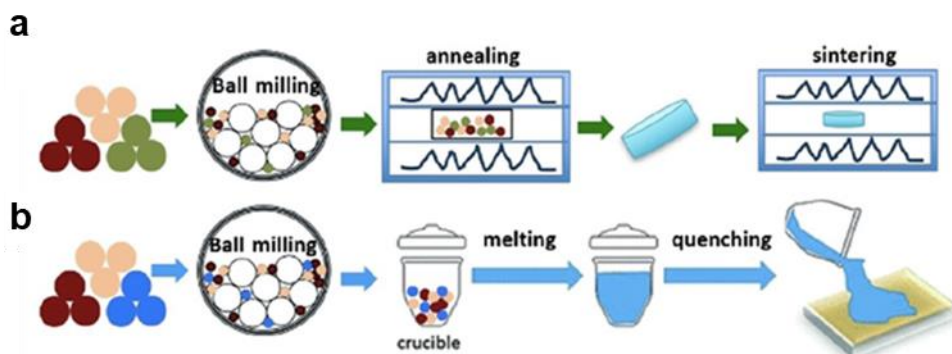
Figure. 2.19. Schematic diagrams of solid methods to the synthesis of NASICON solid-state electrolyte: (a) solid-state reaction method; (b) melt-quenching method.

2.3.1.2. Wet-chemical methods

Wet-chemical methods in comparison with solid-state reaction method and melt-quenching method, require lower heat treatment temperatures and allow better control of particle size and morphology in solid-state electrolytes. Liquid method includes sol-gel, co-precipitation, and chemical vapor deposition (CVD).

2.3.1.2.1. Sol-gel method

Sol-gel synthesis of solid-state electrolytes proceed through intermediate stages of formation of a colloidal solution and further cross-linking followed by annealing (Figure. 2.20). The sol-gel method makes it possible to obtain nanoparticles (down to 100-50 nm) and as a result, solid-state electrolyte at lower annealing temperatures and shorter time compared to solid-state reaction method and the melt-quenching method. In addition, the sol-gel method allows the synthesis of solid-state electrolytes on an industrial scale [110-112].
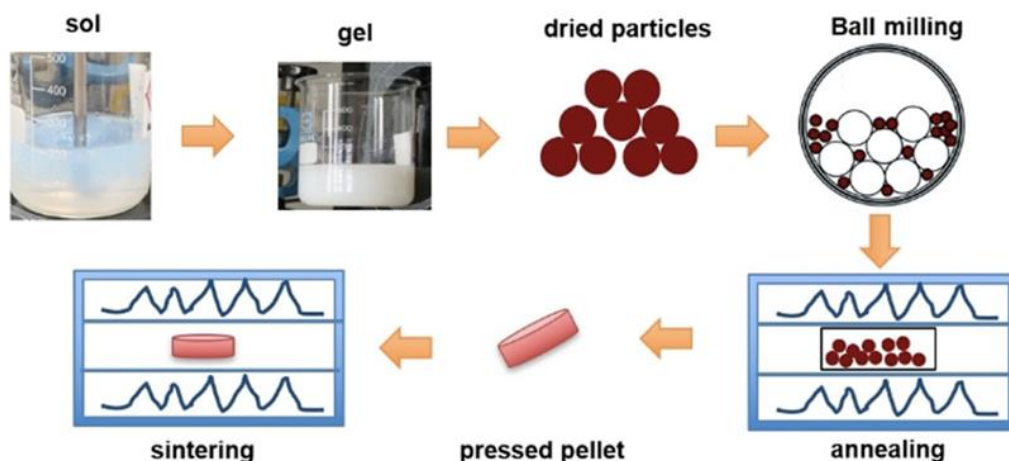
Figure. 2.20. Schematic representation of the sol-gel process for the synthesis of solid-state electrolyte.

For example, in literature [113] the process of obtaining solid-state electrolyte $Li_{1.5}Al_{0.5}Ti_{1.5}(PO_4)_3$ by the sol-gel method in a large volume (up to 1 kg) with high ionic conductivity 6.9×10^{-4} S/cm and relative density 95% has been demonstrated. In the process of sol-gel synthesis, the composition and purity of precursors, the choice of solvent, and the programs of heat treatment have a decisive effect on the final crystal structure, composition, and conductivity of the resulting solid-state electrolytes [113-115]. In literature [116], the influence of the air atmosphere during synthesis heat treatment of $Li_{1.4}Al_{0.4}Ti_{1.6}(PO_4)_3$ prepared by the sol-gel method with the addition of citric acid was studied. It is shown that two-stage heat treatment (dry gel is first annealed in argon and then in air) yields a nanoscale fraction of LATP (40 nm) with less aggregation than that of LATP obtained by the traditional sol-gel method, which makes it possible to achieve high ionic conductivity (5.9×10^{-4} S/cm) and a relative density of 97% [117].

2.3.1.2.2. Co-precipitation method

The co-precipitation method consists in dissolving several precursors (salts) in an aqueous solution, followed by precipitation while maintaining the optimal pH value. After co-precipitation or freeze-drying, the obtained powders are annealed to obtain fine powders. Co-precipitation is suitable for large-scale production of the material, however, the presence of by-products in the final material is the main disadvantage of this method. It was shown in literature that the sintering temperature and holding time affect the phase purity and ionic conductivity of the resulting LATP products [118]. A

sample prepared at 900°C for 6 hours showed a maximum relative density of 97% and a high ionic conductivity of 1.83×10^{-3} S/cm.

2.3.1.2.3. Chemical vapor deposition method

Vapor deposition methods using targets to provide the assembly of solid-state electrolyte films. The CVD process uses the precursor vapor to initiate a chemical reaction or the decomposition of the precursor in the vapor phase to deposit thin films. The chemical process in a CVD reactor can be activated thermally, plasma or optically [119-120]. The advantage of CVD is that the kinetic energy of the deposited particles is generally lower than that of PLD or magnetron sputter deposition, which improves film quality. Although this method can be used to prepare solid-state electrolyte films with a thickness of micron or even nanometer, the high cost of equipment and reagents and energy consumption limit the large-scale application of this method.

2.3.2. Sintering of solid-state electrolyte ceramic

The sintering process of the solid-state electrolyte is affected by the sintering method, sintering temperature and holding time. And then affect the overall performance of the final solid-state electrolyte ceramics.

2.3.2.1. Traditional sintering method

Generally, the sintering process of solid electrolytes is usually carried out in a tube or box muffle furnace. The solid electrolyte powder pressed into a sheet or spherical shape using a steel mold is placed on an alumina or magnesium oxide plate, heated to the sintering temperature of the solid-state electrolyte at a corresponding heating rate and kept for a certain period of time to complete the densification process of the solid-state electrolyte tablet.

With precise control of temperature and sintering time, $Li_{1.5}Al_{0.5}Ti_{1.5}(PO_4)_3$ show ionic conductivity at room temperature of 4.22×10^{-4} S/cm after heating at 825°C for 8 h and 5.08×10^{-4} S/cm S/cm after heating at 850°C for 12 h [121]. For the sol-gel method, there is information on the synthesis of LATP solid electrolytes at various sintering temperatures (700-900°C). It was found that the best ionic conductivity (6.0×10^{-4} S/cm) and the highest density (95%) were obtained after sintering at

850°C.
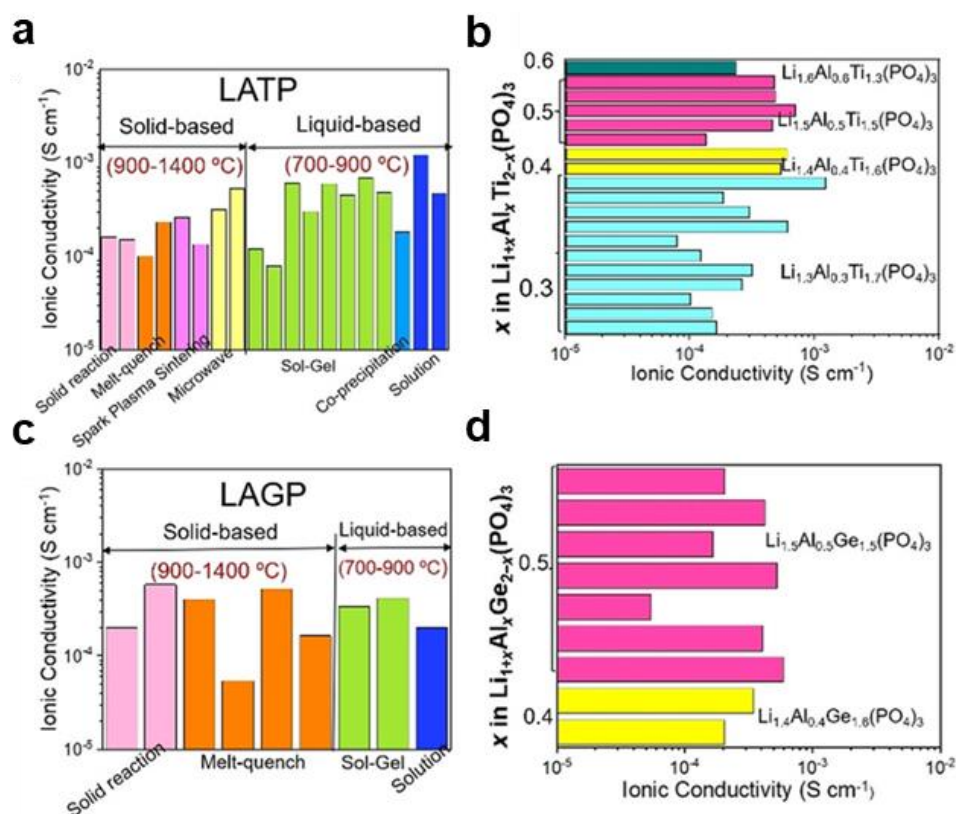
Figure. 2.21. Dependence of ionic conductivity on sintering temperatures (a, c) and composition (b, d) for LATP and LAGP synthesized by different methods.

2.3.2.2. Cold sintering method

A recently developed approach, cold sintering, can densify ceramics near 200°C by incorporating a transient solvent phase and uniaxial pressure into the process [122]. As a consequence, LATP solid state electrolyte can be sintered at a temperature that is an order of magnitude lower than through conventional means. Cold sintering of ceramic electrolytes requires the application of a small amount of solvent, high pressure, and modest temperatures to leverage a dissolution-precipitation process that reduces sintering temperatures, nevertheless, this process can lead to amorphous grain boundaries that are detrimental to ionic conduction. The addition of second phase sintering aids can effectively alleviate this problem, such as LiTFSI, lithium borate, lithium metaborate, boron oxide [123].

Although densification of LAGP and LAGP composites is achieved at 120°C to relative densities of 85% using water as a transient solvent. Cold sintered solid electrolytes have low ionic conductivities of about 10^{-6} S/cm at room temperature. Given that cold sintered electrolytes show the same crystal

structure within grains, it is speculated that a key challenge lies in amorphous, low-conductivity grain boundaries that may be a result of incongruent dissolution in water of the constituent elements.
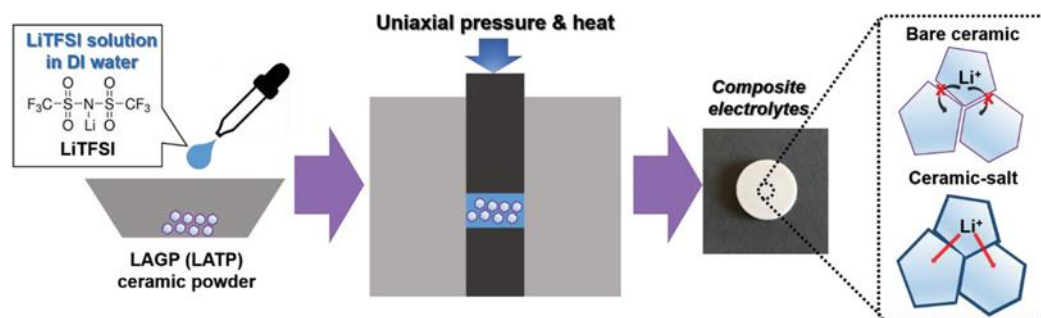
Figure. 2.22. Schematic diagrams of cold sintering method to produce composite electrolytes comprised of solid-state electrolyte ceramics and Li salts. Processing temperature of 130°C.

2.3.2.3. Fast sintering methods

To reduce lithium losses during synthesis heating treatment of solid-state electrolytes, several fast-sintering methods have been developed: SPS (spark plasma sintering) [124-126], FAST (field assisted sintering technique) [121, 127] and microwave sintering (MW) method [128-129].

The SPS method uses resistive heating at a high rate with the flow of electric current (>100°C/min) [130-131]. In the FAST method, voltage is applied to the sample during sintering, realization of sintering based on the resistance heating effect of the material. During sintering with the help of microwave, electromagnetic energy directly penetrates into the sample and is converted into heat through molecular interactions, which leads to rapid volume heating [132]. In the literature [128, 133], LATP ceramic tablets were obtained by microwave sintering method from amorphous LATP precursor powders in 10 minutes. There were no side phases in the obtained LATP sample, the tablet had a high relative density (88%) and a high ionic conductivity of 3.5×10^{-4} S/cm. Despite their instrumental complexity, these methods exhibit high synthesis rates while providing precise phase control. In addition, high heating rates, local heating at grain boundaries, or increased diffusion by applying an external electric field improve the conductive properties of the obtained solid-state electrolytes.

One of the new methods for obtaining ceramic materials with the possibility of preserving volatile elements and the single-phase of ceramic sample is Ultrafast high-temperature sintering (UHS) method [134]. This method consists in using joule heating of the carbon material. A high direct current (>20A) is passed through a narrow strip of carbon felt. A sample (one or more) is inserted inside this strip.

Heating (10^5 K/min) to the processing temperature (which in this method is much higher than the classical sintering temperature) occurs from a few milliseconds to tens of seconds. The sintering itself takes place over a period of several seconds. The advantage of the method is, firstly, in an extremely short sintering time (<1 min), secondly, in the ability to simultaneously sinter a large number of samples, which is limited only by the size of the felt and the power of the source, and, thirdly, the ability to sinter samples of complex shape, since no pressure is applied in UHS. In this case, carbon acts as a miniaturized furnace, the rapid heating of which allows materials to be sintered under nonequilibrium conditions. The small size and high heat capacity of such a "furnace", in turn, allows to quickly dissipate heat and cool the reaction area, thereby quickly quenching the sample without excess of heat [135-139].

2.3.3. Chapter conclusion

Active research efforts to synthesize high-quality $Li_{1+x}Al_xTi_{2-x}(PO_4)_3$ solid-state electrolyte powders with pure phase through various methods have been proposed. By adjusting various parameters in the synthesis process (such as concentration of precursors, temperature, time, etc.), the crystallinity, the micromorphology as well as content of Li in the final product can be adjusted for obtaining high relative density and high ionic conductivity ceramic solid-state electrolyte.

2.4. Mechanisms of growth of lithium filaments in solid-state electrolyte ceramic

Solid-state electrolytes were considered a potential solution to the problem of protrusion growth in them due to their high mechanical strength. According to the Monroe and Newman model, filaments growth can be suppressed if the shear modulus of the solid-state electrolyte is 1-2 times higher than that of Li metal (4.8 GPa) [140]. The following common inorganic solid-state electrolytes have excellent mechanical properties: $Li_7La_3Zr_2O_{12}$ with an elastic modulus of 100 GPa [141], $Li_{1.3}Al_{0.3}Ti_{1.7}(PO_4)_3$ with a high elastic modulus of 125 GPa, etc [142].

Despite the fact that a significant increase in the ionic conductivity of solid-state electrolytes has now been achieved, the suppression of the growth of lithium protrusions and the formation of cracks remains two major interrelated problems. Corresponding problems in the form of a short circuit and poor cycling prevent large-scale commercialization of lithium-conductive ceramics [143-144].

It has been established that lithium protrusions and cracks in solid-state electrolytes originate at the lithium metal anode/solid-state electrolyte interface, mainly inside the initial defects, such as open pores, voids, cracks, and grain boundaries [145-146]. At a current density above the critical value, the driving force for the growth of lithium filaments exceeds the mechanical resistance force of the solid-state electrolyte material. General, the growth of filaments leads to the propagation of cracks inside the solid-state electrolyte (Figure. 2.23), and the newly formed crack provides free space for further growth of filaments, which ultimately leads to a short circuit [147].
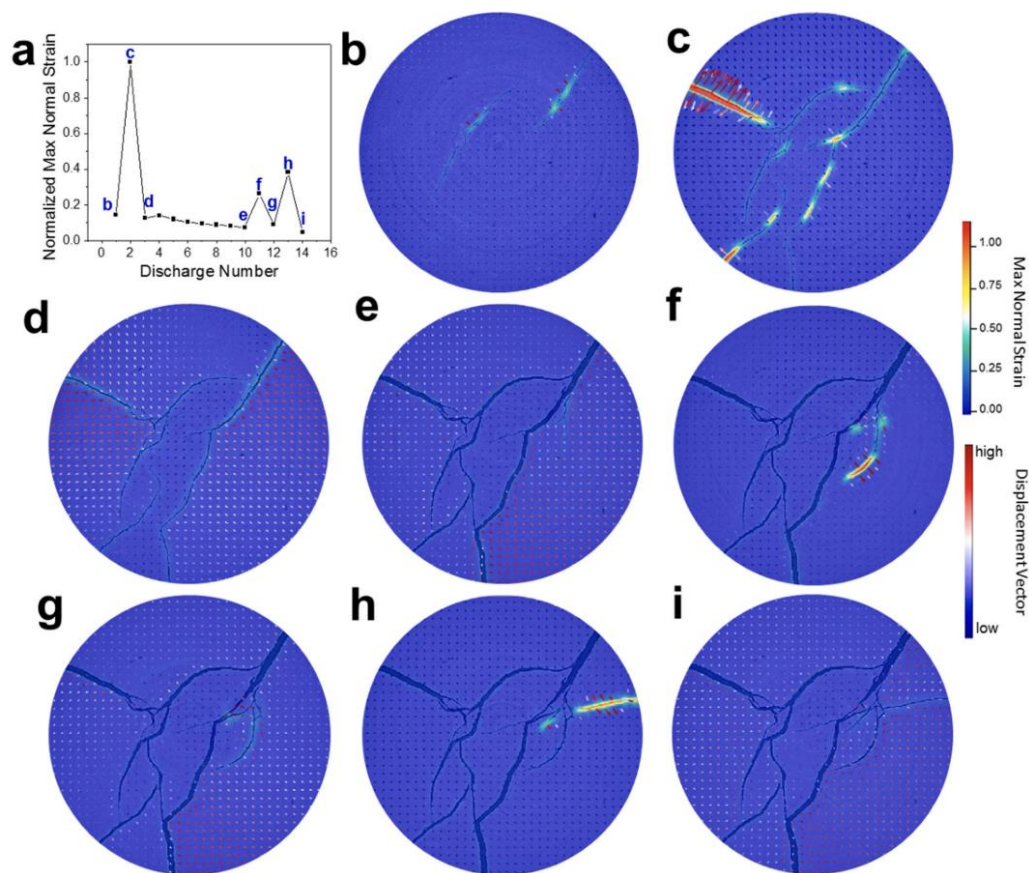
Figure. 2.23. Deformation of solid-state electrolyte during discharge process. (a) Graph of the maximum normal strain during the cyclic discharge-charge process; Strain distribution observed in the same sample after (b)1st, (c) 2nd, (d) 3rd, (e) 10th, (f) 11th, (g) 12th, (h) 13th and (i) 14th cycles.

According to the literature, two mechanisms for the formation of lithium filaments in solid-state electrolytes can be distinguished: (1) crack growth from the surface of solid-state electrolyte/ lithium metal anode and (2) volumetric deposition of lithium inside the solid-state electrolyte as a result of its electronic conductivity at the grain boundaries.
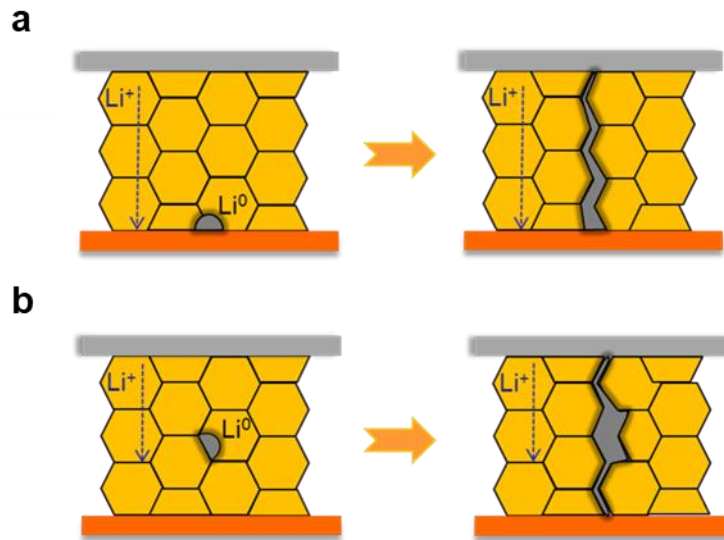
Figure. 2.24. Mechanisms of formation and growth of lithium filaments in solid-state electrolytes: (a) formation of lithium filaments from surface defect; (b) formation of lithium filaments in the voids inside of the solid-state electrolyte.

(1) Formation of filaments from the surface defect of solid-state electrolyte

The growth of lithium filaments starts from a surface (interface of solid-state electrolyte/lithium metal anode) defect when the applied current density reaches a critical value [148]. This phenomenon strongly depends on the properties of solid-state electrolytes, since during battery charging, lithium will penetrate into defective areas (mainly grain boundaries, voids as a result of incomplete electrolyte-electrode contact) and create stresses at the crack tip, which will lead to crack propagation. Thus, the growth of protrusions in this model is controlled by such factors as the defectiveness of the solid-state electrolyte and the kinetics of filament growth, which in turn depends on the surface morphology, the size of defects, and the relative density of the electrolyte material.

(2) Formation of filaments inside of solid-state electrolyte.

Relatively recently, a new theory was presented, which suggests that the reason for the formation of lithium filaments is the reduction of lithium ions in the voids of solid-state electrolyte [56, 149]. This process is caused by the electronic conductivity of local grain boundaries in the ceramics. This model is confirmed by the results of theoretical simulation, according to which the deposition of lithium and further growth of filaments preferably occur

at the boundaries of solid-state electrolyte bulks. Thus, in the presented mechanism, the main factor affecting the growth of lithium filaments is the bulk and boundary electronic conductivity of solid-state electrolyte.

According to the mechanism presented above, the main factors that must be taken into account to suppress the formation and growth of lithium filaments in solid-state electrolyte are:

(1) Surface contact between solid-state electrolyte and lithium metal anode

The surface contact of the solid-state electrolyte and lithium metal anode is due to the physical contact and chemical stability of the battery components (electrolyte, electrodes) upon contact. The physical interaction is determined by plasticity, pressure and roughness, which depend on the property of ceramic, lithium metal and testing conditions. Perfect contact of interface is almost impossible to achieve as a result of the microscopic voids on surface. These defects lead to point contact, resulting in the formation of regions with a higher current density and, as a consequence, the longitudinal growth of lithium protrusions. On the other hand, the chemical stability of the materials used is determined by chemical reactions between solid-state electrolyte and lithium metal, which cause volume changes and reaction by-product [150]. Thus, the mixed conductivity of (ionic and electronic) surface layer is the result of the destruction of the solid-state electrolyte and the degradation of the cell.

(2) Properties of solid-state electrolyte

The kinetics of Li-ion transfer and the mechanism of formation of lithium filaments are significantly affected by such characteristics of ceramics as relative density, ionic conductivity, mechanical strength, and crack resistance, etc. It is known that there is a higher concentration of Li-ions at the grain boundaries, which contributes to the propagation of lithium protrusions along the grain boundaries. Thus, according to the results obtained, the ionic conductivity and strength of the solid-state electrolyte determine the distribution of mechanical stress on the surface of the contact and the local rate of electrochemical deposition of lithium. For example, the solid-state electrolyte with low ionic conductivity contributes to an increase in the point voltage at the interface. This value affects both the kinetics of electrochemical reactions and the possibility of deformation of the solid-state electrolyte at the point of contact with the anode. On the other hand, solid-state electrolyte with high mechanical strength and crack

resistance will reduce the stress concentration.

(3) External conditions

Temperature, and external pressure also influence the formation and growth of lithium protrusions through the solid-state electrolyte. They are important factors as a result of its influence on the elasticity and ductility of the lithium metal anode. Changes in the lithium microstructure, which depend on the deformation of the metal anode, have a significant effect on the growth of dendrites [151]. Based on the above theoretical models, various strategies have been developed in the literature to regulate the growth of lithium filaments through interface design, such as solid-state electrolyte modification, and environmental optimization. For example, interface design by coating lithium metal anode or solid-state electrolyte with gold, aluminum, silicon, or LiF, etc. Improvements in interfacial stability are also being developed as a result of the use of a functional layer between the solid-state electrolyte and the lithium metal anode [152].

The contribution of defects to the process of lithium protrusion growth and crack formation has been demonstrated by in-situ and ex-situ studies (Figure. 2.25) [148, 153].
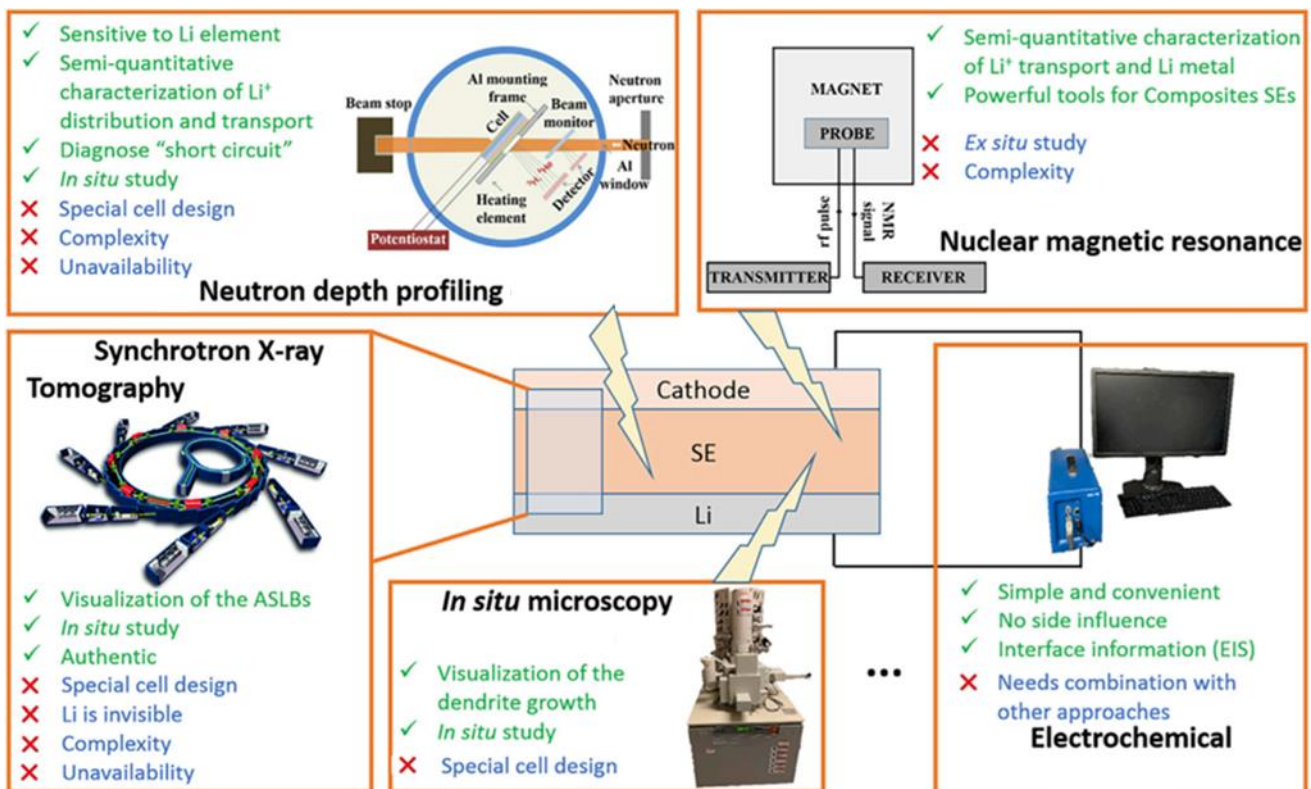
Figure. 2.25. Methods for studying the growth of lithium filaments (green indicates the advantages of the method,

blue indicates the disadvantages).

According to in-situ scanning electron microscopy (SEM), it was found that the deposited Li grows along the grain boundaries and causes cracks in the Li_2S-P_2S_2 solid-state electrolyte [154], also in polycrystalline $Li_{6.25}La_3Al_{0.25}Zr_2O_{12}$ Li protrusions also predominantly grow along grain boundaries [155]. Using the focused ion beam in dual beam configuration with scanning electron microscope (FIB-SEM), it was found that the loss of surface contact caused by the volume change of the electrode and electrolyte leads to a decrease in the battery capacity during operation, which is a possible cause of poor cycling [156]. Using operando optical microscopy, it was shown that filaments formed in $Li_7La_3Zr_2O_{12}$ have different types or morphologies: straight, branching, exfoliating, and diffuse [157]. Using an atomic force microscope, the mechanical stress caused by the growth of lithium whiskers had been quantitatively measured at a certain applied voltage [158]. Using X-ray computed tomography scan (CT), the growth of lithium filaments was also observed only along the crack region [147, 159]. The above experimental results demonstrate the phenomena of lithium filament growth and crack propagation within solid-state electrolytes and thus form a basic representation of this process. However, a more detailed theoretical understanding of the mechanisms requires additional systematic experimental and theoretical studies.

The formation and growth rate of lithium filaments in solid-state electrolytes were theoretically studied by studying the dependence of their growth on the electrochemical potential [160]. The influence of solid-state electrolyte bending on the cell potential and lithium capacity was studied in an electrochemical-mechanical model [161]. The coupled multi-physics field model has shown that excess surface electrons significantly affect the site of Li nucleation within the grain boundaries of polycrystalline $Li_7La_3Zr_2O_{12}$ [162-165].

By numerical simulation of the microstructure of the solid-state electrolyte, the properties of this material were studied, as well as the influence of operating conditions, including temperature and external pressure. It was found that the pressure in battery system and the electrochemical properties of the electrolyte can affect surface deposition and mechanical stability.

All presented numerical simulation models provide a partial understanding of surface hindrances and lithium protrusion growth. However, the currently available modeling works do not take into account both electrochemical and mechanical aspects, moreover, these models do not provide insight

into the dynamics of destruction of the solid-state electrolyte during charging and discharging.

So far, in the literatures that has been published, there are 4 main routes for suppressing the growth of lithium protrusions in solid-state electrolytes:

(1) Modification of the electrode structure and current collector to relieve stress during lithium deposition [166].

(2) Interfacial modification to improve the contact between the solid-state electrolyte and the electrode, especially lithium metal anode [167].

(3) Improving the mechanical properties of solid-state electrolytes by increasing their relative density to suppress filament growth and improve battery performance [168].

(4) Preservation of residual stresses on the surface or inside the solid-state electrolyte or the application of pressure to the battery system during operation [153, 169].

2.5. Conclusion from the literature review

Utilization of solid-state electrolytes (SSEs) is deemed to one of the most promising approaches to suppress Li metal dendrite growth and ensure the safety of LMBs, of which the NASICON type solid-state electrolytes with high mechanical strength, high ionic conductivity, electrochemical stability and wide electrochemical window have been extensively developed in solid-state Li metal batteries. Particularly, $Li_{1+x}Al_xTi_{2-x}(PO_4)_3$ (LATP, x=0.3-0.5), a typical NASICON-type SSE, possesses high ionic conductivity ($\sim 10^{-5}$-10^{-4} S/cm) and excellent stability at an environment with water and oxygen, which is very promising for high performance solid-state batteries. However, it is still a big challenge to obtain high-quality SSE membranes after sintering, which seems to be one of the primary issues to realize the commercial application of all-solid-state batteries. Moreover, the improper sintering programs would cause a large number of defects (voids and cracks) inside the SSE tablets and the second phase induced by incomplete reaction or overheating, which will seriously affect the relative density, ionic conductivity and mechanical strength of the SSE tablets. Despite being far from commercialization, many efforts have been paid for achieving promising results from the benefits of special sintering approaches lowering energy consumption during compaction of ceramic. Another favorable large-scale approach is based on utilizing sintering additives to enhance densification of electro-ceramic at relatively low temperatures by liquid phase assisted sintering. However, the small

amount of foreign additives (< wt.10%) added and the uniformity of mixing need to be strictly controlled for making suitable ceramics, otherwise it will have a negative impact on the relative density, ionic conductivity and the overall strength of the SSE conductive ceramics due to the local variation of composition with the secondary amorphous or crystalline phase emerging at grain boundaries. Therefore, the issue of high-quality of precursor powders of the LATP solid-state electrolyte with controllable composition, shape and size produced by reproducible and scalable synthetic approaches to obtain highly conductive and dense solid-state electrolyte still remain a big challenge, which plagues the scientific research field and the industry.

3. Experimental part

3.1. Reagents and materials used in experiments

In order to synthesize $Li_{1.3}Al_{0.3}Ti_{1.7}(PO_4)_3$ solid-state electrolyte ceramic materials by solid state reaction method and molten salt quenching method, the following reagents are used: The lithium carbonate (Li_2CO_3, 99.5%, Macklin Biochemical Co., Ltd., China), aluminum oxide (Al_2O_3, 99.5%, Baikowski Co., Ltd., France), titanium oxide (TiO_2, 99.999%, Merck & Co., Germany), and ammonium dihydrogen phosphate ($NH_4H_2PO_4$, 99.5%, Macklin Biochemical Co., Ltd., China).

In order to synthesize $Li_{1.3}Al_{0.3}Ti_{1.7}(PO_4)_3$ solid-state electrolyte ceramic materials using polymerized matrices, the following reagents are used: Titanium(IV) butoxide ($Ti(OC_4H_9)_4$, 99.5%, Merck & Co., Germany), lithium nitrate ($LiNO_3$, 99.5%, Macklin Biochemical Co., Ltd., China), aluminum nitrate nonahydrate ($Al(NO_3)_3 \cdot 9H_2O$, 99.5%, Macklin Biochemical Co., Ltd., China), ammonium dihydrogen phosphate ($NH_4H_2PO_4$, 99.5%, Macklin Biochemical Co., Ltd., China), hydrogen peroxide (H_2O_2, 37%, Chimmed, Russia), acrylamide ($CH_2=CHC(O)NH_2$, 99.5%, Macklin Biochemical Co., Ltd., China) and N,N'-methylenebisacrylamide ($CH_2[NHC(O)CH=CH_2]_2$, 99.5%, Macklin Biochemical Co., Ltd., China).

Zirconia (ZrO_2, 99%, MITR, China) milling jars and yttrium-doped zirconia milling balls (ZrO_2: 94.8%; Y_2O_3: 5.2%, MITR, China) were used to process the powders. The solid-state electrolyte green body tablets are placed on magnesium oxide (MgO, 99%, Purshee, China) and alumina plates (Al_2O_3, 99%, Purshee, China) for sintering. High-purity platinum target (Pt, 99.99%, Sberbank, Russia). is used to prepare sputtering layers on the solid-state electrolyte surface for subsequent ionic conductivity measurements and battery testing.

In order to test the electrochemical performance of the solid-state electrolyte in battery, the following reagents are used: Lithium nickel manganese cobalt oxides ($LiNi_xMn_yCo_{1-x-y}O_2$, 99.95%, BTR New Materials Group Co., Ltd., China), Lithium iron phosphate ($LiFePO_4$, BTR New Materials Group Co., Ltd., China), Polyvinylidene fluoride ($-(C_2H_2F_2)_n-$, Arkema S.A., France), Lithium metal (Li, 99.95%, Zhongneng Lithium Industry Co., Ltd., China), Super-P (C, 99.95%, TIMCAL, China), Aluminum foil (Al, 99.99%, Xfeile New Material Co., Ltd., China), Copper foil (Al, 99.99%, Yili Copper Industry Co., Ltd., China), N-Methyl-2-pyrrolidone (C_5H_9NO, A.R., Macklin Biochemical Co.,

Ltd., China), Celgard@2450 separator ((C_3H_6)$_n$, 99%, Celgard, China), fluoroethylene carbonate ($C_3H_3FO_3$, 99.95%, DUODUO, China), Dimethoxyethane ($C_4H_{10}O_2$, 99.95%, DUODUO, China), Lithium bis(trifluoromethanesulfonyl)imide ($LiN(CF_3SO_2)_2$, 99.95%, DUODUO, China).

3.2. Research methods

3.2.1. Phase analysis

The analysis of the crystal structure of the obtained samples was carried out on Dmax-2500 X-ray diffractometer (Rigaku Co., Ltd., Japan) with CuKα radiation ($\lambda = 1.54178$Å), at a voltage of 50 kV and current of 250 mA in the angle range $2\theta = 10-60°$ with a speed of 2°/min. The resulting spectra were processed using the WinXPOW (STOE & Cie GmbH., Germany) program, which allows profile analysis, phase search using the PDF2 library, the size of the coherent scattering region (CSR), and the indexing of crystal chemical cells. Analysis of the obtained spectra was carried out by the corundum number method (RIR), which is equal to the ratio of the maximum phase lines for a mixture of the studied phase and corundum in a mass ratio of 1:1. For most compounds, these values are presented in the database. However, for the LATP phase of interest to us, the corundum number has not been determined, therefore, in this work, it was obtained from a mixture of pure LATP phase and Al_2O_3 in equal mass fractions according to the following formula:

$$RIR_{LATP} = \frac{I_{LATP}^{100\%}}{I_{Corundum}^{113}} \quad (1)$$

Next, the X-ray patterns of the powders were indexed using the Pseudo-Voigt profile function to determine the integrated intensities. Then the mass fraction of the components in the mixture is determined by the following formula:

$$\omega_a = \frac{\frac{I_a^{max}}{RIR_a}}{\sum_{i=1}^{n} \frac{I_i^{max}}{RIR_i}} \quad (2)$$

where I_a^{max} and RIR_a are the intensity of the maximum line and the corundum number of the determined phase a, I_i^{max} and RIR_i are the intensity of the maximum line and the corundum number of any phase in the mixture, where i is its number, n is the total number of phases in the mixture. As a result, XRD made it possible to determine the qualitative phase composition, as well as the volume and parameters of the unit cell.

Another method for qualitative analysis of the phase composition was Raman spectroscopy using an Enspectr R532 spectrometer with a laser wavelength of 532 nm. The measurement was carried out at a laser power of 4 mW and an objective magnification x20. The results obtained were analyzed by comparing them with the spectra of pure phases. The Raman spectrum for LATP is known in the literature and has been analyzed in detail (Figure. 3.1). At Raman shifts in the range of 850-1130 cm^{-1}, the observation of maxima, which is typical attributed to the stretching of the P-O bonds. Bending of these bonds also could be observed at lower shifts ~ 400-680 cm^{-1}. Also, the LATP spectrum is always characterized by the presence of a number of maxima at 200-400 cm^{-1}, which is attributed to the vibration of the Ti^{4+} and PO_4^{3-} bonds etc [177]. It should be noted that the highest peaks (Figure. 3.1) always consist of three components: A (969 cm^{-1}), B (989 cm^{-1}) and C (1007 cm^{-1}), the intensity of which and half-width are redistributed during doping of Al into the crystal structure of LATP. The literature also describes in detail the Raman spectra for the main foreign phases obtained during the synthesis, such as $AlPO_4$, TiO_2, $LiTiPO_5$, Li_3PO_4, etc. However, Raman spectroscopy does not allow quantitatively determining the phase composition, since some substances are not Raman-active, and for most substances, proportionality factors between concentration and final intensity are not determined, which requires additional analytical studies for quantitative analysis [180, 186].
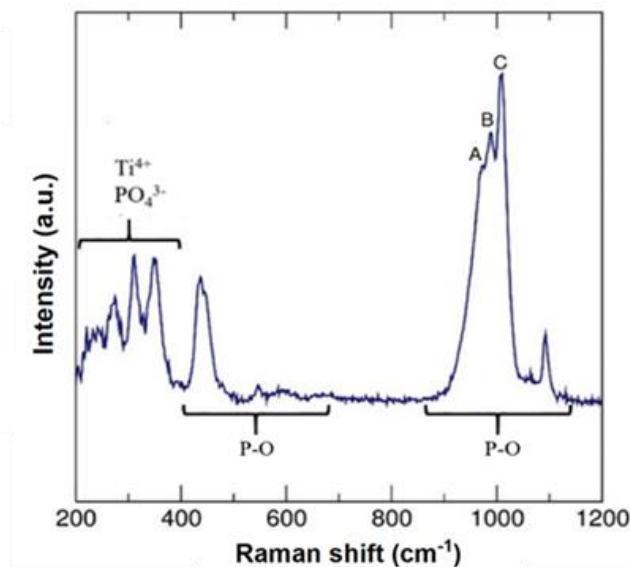
Figure. 3.1. Theoretical description of the Raman spectrum for LATP.

3.2.2. Microstructure analysis

The particle size of precursors, LATP powders, as well as the microstructure of SSE tablet (grain

size, pores, cracks etc.) were determined by scanning electron microscopy (SEM) using a Supra 50 VP LEO electron microscope using SE2 detector and accelerating voltage range 5-10 kV. However, JEOL's JSM-6340F and Gemini SEM 500 were also used to obtain higher resolution micrographs of nanoparticles.

Sample preparation of ceramic for SEM was carried out according to the following method: ceramic tablet after sintering was divided into two parts and the longitudinal section was polished using SiC sandpaper from 800 to 5000 mesh step by step. Then the polished samples were immersed in ethanol followed by ultrasonic cleaning and then dried in air. Next, reheat process was carried out at 800°C for 30 min to reveal the microstructure.

Scanning electron microscope (SEM) images can also be used for particle or grain size analysis. The Origin software (OriginLab Co., Ltd., USA) was used to statistically process all the obtained data and construct particle size distribution histograms. Statistical analysis of the images was carried out using the ImageJ. To determine the average grain size, at least 3 SEM images and at least 200 grains per image were used. We equivalently convert polygonal grains into circles with similar areas, and use the diameter of the equivalent circle as the characteristic size of the grain. The Boltzmann function and the log-normal function were used to fit the particle size distribution data and the aggregate particle size data to obtain a cumulative particle size curve and function equation.

$$\tilde{x} = \frac{1}{n}\sum_{i=1}^{n} x_i \quad (3)$$

$\tilde{x}$ is the average particle size (1.225 times the average diameter of the equivalent circle), n is the number of measured particles.

$$\tilde{\sigma} = \sqrt{\frac{\sum_{i=1}^{n}(\tilde{x}-x_i)^2}{n(n-1)}} \quad (4)$$

$\tilde{\sigma}$ is the standard deviation of a normal distribution. The distribution function of the powder size distribution is as follows:

$$p(x) = \frac{1}{\tilde{\sigma}\sqrt{2\pi}} \cdot \exp\left[-\frac{(x-\tilde{x})^2}{2\tilde{\sigma}^2}\right] \quad (5)$$

The particle size of the powders was also determined by dynamic light scattering (DLS) using Zetasizer Nano ZS equipment (Malvern Instruments Ltd., UK). During sample preparation, LATP powders (RI=1.6; α=0.01) were dispersed in ethyl alcohol (viscosity 1.04 Pa·s, RI=1.36 at T=25°C) and diluted to an almost transparent solution with concentration ~ $5 \cdot 10^{-3}$ mg/ml. Next, using Zetasizer software, the particle size distribution was obtained.

The size of the nanoparticles was analyzed using the XRD method. For particles with a size of less than 200 nm, the Scherrer formula is fulfilled, which relates the broadening of the peaks in the X-ray diffraction pattern to the size of the ceramic:

$$d = \frac{\lambda}{\beta cos\theta} \quad (6)$$

where λ is the wavelength of X-ray radiation (for CuKα λ=1.5406Å), β is the half-width of the selected maximum, $cos\theta$ is the cosine of the angle at which the maximum is located. In this work, the size of LATP particles was determined from the broadening of the line with Miller indices, which corresponds to the angle $2\theta = 24.492°$.

3.2.3. Thermal analysis

To determine the characteristic temperatures during heat treatment, the obtained samples were analyzed thermally by thermogravimetric analysis (TGA) and differential scanning calorimetry (DSC) in the temperature range from 30°C to 1000°C and a heating rate of 10°C/min using Netzsch STA 409 PC Luxx (Erich NETZSCH GmbH & Co. Holding KG, Germany). TG and DSC were also used to study the thermal stability and composition of the titanium (IV) peroxo complex and other precursors.

The linear shrinkage of the pressed samples was measured under the appropriate thermal conditions at a heating rate of 2°C/min in a DIL 402 Expedis Classic horizontal dilatometer (Erich NETZSCH GmbH & Co. Holding KG, Germany). To analyze the behavior, the powder under study was preliminarily pressed into cylindrical tablets with 9 mm diameter and 2 mm thickness and placed in the device.

3.2.4. Determination of relative densities of prepared samples

In order to accurately measure the relative density of the SSE tablets after sintering, we polished the surface of the sintered tablet to mirror (using 300mesh, 800mesh, 2000 mesh, 4000mesh SiC sandpaper step by step), and used ultrasonic cleaning in alcohol solution, and then dry under 60°C for all night. Weigh and measure the diameter and thickness of completely dry LATP SSE tablet and calculate the density based on these data. The density of green body skips the polishing and clearing process, and directly measures the diameter, thickness and weight after drying. Then the geometric

density value was obtained according to the following formula:

$$\rho_{geom} = \frac{m}{\pi r^2 h} \quad (7)$$

where m is the mass of the tablet, r and h are the radius and thickness, respectively.

Calculate X-ray density from XRD data, determine unit cell volume and its mass. Afterwards, the relative density is obtained as the ratio of the geometric density to the theoretical density:

$$\rho_{rel} = \frac{\rho_{geom}}{\rho_{xrd}} \quad (8)$$

where ρ_{rel} and ρ_{xrd} are the relative and X-ray densities, respectively.

The geometric porosity was calculated as the relative difference between the X-ray and geometric densities:

$$Relative\ density = \frac{\rho_{geom}}{\rho_{xrd}} \times 100\% \quad (9)$$

3.2.5. Electrochemical study of solid-state electrolytes

Before determining ionic conductivity, the required sample preparation of ceramic tablets was to create good ohmic contacts between samples and current collectors. Thin layer of platinum (30 nm) on both sides was deposited on the tablet bases using Quorum Q150T ES magnetron sputter (Quorum Technologies Co., Ltd., Great Britain) to achieve this goal. Then the samples were clamped between the current collector, ionic conductivity was measured on Autolab M204 potentiostat (Metrohm AG Inc., Switzerland) by impedance spectroscopy at frequencies in the range from 1 MHz to 0.1 Hz.

In an alternating current circuit, the impedance will be represented by two components that can be represented in a complex notation:

$$Z = ReZ - iImZ = Z_0 cos\varphi - iZ_0 sin\varphi \quad (10)$$

where $ReZ=Z_0cos\phi$ and $ImZ=Z_0sin\phi$ are active and reactive resistance, Z_0 is the impedance amplitude, ϕ is the phase shift. In this case, active resistance corresponds to power losses due to thermal processes, while reactive resistance corresponds to inductive and capacitive ones. However, in the experiment, when changing the frequency of the alternating current, we measure the data array of the amplitude of the impedance Z_0, which is equal to the ratio of the voltage and current amplitudes, the

phase shift ϕ and the frequency ω. Further, according to the formulas presented above, the dependence of the imaginary part of the impedance on the real part (Nyquist coordinates) is constructed, which is called the impedance spectroscopy (Figure. 3.2) [187].
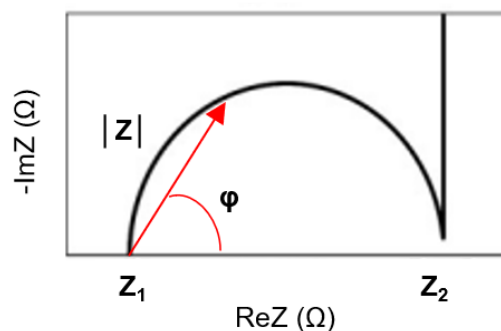
Figure. 3.2. Impedance spectroscopy of solid-state electrolyte.

According to the literature, for solid-state electrolytes, the defining points on the impedance spectroscopy are:

1) Z_1 is the initial point of the hodograph at ImZ=0 (or its approximate continuation up to the intersection with the ReZ axis). This value is the active resistance corresponding to the intra-grain conductivity, which is calculated as a result by the following formula:

$$\sigma_{grain} = \frac{h}{\pi r^2 \cdot Z_1} \quad (11)$$

where h and r are the height and radius of the SSE tablet.

2) Z_2 is the intersection of the arc (or its continuation) with the ReZ axis. This value is also the total resistance, which is contributed by both the conductivity inside the grain and the grain boundary conductivity, which is determined by a similar formula:

$$\sigma_{total} = \frac{h}{\pi r^2 \cdot Z_2} \quad (12)$$

It is also worth noting that a further increase in the impedance is associated with a voltage drop across the contacts

The cycling performance of battery (MTI EQ-PSC) with LATP ceramic tablets was studied using the Neware battery testing system. Li‖LATP‖Li symmetric cells was test at a current density of 0.1 mA/cm^2 with a stripping/plating period of 1 h at 25°C. The cycling performance of Li‖LATP‖NCM111

full cell was test at a current density of 0.1 mA/cm^2 at 25°C.
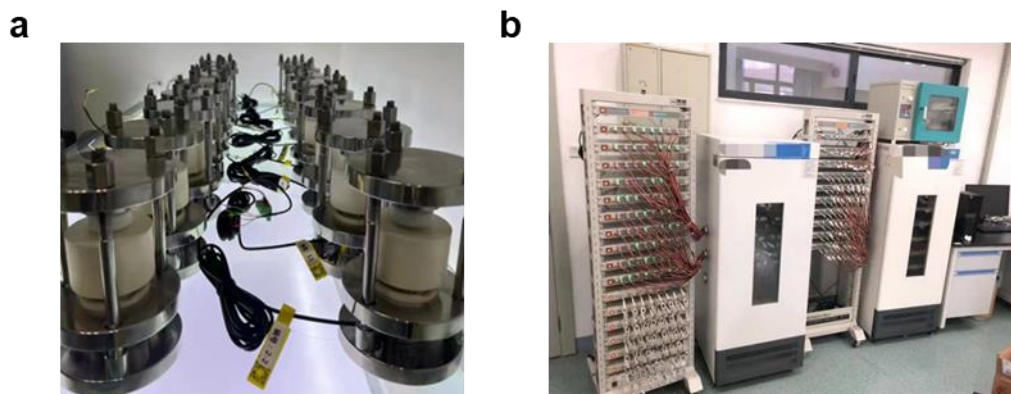
Figure. 3.3. (a) MTI EQ-PSC; (b) Neware battery testing system.

3.2.6. Study of mechanical characteristics of solid-state electrolytes

The elastic modulus of solid-state electrolyte materials can be evaluated by indentation experiments. The elastic modulus and hardness of the material were obtained by the Oliver-Pharr method. The slope of the curve when the load is unloaded indicates is the stiffness (S) of the material and is usually affected by the testing machine itself and the test material. The elastic modulus E of the test material is calculated by the following equation:

$$E = \frac{1}{2} \times \frac{dF}{dh} \times \sqrt{\frac{\pi}{A}} \ (13)$$

F is the load, h is the displacement, and A is the contact area. The subsequent measurement of the elastic modulus was completed using the NanoScan-4D and MX-0580 mechanical testing equipment.

3.3. Research methodologies

This section is devoted to the development of methods for the synthesis and analysis of the studied connections. In this work, we tried to synthesize Li$_{1.3}$Al$_{0.3}$Ti$_{1.7}$(PO$_4$)$_3$ solid-state electrolyte using classic solid-state methods and also developed a new, polymerized matrices-based method for the synthesis of Li$_{1.3}$Al$_{0.3}$Ti$_{1.7}$(PO$_4$)$_3$ solid-state electrolyte powders with ultrafine controllability. We discussed in detail the effects of temperature, time and initial powder particle size on the solid-state electrolyte sintering process, laying the foundation for battery testing and mass production of solid-state electrolytes. At the same time, through the use of bimodal system and the introduction of glass additives, combined with a specially designed sintering procedure, the various indicators of LATP

solid-state electrolyte ceramics are maximized.

3.3.1. Synthesis of LATP powders

$Li_{1.3}Al_{0.3}Ti_{1.7}(PO_4)_3$ powders were synthesized by the conventional solid-state reaction, molten salt quenching method and wet-chemical method. Thermal behavior of precursors in the solid-state reaction and molten salt quenching method for the synthesis of LATP have been investigated using thermal analysis (Figure 3.4).
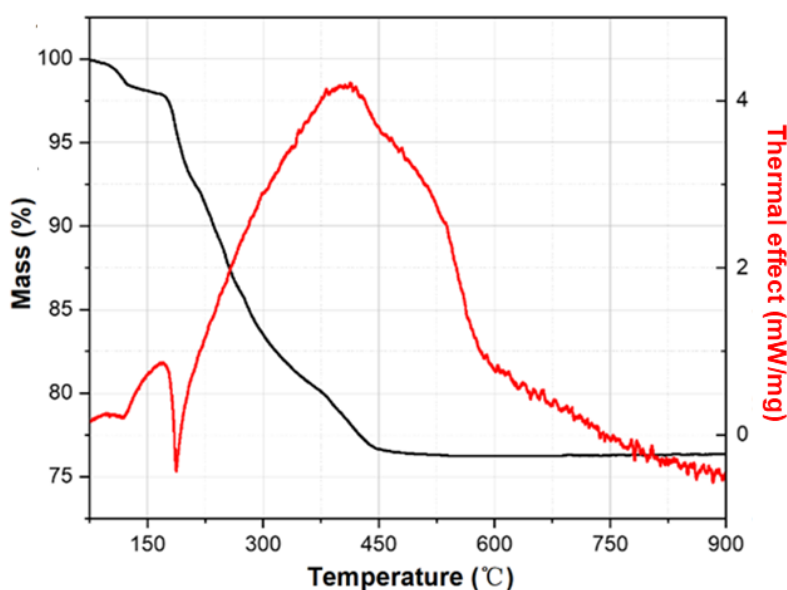
Figure. 3.4. Results of TG and DSC for precursors in the solid-state reaction, molten salt quenching method for the synthesis of LATP.

As a result of TG and DSC curves, complete thermal decomposition of precursors occurs at ~ 450°C, after which the solid-state reaction will take place. However, large particles, which are characteristic of solid-state synthesis, require a sufficiently high energy for diffusion, so the temperature of solid-state synthesis is usually more than 700°C [72, 170].

3.3.1.1. Solid state reaction method

Ball milling method was used to process the synthesized powders. All the powders were preliminarily ground in an agate mortar before ball milling until there were no significant large blocks.

Here we use ball milling balls with a diameter of 4.5-5.0 mm (5 times the mass of all powders in total), and acetone is used as a solvent (15 ml of acetone was added for every 10 g of powder). The starting speed was 250 rpm, the rotation speed was 500 r/min, and the time was 45 mins. Then the mixed powder after drying was heated in the platinum crucible at 700-1200°C for 10 h. $Li_{1.3}Al_{0.3}Ti_{1.7}(PO_4)_3$ powders were synthesized according to the following core reaction [171]:

$$0.65\ Li_2CO_3 + 0.15\ Al_2O_3 + 1.7\ TiO_2 + 3\ NH_4H_2PO_4 \rightarrow\ Li_{1.3}Al_{0.3}Ti_{1.7}(PO_4)_3 + 0.65\ CO_2 + 3\ NH_3 + 4.5\ H_2O\ \ (14)$$
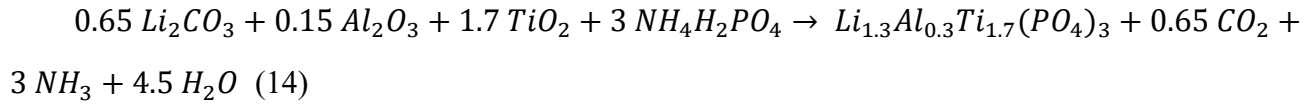
Finally, we used the wet ball milling method to control the particle size. Here we used ball milling balls with diameters of 1.0-1.2 mm and 2.0-2.2 mm (weight fraction of 50%:50%), the total amount of ball milling balls is 10 times the mass of the powder, and acetone was used as a solvent (15ml of acetone is added for every 10 g of powder). The revolution speed was 350 r/min, and the rotation speed was 700 r/min. Setting time was 2.5 h., Dynamic light scattering (DLS) method has been applied to estimate the particle size. with followed SEM images to determine the particle size of LATP powder. 18,000-mesh nylon filter was used to remove unground large particles and ball milling balls, with followed washing product with acetone and drying in an oven to obtain LATP powder.

3.3.1.2. Molten salt quenching method

3.3.1.2.1. Synthesis of 13Li₂O-3Al₂O₃-34TiO₂-30P₂O₅ glass

All the powders were preliminarily ground in an agate mortar before ball milling until there were no significant large blocks. Here we use ball milling balls with a diameter of 4.5-5.0 mm (5 times the mass of all powders in total), and acetone is used as a solvent (15 ml of acetone is added for every 10 g of powder). The starting speed is 250 rpm, the rotation speed is 500 rpm, and the time is 45 mins. The mixture was placed in a magnesium oxide crucible and heated to 700°C and kept for 4 h to remove volatile components. Then the mixture was heated to 1450°C and hold for 2 h to melt and homogenize the mixture. Next, the melt was poured onto a stainless plate and cooled down in air to room temperature. The resulting glass sample is shown in Figure. 3.5 [107, 172-173].
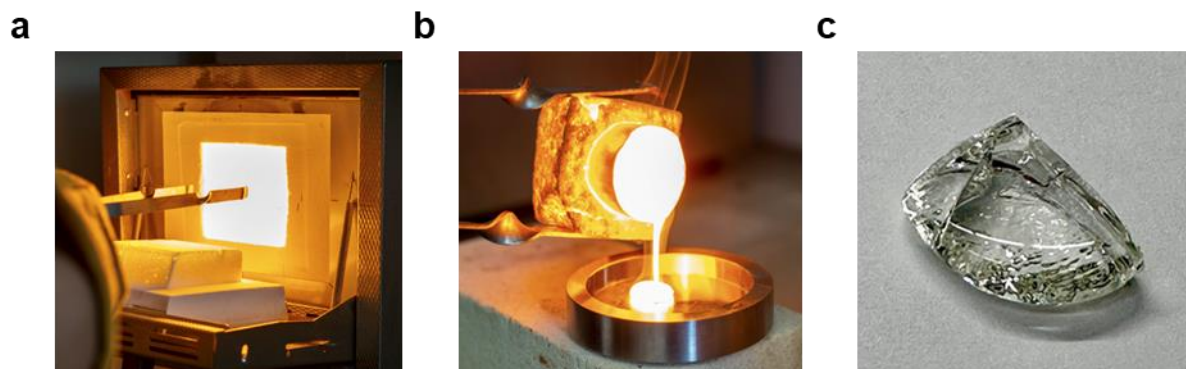
Figure. 3.5. (a-b) Photos of quenching method; (c) photo of LATP glass.

In order to obtain nanoscale glass powder, the obtained glass was first broken with a hammer, and then ground by wet ball milling method for 5 h, 4 h and 2 h using yttrium-doped zirconia milling balls with a diameter of 12 mm, 4.5-5.0 mm and 2.0-2.2 mm (10 times the mass of all powders in total), and acetone was used as a solvent (15ml of acetone is added for every 10 g of powder), respectively. Dynamic light scattering (DLS) method was applied to estimate the particle size after each step of milling and use SEM images to confirm the particle size of glass powder when all steps are finished. 18,000-mesh nylon filter was used to remove unground large particles and ball milling balls, with followed washing product with acetone and drying in an oven to obtain LATP glass powder.

3.3.1.2.2. Crystallization of LATP glass

The obtained glass was annealed at 500°C for 2 hours to relieve thermal stress, and then cooled with the furnace. After crushing and ball milling, here we used ball milling balls with a diameter of 2.0-2.2 mm (10 times the mass of the powder in total), and acetone is used as a solvent (15 ml of acetone is added for every 10 g of powder), the revolution speed is 300 rpm, the rotation speed is 600 rpm, and the time is 1.5h, the powder was kept at 800°C for 4 h to obtain the final powder (the heating rate is 2°C/min). Finally, we used the wet ball milling method to control the particle size of the synthesized LATP powder till ~600nm. We use ball milling balls with diameters of 1.0-1.2mm and 2.0-2.2mm (mass ratio is 50%:50%), the total amount of ball milling balls is 10 times the mass of the powder, and acetone is used as a solvent (15 ml of acetone is added for every 10 g of powder). The revolution speed is 350 rpm, and the rotation speed is 700 rpm. Dynamic light scattering (DLS) method was applied to estimate the particle size after each step of milling and use SEM images to confirm the

particle size of glass powder when all steps are finished. 18,000-mesh nylon filter was used to remove unground large particles and ball milling balls, with followed washing product with acetone and drying in an oven to obtain LATP powder [107, 172-173].

3.3.1.3. Synthesis using polymerized matrices

3.3.1.3.1. Homogenization of inorganic precursors for LATP in polymer matrix

Required reagents were used as ion precursors in a molar ratio of Li: Al: Ti: P = 1.3: 0.3: 1.7: 3. Firstly, $Ti(OC_4H_9)_4$ was dissolved in a solution of nitric acid (8 M) and the equal volume of H_2O_2 to form Ti-based complex, and then other salts were added with a stoichiometric molar ratios of the components of $Li_{1.3}Al_{0.3}Ti_{1.7}(PO_4)_3$.

According to the literatures, citric acid is most often used as a complexing agent of Ti^{4+} ions to obtain LATP using sol-gel method. However, the addition of phosphate ions to this solution leads to the formation of a grey gel-like precipitate (Figure. 3.6a, right), the mechanism of formation of which is clearly not known. To prevent side reactions of co-precipitation and redistribution of precursors, which do not allow to obtain samples of sufficient high phase purity, hydrogen peroxide in an acidic medium was tested as a complexing agent for Ti (IV).

The resulting titanium peroxo complex has a characteristic bright scarlet color and remains stable even after the addition of PO_4^{3-} ions (Figure. 3.6a, left). The composition of this complex to determine the optimal ratio of Ti^{4+} ions and hydrogen peroxide was studied by spectrophotometry. The results of all procedures used (Figure. 3.6b-e) under conditions of a strongly acidic (pH=1) synthesis medium corresponded to a coordination number equal to one, which corresponds to the chemical formula $[TiO_2(H_2O)_4](NO_3)_2$ and is confirmed by literature. This chemical transformation after the dissolution of titanium n-butoxide can be represented by the following reaction:

$$Ti(OC_4H_9)_4 + 2\,HNO_3 + H_2O \rightarrow TiO(NO_3)_2 + 4\,C_4H_9OH \quad (15)$$

$$TiO(NO_3)_2 + 3\,H_2O + H_2O_2 \rightarrow [TiO_2(H_2O)_4](NO_3)_2 \quad (16)$$
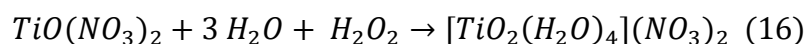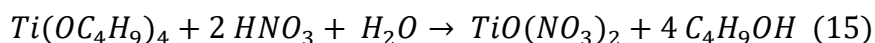
The resulting molar ratio of reagents $Ti(C_4H_9O)_4:H_2O_2=1:1$ was determined using spectrophotometric study using a UVmini-1240 spectrometer, Shimadzu (Japan) by a number of methods and this ratio was further used to optimize the polymerized matrices method for obtaining LATP. The maximum optical density was observed at a wavelength of $\lambda \sim 420$ nm. The stoichiometry

and stability of the titanium (IV) peroxo complex was determined using spectrophotometric approaches through: 1) Isomolar series method, 2) Asmus straight-line method and 3) Harvey-Manning slope ratio method, respectively [174-177]. 25 ml of solutions of hydrogen peroxide and Ti^{4+} with a concentration of 0.01 M in 8 M nitric acid have been prepared (Table. 3.1) for each method (details are presented in SI). To establish equilibrium, optical measurements were carried out after 2 hours mixing of precursors. The reference solution was 8M nitric acid. Also, the isomolar series method (Figure. 3.6b) made it possible to determine the stability constant for the resulting Ti (IV) peroxo complex, which was $\beta=7.2\times10^6$ and characterizes it as highly stable.
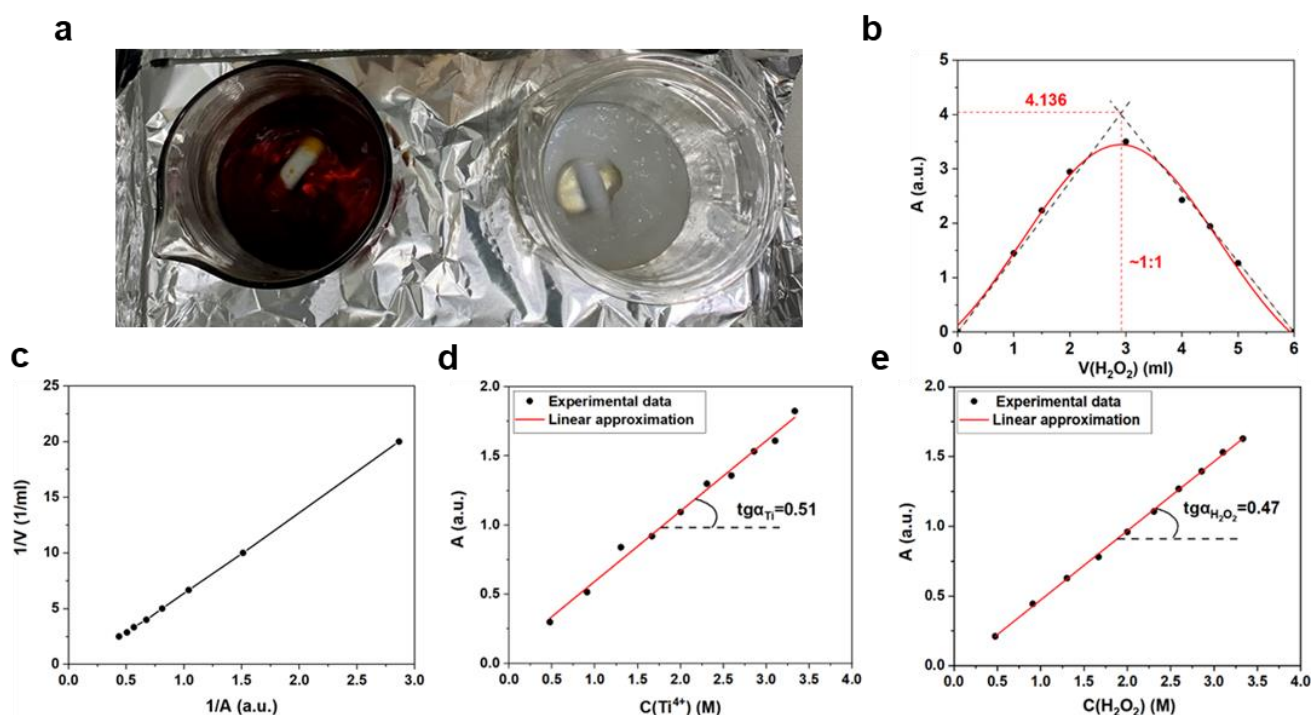
Figure. 3.6. (a) Comparison of the stability of solutions of peroxo (left) and citrate (right) Ti(IV) complexes after the addition of phosphate ions. Spectrophotometric study of titanium peroxo complex Ti^{4+} by methods: (b) isomolar series; (c) direct line of Asmus; (d) series of equilibrium shift for metal; and (e) series of equilibrium shift for ligand in the Harvey-Manning slope ratio method.

After all precursors for LATP were mixed, the mixture was thoroughly dried before heating in the muffle furnace. The composition and thermal stability of the Ti (IV) peroxo complex after its drying from solution has not presented in literature before. The $[TiO_2(H_2O)_4](NO_3)_2$ complex with the optimal ratio of reagents was gradually dried at a temperature of 60°C with constant stirring. As a result, light yellow powder (Figure. 3.7a) [181] was obtained, the thermal stability of which was studied by various

physical methods of analysis. Thus, the TG data (Figure. 3.7b) correspond to a mass change of 29.5%, which occurs at temperatures below 350°C. It should be noted that the solid-state reaction for LATP occurs at 500-700°C depending on the particle size, which is preceded by thermal decomposition of all precursors. The Ti^{4+} citrate complex used in the literature is stable at temperatures up to 600°C, which prevents the solid-state reaction and is not suitable for the synthesis of LATP nanoparticles, for which the synthesis temperature is also ~ 600°C [182]. The selected titanium complex, the temperature of complete decomposition of which is ~ 400°C, is suitable for this task. Also, according to the results of TG, the molar mass of the powdered complex was 114 g/mol, which corresponds to the formula $TiO_2 \cdot H_2O_2$. This titanium peroxo complex has been presented in literatures, describing changes in the properties of anatase TiO_2 after the addition of hydrogen peroxide [183]. The chemical change of the titanium peroxo complex during the drying process corresponds to the following reaction:

$$[TiO_2(H_2O)_4](NO_3)_2 \rightarrow TiO_2 \cdot H_2O_2 + 2\,H_2O_2 \uparrow + 2\,HNO_3 \uparrow \quad (17)$$
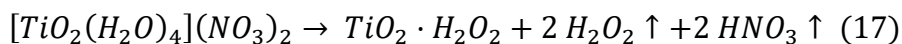
The results of DSC also made it possible to study the thermal behavior of this complex in more detail. So, in the temperature range up to 200°C, an endothermic process of destruction of bonds in the complex occurs. After that, the decomposition reaction of hydrogen peroxide occurs according to the following reaction:

$$2\,H_2O_2 \rightarrow 2\,H_2O + O_2 \quad (18)$$
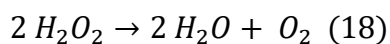
Also, the resulting solid-state complex $TiO_2 \cdot H_2O_2$ was studied by X-ray phase analysis (Figure. 3.7c). The obtained data indicate the structure of anatase (comparison card number in the PDF2 library 21-1272). However, the presence of an additional peak at low diffraction angles of nearly 5° (corresponding interlayer distance of ~17.7 Å) that could be partially observed in measured XRD, could indicate the formation of a superstructure. In the literatures, the researchers attribute this X-ray maximum to the formation of a layered structure, in the interlayer space of which there are H_2O_2 molecules [184]. Peak broadening was also used to determine the average particle size, which was ~3 nm. Some researchers had already mentioned the phenomenon of a significant reduction in the particle size of anatase when modified with hydrogen peroxide, which is a good dispersant, reacting with titanium (IV) ions, modifying the particles both on the surface and inside [185].
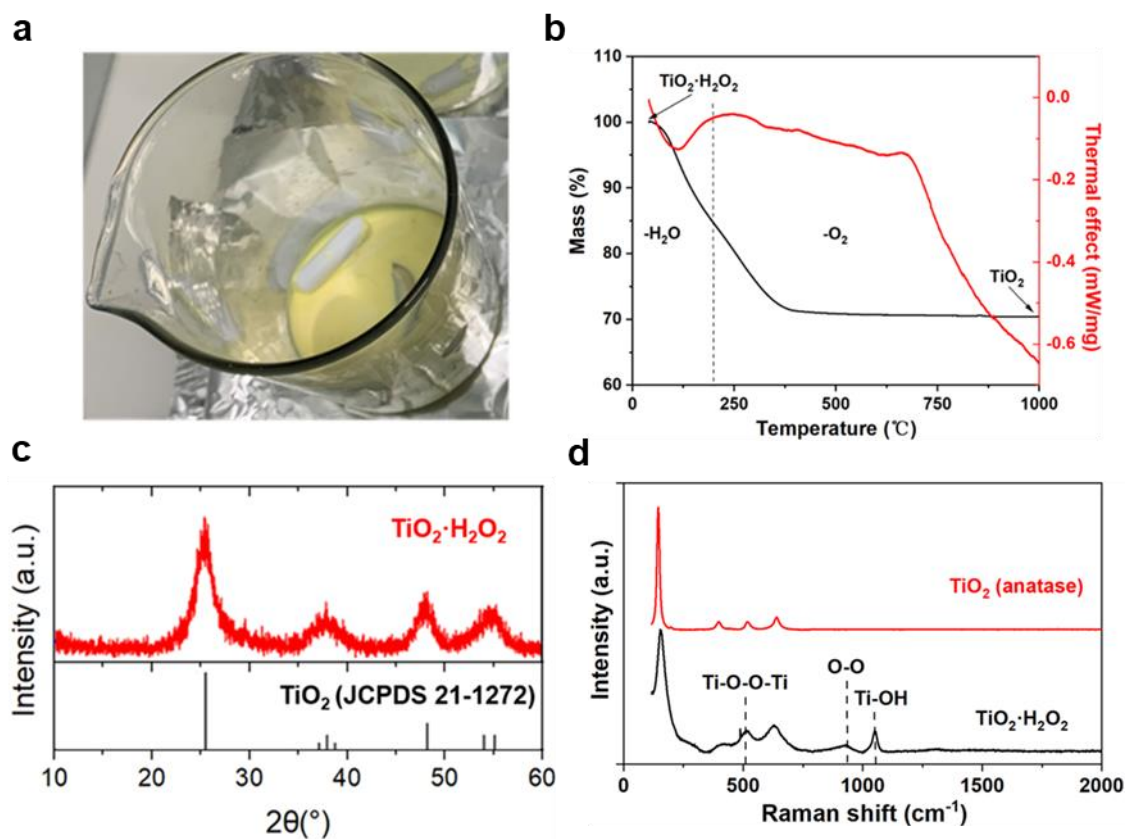
Figure. 3.7. (a) $TiO_2 \cdot H_2O$ powder. Studies of the solid-state Ti (IV) peroxo complex by the following methods: (b) TG and DSC; (c) XRD analysis and (d) Raman spectroscopy of the sample.

Another method that indirectly confirms the presence of peroxo groups in the structure of the resulting solid-state Ti (IV) complex is Raman spectroscopy (Figure. 3.7d) [178-180]. Thus, in the spectrum of $TiO_2 \cdot H_2O_2$, peaks characteristic of anatase are observed: 140 cm^{-1} (E_g), 510 cm^{-1} (B_{1g}), and 615 cm^{-1} (E_g). However, the presence of additional maxima at 630 cm^{-1} (symmetric Ti-O-O-vibrations), 920 cm^{-1} (O-O bond stretching) and 1050 (Ti-OH bond vibrations) indicates the formation of a peroxo complex even after solution drying and agrees with literature [186].

Table. 3.1. Sample preparation conditions for spectrophotometric measurements by various methods.

Method	$C_{H_2O_2}^0$, M	C_{Ti}^0, M	№ Solution	V_{H2O2}, ml	V_{Ti}, ml	$C_{H2O2} \cdot 10^3$, M	$C_{Ti} \cdot 10^3$, M
Isomolar series method	0.01	0.01	1	1.00	5.00	1.70	8.30
			2	1.50	4.50	2.50	7.50
			3	2.00	4.00	3.30	6.70
			4	3.00	3.00	5.00	5.00
			5	4.00	2.00	6.70	3.30
			6	4.50	1.50	7.50	2.50
			7	5.00	1.00	8.30	1.70
Asmus straight-line method	0.01	0.01	1	1.00	0.05	5.00	0.25
			2	1.00	0.10	5.00	0.50
			3	1.00	0.15	5.00	0.75
			4	1.00	0.20	5.00	1.00
			5	1.00	0.25	5.00	1.25
			6	1.00	0.30	5.00	1.50
			7	1.00	0.35	5.00	1.75
			8	1.00	0.40	5.00	2.00
Harvey-Manning slope ratio method	0.01	0.01	1	0.05	1.00	0.25	5.00
			2	0.10	1.00	0.50	5.00
			3	0.15	1.00	0.75	5.00
			4	0.20	1.00	1.00	5.00
			5	0.25	1.00	1.25	5.00
			6	0.30	1.00	1.50	5.00
			7	0.35	1.00	1.75	5.00
			8	0.40	1.00	2.00	5.00

At the next step, this promising peroxo-complex of Ti^{4+} has been used as precursor for future synthesis of LATP. To provide uniform hogenezation of all precursor's polymer matrix has been tested. The resulting mixture was converted into polymerized matrices by copolymerization of acrylamide and N,N'-methylenebisacrylamide (Bis-acrylamide) at 60°C. The synthesis of LATP-precursors laced with a polymer matrix (Figure. 3.8) was carried out by adding acrylamide monomer and N,N'-methylenebisacrylamide crosslinker to the reaction in the following mass ratios of monomer to titanium (IV) butoxide of 2, 4, 8, 12, and 16, and the amount of acrylamide and N,N'-methylenebisacrylamide as well as other ingredients are shown in Table. 3.2.

Figure. 3.8. Optical photo of the obtained polymer matrix.

Table. 3.2. The amount of acrylamide (AAm) and N,N'-methylenebisacrylamide (Bis-AAm) as well as other ingredients for 10 g of LATP.

Ratio	$Ti(OC_4H_9)_4$ (g)	AAm (g)	Bis-AAm (g)
2	14.00	19.83	4.96
4	14.00	45.80	11.45
8	14.00	89.20	22.30
12	14.00	132.60	33.10
16	14.00	176.00	44.00

Note: Ratio is the mass ratio of monomer to titanium (IV) butoxide.

The ratio of acrylamide/ N,N'-methylenebisacrylamide was fixed as 4/1. Other inorganic components have been used to preserve a mentioned above molar ratio of LATP. The concentration of the reaction mixture was varied and diluted up to 10 times. The polymerized matrices were dried at 60°C for 24 hours.

3.3.1.3.2. Thermal treatment of prepared composite for LATP synthesis

The optimal studied ranges of thermal treatment in the course of synthesis using polymerized matrices, as well as the stages of decomposition occurring in this process, were determined by thermogravimetry (TG) with differential scanning calorimetry (DSC) using a Netzsch STA 409 PC Luxx synchronous thermal analyzer. The temperature was changed from 30°C to 1000°C at a rate of 10°C/min. TG and DSC were also used to study the thermal stability and composition of the titanium (IV) peroxo complex and other precursors.

$$[TiO_2(H_2O)_4](NO_3)_2 \rightarrow TiO_2 \cdot H_2O_2 + 2\,H_2O + 2\,HNO_3 \quad (19)$$

$$TiO_2 \cdot H_2O_2 \rightarrow 2\,TiO_2 + 2\,H_2O + O_2 \quad (20)$$
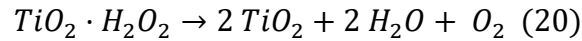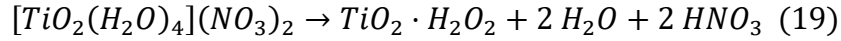
The dried polymer matrix composite was milled into powder at 700 rpm for 30-45 min and heated in a muffle furnace in magnesium oxide crucible to synthesize LATP. The synthetic temperature program was as follows: heat the polymer matrix precursor to 200°C for 3 h, then heat to 600°C for 3 h, finally heat to 600-800°C for 5 h for the synthesis of LATP powder. The heating rate was selected as 2°C/min. After all the steps, samples were cooled with the furnace. The resulting powders were given names reflecting the temperature of synthesis and the relative ratio of monomer to titanium (IV) butoxide:

Table. 3.3. LATP sample name list.

Sample name	Relative ratio	Synthesis temperature, °C	Concentration of Ti^{4+}, M
800-1.0	2	800	0.400
800-2.5	4	800	0.160
800-5.0	8	800	0.080
800-7.5	12	800	0.053
800-10.0	16	800	0.040
700-1.0	2	700	0.400
700-2.5	4	700	0.160
700-5.0	8	700	0.080
700-7.5	12	700	0.053
700-10.0	16	700	0.040
600-1.0	2	600	0.400
600-2.5	4	600	0.160
600-5.0	8	600	0.080
600-7.5	12	600	0.053
600-10.0	16	600	0.040

3.3.2. Fabrication of ceramic SSEs

3.3.2.1. Molding of LATP powders

To form tablets from LATP powders and crushed glass powders, 0.2 g of each sample were

pressed using a stainless mold with a diameter of 9 mm (Hench Technology Co., Ltd., China) on a laboratory press (Carver Inc., USA) at uniaxial pressure of 150 MPa for 2 minutes. The green body tablets after press have a diameter of 9 mm and thickness of ~2 mm. The values of volume change of the obtained tablets before and after sintering were determined and the relative densities were calculated from the obtained theoretical LATP X-ray density.

3.3.2.2. Determination of the sintering program of LATP ceramic samples

In order to determine the optimal sintering program for powder samples of 600nm and 300nm size $Li_{1.3}Al_{0.3}Ti_{1.7}(PO_4)_3$, (named LATP-1 and LATP-2) heat treatment was carried out in the temperature range of 700-1200°C with different duration from 0.5-10 h. Precise characterization of samples was treated in the temperature range of 750-1000°C with different durations:

1) 0.5 hours (samples 750°C-0.5-1, 800°C-0.5-1, 850°C-0.5-1, 900°C-0.5-1, 950°C-0.5-1, 1000°C-0.5-1, 750°C-0.5-2, 800°C-0.5-2, 850°C-0.5-2, 900°C-0.5-2, 950°C-0.5-2 and 1000°C-0.5-2, respectively);

2) 2 hours (samples 750°C-2-1, 800°C-2-1, 850°C-2-1, 900°C-2-1, 950°C-2-1, 1000°C-2-1, 750°C-2-2, 800°C-2-2, 850°C-2-2, 900°C-2-2, 950°C-2-2 and 1000°C-2-2, respectively);

3) 6 hours (samples 750°C-6-1, 800°C-6-1, 850°C-6-1, 900°C-6-1, 950°C-6-1, 1000°C-6-1, 750°C-6-2, 800°C-6-2, 850°C-6-2, 900°C-6-2, 950°C-6-2 and 1000°C-6-2, respectively);

4) 10 hours (samples 750°C-10-1, 800°C-10-1, 850°C-10-1, 900°C-10-1, 950°C-10-1, 1000°C-10-1, 750°C-10-2, 800°C-10-2, 850°C-10-2, 900°C-10-2, 950°C-10-2 and 1000°C-10-2, respectively);

Sintering was carried out in KSL-1200X-J muffle furnace (MTI, China). The heating rate was 2°C/min. The study of the microstructure of the obtained samples was carried out using scanning electron microscopy. Electrochemical properties were analyzed using impedance spectroscopy. The resulting tablets were manually crushed with an agate mortar with pestle and examined by XRD to determine the phase composition. The program with the optimal temperature and sintering time was determined from the values of the relative density and ionic conductivity obtained in each series of experiments.

3.3.2.3. Study of thermal behavior of LATP glass sample

The linear shrinkage of pressed LATP glass samples were measured in isothermal and polythermal programs up to 1000°C at a heating rate of 2-5°C/min in a DIL 402 Expedis Classic horizontal dilatometer.

3.3.2.4. Fabrication of SSEs from composite powder system

3.3.2.4.1. Bimodal powder as precursor for SSE

Mixed 60nm size and 600nm size LATP powder (hereinafter bimodal powder system) were prepared in 0/100, 5/95, 10/90, 15/85, 20/80 and 100/0 various weight fractions, respectively. The powders were thoroughly mixed using a planetary milling method. Zirconium dioxide milling balls with a diameter of 2.0-2.2 mm (10 times the mass of the powder in total), and acetone is used as a solvent (20ml of acetone is added for every 10g of powder). The revolution speed is 200 rpm, the rotation speed is 400 rpm, and the time is 1.5 h. Use 18,000-mesh nylon filter to remove ball milling balls and dry acetone in an oven. To obtain tablets with different ratios of bimodal powder system, 0.2 g of each sample were pressed using a stainless mold with a diameter of 9 mm (Hench Technology Co., Ltd., China) on a laboratory press (Carver Inc., USA) at uniaxial pressure of 150 MPa for 2 minutes. Also, after determining the densities of the obtained tablets, the relative densities were calculated from the obtained theoretical LATP X-ray density.

The determination of the optimal sintering program for bimodal powder systems with different ratios of components were carried out at 900°C for 6 hours in KSL-1200X-J muffle furnace (MTI, China) with a heating rate of 2°C/min.

According to the data of relative density, microstructure, ionic conductivity and elastic modulus obtained from each system, the optimal ratios and sintering program of the bimodal system was determined.

3.3.2.4.2. Composite glass-ceramic powder as precursor for SSE

Mixture of ~ 60 nm size LATP glass powder and 600nm size LATP powder (hereinafter glass-ceramic powder system) were prepared in 0/100, 1/99, 3/97, 5/95, 10/90, 15/95 and 20/80 various mass ratios, respectively. The powders were thoroughly mixed using a planetary milling method. Zirconium

dioxide milling balls with a diameter of 2.0-2.2 mm (10 times the mass of the powder in total), and acetone is used as a solvent (20ml of acetone is added for every 10g of powder). The revolution speed is 200 rpm, the rotation speed is 400 rpm., and the time is 1.5 h. Use 18,000-mesh nylon filter to remove ball milling balls and dry acetone in an oven. To obtain tablets with different ratios of glass-ceramic powder system, 0.2 g of each sample were pressed using a stainless mold with a diameter of 9 mm (Hench Technology Co., Ltd., China) on a laboratory press (Carver Inc., USA) at uniaxial pressure of 150 MPa for 2 minutes. Also, after determining the densities of the obtained tablets, the relative densities were calculated from the obtained theoretical LATP X-ray density.

The determination of the optimal sintering program for composite glass-ceramic systems with different ratios of components was carried out using the methods of 1-step heating treatment method and 2-steps heating treatment method. 1-step heat treatment of mixed powders with mass ratios of glass-ceramic as 0/100, 1/99, 3/97, 5/95, 10/90, 15/95 and 20/80 was carried out at 900°C for 6 hours to achieve compaction of all components in KSL-1200X-J muffle furnace (MTI, China) with a heating rate of 2°C/min. In the case of 2-steps method, densification process was carried out at a constant temperature of 570°C for 6 hours to achieve glass densification, then sintered at 900°C for 6 hours in KSL-1200X-J muffle furnace (MTI, China) with a heating rate of 2°C/min.

According to the data of relative density, microstructure, ionic conductivity and elastic modulus obtained from each system, the optimal ratio of the composite glass-ceramic powder system and the sintering program were determined.

3.3.3. Multiphysics simulation

3.3.3.1. Software description

In this PhD thesis, the following software has been used to complete the model construction, solution and data analysis.

1. The physical structure was built using: Python 3, Matlab 2020a, Solidworks 2022, AutoCAD2020 and ProE 4.0.

2. The solution of the model is based on: COMSOL Multiphysics 6.0, SIMULIA Abaqus FEA.

3. The analysis of the solution results and the drawing of the figures are based on: Python 3, Matlab2020a and OriginLab 2021.

3.3.3.2. Mathematical model construction

As aforementioned in the literature review, the failure of solid-state electrolyte with the nucleation of Li metal was widely accepted as the electro-chemo-mechanical process, which can be distinguished into different electrochemical processes containing mass-transfer, charge-transfer kinetics and constitutive damage mechanics.

Firstly, Butler-Volmer equation coupled with Nernst-Planck equation was yielded to describe the electrodeposition of Li metal inside the solid-state electrolytes [188-189]:

$$i = i_0 \, exp(\frac{\alpha \Delta \mu_{e^-}}{RT})[exp(\frac{\alpha F}{RT}\eta) - exp(-\frac{\beta F}{RT}\eta)] \quad (21)$$

where i_0 is the exchange current density, $\Delta \mu_{e^-}$ is the electrochemical potential change induced by the local strain, α and β are the anodic and cathodic transfer coefficients, and η is the overpotential. Based on Monroe and Newman's theory, $\Delta \mu_{e^-}$ can be expressed as [140, 190-191]:

$$\Delta \mu_{e^-} = -\frac{1}{2}(\bar{V}_{Li} + t_- \bar{V}_{Li^+}) \times \{-2\gamma\kappa + n[\tau_d{}^{Li} - \tau_d{}^{LAGP}]\} + \frac{1}{2}(\bar{V}_{Li} - t_- \bar{V}_{Li^+})(\Delta \, p_{Li} + \Delta p_{LAGP}) \quad (22)$$

where $\bar{V}_i$ is related molar volume, γ is surface energy, κ is mean curvature, $\boldsymbol{n}$ is unite vector pointing from Li metal to ceramic SSE with NASICON (LAGP was considered as model SSE), $\boldsymbol{\tau_d}$ is the deformation stress and p is pressure.

To investigate the effect of grain boundary on the electro-chemo-mechanical failure of solid-state electrolyte closer to reality, Voronoi domain $D \subset R^2(R^3)$ is applied to partition a plane with a set of random points $E=\{A_i\}$, and thus $A_i \in D$. Hence, the polygon cell can be given as [192-194]:

$$zi(A_i) = \{P \in D | d(P, A_i) < d(P, A_j), \forall j \neq i\} \quad (23)$$

where $d(P_i, P_j)$ is the Euclidean distance between points P_i and P_j. The distribution of each polygon is spatially random by using repulsion distance.

We choose elastic modulus as the primary index to evaluate the mechanical properties of solid-state electrolyte ceramic materials. Here, the grain inside SSE was considered as basic single crystal viscoplastic model, which is proposed by Cailletaud et al. Although the grains have some elastic-plastic deformation ability in the model setting, due to its huge elastic modulus (> 150 GPa), the impact of this deformation ability on the final crack propagation mechanism is almost negligible. The small strain in the single crystal system can be described as follow [195-196]:

$$\dot{\gamma}^s = \left| \frac{|\tau^s - x^s| - r^s - \tau_0}{K} \right|^n sign(\tau^s - x^s) = \dot{v}^s \eta^s \quad (24)$$

where $\dot{\gamma}^s$=is viscoplastic shear, τ^s=is resolved shear stress, r^s=is the isotropic hardening variable, x^s is the variable about kinematic hardening, the $\dot{v}^s$ is the accumulated value of $\dot{\gamma}^s$ and

η^s is the sign of $(\tau^s - x^s)$. Moreover, the slip rate can be given by the means of τ^s, r^s and x^s. Resolved shear stress τ^s and viscoplastic strain rate tensor $\dot{\varepsilon}_{\sim}^p$ are associated with the orientation tensor $\boldsymbol{m}_{\sim}^s$ [197-198]:

$$\tau^s = \boldsymbol{m}_{\sim}^s : \boldsymbol{m}_{\sim}; \quad \dot{\varepsilon}_{\sim}^p = \sum_s \dot{\gamma}^s \boldsymbol{m}_{\sim}^s \quad (25)$$

where orientation tensor $\boldsymbol{m}_{\sim}^s$ can be yielded as the symmetric part of tensorial product of normal to the slip plane $\underline{n}^s$ and slip direction $\underline{l}^s$ of $\boldsymbol{m}_{\sim}^s = \frac{1}{2}(\underline{n}^s \otimes \underline{l}^s + \underline{l}^s \otimes \underline{n}^s)$. The state variables ρ^s and α^s can be used to determine the hardening variables $r^s = bQ \sum_p h_{sr}\rho^r$ and $x^s = c(\eta^s - dx^s)\dot{v}^s$, where b, Q and c are material parameters calibrated in the low-viscous system.

To extend to the system, the cleavage is accepted as a typical failure behavior that appears on the plane where the cohesive force is smaller than external loading. The normal stress is assumed as the critical variable for cleavage, which can be yielded as $\sigma^{cl} = \underline{n} \cdot \boldsymbol{\sigma}_{\sim} \cdot \underline{n}$. When the stress reaches the threshold R^{cl}, cleavage failure happens. Therefore, a pseudo-strain is taken into consideration of the cleavage opening [199]:

$$\dot{\varepsilon}_{\sim}^{cl} = \langle \frac{\sigma^{cl} - R^{cl} - Q(1 - \exp(-b\delta^{cl}))}{K} \rangle^n \underline{n} \otimes \underline{n}. \quad (26)$$

Furthermore, the damage of grain boundary is introduced inside the classical crystal plasticity model. At initial stage, grain boundary is stiff enough in the normal direction for the grains' pasting without damage. Moreover, only in-plane shear is adopted by grain boundary and thus an anisotropic elastic tensor can be given as [200]:

$$\Lambda_{\approx} = diag(E, \eta, \eta, \mu, \eta, \mu). \quad (27)$$

η is tiny to bring the effect on the successive process. Owing to the anisotropy considered above, based on the introduction of a variable to describe scalar damage (D), the free energy associated with the elasticity is modified as [201]:

$$G = \frac{1}{2}(1 - D)\boldsymbol{\varepsilon}_{\sim}^e : \Lambda_{\approx} : \boldsymbol{\varepsilon}_{\sim}^e \quad (28)$$

Taking the opposite of the partial derivative of G with respect to D,

$$Y = -\frac{\partial G}{\partial D} = \frac{1}{2}\boldsymbol{\varepsilon}_{\sim}^e : \Lambda_{\approx} : \boldsymbol{\varepsilon}_{\sim}^e = \frac{1}{2(1-D)^2}\left(\frac{\sigma_{11}^2}{E} + \frac{\sigma_{12}^2 + \sigma_{13}^2}{\mu}\right) = \frac{1}{2(1-D)^2}\left(\frac{\sigma_n^2}{E} + \frac{\tau^2}{\mu}\right) \quad (29)$$

where $E=$is elastic modulus and $\mu=$is displacement. Therefore, a variable about the damage stress σ_d can be yielded as:

$$\sigma_d = \sqrt{\sigma_n^2 + E/\mu\,\tau^2} = (1 - D)\sqrt{2EY} \quad (30)$$

The flow rules of damage in constitutive equations with the acceptation thermodynamics with convex potentials is gained as follow [199-201]:

$$\dot{D} = \frac{\partial F_d}{\partial Y} = [\frac{(1-D)\sqrt{2EY}}{A}]^r (1 - D)^{-k} = \left(\frac{\sigma_d}{A}\right)^r (1 - D)^{-k} \quad (31)$$

where F_d is the damage potential function and A is crack area.

3.3.3.3. Boundary condition setting

In the overall model definition, we set the Li metal as an indestructible deformable material with a certain elastic modulus and Poisson's ratio. Therefore, along with the deposition of fresh Li at the Li/solid-state electrolyte interface, it is also accompanied by the compression and mechanical deformation (both elastic deformation and plastic deformation) of Li metal in some inner regions. From the perspective of simplifying the model, we did not consider the creep effect of Li metal which will be demonstrated in our follow-up work. Because the creep of Li metal mainly acts on the process of filling the defect area or extending to the extra space. In the model, we assume that Li metal has completely filled the defect area.

For the multiphysics model used here, the core boundary conditions are set as follows:

1) Damage-Crack transformation process

Based on the basic mechanical properties such as the elastic modulus of the material, when different finite element divisions of the material are subjected to different stresses, the deformations that occur are also different. Therefore, we give here the basic settings based on material damage and cracks:

1. When the stress in the finite element region is less than 20% of the material's intrinsic properties, we believe that the deformation occurring at this time is reversible deformation. That is, the stress will not cause damage to the material.

2. When the stress in the finite element region is 20-100% of the material's intrinsic properties, we believe that the deformation occurring at this time is irreversible deformation. That is, the stress will cause damage to the material. The residual mechanical properties of the material after damage are expressed by the above model and normalized to a damage index ranging from 0-1.

3. The cracks must occur in areas where the material is damaged. Therefore, we gave a damage index of 0.8 (80%) as the critical point for artificial calibration. That is, the part in the finite element region with a damage degree between 0 and 0.8 is regarded as the initiation area of microcracks. The expansion of microcracks is mainly concentrated in the finite element region where the damage index is greater than 0.8.

2) Electron conduction

To simplify the model, lithium filament is set as the only electronic conductor and the electronic conductivity of the solid electrolyte is not considered. At the same time, there is no breaking Li dendrite the failure process of solid electrolyte.

3) Ionic conduction

It is assumed that only solid electrolytes with less than 80% of damage degree is capable of ionic conductivity. The ionic conductivity of solid electrolyte with a damage degree more than 80%, and void region is set as 0.

4) Electrochemical deposition processes

The area of electrochemical deposition (circumferential thickening of lithium dendrites) is limited to the contact area between lithium dendrites and solid electrolytes with a damage degree of less than 80%. The deposition process is limited by Fick's law and the B-V equation.

5) Process of material stress and damage

The outer boundary of the solid electrolyte is set as free from external forces and can be deformed freely. At the same time, lithium metal material is given certain ductility and adhesion and the solid electrolyte material is defined as an ideal brittle ceramic material, regardless of the compressibility and anisotropy of the material.

4. Results and discussion

Modeling results

4.1. Numerical simulation by phase-field method to establish the required physic-chemical and morphological properties of the solid-state electrolyte

In theory, due to the weak mechanical properties of lithium metal, the use of solid-state electrolyte (SSE) can inhibit the growth of lithium filaments in SSB. But lithium filaments grow along the solid-state electrolyte grain boundaries and surface and internal defects, which is obstacle issue that has to be considered. Tremendous endeavor has been concentrated to monitor the mechanical failure of SE using high-tech characterization, e.g., synchrotron X-ray computed tomography, environmental transmission electron microscopy, neutron scattering, yet, the evolution of stress field inside SE along with the growth of Li metal is arduous to be pictured and analyzed preciously. Thus, the insight into the propagation of Li metal and corresponding perturbation on the surrounding stress field is accepted as the top priority to reveal the failure process of SSE unambiguously for prolongating the cyclic performance of solid-state batteries, which can be regarded the linkage of electrochemical process and mechanical process. Multiphysics modeling is a mesoscale simulation method which is applied in the PhD work to quantitatively understand the microstructure evolutions. The influence of the microscopic morphology and sintering quality of the solid-state electrolyte on the damage of the lithium filament to the solid-state electrolyte is explored here

4.1.1. Influence of morphological features in solid-state electrolyte on damage propagation originated from Li filaments formation

To reveal the role of microstructural features of defects and as a result of Li filaments in SSE on its disintegration during propagation of Li filaments, the monocrystal SSE with NASICON structure has been considered to simplify time consumption of modeling.

4.1.1.1. Shape of defects in Solid-state electrolyte
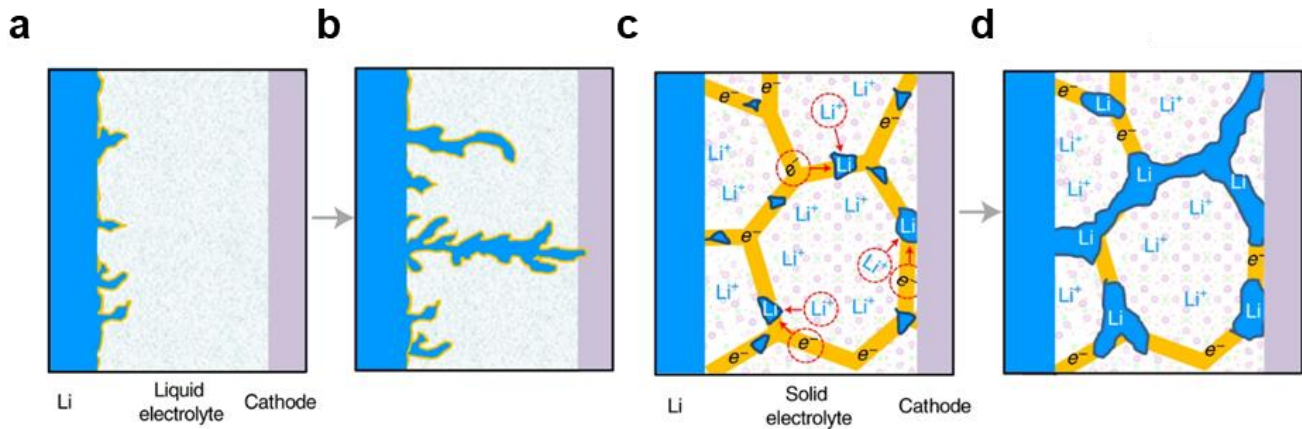
Figure. 4.1. Schematic images of Li anodes cycled in the liquid (a, b) and solid electrolytes (c, d).

In common liquid electrolyte lithium batteries, as the deposition process proceeds, lithium dendrites can have a series of different morphologies from fibrous/filamentous to mossy due to the uniform electrical properties and lack of mechanical properties of the liquid electrolyte. However, in solid-state electrolyte batteries, the morphology of lithium filaments is affected by the mechanical and electrical properties of the SSE, and usually can extend along the grain boundaries or through ceramic defects (voids, cracks). In this case, the morphology of lithium filaments is related to the initial defect morphology, grain boundary morphology, and subsequent crack morphology. It is also affected by the different electronic conductivity and ionic conductivity of grains and grain boundaries. [202].
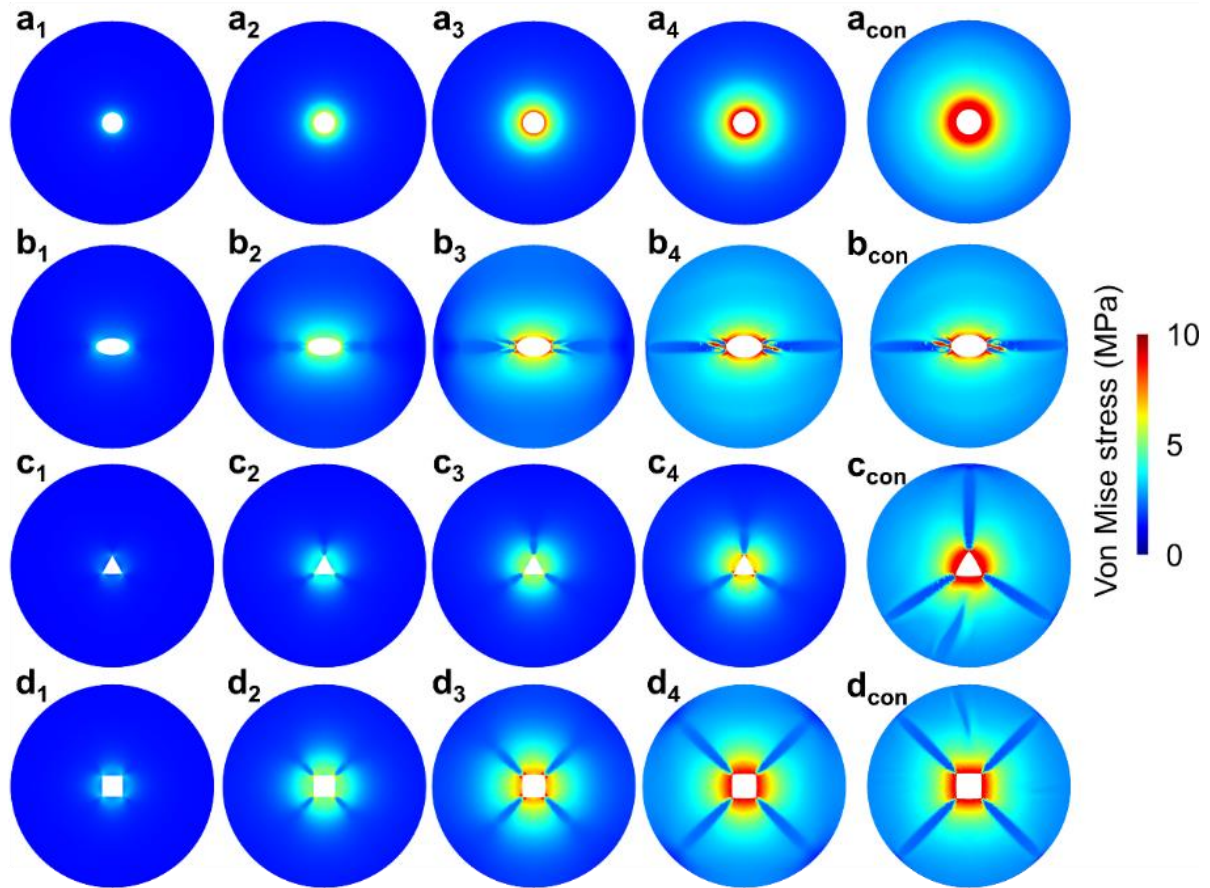
Figure. 4.2. Evolution of stress distribution around Li filaments inside solid electrolyte. Visualization of von Mises stress around Li filaments with geometries of (a) cylinder, (b) elliptical cylinder, (c) triangular prism, and (d) cube. The subscript of Arabic numerals represents the key steps with same calculating time, and the subscript of "con" means the convergence of calculation (final state).

The geometry of Li filaments in solid electrolyte has been revealed as triangle at the triple junction, cylindrical whiskers or dendrites, sheet-like or branch-like, by experimental techniques. It is found that the Li filament geometry is shaped by current density, solid electrolyte, and local fields.

Here, typical geometries for a single Li filament, cylinder, elliptical cylinder, triangular prism, and cube, are chosen to investigate the local effect of the geometry on the failure process of solid electrolyte in bulk. As seen in the distribution of von Mises stress caused by the growth of Li filament, the region surrounding the Li filament shows an obvious stress increase, which is induced by the extrusion from the circumferential expansion of Li filament. Along with the growth of Li filament, the area with higher stress gradually enlarges. ***Typically, when the geometry of Li filament is set as the cylinder, the high-stress region is relatively uniform compared with that created by Li filaments with***

other geometries.

Moreover, the high-stress region will be separated when there is structural fluctuation on edge of the Li filaments. Two separated regions show up in parallel with the ellipse axis when the geometry of Li filament changes to the elliptical cylinder. Three and four separated regions are seen in parallel with the sides of triangle and rectangle when the geometry of Li filament inside solid electrolyte appears as triangle prism and cube, respectively.

It is worth noting that the boundaries that separate the different high-stress regions exhibit relative low stress, which can be expected as the region for the release of stress caused by local displacement. The great structural fluctuation at the corner of cube or the vertex of elliptical cylinder are responsible to the stress concentration.

In contrast to the subsequent experimental data, when the solid-state electrolyte is sintered at low sintering temperature, the direct connection of the grains is not sufficient, so the defects often present sharp corners. When the solid-state electrolyte is sintered at an excessively high temperature, the abnormally grown grains will cause regional stress concentration and defects, and also present sharp corners. Therefore, it is meaningful to explore the optimal sintering program of the solid-state electrolyte. Not only can the relative density and mechanical properties of the solid-state electrolyte itself be improved, but the round defect boundary can also relieve the stress concentration caused by the penetration of lithium filaments.

4.1.1.2. Number and size of lithium filaments
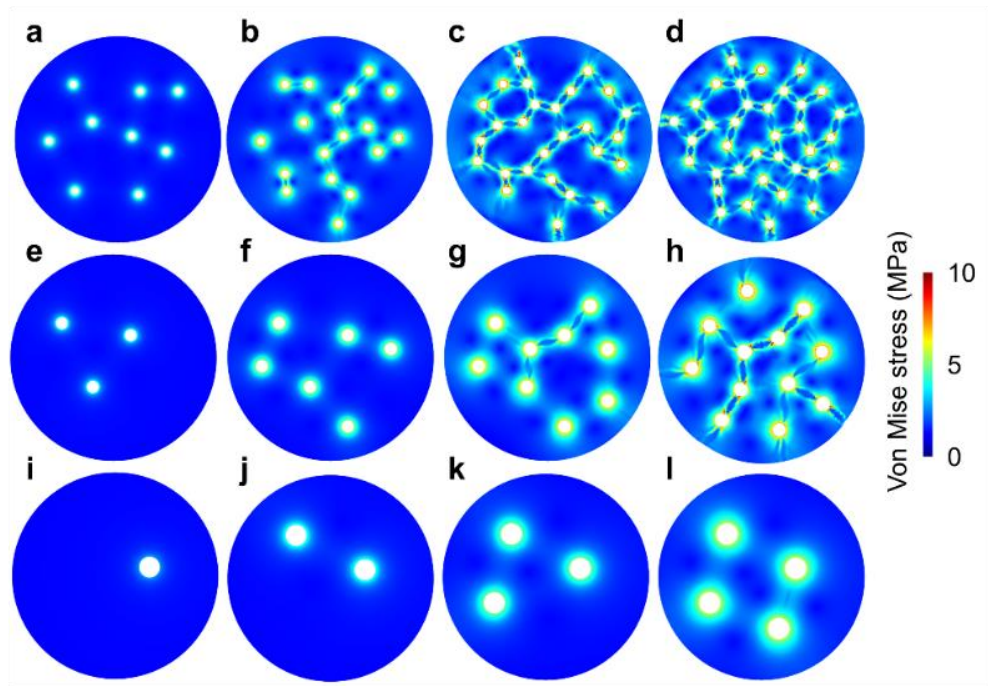
Figure. 4.3. Distribution of von Mises stress inside solid electrolyte with multiple Li filaments within equal calculation time. Stress field within solid electrolyte caused by growth of (a) 9, (b) 18, (c) 27 and (d) 36 small-size Li filaments; (e) 3, (f) 6, (g) 9 and (h) 12 medium-size Li filaments; (i) 1, (j) 2, (k) 3 and (l) 4 large-size Li filaments. The integral volume of filaments for (a, e, i), (b, f, j), (c, g, k), (d, h, i) has fixed.
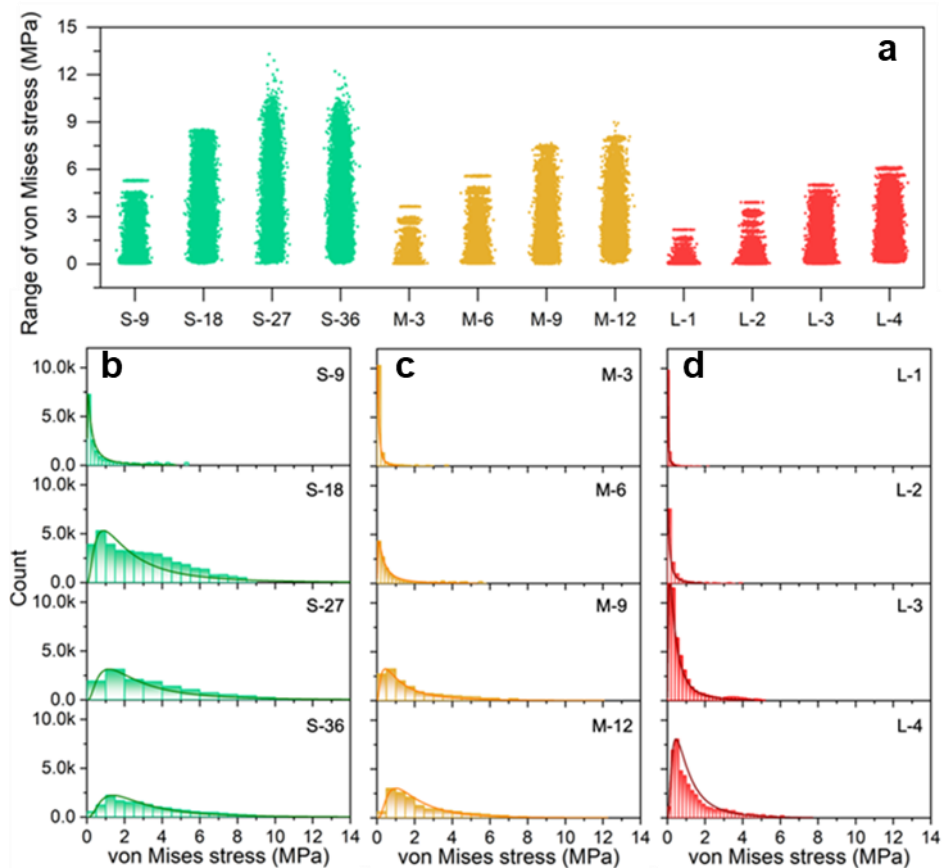
Figure. 4.4. Distribution of von Mises stress inside solid electrolyte with multiple Li filaments. (a) Range of von Mises stress inside solid electrolyte induced by growth of multiple Li filaments. Total volume of Li filaments with various sizes was set as equal and the geometry of Li filaments is fixed as cylinder. S-9, 18, 27, 36 represent Li filaments in small size and with number of 9, 18, 27, 36 in the same model volume. M-3, 6, 9, 12 represent Li filaments in medium size and with number of 3, 6, 9, 12. L-1, 2, 3, 4 represent Li filaments in large size and with number of 1, 2, 3, 4. (b-d) Frequency histogram for distribution of von Mises stress inside solid electrolyte with multiple Li filaments in (b) small, (c) medium and (d) large size.

The failure process of a real solid electrolyte will be more complicated and the interplay between contiguous Li filaments will influence the local fields. To make our modeling closer to reality, the investigation of the failure of solids electrolyte was expanded to a complex model containing multiple Li filaments, of which the geometry is selected as cylinder. The size and number of multiple Li filaments are varied whereas the total volume of Li filaments in one series with different sizes (such as S-9, M-3 and L-1) is fixed. The relative position of Li filaments inside solid electrolyte was generated using random function. Combining with the visualization of stress distribution (Figure. 4.3), it is found that von Mises stress in solid electrolyte shows two classes of distribution, around the isolated Li filaments and linkage between two adjacent Li filaments. When the number of Li filament is small, there is only lighter stress surrounding the filaments. With the increasing number of filaments, stress filed propagates and integrates as a connected region of higher stress within the solid electrolyte. For small-size Li filaments (Figure. 4.3a-d), the mean distance between two filaments is shortened with the increase of number, resulting in an integrated stress field covering the adjacent filaments. Moreover, the adjacent filaments are linked by the low stress region probably caused by the release of stress from local displacement. In contrast, the integrated stress field between adjacent filaments is weakened with the enlargement of Li filaments size (Figure. 4.3e-l).

The von Mises stress decreases with the increase of Li filament size while it increases with the rising number of filaments inside solid electrolyte (Figure. 4.4a). ***Therefore, under the condition of same volume of Li inside solid electrolyte, less-and-large Li filaments contribute to lower stress, while plenty-and-small Li filaments endow the bulk of solid electrolyte with locally high stress field.***

4.1.1.3. Effects of voids inside of SSE
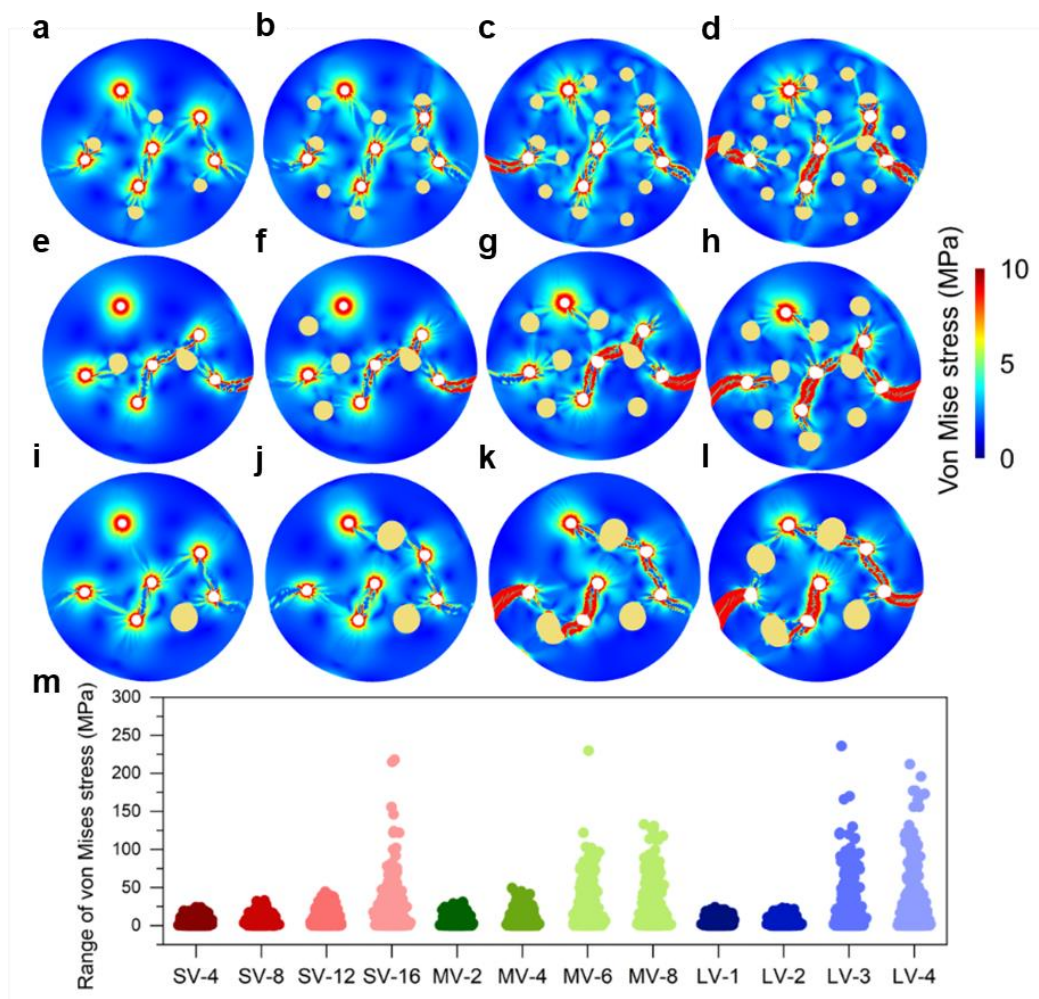
Figure. 4.5. Effect of voids on the distribution of von Mises stress inside solid electrolyte at convergence state. Distribution of von Mises stress inside solid electrolyte containing 6 grown Li filaments and (a) 4, (b) 8, (c) 12 and (d) 16 small-size voids; (e) 2, (f) 4, (g) 6 and (h) 8 medium-size voids; (i) 1, (j) 2, (k) 3 and (l) 4 large-size voids. Voids and Li filaments are represented by brown regions and white regions, respectively. (m) Range of von Mises stress inside solid electrolyte caused by the voids and the growth of Li filaments. Total volume of voids with different size was set as equal.

In a real solid electrolyte pellet, a certain number of internal voids is inevitably formed during the sintering process due to the distribution of grain size, relative density change, anisotropic growth of grains, etc. In this study, the pre-existing voids in solid electrolyte were considered to visualize the damage process and to evaluate the effect of size and number of voids on the failure of solid electrolyte

with certain amount of Li filaments inside.

As shown in Figure. 4.5, the high-stress regions caused by the compression from the growth of Li filaments mainly surround the Li filaments, and they can be disturbed by the near stress filed to show radial shape. The interior of two high-stress regions between Li filaments presents an under-stress region, illustrating the stress-releasing for the local displacement. Moreover, the high-stress regions tend to connect with each other, and their propagation can bypass the internal voids. Within the same damaging time of 2.5 s, the distribution of von Mises stress shows a negligible difference with the increased number of voids inside, varying from 4 to 16 (Figure. 4.5a-d). The same tendency for the distribution of von Mises stress can be observed inside the bulk of electrolytes with medium-size and large-size voids. ***The discreteness for the distribution of von Mises stress is enlarged with the increased number of voids. Therefore, the number of internal voids delivers a more significant effect on the stress and displacement fields as compared to the size.***

4.1.1.4. Shape of interfacial defects on SSE
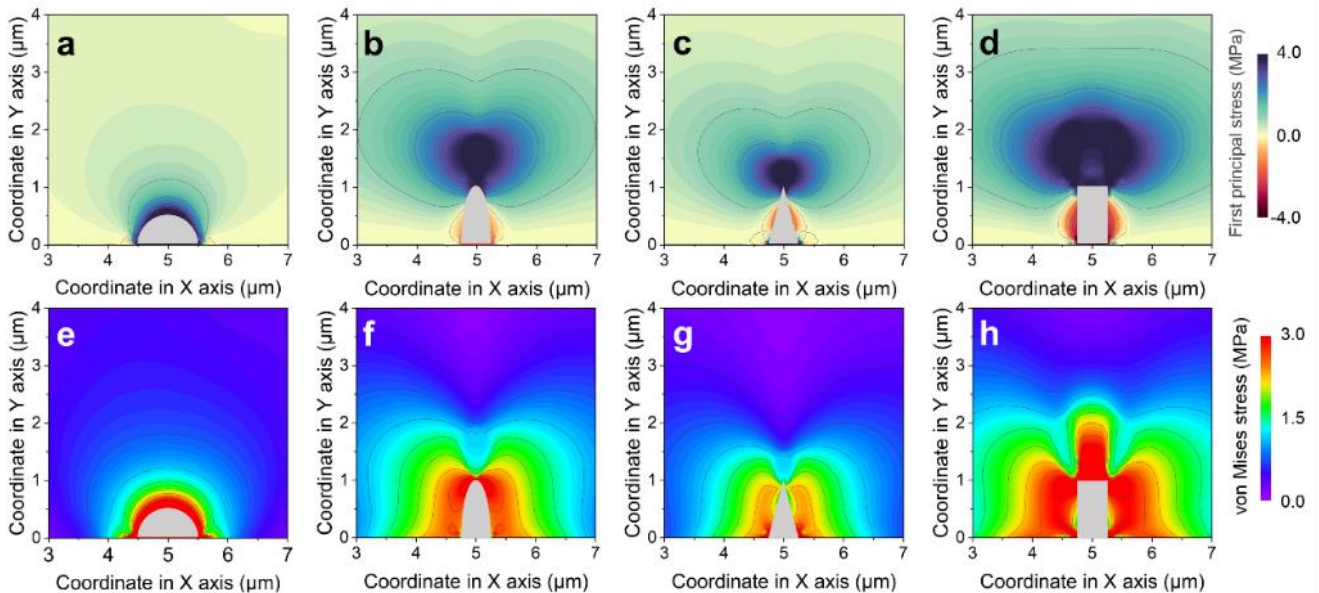
Figure. 4.6. Distribution of stress field induced by electrodeposition of Li inside interfacial defect. a-d) Visualization of first principal stress and e-h) von Mises stress caused by the electrodeposition of Li at the interface of SSEs with (a, e) semi-spherical, (b, f) semi-elliptical, (c, g) pyramidical and (d, h) cubic interfacial defects. The results were captured once the electrodeposited Li metal crammed the inner space of interfacial defects.

From the visualization of the first principal stress distribution inside the solid-state electrolyte, obvious compressive stress region appears above the top of interfacial defect with various shapes due to the electrodeposition of Li metal inside the limited inner space of interfacial defects (Figure. 4.6a-d). All compressive stress spreads inward the solid-state electrolyte with semi-spherical defect in water-wave shape due to its isotropic (Figure. 4.6a). Whereas the tensile stress regions cover the side of other interfacial defects and the compressive stress spreads inside the bulk in different orientations, of which the compressive stress regions are separated into several parts on the top of different interfacial defects, such as semi-elliptical (two parts), pyramidic (two parts) and cubic (three parts) (Figure. 4.6b-d).

As shown in Figure. 4.6e-h, the distribution of von Mises stress outside the semi-spherical defect shows a circle-shape, while a symmetric and butterfly-shape distribution appears outside the semi-elliptical and pyramidic defects. Apart from the symmetric regions of stress, a third high-stress region is observed on the roof of cubic defect (Figure. 4.6h). Therefore, the high-stress regions generated from the compression of electrodeposited Li inside the limited space of interfacial defect is strongly related to the fluctuation at the boundary of interfacial defects against the solid-state electrolytes.

The stress regions of the electrodeposited Li inside the electrolyte with semi-spherical defect in X axis is the strongest among others, whereas it exhibits the weakest stress field generated inside the solid-state electrolyte. Meanwhile, in the direction along with Y axis, the cubic interfacial defect shows the greater stress field inside solid-state electrolyte, which is presented by the highest stress and the longer propagation length inside solid-state electrolyte. Therefore, the results indicate that the stress inside the solid-state electrolyte induced by the restricted electrodeposition of Li metal is strongly correlated to the geometry of interfacial defect, of which the cubic defect can cause the strongest stress inside the solid-state electrolyte than among the other defects.

4.1.1.5. Size of interfacial defects

The failure process of the SSE was visualized by the relative damage. The relative damage correlates with the mechanical strains in the SSE resulting from the formation of lithium protrusions and varies from 0 to 1 (Fig. 4.7 a-d). At small stress values, the distortions in the SSE are reversible

and the relative damage corresponds to 0. Defects due to microcrack initiation correspond to a relative damage of 0 to 0.8. The formation of the crack from the lithium polygon to the edge of the SSE was considered as a complete failure. The calculations were stopped at this point.
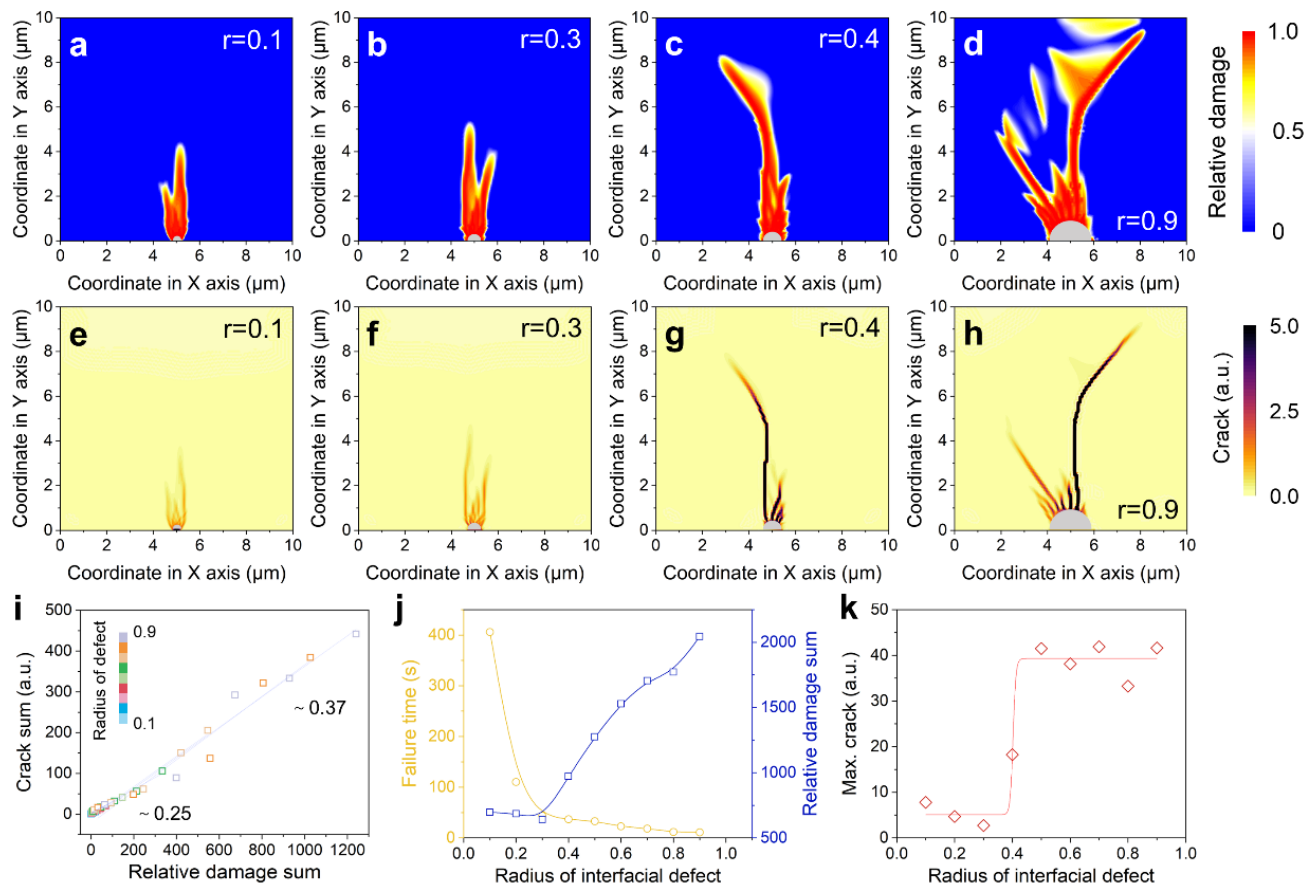

Figure. 4.7. Effect of size of interfacial defect on the mechanical failure. a-d) Visualization of the corresponding damage region inside the solid-state electrolyte with the semi-spherical interface defect in radius of (a) 0.1 μm, (b) 0.3 μm, (c) 0.4 μm and (d) 0.9 μm. e-h) Generation of crack inside soldi-state electrolyte with the semi-spherical interface defect in radius of (e) 0.1 μm, (f) 0.3 μm, (g) 0.4 μm and (h) 0.9 μm. (i) Relationship between relative damage and crack during the growth of Li metal anode. j-k) Effect of the size of interfacial defect on the mechanical failure of solid-state electrolyte that represented by(j) failure time and damage sum as well as the (k) maximum crack.

To investigate the effect of size of the interfacial defect on the mechanical failure inside the solid-state electrolyte, the semi-spherical interface defects with different radius ranging from 0.1 μm to 0.9 μm were exampled to illustrate the mechanical failure during the deposition of Li metal. As the consequence of the generated stress field, the morphology of damage region is intimated with the size of interfacial defect. When the radius of semi-sphere is smaller than 0.4 μm, flame-like relative damage

region is detected above semi-spherical interface defects, of which its height increases along with interfacial defect's larging (Figure. 4.7a-b). While the radius of semi-sphere further increases to 0.4 μm, a thin-and-long damage region appears with the length of about 8 μm (Figure. 4.7c). Once the radius of interfacial defect exceeds 0.4 μm, a distinguished branch emerges on the top of straight damage region with the total length of 9 μm at the position of Y=0.6 μm (Figure. 4.7d). Furthermore, the cracks are generated the familiar morphologies with the damage region. Slight crack can be revealed within the solid-state electrolyte with small-sized semi-spherical interface defects (r<0.4) (Figure. 4.7e-f), whereas the cracks change to greater and longer along with the expand of semi-sphere (Figure. 4.7g-h).

The linear relationship with slope of ~0.25 between the crack sum and relative damage sum is almost unchangeable with the increase of seme-sphere's radius from 0.1 to 0.6 μm. Once the radius changes to over 0.6 μm, the slopes slightly increase to ~ 0.37, which can be explained that the introduction of overlarge interfacial defect can damage the integrity of solid-state electrolyte (Figure. 4.7i). Eventually, the failure time and corresponding relative damage sum were derived from our calculation results to illustrate the effect of size of interfacial defects on the mechanical failure of solid-state electrolyte. As shown in Figure. 4.7j, the failure time is shortened rapidly from 400 s to 50 s when the radius is up from 0.1 μm to 0.4 μm, and change slowly when radius is greater than 0.4 μm. However, the change tendency of the relative damage sum is converse to that of failure time. The maximum values of crack are concentrated about 6 even with the radius of semi-sphere is smaller (0.1-0.3 μm), which is rapidly enlarged to about 40 after the size is greater than 0.4, where 0.4 is the inflection point (Figure. 4.7k). ***To sum up, it takes longer time to cause the mechanical failure of the solid-state electrolyte with small size of interfacial defect (≤0.3 μm), while greater failure happens rapidly when the radius of semi-spherical interface defect is greater than 0.4 μm. Therefore, the mechanical failure occurs whenever interfacial defects are present, of which its degree is governed by size of interfacial defect.***

4.1.2. Influence of morphological features in multi-grain solid state electrolyte on damage propagation originated from Li filaments formation

In the previous simulations, in order to more clearly show the influence of the pores inside the

solid-state electrolyte and the lithium filaments on the disintegration process, we set the solid-state electrolyte material as a homogeneous material as a whole. But in reality, grain boundaries (areas affected by grain boundaries, usually 10 nm in width) often have different mechanical properties from grain materials. Here, eterostructure model has been developed to discuss the effect of grain boundaries on the damage process in solid electrolytes

In the perspective of materials, grain boundaries and microstructural heterogeneity in polycrystalline SSE powerfully affect the bulk properties, especially mechanical properties controlled by deformation and fracture caused by the growth of Li metal inside the polycrystalline SSE. Based on Hall-Petch relationship, the grain size can be identified as the primary parameter for the failure mechanism of polycrystalline materials, who also is controlled by the existence of grain boundary. Accordingly, the electro-chemo-machinal failure of SSE during the development of Li filament can be associated to the properties of grain size and grain boundary, of which failure process with the effect of grain size as well as the boundary are strongly required to be investigated well. To prepare high-quality solid-state electrolyte ceramics, what size of precursor powder should be selected is a question that has not been systematically explored. Currently available commercial NASICON type solid-state electrolyte powders usually have only three sizes: ~ 300nm, ~ 600nm, ~ 3-5 μm. But whether these three sizes are optimal is an open question.

Nevertheless, the dynamic evolution of stress field around the Li filaments and corresponding damage propagation is hard to be monitored even with the state-of-the-art characterization, which is crucial for designing the reinforced SSE. Although the grain boundaries have been taken into the theoretical consideration for studying the mechanical failure of SSE using phase-field method via the simulation of development of Li metal along grain boundaries and the generated stress, the failure of SSE associated with the fracture is still missed. Indeed, the failure of polycrystalline SSE can be contemplated as the mechanical results of the dynamic loading from the development of Li metal. Herein, the investigation of the propagation of damage originated from Li metal developing inside polycrystalline SSE was conducted theoretically based on the combination of electrochemical kinetics and the constitutive equations.

4.1.2.1. Effect of Grain Size
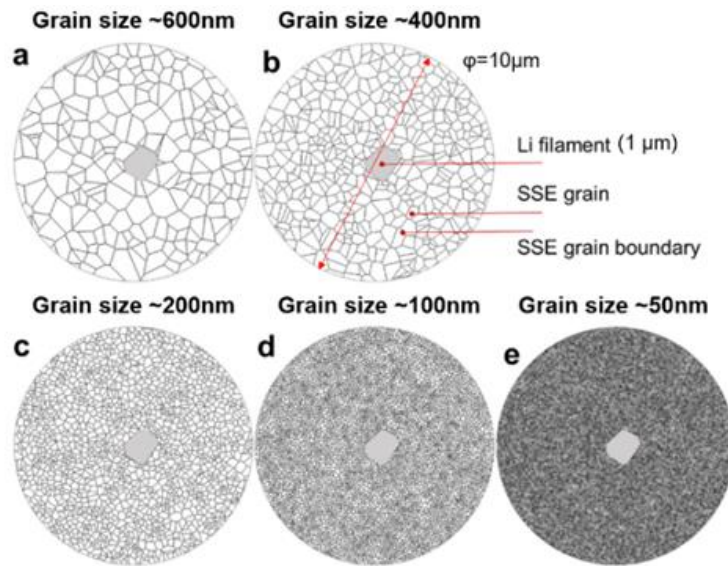
Figure. 4.8. Geometrical model of the polycrystalline SSEs with different grain size.

Firstly, Voronoï tessellation is applied to generate a series of SSE with randomly distributed convex polygon grain to evaluate the effect of the growth of Li filament inside the open void on the disintegration process of SSE, of which the open void comes from the sintering process and Li filament is placed in the center of SSE with the shape of random octagon with size of 1.0 μm (Figure. 4.8).
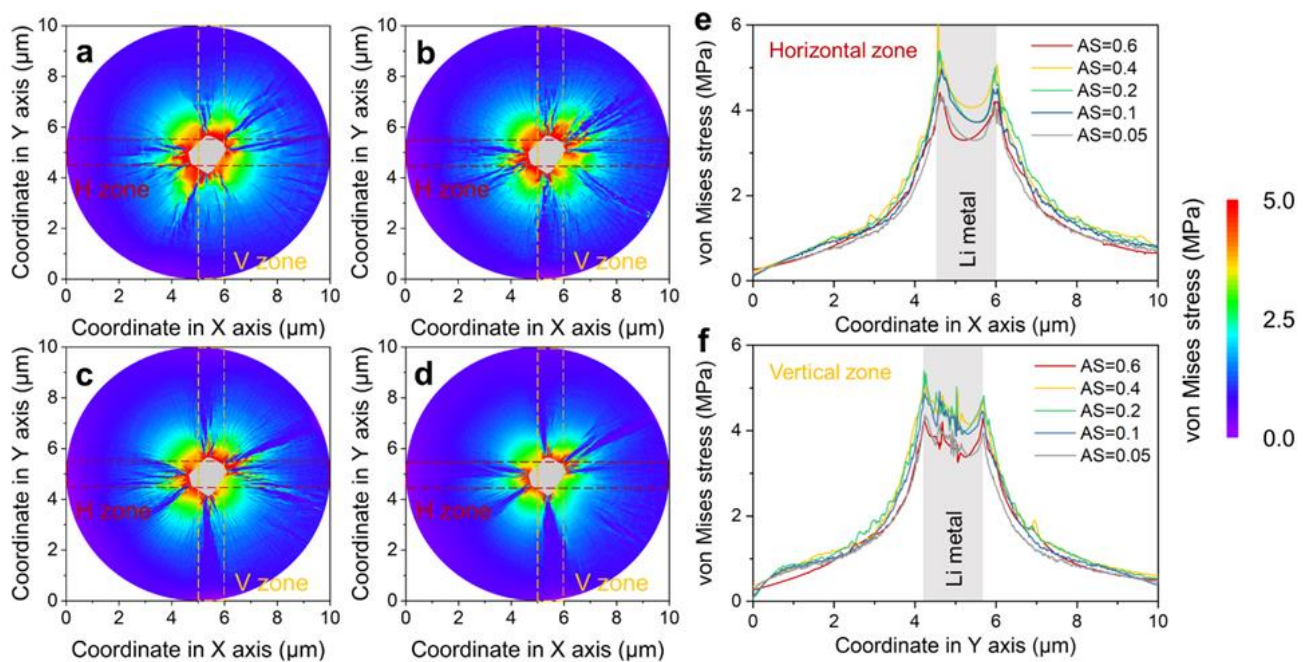
Figure. 4.9. Stress field inside SSE with different grain size. a-d) Visualization of von Mises stress caused by the development of Li filament inside the SSEs with different average grain size of (a) 400 nm, (b) 200 nm, (c) 100 nm and (d) 50 nm at final stage. e-f) Variation of von Mises stress (e) along X axis at Y=5.0 μm and (f) along Y axis at X=5.5 μm. The slide width is 1.0 μm. AS is the abbreviation of average size of grain, and the unit is μm.
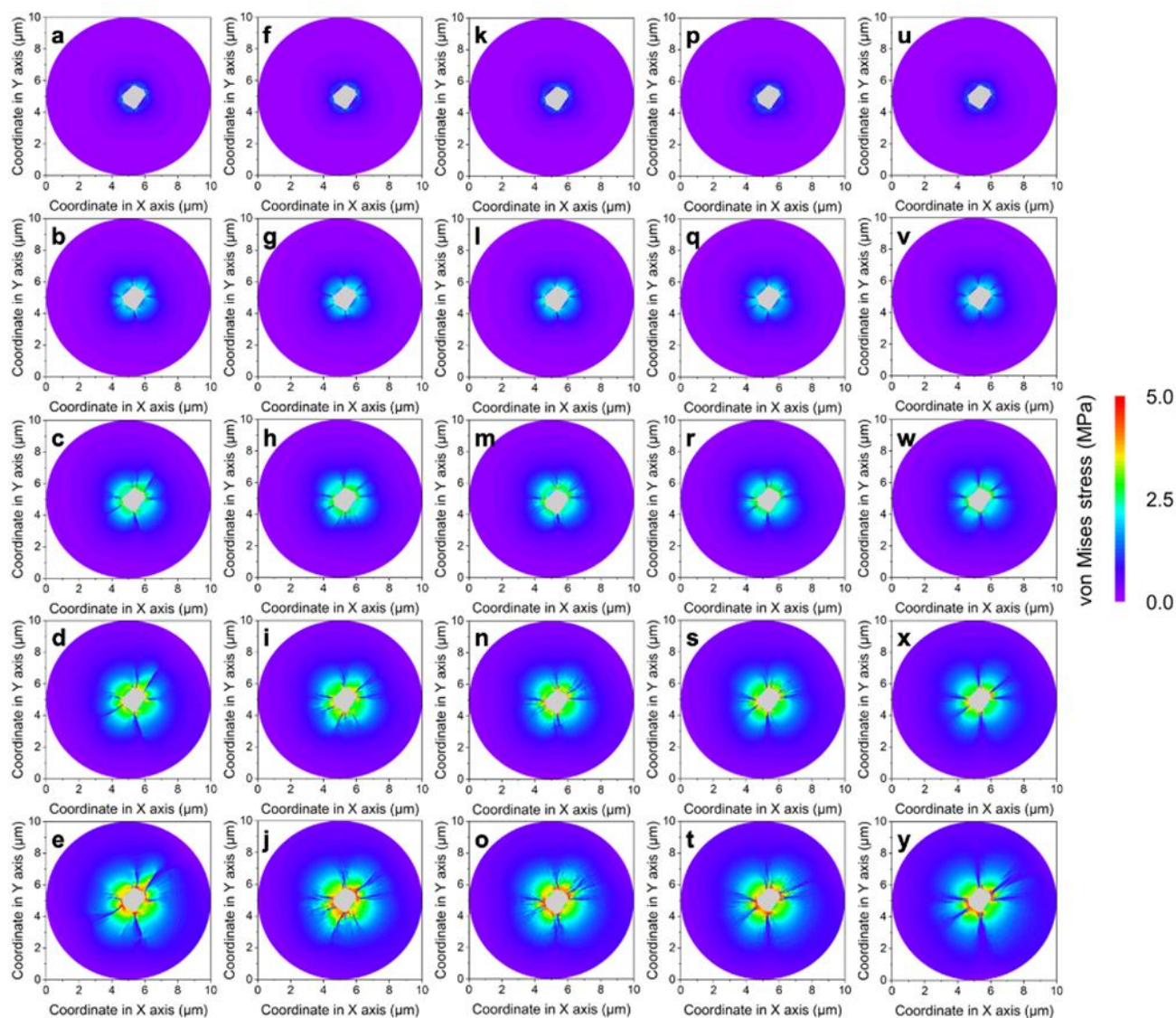
Figure. 4.10. Evolution of stress field along with the development of Li filament. a-e) Visualization of von Mises stress inside the SSE with 600nm size at calculation time of (a) 0.2 s (b) 0.4 s (c) 0.6 s, (d) 0.8 s, and (e) 1.0 s. f-j) Visualization of von Mises stress inside the SSE with 400 nm size at calculation time of (f) 0.2 s, (g) 0.4 s, (h) 0.6 s, (i) 0.8 s, and (j) 1.0 s. k-o) Visualization of von Mises stress inside the SSE with 200 nm size at calculation time of (k) 0.2 s, (l) 0.4 s, (m) 0.6 s, (n) 0.8 s, and (o) 1.0 s. p-t) Visualization of von Mises stress inside the SSE with 100 nm size at calculation time of (p) 0.2 s, (q) 0.4 s, (r) 0.6 s, (s) 0.8 s, and (t) 1.0 s. u-y) Visualization of von Mises

stress inside the SSE with 50 nm size at calculation time of (u) 0.2 s, (v) 0.4 s, (w) 0.6 s, (x) 0.8 s, and (y) 1.0 s.
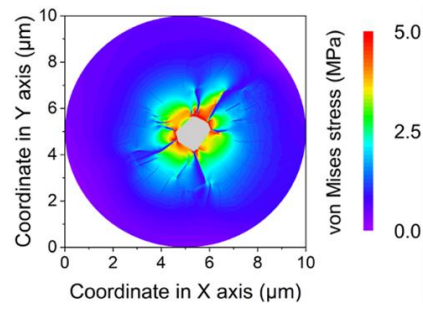

Figure. 4.11. Visualization of von Mises stress caused by the development of Li filament inside the SSE with 600 nm size at final stage.
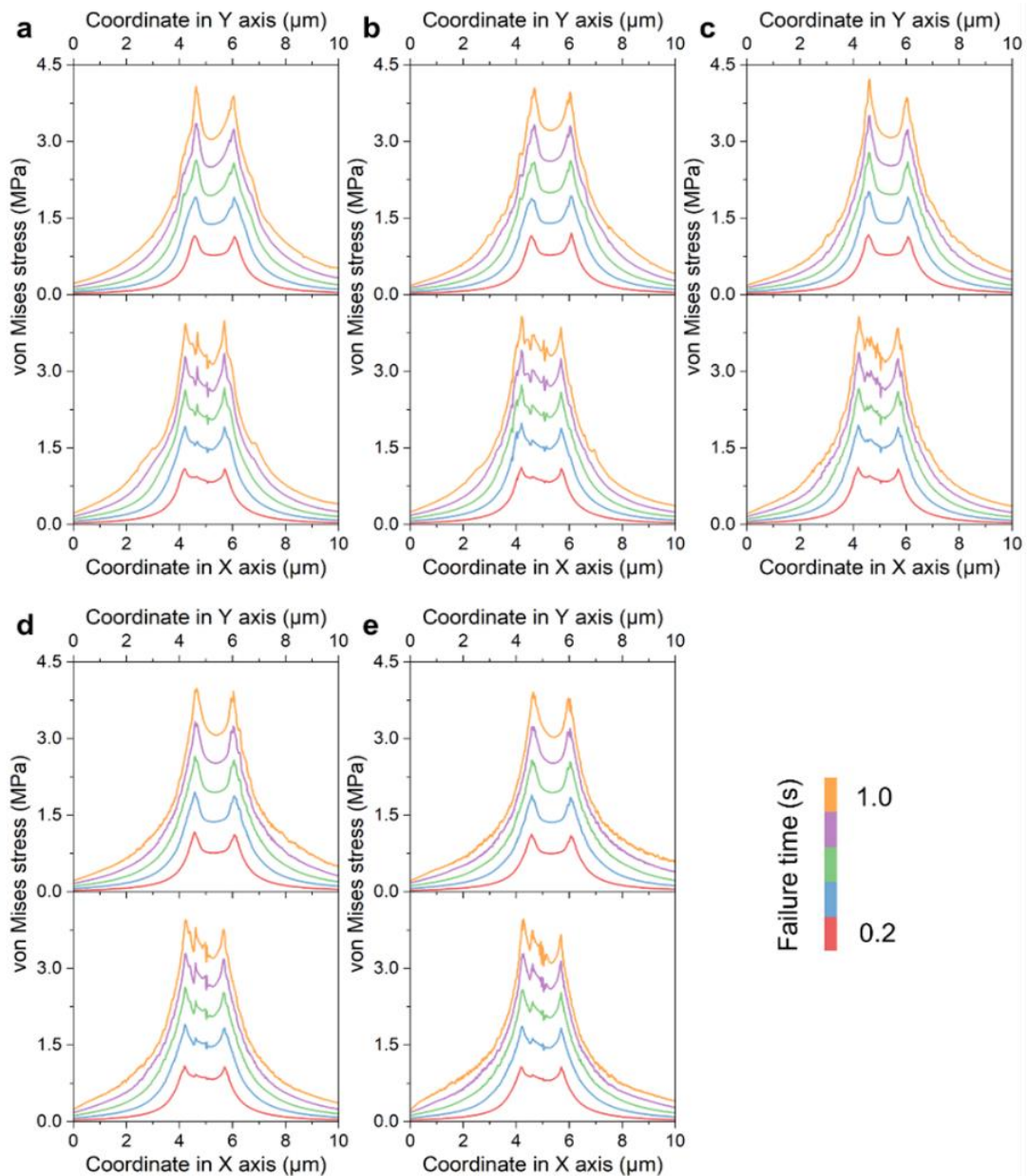
Figure. 4.12. Variation of von Mises stress along X axis at Y=5.0 μm and Y axis at X=5.5 μm inside SSE with (a) 600 nm, (b) 400 nm, (c) 200 nm, (d) 100 nm and (e) 50 nm size. The width of slide is 1.0 μm.

Initially, the stress is concentrated at the interface of Li/SSE with the development of Li filament after filling up the open void. Following, the generated stress spreads from the Li/SSE interface to the bulk of SSE. Eventually, the developing Li filament is surrounded by the high stress field due to the compressive stress from the growth of Li filament, which is separated around the corners of polygon cross-section of the Li filament (Figure. 4.11 and Figure. 4.9a-d). The region of the von Mises stress surrounding Li filament decreases with decreasing grain size. Specifically, the variations of von Mises stress along X-axis and Y-axis were sliced into 1.0-μm slide, showing same trends along with both X and Y axis inside the SSE (Figure. 4.9e-f and Figure. 4.12). Whereas, the fluctuation of von Mises appears when the grain size is over 0.6 μm, and becomes more visible and frequent with the decrement of average size. Moreover, the von Mises stress on the Li/SSE surface with 400 nm, 200 nm, and 100 nm are greater than that with 600 nm and 50 nm, of which SSE with 200 nm size shows the strongest stress. Therefore, the stress near the interface of Li/SSE during the development of Li filament has a great impact on the whole SSE, of which the stress generated stress inside the SSE could spread forward through the opening and sliding of GB and is controlled by the refinement of grains.
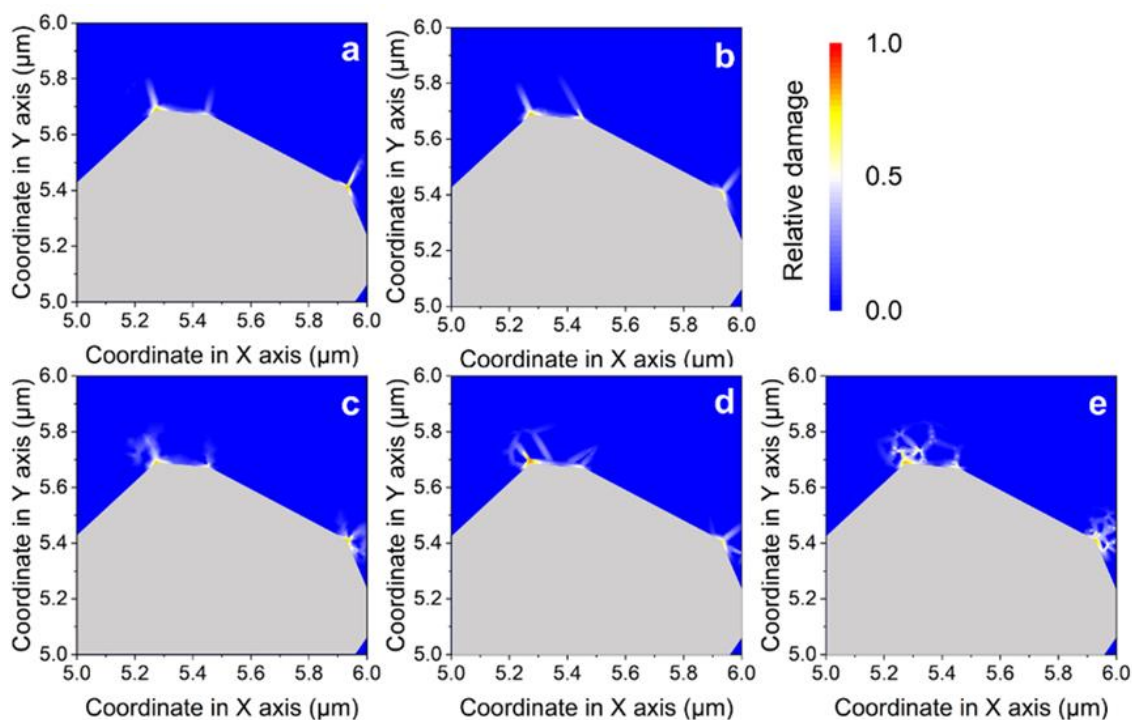
Figure. 4.13. Development of damage from the corner of octagon Li filament inside the SSE with average size (AS) of (a) 600 nm, (b) 400 nm, (c) 200 nm, (d) 100 nm and (e) 50 nm at calculating beginning of 0.1 s.
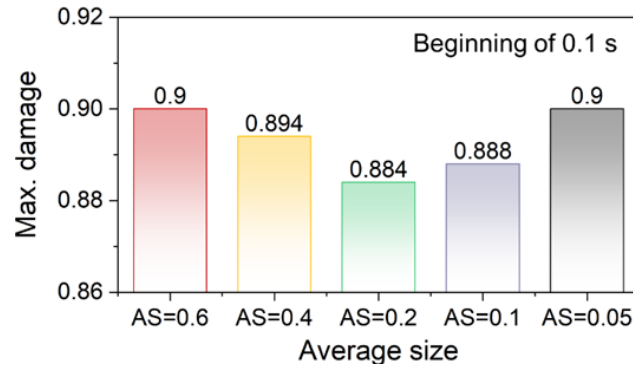
Figure. 4.14. Max. damage inside the SSE with average size (AS) of 0.6 μm, 0.4 μm, 0.2 μm, 0.1 μm and 0.05 μm at beginning calculating time of 0.1 s.
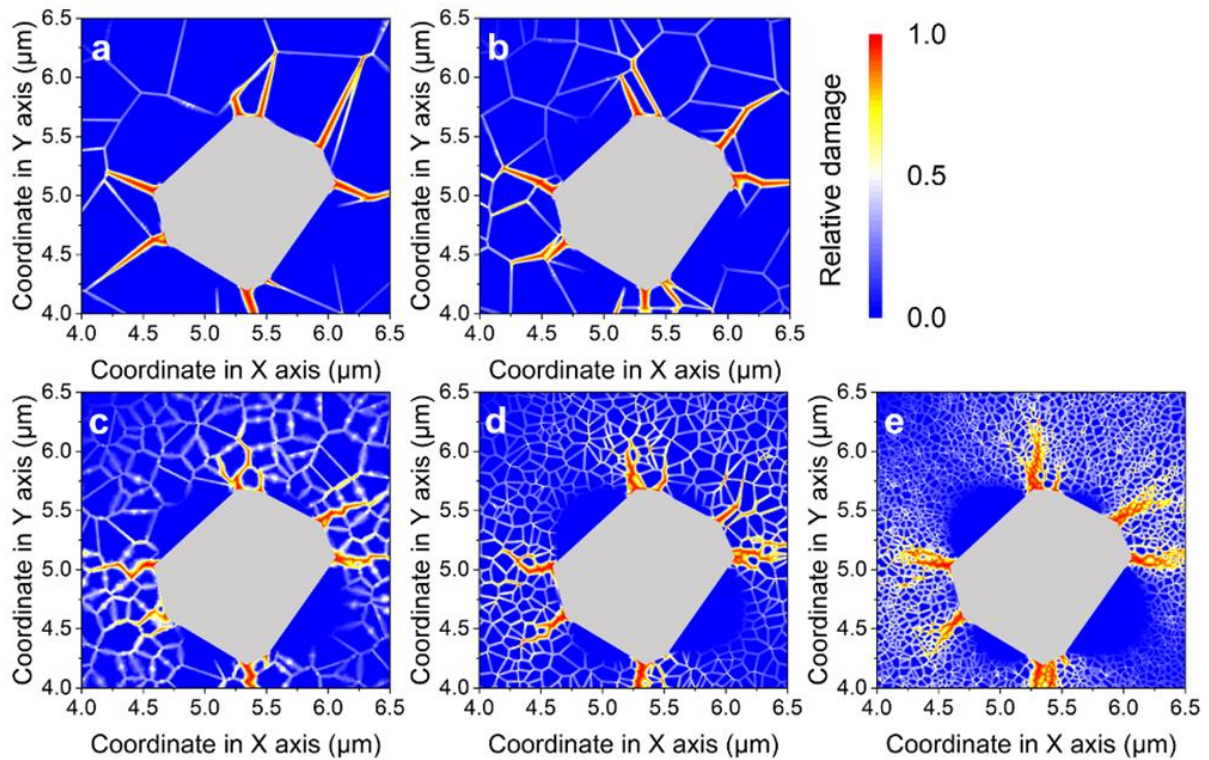

Figure. 4.15. Damage developing from the corner of octagon Li filament inside the SSE with average size (AS) of (a) 0.6 μm, (b) 0.4 μm, (c) 0.2 μm, (d) 0.1 μm and (e) 0.05 μm at calculating time of 0.5 s.
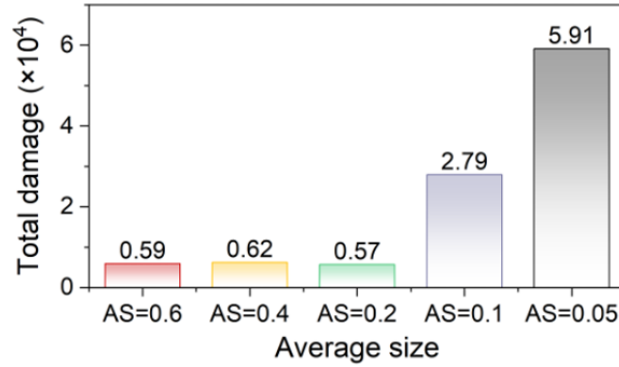
Figure 4.16. Total damage inside the SSE with average size (AS) of 0.6 μm, 0.4 μm, 0.2 μm, 0.1 μm and 0.05 μm at calculating time of 0.5 s.
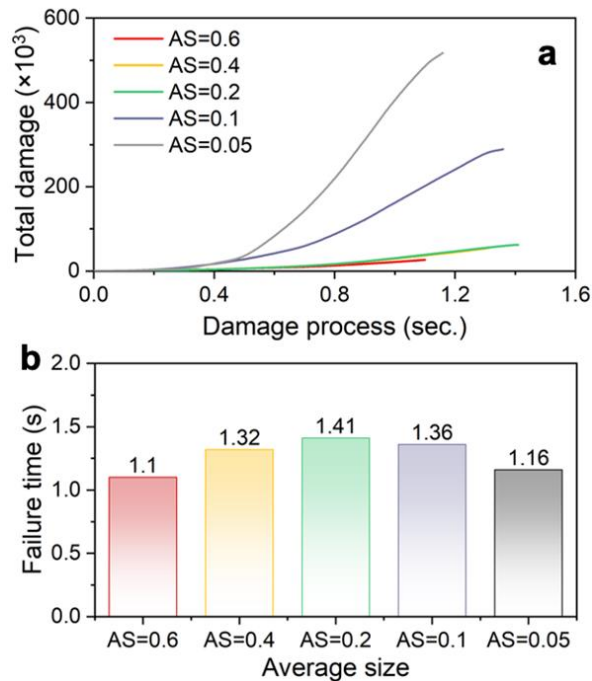
Figure. 4.17. (a) Evolution of total damage inside SSE with different average grain size during the damage process. (b) Failure time of SSE with different average grain size during the growth of Li filament.

Following, the damage is visualized inside the SSE with different grain size, which originates at the corners of octagon Li filament caused by the opening and sliding of GB under the compressive stress (Figure. 4.13). Furthermore, tiny difference of the max. damage inside the SSE with different grain size appears at the beginning of damage, and the minimal damage of 0.884 occurs with that of AS=0.2 μm (Figure. 4.14). As the growth of Li filament inside the SSE, obvious damage originates from the GB at the corners of octagon (Figure. 4.15a-c). Besides, the flocculent-type damage is formed

101

along the GB and grains toward the SSE when the grain size is excessive refinement (AS=0.1 and 0.05 μm) (Figure. 4.15d-e). At the intermediate stage of 0.5 s, the total damage increases sharply when the flocculent damage appears (Figure. 4.16), indicating that the flocculent damage is more harmful. Additionally, when the SSE is overrefined with AS <0.2 μm, the damage rate arises up sharply inside the SSE during the damage process, and SSE with AS=0.2 μm takes the longest time of 1.41 s with the relatively smaller total damage at the final failure (Figure. 4.17a-b).
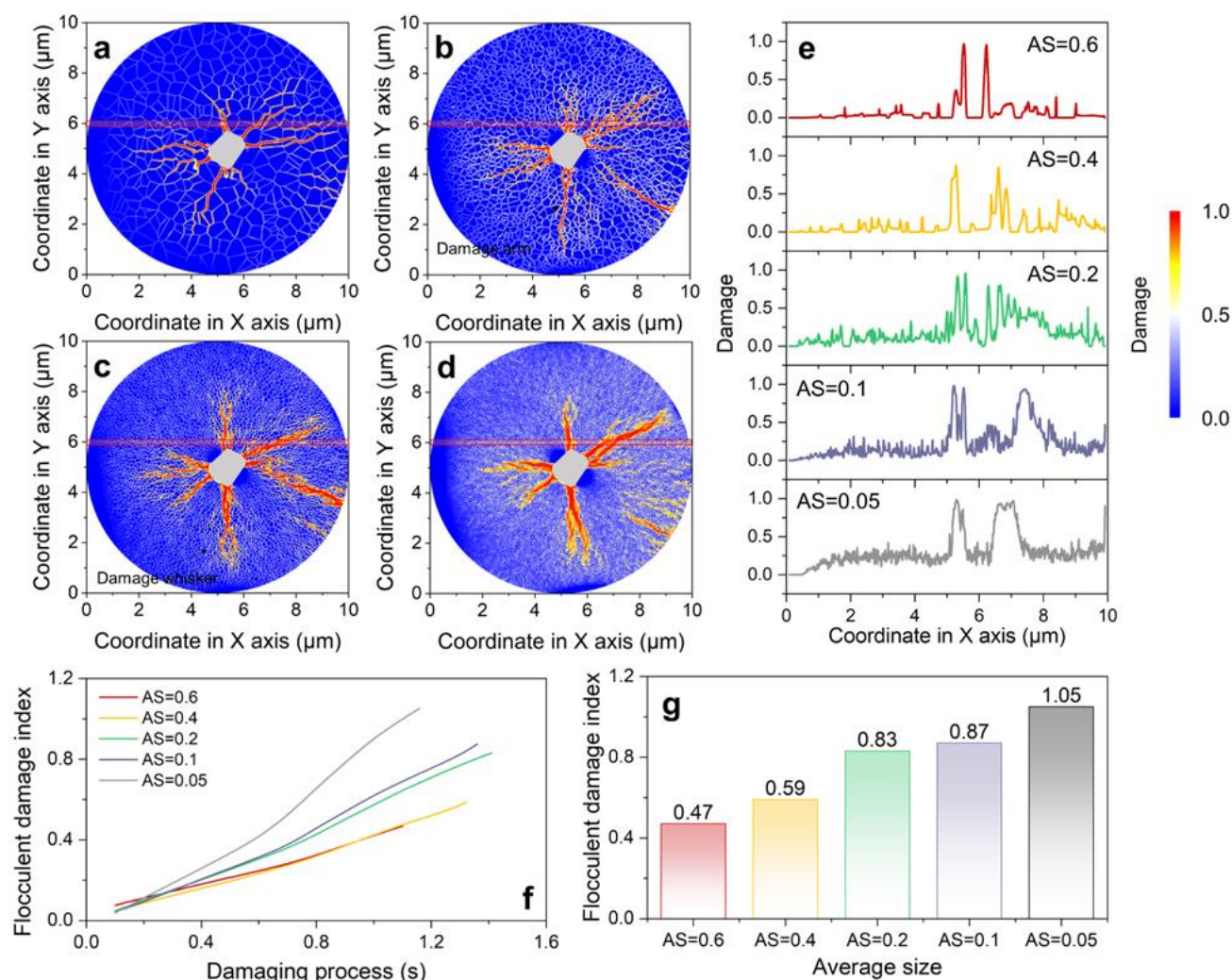
Figure. 4.18. Flocculent damage inside SSE with different grain size. a-d) Generation of damage inside SSE with different grain size of (a) 400 nm, (b) 200 nm, (c) 100 nm and (d) 50 nm. (e) Variation of damage along X axis at y=6 μm inside SSE with different grain size. The slide width is 0.2 μm and marked with red square in figures a-d. (f) Flocculent coefficient of the total damage inside SSE with different grain size during damage process. (g) Flocculent index of damage inside the SSE with different grain size at final stage.
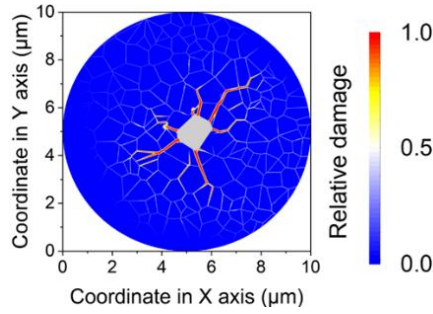
Figure. 4.19. Visualization of von Mises stress caused by the infiltration of Li filament inside the SSE with 600 nm size.
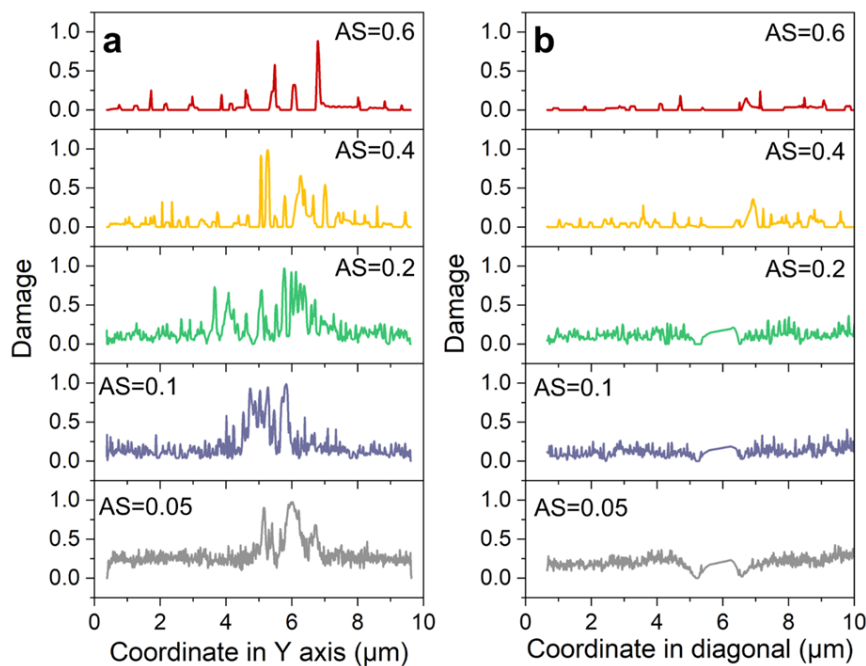
Figure. 4.20. Variation of damage along (a) Y axis at x=7 μm and (b) diagonal line y=x in SSE with different average grain size in Figure. 3.18.

As shown in Figure. 4.19 and Figure. 4.20a, damage propagates from the corners of octagon Li filament though GB inside SSE due to the opening and sliding of the GB when the relative grain size is big enough (600 nm and 400 nm), forming the serious thick and giant damage, named as damage arms. The damage of grain gradually occurs near the octagon Li filament with middle grain of 200 nm, which propagates through the GB and grains away (Figure. 4.18b). Moreover, the damage also appears at the non-defected region, which can be explained with the accumulation of opening and sliding of the GB. As shown in Figure. 4.18c-d, damage sweeps up both of GB and gains in the SSE with overfine grain of 50 nm and 100 nm, forming thick damage arms with tiny-continue-network shape damage

like the flocculent with plenty of branched and thin damage whiskers inside the SSE. Especially, the damage arms and whiskers are stronger with 50 nm size, which is more conspicuous within the overfine grain size of SSE. Along with X and Y axis, the width of damage in the main damage region is greater than 0.8, which increase as the grain size decreases (Figure. 4.20a and 4.18e). Simultaneously, the fluctuation of damage along selected region increases gradually with the refinement from 0.6 to 0.05 μm (Figure. 4.20). Furthermore, the reciprocal dispersion coefficient of damage was defined as the flocculent index for the damage distribution, which increases with the refinement of grain during the damage process (Figure. 4.18f). Not only the increase rate of flocculent index but also the eventual value increase with the refinement of grain, where 0.2 μm is proposed as the threshold of AS to reinforce SSE (Figure. 4.18g).
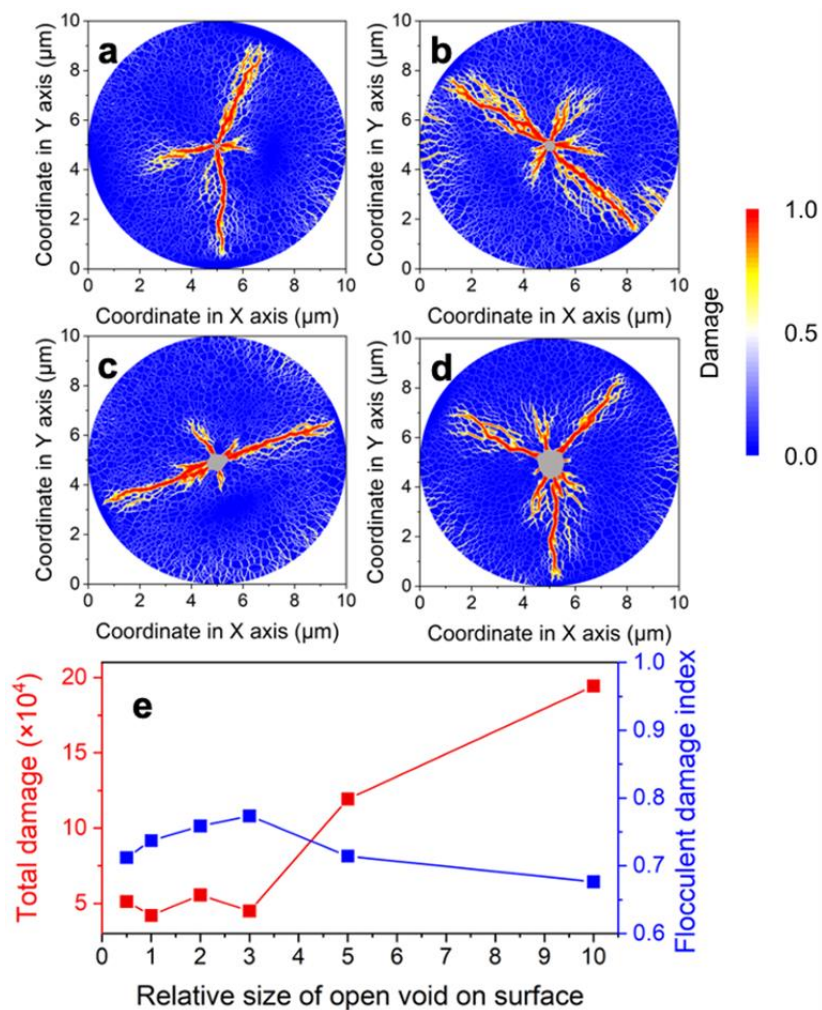
Figure. 4.21. Generation of damage inside SSE with average grain size of 0.2 μm caused by the development of Li filament with size of (a) 1, (b) 2, (c) 3, (d) 5 at final stage. (e) Total damage and corresponding flocculent damage

index inside the SSE caused by the development of Li metal with different relative sizes. Relative size of Li metal represents the ratio between average size of Li metal to that of grains.
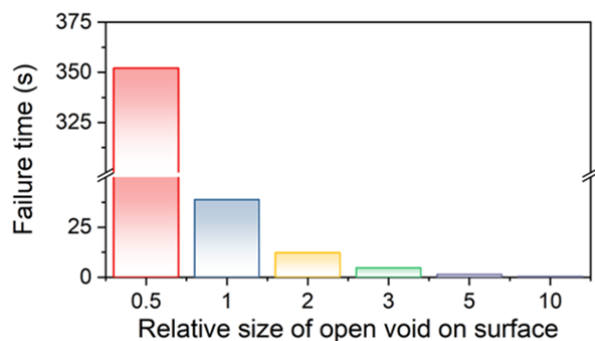
Figure. 4.22. Failure time of SSE with average grain size of 0.2 μm caused by the development of Li filament with different relative sizes.

Moreover, flocculent damage of SSE is hardly affected by relative size of Li filament inside SSE, while the failure time is prolongated obviously with the smaller Li filament (Figure. 4.21-22). Thus, the damage behavior of SSE could be controlled by grain size, whereas over-refinement will bring out giant damage degree with more harmful flocculent damage.
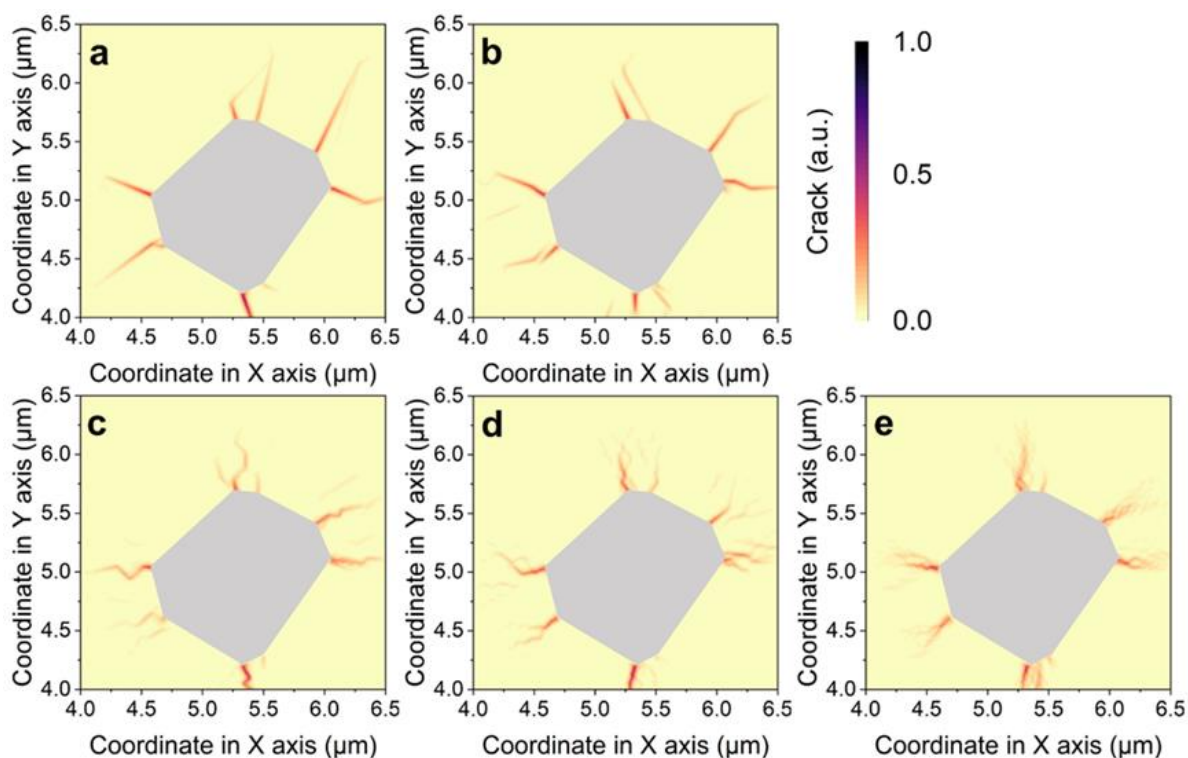
Figure. 4.23. Visualization of crack from the developing Li filament inward SSE with (a) 600 nm (b) 400 nm, (c) 200 nm, (d) 100 nm and (e)50 nm size at calculating time of 0.5 s.
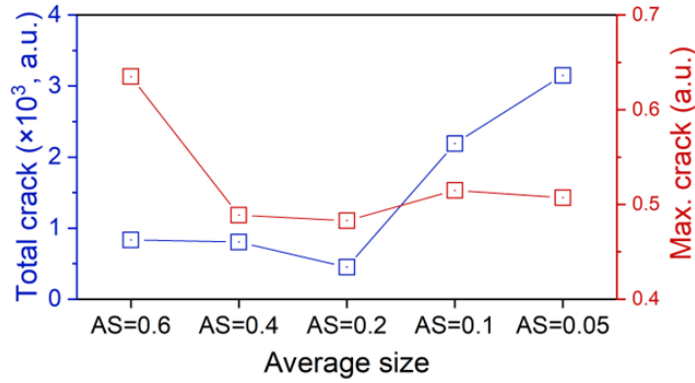
Figure. 4.24. Total crack and corresponding maximum crack inside the SSE with average size (AS) of 0.6 μm, 0.4 μm, 0.2 μm, 0.1 μm and 0.05 μm at calculating time of 0.5 s.
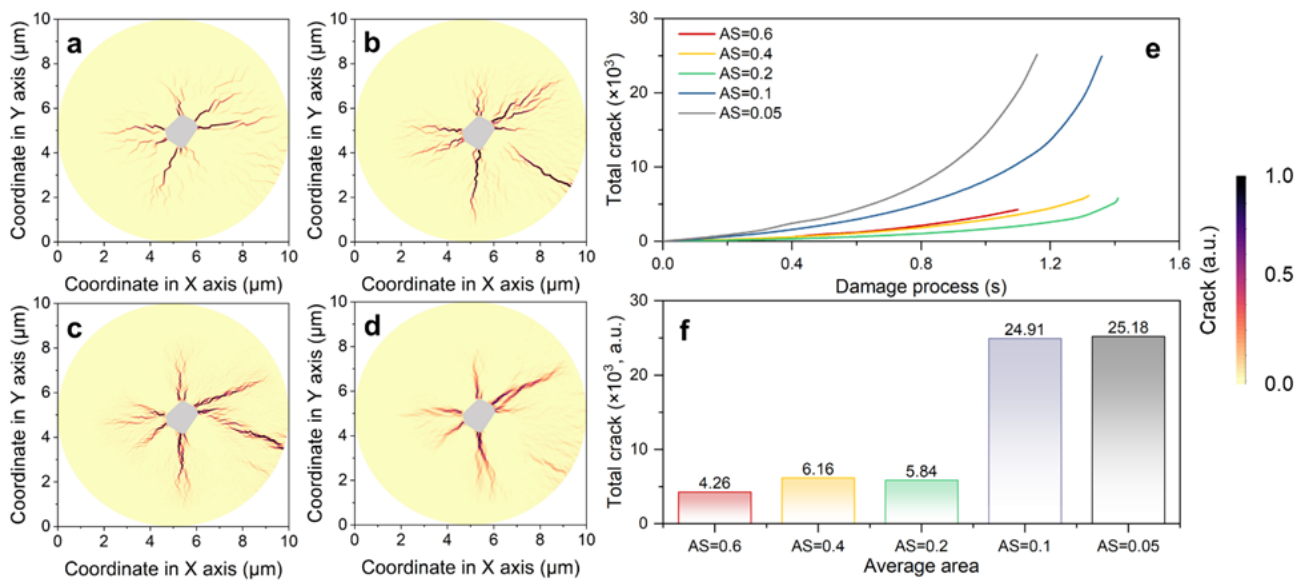
Figure. 4.25. Disintegration of SSE with different grain size. a-d) Visualization of crack from the developing Li filament inward SSE with different grain size of (a) 400 nm, (b) 200 nm, (c) 100 nm and (d) 50 nm at final stage. (e) Evolution of crack inside polycrystalline SSE with different grain size during the damage process and corresponding (f) total crack at final stage.
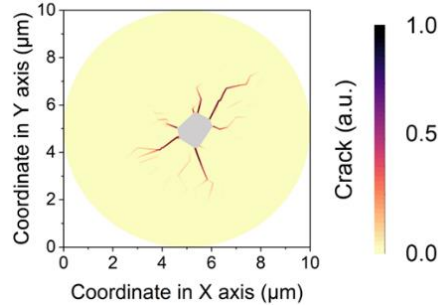
Figure. 4.26. Visualization of crack from the developing Li filament inward SSE with 600 nm size at final stage.

Same as the origination of damage, the crack is rooted in each tip of octagonal Li filament at calculating time of 0.5 s, and SSE with 600 nm and 400 nm size exhibit thick and straight crack. When the average grain size is over 200nm, tortuous and interlaced crack show up with smaller max. crack (Figure. 4.23-24). At the final stage, massive whiskery cracks are paralleled with the direction of main crack from corners of octagonal Li filament (Figure. 4.26 and 4.25a-d). Typically, the main cracks inside SSE with overfine grain size of 100 nm and 50 nm are woven by many zigzag whiskers, which is consisted with the flocculent damage of SSE (Figure. 4.25c-d). Interestingly, although the compression from the growth of Li filament is applied from the center, the cracks actually initiate from the surface, and propagate inward SSE (Figure. 4.25b-c), which can be explained by the mechanical lever with opposite forces at both ends during the evolution of stress. As shown in Figure 4.25e, the cracking rate is slowed down with the refinement of SSE from 600 nm to 200 nm, while that increases uncontrollably with accelerated cracking speed overfine grain size (100 nm and 50 nm). Thus, the obvious disintegration occurs through the GB with the refinement of average grain size from 600 nm to 200 nm, which can smash either GB or overfine SSE (100 nm and 50 nm). Ultimately, the total crack generated inside the SSE with overfine average rain size of 100 nm and 50 nm is 4 times greater than that in other SSEs (Figure. 4.25f). ***Thus, the appropriate refinement of grain can retard crack during the development of Li filament, while the overrefinement will aggravate the disintegration process.***

4.1.2.2. The effect of the relative strength of grain boundaries

Subsequently, a series of grain boundaries (GB) with different strength, were selected to reveal the effect of GB on the damage behavior during the growth of Li filament. λ has been varied in the

experiment from 0.05 to 1, where λ is elastic modulus ratio between grain boundary and grain.
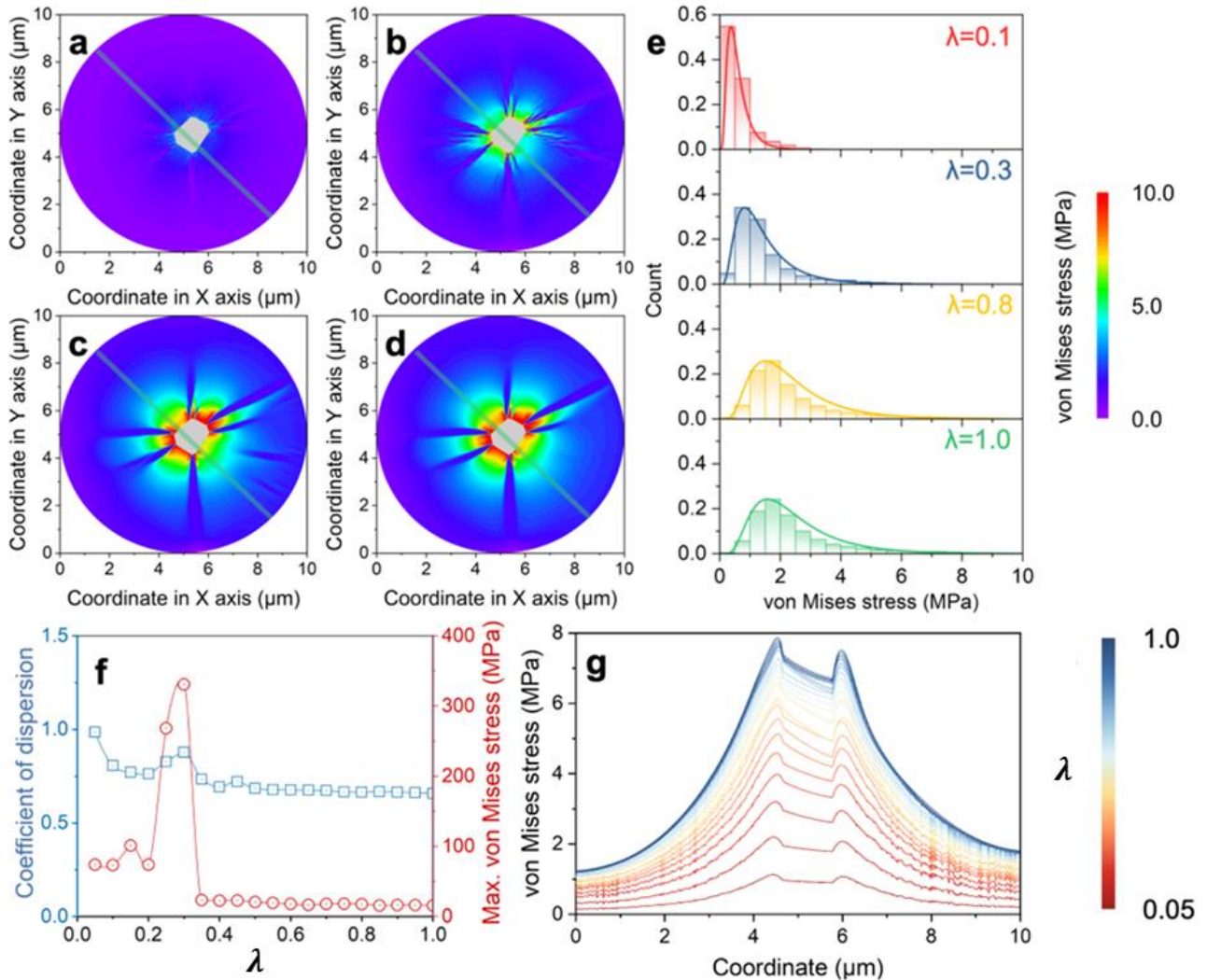
Figure. 4.27. Stress field inside SSE with different strength of grain boundary. a-d) Visualization of von Mises stress around Li filament inside SSE with different GB of (a) λ=0.1, (b) λ=0.3, (c) λ=0.8, (d) λ=1.0. (e) Statistical distribution of von Mises stress inside SSE with GB of λ=0.1, λ=0.3, λ=0.8 and λ=1.0. (f) Coefficient of dispersion of von Mises stress and related maximum inside SSE with different GB with relative strength ranging from 0.05 to 1.0. λ represents relative strength, which is considered as the ratio of elastic modulus of boundary to that of grain. (g) von Mises stress varied along diagonal line of visualization in a series of SSE with width of 0.1 μm, which marked with green.
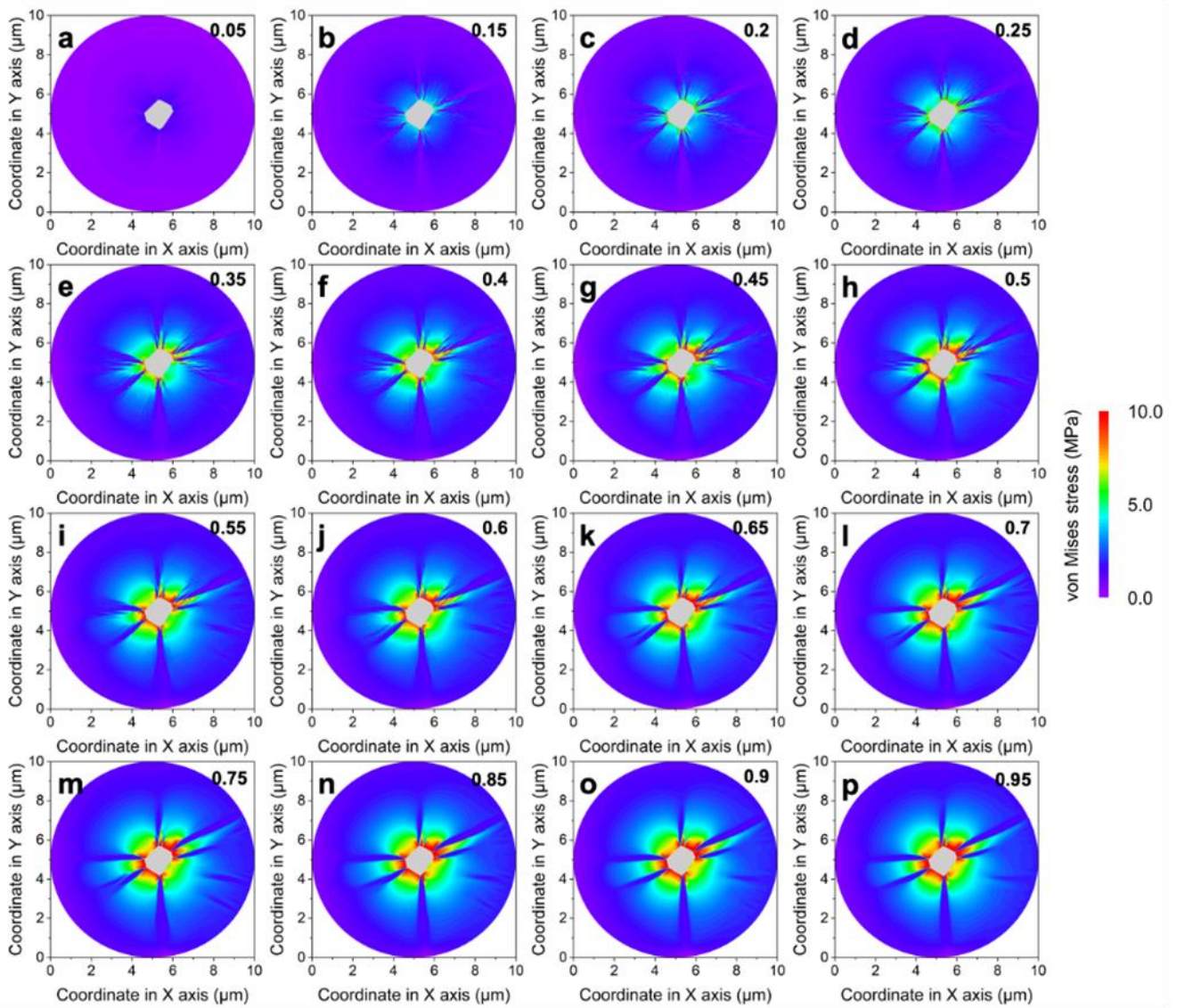
Figure. 4.28. Stress field caused by the development of Li filament inside SSE. Visualization of distribution von Mises stress around Li filament inside SSE with different GB of (a) λ=0.05, (b) λ=0.15, (c) λ=0.2, (d) λ=0.25, (e) λ=0.35, (f) λ=0.4, (g) λ=0.45, (h) λ=0.5, (i) λ=0.55, (j) λ=0.6, (k) λ=0.65, (l) λ=0.7, (m) λ=0.75, (n) λ=0.85, (o) λ=0.9, and (p) λ=0.95.
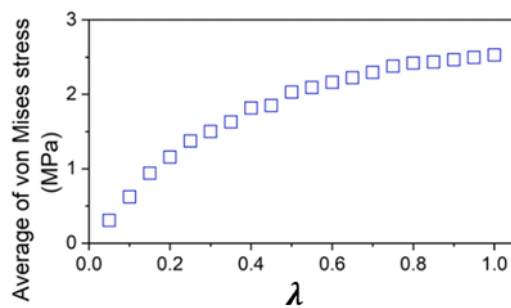
Figure. 4.29. The average of von Mises stress inside the SSE with different GB ranging from λ=0.05 to 1.0.

As shown in Figure. 4.27a, only weak distribution of stress appears around Li filament when λ is lower than 0.1, while the distribution becomes more distinguished with the increment of λ from 0.1 to 1, which generates greater compressive stress against the surrounding SSE with the development of Li filament (Figure. 4.27b-d and Figure. 4.28). Additionally, the high-stress regions are separated from each corner of Li filaments into eight parts (Figure. 4.27b), which also has been cut by the weak GB, illustrating that the stress could be dissipated through the opening and sliding of GB. With the strengthening of SSE, the distribution of von Mises stress from corner of Li filament and existence of GB changes slighter and barely difference appears after λ>0.8 (Figure. 4.27c-d and Figure. 4.28), and the stress is stronger and widely distributed in SSE with tough GB due to the stronger interaction between different grains with reinforced GB (Figure. 4.27e and Figure. 4.29). Moreover, coefficient of dispersion and corresponding max. von Mises stress inside the SSE decrease with the increase of strength except for λ=0.3, while the maximum stress is greater than 300 MPa when λ=0.3 due to severe collision and compress between grains (Figure. 4.27f). When the strength of grain boundaries is relatively low of λ<0.3, the bonding between grains can be expected to be very weak. Thus, greater local rotation of grains appears with enhanced local displacement, while damage and opening of grain boundaries occur easily at the grain boundaries with weak resistance, leading to the severe collision and compress between grains with stronger stress concentration. When λ>0.3, strength of GBs is strong enough to realize the lower and more uniform stress due to the suppressed local rotation of grains inside SSE. Therefore, λ=0.3 can be predicted as a threshold for tuning the disintegration behavior of SSE with the development of Li filament (Figure. 4.27f). As shown in Figure. 4.27g, von Mises stress along with diagonal line of SSE increases obviously from edge of SSE to the center Li filament and the overall stress grows with the increment of GB's strength. Meanwhile, the burr-like distribution in the edge region gradually disappears, which suggests that the spread of stress along the GB is suppressed with the increment of λ.
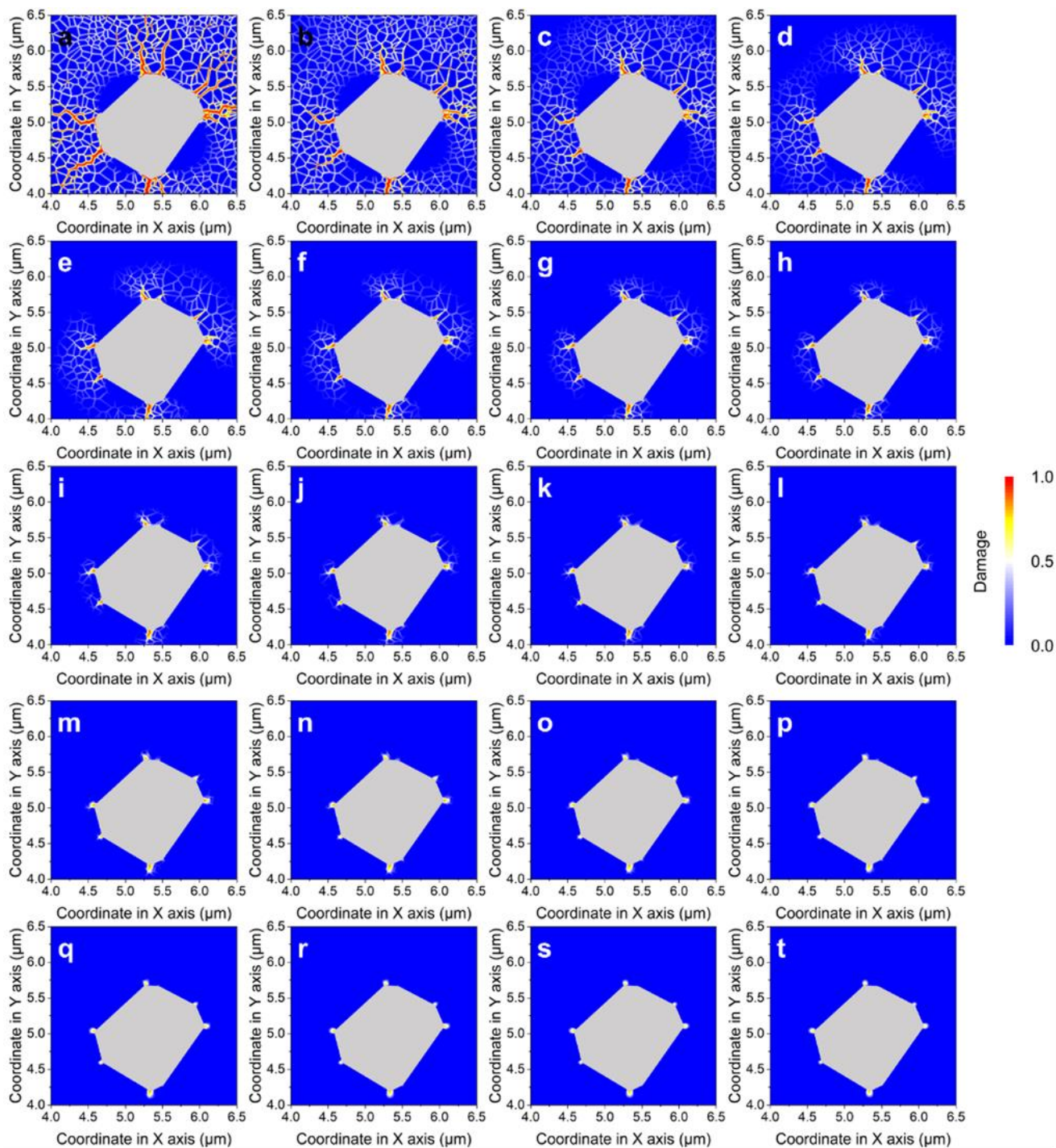
Figure. 4.30. Development of damage from the corner of octagon Li filament inside the SSE with different GB of (a) λ=0.05, (b) λ=0.1, (c) λ=0.15, (d) λ=0.2, (e) λ=0.25, (f) λ=0.3, (g) λ=0.35, (h) λ=0.4, (i) λ=0.45, (j) λ=0.5, (k) λ=0.55, (l) λ=0.6, (m) λ=0.65, (n) λ=0.7, (o) λ=0.75, (p) λ=0.8, (q) λ=0.85, (r) λ=0.9, (s) λ=0.95, and (t) λ=1.0 at calculating beginning of 0.3 s.
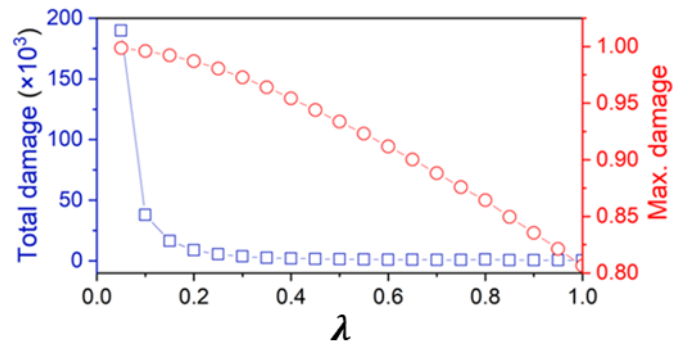
Figure. 4.31. Total damage and corresponding maximum of damage inside the SSE with different GB ranging from λ=0.05 to 1.0 at calculating time of 0.3 s.

Similarly, the damage originates from the corners of octagon Li filament, while the flocculent damage with net-shape appears around the main damage with weak GB and shift gradually to the decreased and concentrated dot-like damage along strengthening GB at the beginning of 0.3 s (Figure. 4.30-31).
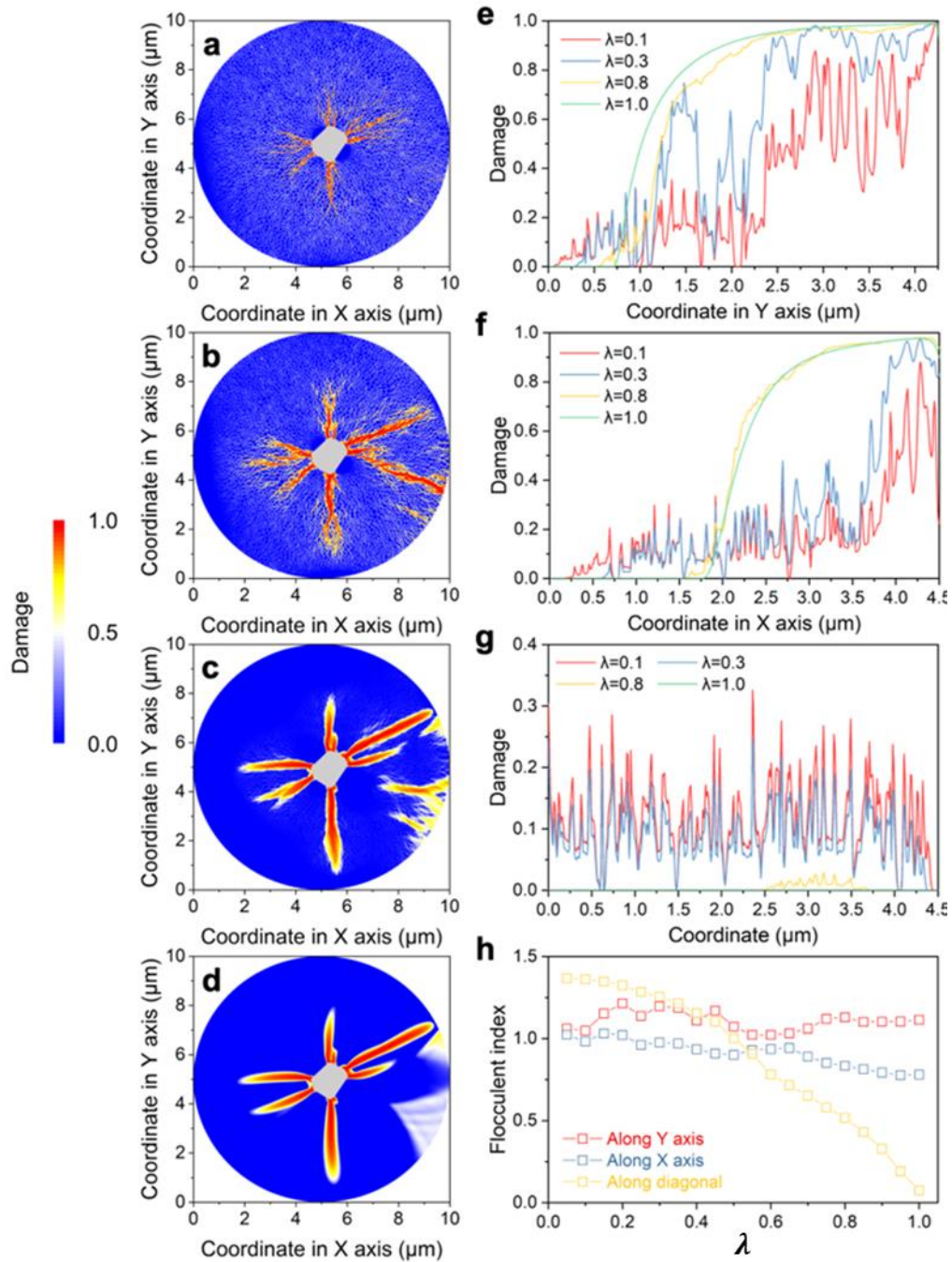
Figure. 4.32. Effect of strength of grain boundary on the flocculent damage of SSE. a-d) Damage propagation from corners of Li filament inside SSE with different GB of (a) λ=0.1, (b) λ=0.3, (c) λ=0.8, and (d) λ=1.0. e-g) Damage varied along with (e) Y axis from 0 to 4.3 μm at X=5.35 μm, (f) along X axis from 0 to 4.5 μm at Y=5.1 μm, and (g) along diagonal line axis from 0 to 4.5 μm. The width of slide line is 0.1 μm. (h) Flocculent index of damage along axis in SSE with different GB and λ ranges from 0.05 to 1.0.
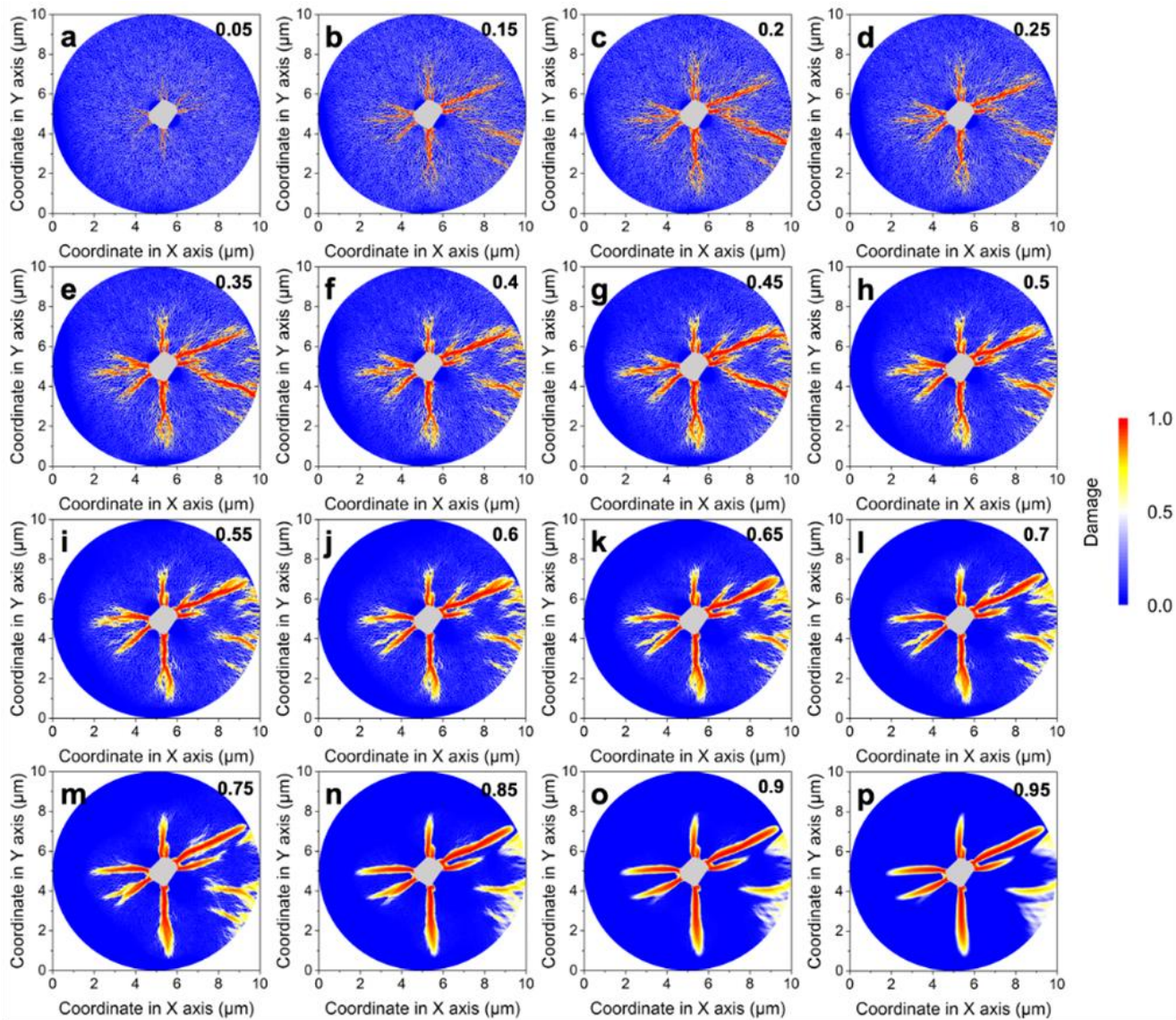
Figure. 4.33. Damage caused by the development of Li filament inside SSE. Propagation of damage from the tips of Li filament inside SSE with different GB of (a) λ=0.05, (b) λ=0.15, (c) λ=0.2, (d) λ=0.25, (e) λ=0.35, (f) λ=0.4, (g) λ=0.45, (h) λ=0.5, (i) λ=0.55, (j) λ=0.6, (k) λ=0.65, (l) λ=0.7, (m) λ=0.75, (n) λ=0.85, (o) λ=0.9, and (p) λ=0.95.
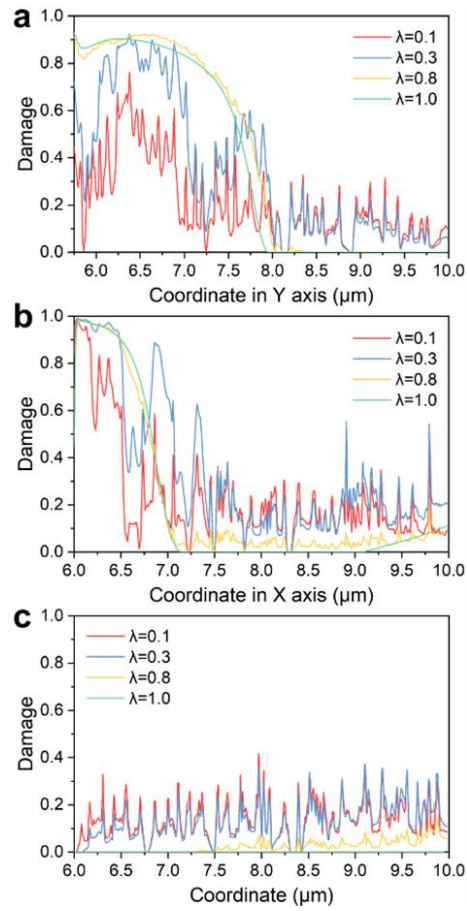
Figure. 4.34. The variation of damage along with (a) Y axis from 5.7 to 10 μm at X=5.35 μm, (b) X axis from 6.0 to 10 μm at Y=5.1 μm, and (c) diagonal line axis from 6.0 to 10 μm. The width of slide line is 0.1 μm.
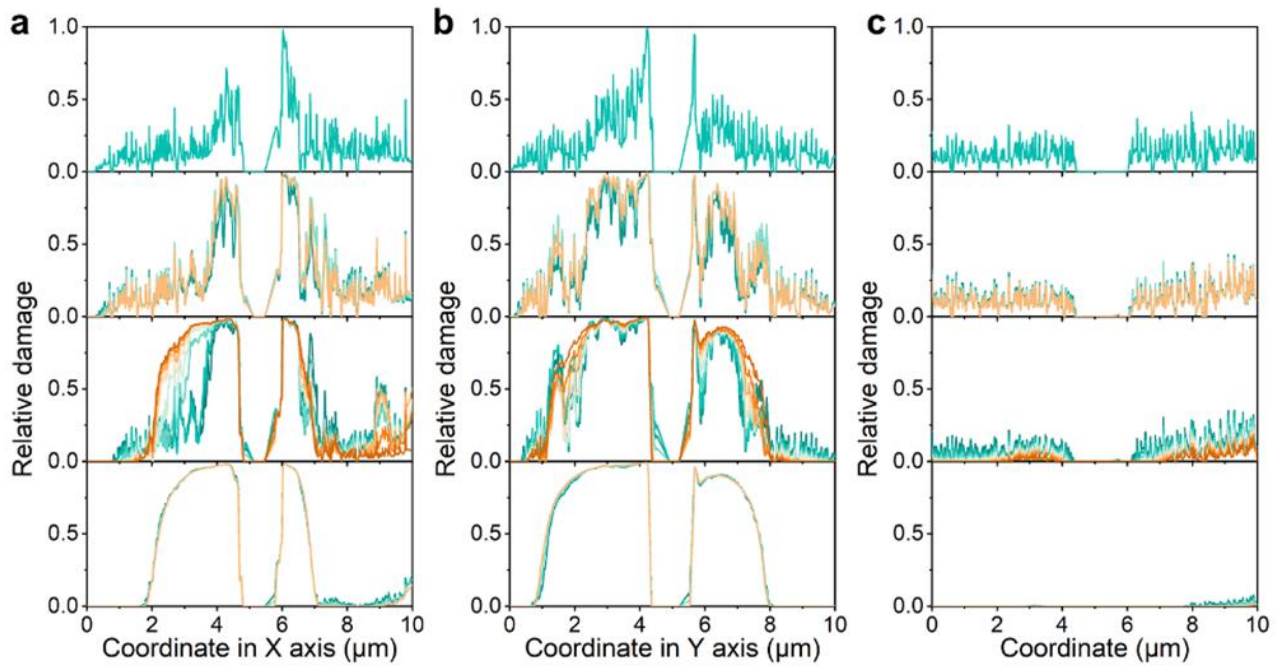
Figure. 4.35. The variation of damage along with (a) Y axis at X=5.35 μm, (b) X axis at Y=5.1 μm, and (c)

diagonal line axis. The width of slide line is 0.1 μm. With λ of 0.1, 0.3, 0.8 and 1.0 (from up to down).
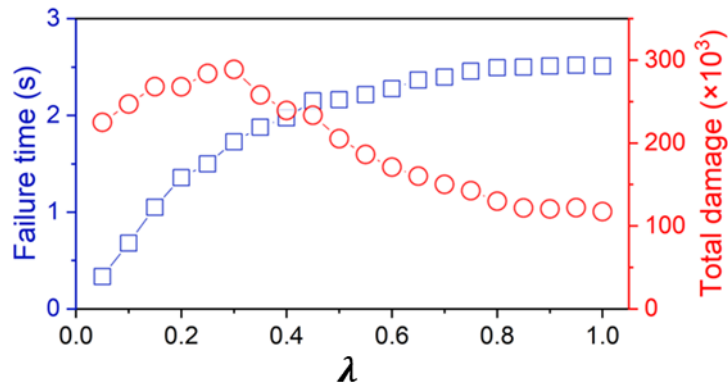
Figure. 4.36. Failure time of SSE and corresponding total damage in SSE with different GB with relative strength ranging from 0.05 to 1.0.

As damage processes, several whisker-like damages with multi-branches are originated at the tip of octagon Li filament and develop inward the SSE with λ<0.3, while the whisker-like damage changes to be stronger with increment of λ (Figure. 4.32a-b and Figure. 4.33a-d). As whisker-like damages propagate inside the SSE, minor damage diffuses along GB to form flocculent damage due to the weeny dislocation of adjacent grains between loose-interaction grains. Moreover, when λ=0.8, 1.0, weeny opening of GB is prevented and thus the damage propagates concentratedly from the corners of Li filament to the bulk of SSE, forming several straight and giant damage regions (Figure. 4.32c-d and Figure. 4.33n-p). Additionally, the variation of damage along Y axis and X axis displays a jagged growth when λ are 0.1 and 0.3, and smooth variation curves increase drastically when λ is beyond 0.8 (Figure. 4.32e-f and Figure. 4.34a-b). Along diagonal, the damage appears unevenly with the average of ~ 0.4 when λ=0.1 and 0.3, while almost none of damage arises up along non-vertex direction when λ>0.8 (Figure. 4.32g and Figure. 4.34c). Lower flocculent index of damage especially along diagonal line illustrates that flocculent damage appears in the SSE with weak GB and gradually absents with the strengthening GB (Figure. 4.35 and Figure. 4.32f). Generally, the total damage of the whole SSE ups with the strengthening GB from λ=0.05 to 0.3 and downs from λ=0.3 to 1.0, which holds relatively steady after λ=0.8. Furthermore, the failure time of SSE is prolongated with the strengthening GB (Figure. 4.36), and the harmful flocculent damage can be suppressed by the strengthening GB in SSE, of which λ=0.8 is suggested as the threshold value for the strength of GB.
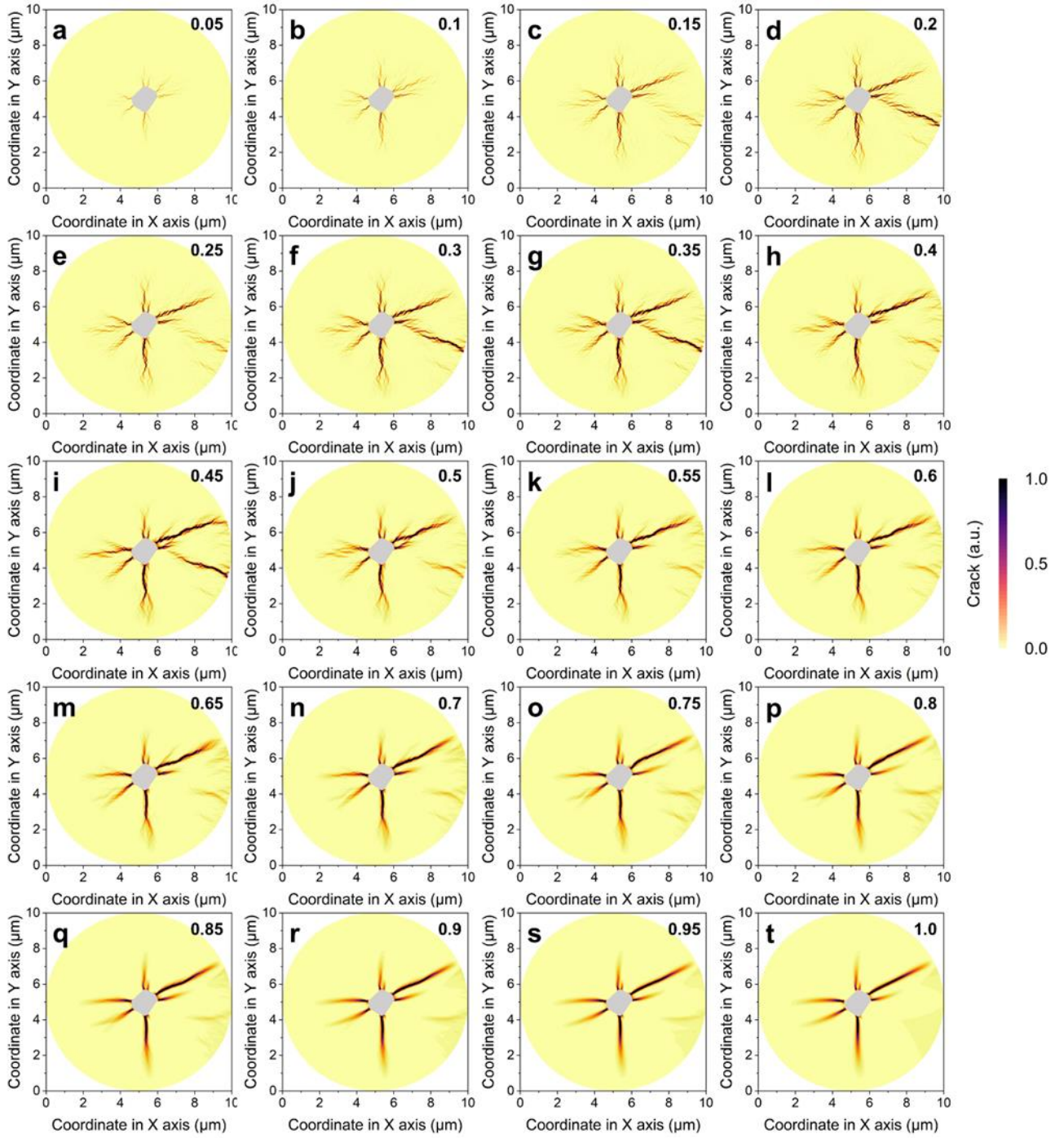
Figure. 4.37. Generation of cracks from the tips of Li filament inside SSE with different GB of (a) λ=0.05, (b) λ=0.1, (c) λ=0.15, (d) λ=0.2, (e) λ=0.25, (f) λ=0.3, (g) λ=0.35, (h) λ=0.4, (i) λ=0.45, (j) λ=0.5, (k) λ=0.55, (l) λ=0.6, (m) λ=0.65, (n) λ=0.7, (o) λ=0.75, (p) λ=0.8, (q) λ=0.85, (r) λ=0.9, (s) λ=0.95, and (t) λ=1.0.
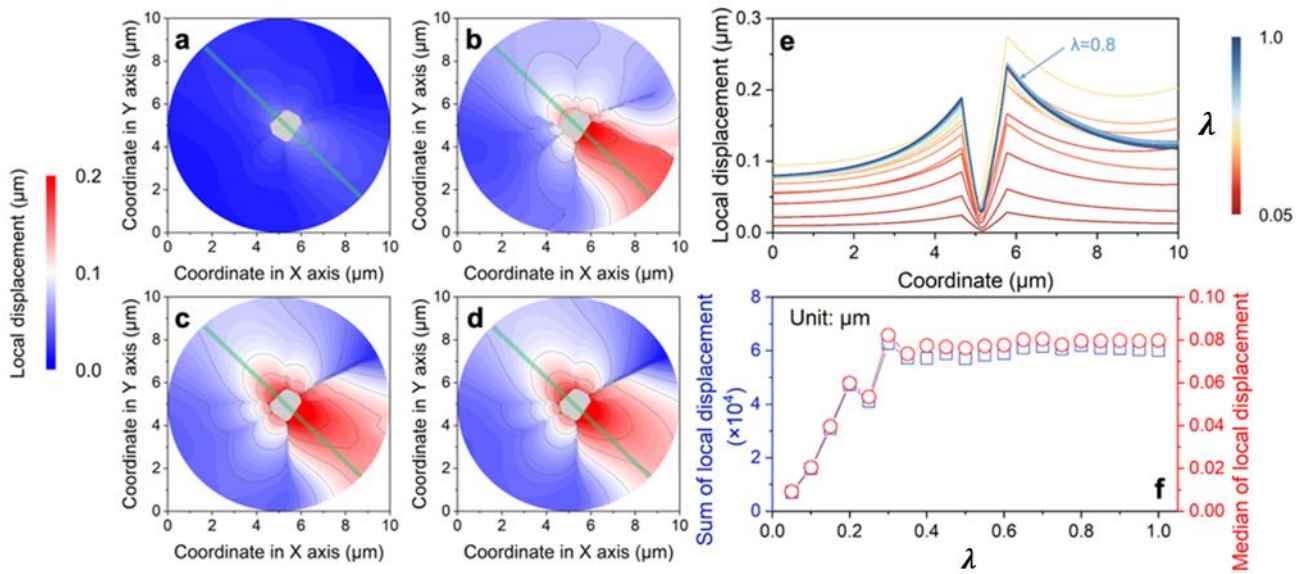
Figure. 4.38. Disintegration of SSE with different strength of grain boundary. a-b) Disintegration represented by the local displacement of SSE with different GB of (a) λ=0.1, (b) λ=0.3, (c) λ=0.8, and (d) λ=1.0. (e) Local displacement varied along diagonal line axis. The width of slide line is 0.1 μm. (f) Sum of local displacement and corresponding median inside SSE with different GB ranging from λ=0.05 to 1.0.
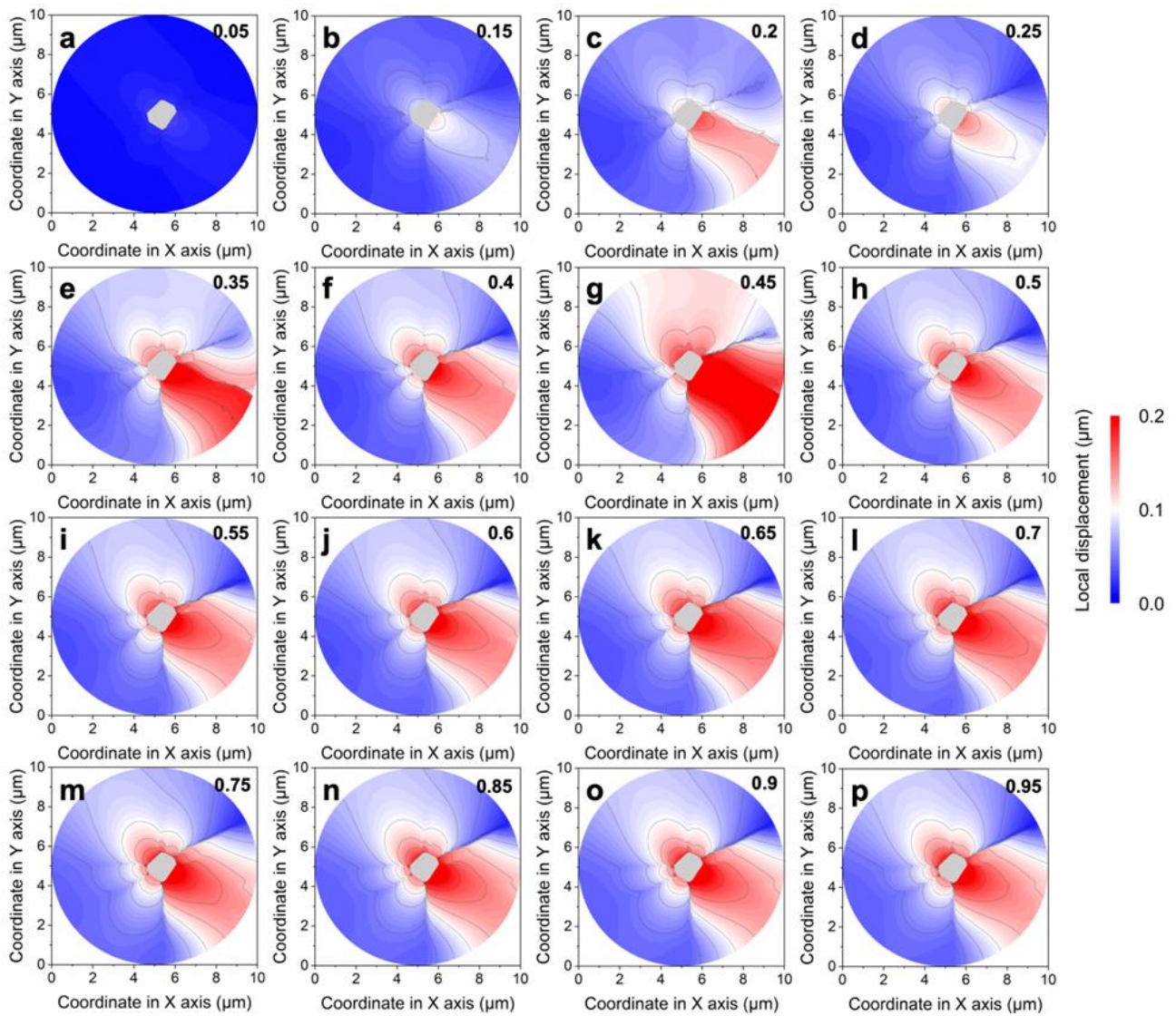
Figure. 4.39. Disintegration of SSE caused by development of Li filament. Disintegration represented by the local displacement of SSE with different GB of (a) λ=0.05, (b) λ=0.15, (c) λ=0.2, (d) λ=0.25, (e) λ=0.35, (f) λ=0.4, (g) λ=0.45, (h) λ=0.5, (i) λ=0.55, (j) λ=0.6, (k) λ=0.65, (l) λ=0.7, (m) λ=0.75, (n) λ=0.85, (o) λ=0.9, and (p) λ=0.95.
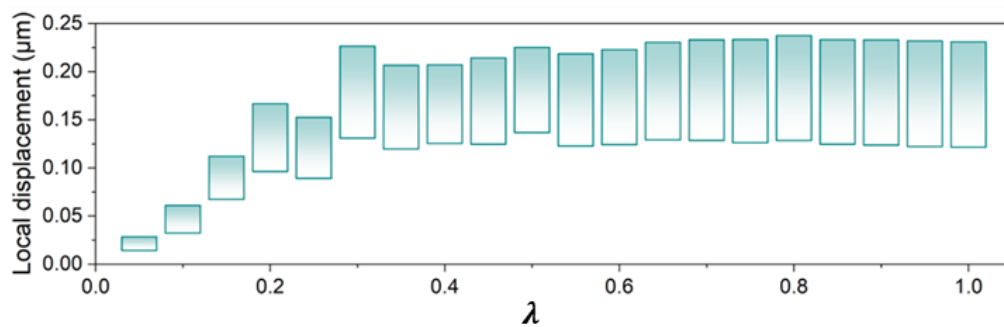
Figure. 4.40. Local displacement inside SSE with different GB with relative strength ranging from 0.05 to 1.0.

Almost all the cracks are initiated from the corners of octagonal Li filament, which is composed of multiple intertwined whisker-like shapes when the strength of GB is not strong enough ($\lambda \leq 0.3$). Subsequently, the crack gradually changes from loose interwoven shapes to the tight intertwine structure with the strengthening GB ($0.3 < \lambda \leq 0.8$), while the crack becomes thick and big rodlike structure inside the SSE (Figure. 4.37). However, from the perspective of the local displacement of SSE with different GB, it can be discovered that the aggregates of grains around each side of octagonal Li filament have been pull away from the initial position by the opening and sliding of GB. Moreover, the SSE with GB over $\lambda = 0.3$ displays two obvious displaced regions on the two larger sides of octagon, which are much greater than that with other regions (Figure. 4.38a-d and Figure. 4.39). The local displacement along diagonal line penetrates the larger sides of octagon and increases with the strengthening SSE to $\lambda = 0.8$, while little change occurs when $\lambda > 0.8$ (Figure. 4.38e). Variously, the displacement degree of SSE is enhanced with the strengthening SSE from $\lambda = 0.05$ to 0.3 and then keeps stable with tough GB after $\lambda \geq 0.3$ (Figure. 4.38f and Figure. 4.40). ***Thus, the disintegration of the SSE represented by the local displacement can be governed by the strength of GB, which can be prolongated effectively with lowered damage degree via strengthening SSE during the growth of Li filament.***

4.1.2.3. Synergistic effects of grain size and relative grain boundary strength
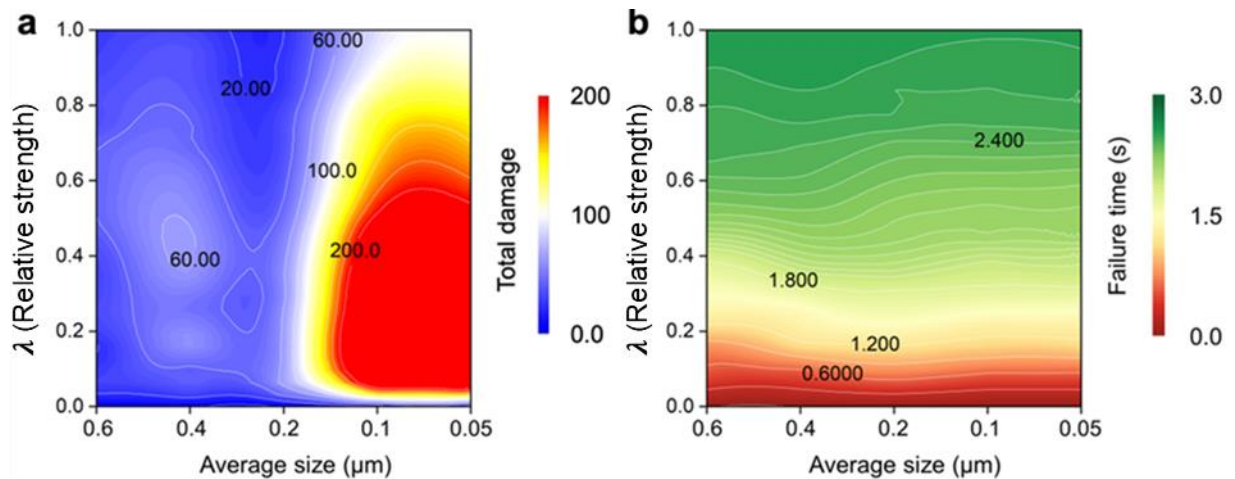
Figure. 4.41. Synergy effect of grain size and boundary strength on the failure of SSE. (a) Total damage and (b) failure time of SSE with different grain size and grain boundary with different strength.

To illustrate the synergetic effect of grain size and boundary strength on the failure of SSE with the development of Li filament, 2D parametric maps of total damage and corresponding failure time were drawn with plenty of simulation results ranging from average grain size AS=0.6 to 0.05 and ratio "Elastic modulus of grain boundaries to grain" λ=0.05 to λ=1.0. As refinement of the SSE is from AS=0.6 to 0.2, the total damage of the whole SSE remains nearly the same, and precipitous growth of total damage shows up after average size <0.2 μm, which can be blame to the flocculent damage distributed inside the whole SSE (Figure. 4.41a). When we focus on a certain of relative strength, like λ=0.2, with the refinement of grain from 0.6 to 0.2, the failure time of solid-state electrolyte increase from 1.1 to 1.4 sec, illustrating that life has been prolongated 28%. After that, the failure time is shortened to 1.4 s and 1.2 s with overfine solid-state electrolyte of AS=0.1 and 0.05. Thus, refinement of grain with the certain range of AS=0.2 can postpone the failure of solid-state electrolyte as well, while overrefinement of grain can not only bring out severe damage, but also foster the failure of solid-state electrolyte. Same aforementioned trend appears in solid-state electrolyte with different strength of grain boundary (Figure. 4.41b). The total damage with the strengthening of GB gradually decreases along the precipitous line of AS=0.1, illustrating, the harmful flocculent damage inside the overfine SSE is suppressed noticeably after λ=0.8 and postpone the failure of SSE. Generally, the refinement of grain and strengthening of GB can be proposed as the effective perspective to improve the lifespan of SSE with the growth of Li filament. The refinement of grain can slightly prolongate the failure time with relative low damage degree, whereas harmful flocculent damage with great damage level will be brought out with the over-refinement. ***The strengthening of GB can crucially postpone the failure of SSE and tune the threshold for the appearance of harmful flocculent damage. Comprehensively, the refinement for grain size of ≥ 0.2 μm with the strengthening for GB to ≥ 0.8 times of grain are posted out as the optimized basic parameter for fraction of NASICON-based SSE for high-performance solid-state batteries.***

To sum up, for the investigation of the failure behavior of SSE during the growth of Li filament, the polycrystalline SSE is geometrically tessellated via Voronoï method under the dynamic stress based on Butler-Volmer electrochemical kinetics, where the grain size and the strength at GB have been taken into consideration. It's noticeably that the compressive stress appears on the interface of Li/SSE during the enlargement of Li filament, of which the stress near the interface spreads outward to the bulk of

SSE via the opening and sliding of GB. As the consequence, the damage originated from the corners-sharp edges of Li filament propagates along the GBs, which spreads spontaneously inside the bulk of SSE. The extraordinary damage induced by flocculent damage appears gradually with the refinement of grain to overfine size, which can be reshaped to giant damages with GB's strengthening. Additionally, the total damage of SSE is slowed down with longer duration through strengthening GB. Therefore, suitable refinement of grain and strengthening of GB can avoid the harmful flocculent damage and prolong the expectation of SSE.

Experimental results

4.2. Study of $Li_{1+x}Al_xTi_{2-x}(PO_4)_3$ powders synthesized by different methods

Analysis the quantitative phase composition of LATP powders is important for selecting the optimal synthesis and sintering conditions, analyzing the ionic conductivity and relative density of ceramics, and its further commercialization.

4.2.1. Solid state reaction method

To determine the optimal conditions for solid-state reaction method, precursor powders obtained after grinding and homogenization by ball milling method were subjected to heat treatment in the range from 700°C to 1200°C for 10 hours then examined by XRD (Figure. 4.42).
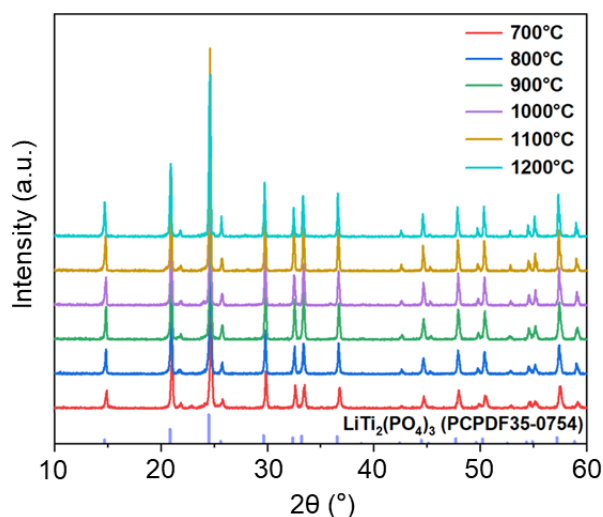
Figure. 4.42. X-ray diffraction patterns of LATP powders obtained by the solid-state reaction method at various synthesis temperatures.

The diffraction patterns of the samples demonstrate a set of reflections indicating the preparation of a substance with the NASICON structure. As a result, all powders are characterized by the content of a small amount of $AlPO_4$ (less than 5 wt.%) (Table. 4.1). The increase in the amount of side phases at low temperature (LATP synthesized at $\leq 700\,℃$) in the literature is explained by the incompleteness of the solid-state reaction due to the low diffusion rate. In connection with the above, the optimal temperature for solid-state reaction method is 800°C, which is characterized by the minimum amount of $AlPO_4$ (~ 1 wt%) in the sample (Table. 4.1) and lower energy consumption. Therefore, it was chosen for further study of sintering behavior of powders.

Table.4.1. Results of phase analysis of the composition in LATP powders obtained by solid-state reaction method.

Samples	Synthesis temperature, °C	Impurities	Mass ratio of impurities, %
LATP-700	700	$AlPO_4$	~ 3
LATP-800	800	$AlPO_4$	~ 1
LATP-900	900	$AlPO_4$	~ 1
LATP-1000	1000	$AlPO_4$	~ 1
LATP-1100	1100	$AlPO_4$	~ 1
LATP-1200	1200	$AlPO_4$	~ 1

It should be noted that the positions of the diffraction peaks of the LATP sample on the diffraction

pattern have different degrees of shift towards larger angles compared to LTP. According to the Wulf-Bragg law, a shift in the position of the diffraction reflection towards large angles means compression of the crystal lattice and a decrease in the interplanar spacing. This indicates that the lattice parameters of LATP have changed compared to LTP. Partial substitution of basic Ti^{4+} cations (ionic radius in the 6th coordination environment 0.605 Å) by cations with a smaller Al^{3+} radius (ionic radius in the 6th coordination environment 0.535 Å) leads to a decrease in the lattice parameters.

The powders obtained by the solid-state reaction method were examined by the SEM to study the microstructure (Figure. 4.43). As a result, the particles of the optimal sample (LATP-800) have a distorted cubic shape, the average size of which is about ~ 570 nm. It should be noted that the results obtained are consistent with the literature.
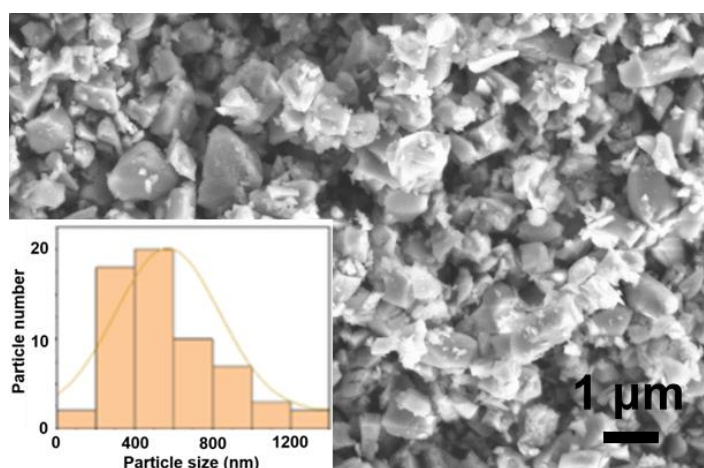
Figure. 4.43. SEM images of LATP sample obtained by the solid-state reaction method synthesized at 800°C for 10 h.

4.2.2. Molten salt quenching method
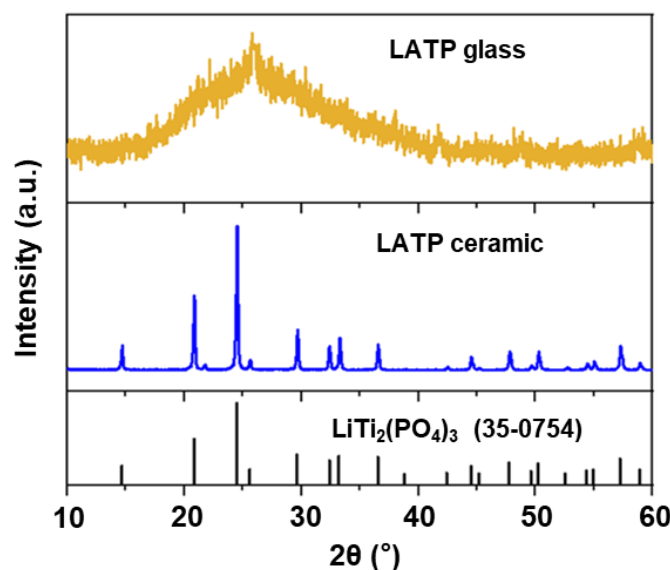
Figure. 4.44. X-ray diffraction patterns of LATP glass and LATP powders obtained by molten salt quenching method.

Figure. 4.44 above show X-ray diffraction pattern for glass phase LATP sample. A pronounced broad reflex (halo) is observed on the X-ray diffraction pattern and there are no distinct narrow diffraction maxima, which confirms the amorphous nature of the glass, which lacks long-range order. In Figure. 4.44 below, the X-ray diffraction patterns for LATP sample made by molten salt quenching method are shown and standard $LiTi_2(PO_4)_3$ (LTP) card (PDF #35-0754) from the ICDD database is included for comparison. The diffraction pattern for the sample shows a set of reflections indicating the preparation of a substance with the NASICON structure. In addition, the (111) maximum at $2\theta = 21.8°$ corresponds to the presence of the $AlPO_4$ impurity phase (PDF #11-0500).

4.2.3. Synthesis using polymerized matrices

4.2.3.1. Morphology of precursor particles in a polymer matrix

Films obtained after copolymerization and drying, with different concentrations of precursors $(C(Ti^{4+}) = 0.04\text{-}0.4$ M), were studied by scanning electron microscopy (SEM) to understand the size of LATP precursor-based particles, the degree of its aggregation and the distance between the formed aggregates (Figure. 4.45). We measured the particle size in the SEM images, as a result, dilution has practically no effect on the average particle size (~ 50 nm), however, it significantly reduces the degree

of their aggregation and increases the average distance between particles from ~ 200 nm at a concentration of 0.4 M up to ~ 800 nm at 0.04 M. The obtained SEM images allow to conclude that a decrease in the concentration of precursors contributes to a more uniform distribution of particles in the polymer matrix, which can have a positive effect on the synthesis of nanoparticles.
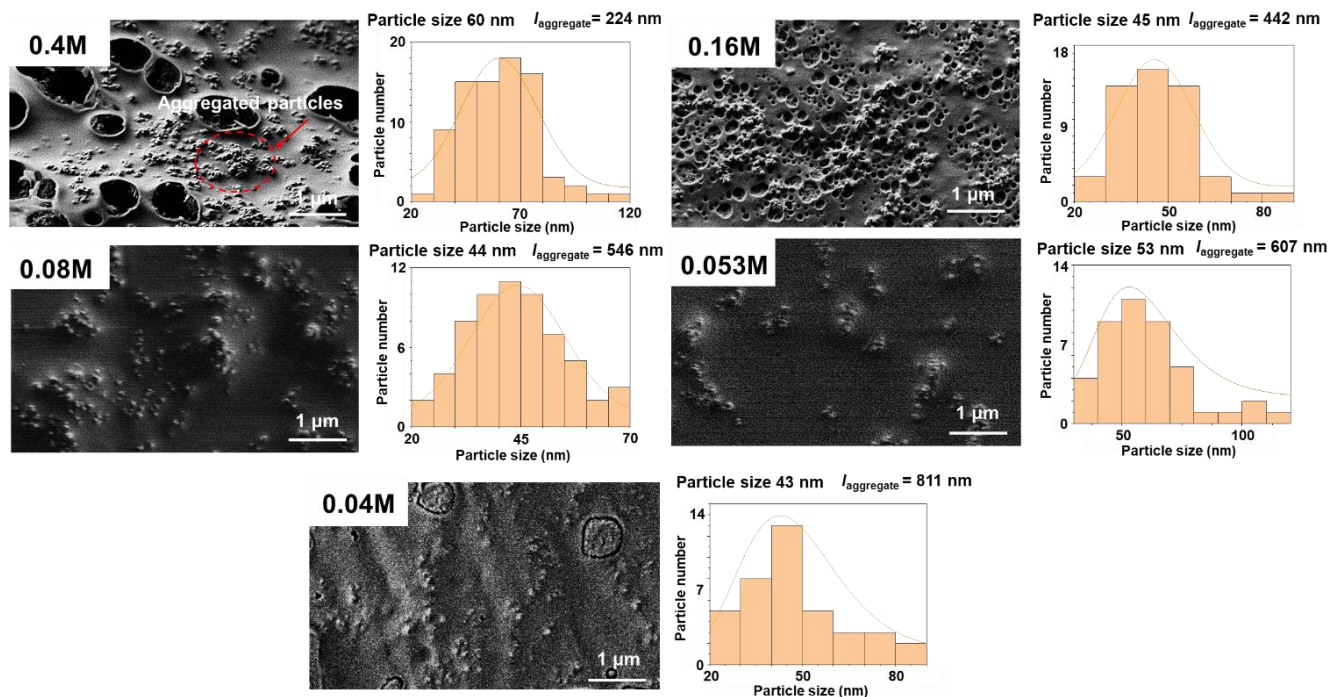
Figure. 4.45. Changes in the morphology of LATP precursor-based particles in the polymer matrix with the decrease of concentration in solutions for the synthesis of LATP.

4.2.3.2. Composition and thermal properties of precursors in polymer matrix

The phase composition of the precursors distributed in the polymer matrix with different initial concentrations was studied by XRD (Figure. 4.46). Thus, the X-ray diffraction patterns of all obtained samples have the same maxima, which indicates the absence of the effect of dilution on the final phases of the precursors. In this case, the largest peaks correspond to ammonium nitrate, since synthesis using polymerized matrices takes place in a strongly acidic HNO_3 solution. As a result, $AlPO_4$, LiH_2PO_4, and TiO_2 crystallize from the solution in the polymer matrix. However, very low concentrations of precursors and the presence of an amorphous halo (polymer matrix) do not allow a more detailed qualitative and quantitative analysis by this method.
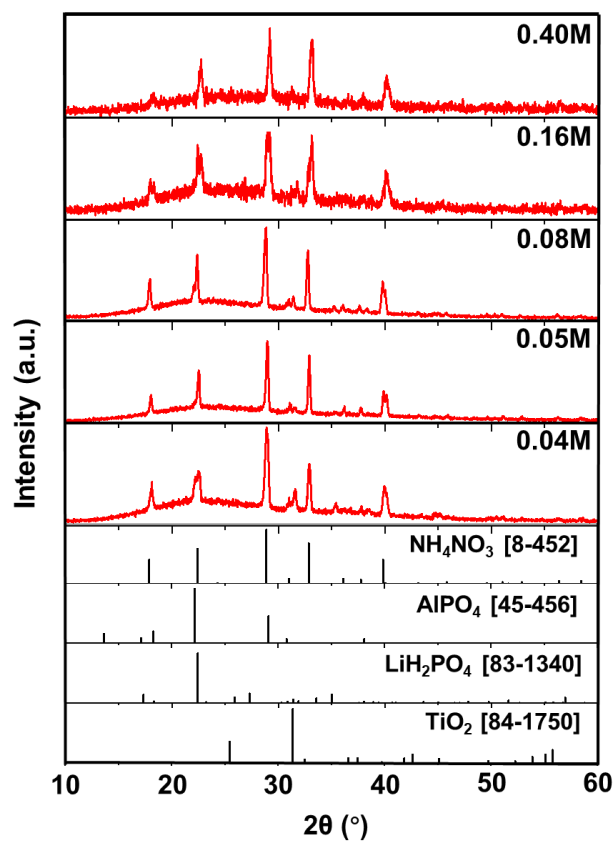
Figure. 4.46. XRD analysis of Composition of precursors with different concentrations in polymer matrix.

Thermogravimetry with differential scanning calorimetry made it possible to study in more detail the chemical composition of precursor polymer matrix (Figure. 4.47). The weight loss with a decrease in the concentration of precursors increased significantly (from 80.2% at $C(Ti^{4+}) = 0.4$ M to 96.3% at $C(Ti^{4+}) = 0.04$ M) as a result of an increase in the mass of the polymer relative to inorganic precursors for LATP.
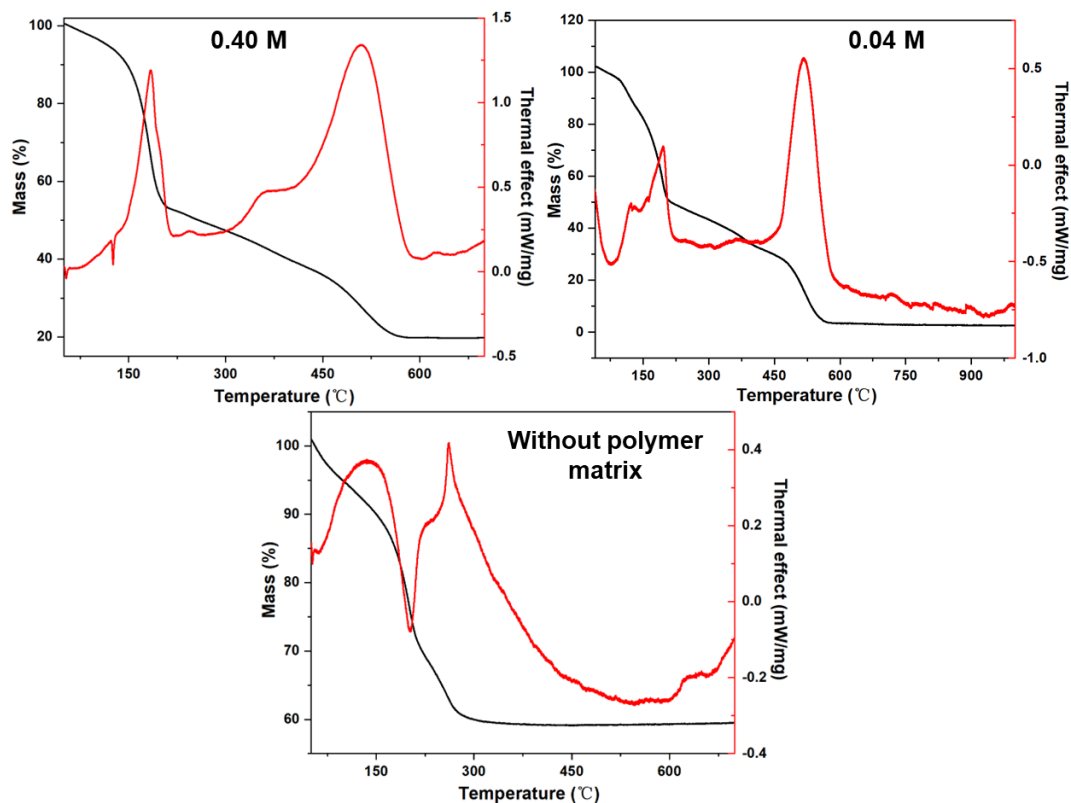
Figure. 4.47. Results of TG and DSC: (a) for polymer matrix films with 0.4 M concentration of precursors and (b) 0.04 M concentration of precursors; c) mixture of precursors without polymer matrix.

After calculations for a concentration of 0.4 M (Figure. 4.47a), the phase composition of the precursors corresponded to the following chemical formulas: $LiH_2PO_4 \cdot 8H_2O$, $AlPO_4 \cdot 3H_2O$, NH_4NO_3 and $TiO_2 \cdot H_2O_2$, and agreed with determined above composition of the peroxo complex of Ti^{4+} along with other chemicals for LATP loaded in the beginning of synthesis.

For a precursor concentration of 0.04 M (Figure. 4.47b), the chemical composition of crystalline hydrates turned out to be increased ($LiH_2PO_4 \cdot 12H_2O$) as a result of a significantly larger amount of water in the initial solution. It is also worth noting that the data obtained using TG and DSC correspond to the XRD results without taking into account the presence of water molecules in the crystal structure. This fact can be explained by the formation of a layered superstructure, the diffraction maxima of which are observed at small angles, which were not studied in the framework of this work, but were presented in the literatures earlier [203].

Also, the study of the thermal behavior of the obtained samples made it possible to study the processes occurring during the heating process and determine the optimal conditions for synthesis.

Mixture of precursors obtained by drying the solution without the polymer matrix was additionally studied (Figure. 4.47c). In this case, the chemical composition of the precursors determined by the change in mass, only corresponds to the solid-state reaction of precursors. As a result, the complete thermal decomposition of all precursors in the mixture occurs at a temperature of $\sim 270°C$, which is much lower than for the solid-state reaction method, the results for which are presented before [204].

However, for particles in a polymer matrix, this temperature increases up to $550°C$ (Figure. 4.47a-b), which is explained by an additional combustion stage of polyacrylamide, according to literatures, active decomposition usually occurs at a temperature of $\sim 450°C$ [205]. At this temperature, the solid-state reaction between the decomposed precursors can already proceed. In this case, the sintering of the obtained particles is prevented by the decomposition of the polymer, accompanied by the release of a large number of gases. As a result, synthesis temperatures in the range of $600-800°C$ is optimal for LATP nanoparticles made by synthesis using polymerized matrices.

4.2.3.3. Phase composition and morphology of LATP particles obtained by the synthesis method using polymerized matrices
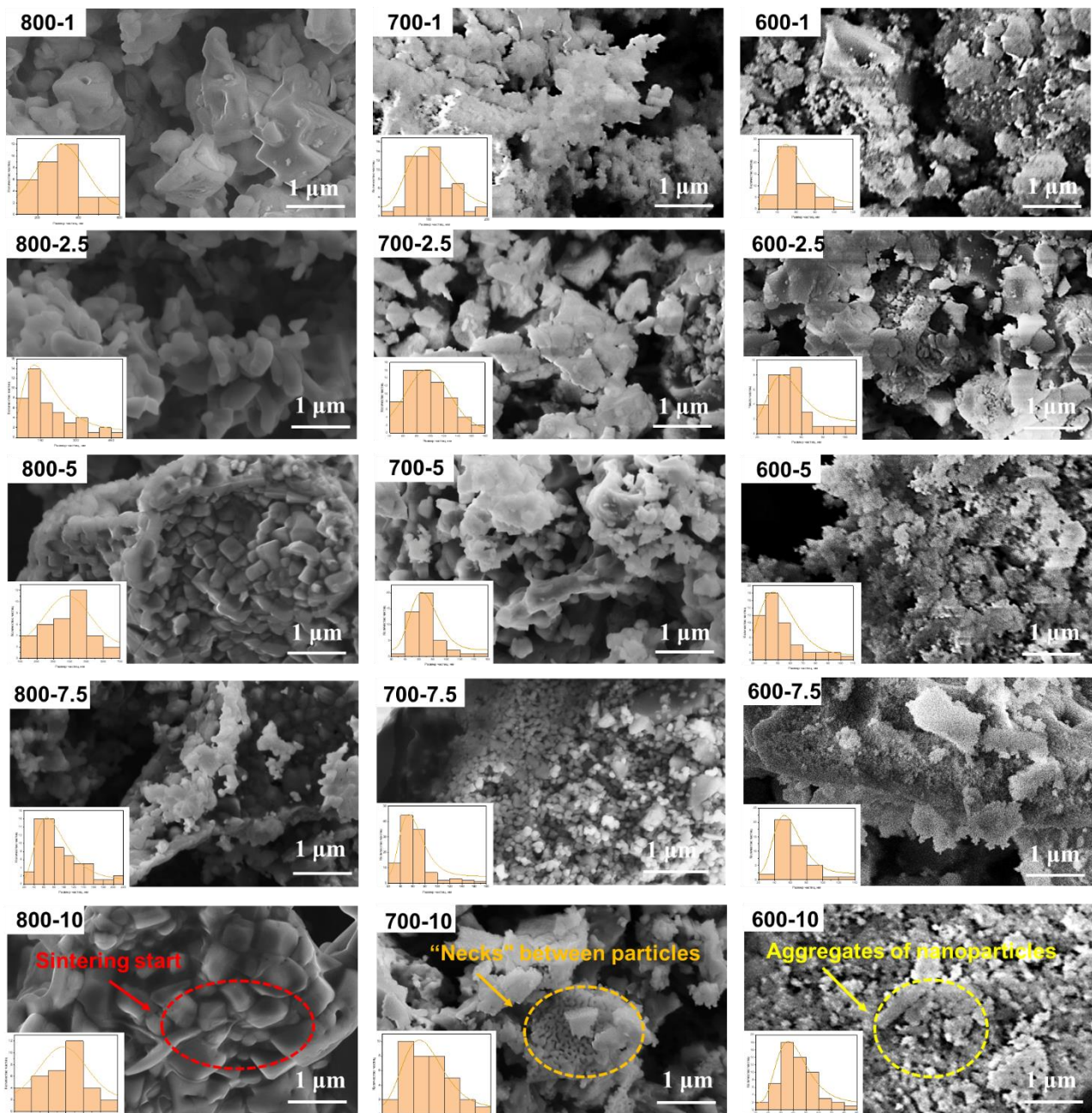
Figure. 4.48. SEM images of LATP powders obtained by synthesis using polymerized matrices at various synthesis temperatures and concentrations of organic/inorganic precursors.

The morphology of LATP powders obtained by synthesis using polymerized matrices under different conditions (precursor concentration and synthesis temperature) was studied by SEM (Figure. 4.48). The synthesis temperature and detailed concentration of the samples are marked in the images, and the specific values are shown in the experimental part. Statistical analysis was performed on at least for 200 particles in SEM images. As a result, the average particle size varied in the range from

400 to 30 nm depending on the conditions (Figure. 4.49a). At the same time, for all series of concentrations, a similar change in morphology was observed with varying synthesis temperature. Thus, regardless of the concentration of precursors, the LATP particles synthesized under 600°C always have a nanometer size. Dilution of the solution with inorganic components and synthesized under 600°C makes it possible to further reduce the average particle diameter down to ~ 30 nm. It is also worth noting that, as a result of such a small size, LATP nanoparticles usually form aggregates of ~ 100 nm.

Increasing the synthesis temperature to 700°C leads to coarsening of LATP particles, which is especially characteristic of samples with a higher concentration of precursors. Thus, increase synthesis temperature from 600°C to 700°C when $C(Ti^{4+}) = 0.4$ M, the average size of LATP particles also increase ~ 2.5 times (from 50 to 120 nm).

It is also worth noting that for low concentration samples synthesized at 700°C, a porous structure is obtained as a result of the onset of sintering processes and the formation of "necks" between particles due to their high thermal activity. 800°C synthesis temperature leads to the formation of large particles with a size up to ~ 600 nm. Similar to grains in ceramics, which indicates the activation of particle sintering processes when synthesize at 800°C. This phenomenon is especially pronounced for samples with a low concentration of inorganic precursors in the polymer matrix, since these conditions make it possible to obtain the smallest particle size, which have a high thermal activity. As a result of the above, the smallest average size (~ 30 nm) was achieved by reducing both the concentration of inorganic precursors in polymer matrix down to 10 times and the synthesis temperature to 600°C for 5 h (sample LATP-600-10).
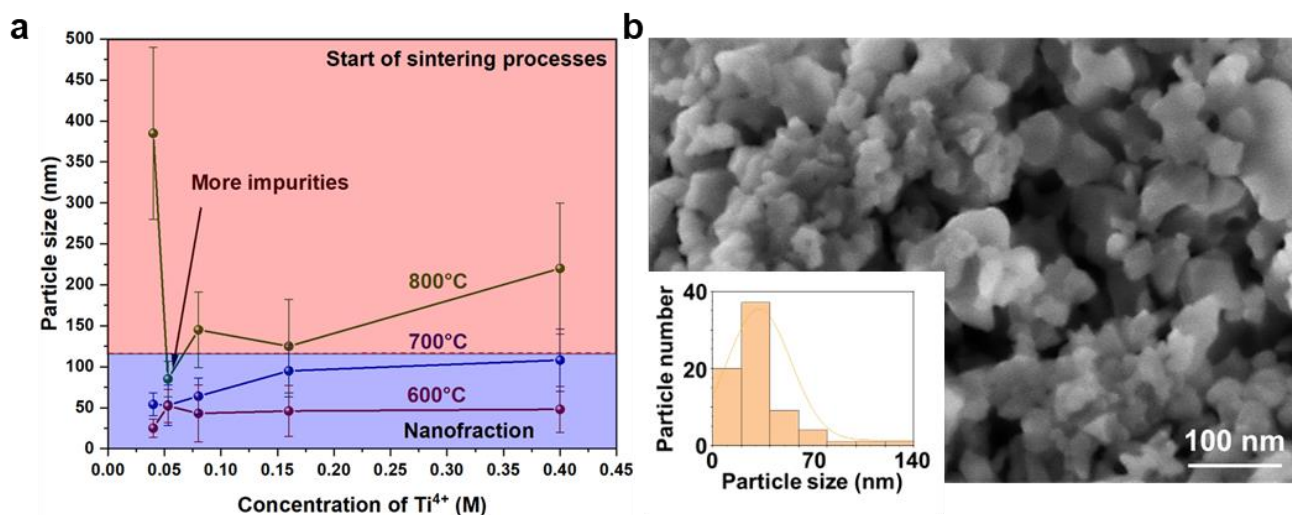
Figure. 4.49. (a) Effect of synthesis temperature and Ti^{4+} concentration on the final particle size of LATP; (b) SEM image of LATP synthesized at 600°C and C(Ti^{4+}) = 0.04 M (sample LATP-600-10).

However, for a more accurate determination of the size of nanoparticles, a scanning electron microscope with a high magnification was also used (Figure. 4.49b). Sample LATP-600-10 predominantly has particles with an average particle size down to ~ 30 nm, which has not previously been presented in the literatures. It also should be noted that the content of particles with a diameter of more than 50 nm does not exceed 10%.
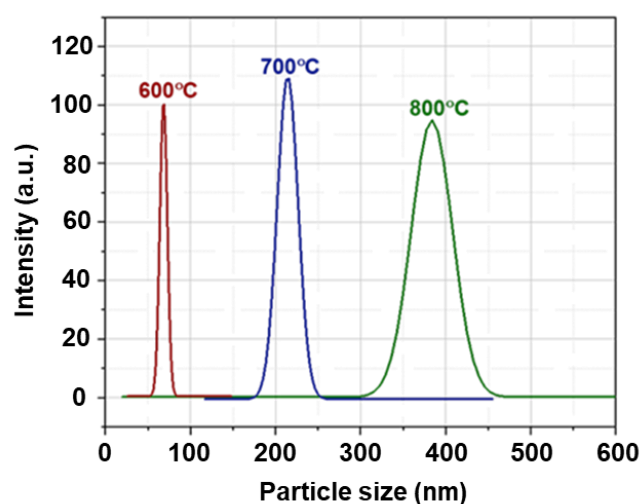
Figure. 4.50. DLS results for LATP samples obtained at different synthesis temperatures and C(Ti^{4+}) = 0.4 M.

Another method for studying the morphology of LATP nanoparticles was DLS, which made it possible to determine the average size of the obtained particles and the distribution width. Thus, the synthesis temperature makes it possible to vary the average size of nanoparticles from ~ 30 to 200 nm (Figure. 4.50), which corresponds to the SEM images presented above.

However, the particle size of LATP synthesized at 800°C obtained by DLS is underestimated in comparison with the SEM images, since large aggregated particles after partial sintering during synthesis quickly settle out of the colloidal solution, which makes it difficult to measure them for a correct assessment of the sizes of not only individual particles, as well as distribution. The minimum particle size (about 30 nm) also corresponded to the sample obtained by reducing both the synthesis temperature and the concentration of inorganic precursors (LATP-600-10).

Raman spectroscopy can qualitatively analyze the composition of the synthesized sample powder.
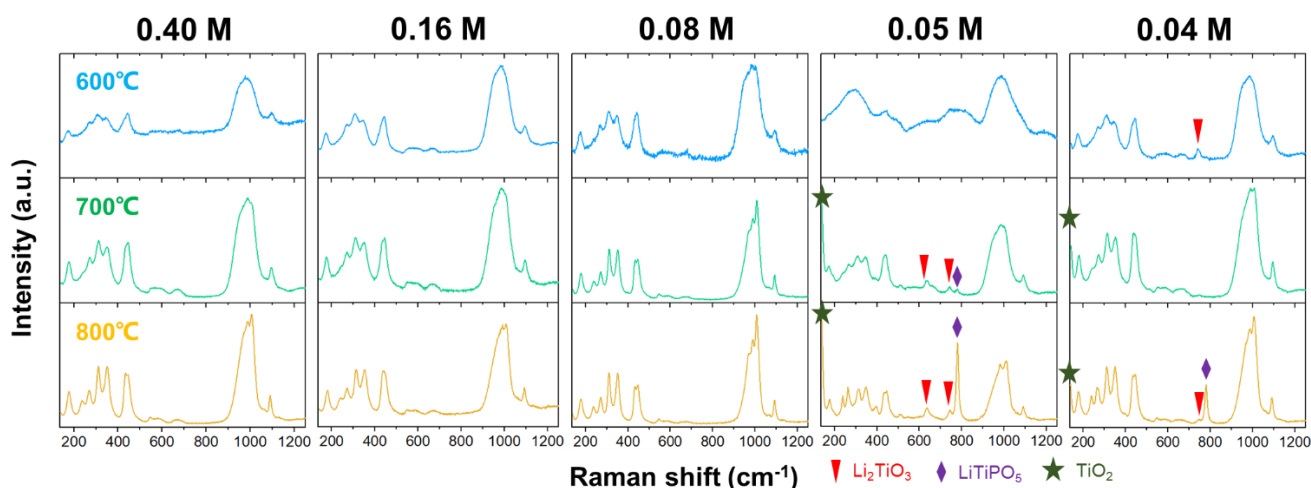
Figure. 4.51. Raman results for LATP samples obtained at different synthesis temperatures and precursor concentrations.

As a result, the presence of characteristic maxima of LATP is observed for all samples. Moreover, LATP powders obtained at relatively high temperatures and low concentrations of precursors, additional peaks appear related to second phases: TiO_2 (anatase, 144 cm^{-1}) [206] and $LiTiPO_5$ (780 cm^{-1}) [110, 207], which corresponds to the XRD results presented above. As the temperature decreases, a characteristic maximum of the impurity has a peak at ~750 cm^{-1}, which corresponds to the Ti-O bond stretching, which is attributed in the literatures to the Li_2TiO_3 [208] compound. It is also worth noting that the samples obtained at 600°C have wider peaks in the Raman spectrum, which occurs as a result of a decrease in the particle size, corresponds to the results obtained by the SEM and DLS [209].

XRD results can quantitatively analyze the composition of the synthesized sample powder.
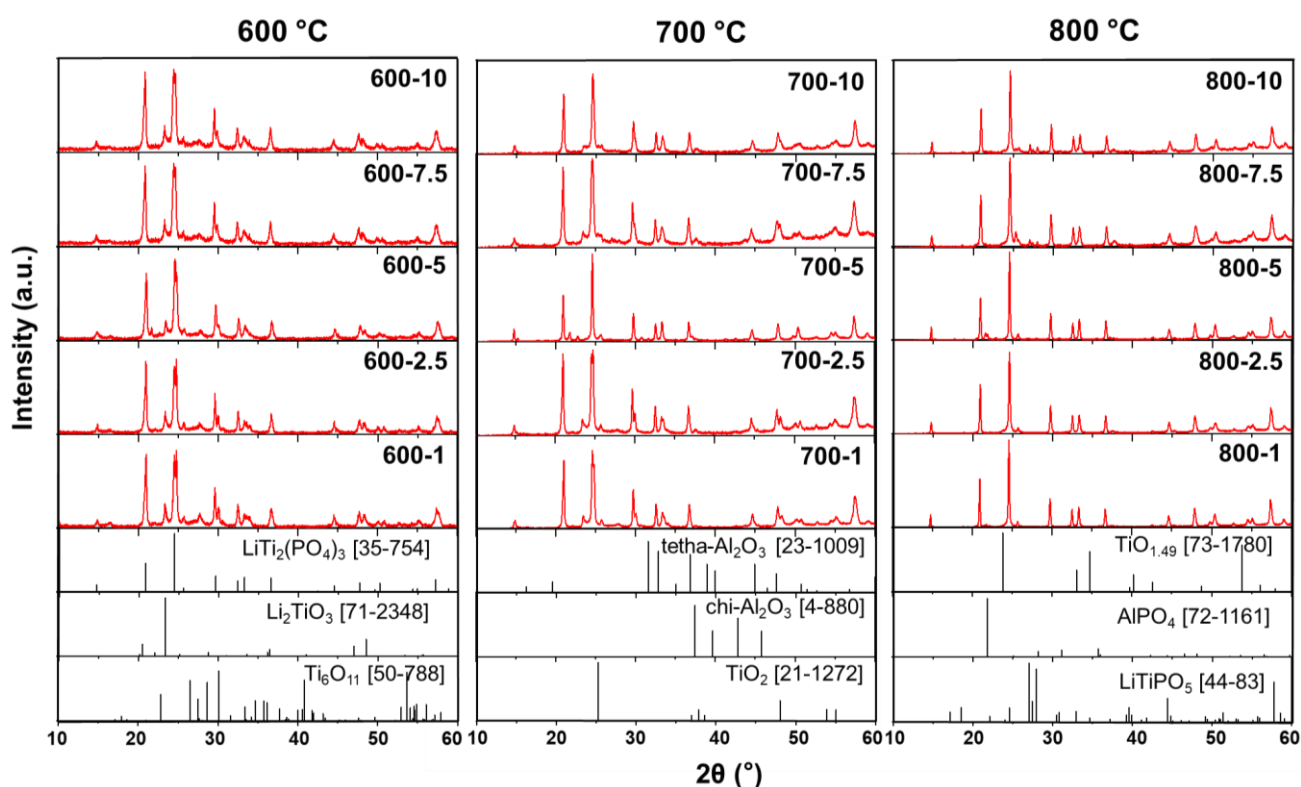
Figure. 4.52. XRD results for LATP samples obtained at different synthesis temperatures and precursor concentrations.

The average size of nanoparticles was also estimated by XRD from the broadening of the peak [113] in the LATP X-ray pattern (Figure. 4.52). The obtained data (Table. 4.2) correspond to the results of SEM and DLS. However, at a relatively high synthesis temperature and low concentration of inorganic precursors (sample LATP-800-10), the particle diameter is ~ 50 nm, which is much smaller than the size presented by other methods. This phenomenon can be explained by the sintering of particles during their synthesis process, which leads to the formation of large agglomerates and limits the use of the Scherrer equation. Here we calculate the size is not the size of LATP particles, but the defect-free region inside the sintered aggregates. In this case, the minimum particle size according to XRD data corresponds to a sample of LATP-600-10 (22 nm), obtained by reducing both the concentration of precursors and the synthesis temperature, which confirms the results of the methods presented above.

It should be noted that the method for obtaining LATP nanoparticles smaller than 60 nm is not presented in any literature. For example, the Pechini sol-gel method and its various modifications make it possible to synthesize LATP particles with minimal size of 100 nm, while the co-precipitation

method is limited down to 200 nm while developed in this PhD thesis approach results to nanoparticles with average size of down to 30 nm.

Table. 4.2. XRD results and calculated size of LATP nanoparticles obtained under different synthesis conditions.

Temperature	800°C					700°C					600°C				
Concentration Ti^{4+}(M)	0.40	0.16	0.08	0.05	0.04	0.40	0.16	0.08	0.05	0.04	0.40	0.16	0.08	0.05	0.04
Impurity phase (%)	~4	~9	~2	~21	~18	~16	~22	~19	~23	~19	~22	~25	~18	~20	~20
$d_{[113]}$ (nm)	169	145	170	104	47	92	83	79	77	45	32	30	26	38	22

According to the XRD results, the qualitative and quantitative composition of LATP powders obtained under various synthesis conditions was also established (Figure. 4.52). Thus, the main characteristic impurity of powders obtained at 600-700°C is Li_2TiO_3 (2θ = 23.362°). It should be noted that the presence of a sufficiently amount of this phase is also observed for the most successful synthesis using polymerized matrices nanoparticles and wet methods presented in the literatures. However, the authors did not carry out a more detailed quantitative composition, considering the resulting powders to be predominantly single-phase.

In this work, the content of Li_2TiO_3 was studied and is ~20 wt.% (Table. 4.2) in samples at 600-700°C (other phases are less than 1 wt.%), which is a fairly successful result for obtaining LATP nanoparticles of such a small size (~ 30 nm). At a higher synthesis temperature, this phase transforms into $LiTiPO_5$ (2θ = 27.059°), which is also a characteristic impurity for LATP, but its quantitative value does not exceed 10 wt.%. Also, the samples obtained at 800°C are characterized by the presence of $AlPO_4$ (2θ = 21.763°) and TiO_2 (2θ = 25.281°) (no more than 5 wt.%), which are obtained during the evaporation of Li_2O and indicate the degradation of the LATP crystal structure at too high synthesis temperature [125, 210].

Energy Dispersive X-ray spectroscopy (EDX), as one of the elemental analysis methods, was used to analyze the samples for comparison with previous data.
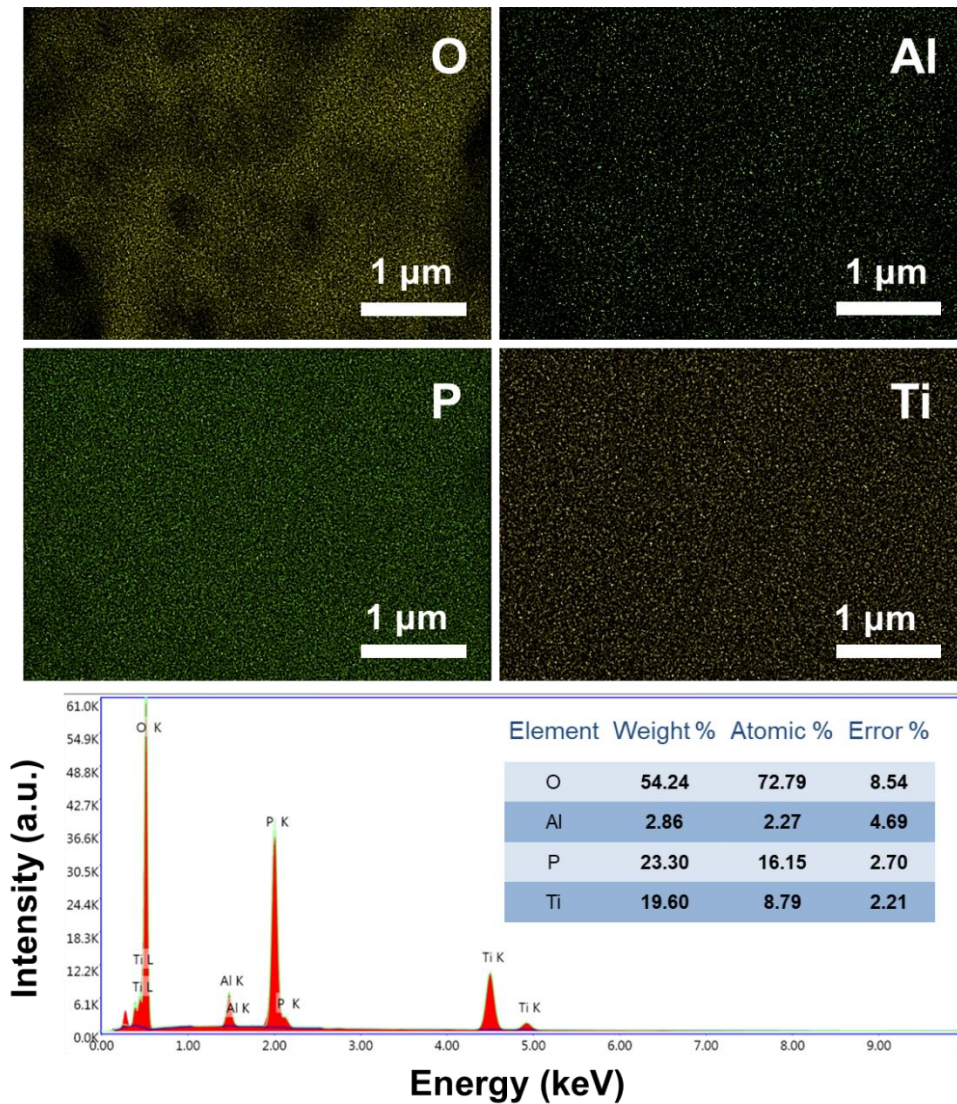
Figure. 4.53. EDX maps and spectrum for sample LATP-600-10.

EDX results are presented for the sample with the smallest particle size (LATP-600-10) in Figure. 4.53. The resulting maps show a uniform distribution for oxygen, phosphorus, titanium, and aluminum. Lithium cannot be determined by this method due to its low molecular weight. It should be noted that the content of other elements was not found.

4.3. Selection of effective sintering modes for submicron particles of LATP composition

4.3.1. Study of sintering behavior of submicron size LATP particles

The indexes of the obtained samples and the corresponding sintering conditions are presented in Table. 4.3. The LATP powders synthesized by the classical method, after different time wet ball milling

treatment, obtained the average particle size of ~600nm and ~300nm respectively, we named them LATP-600nm and LATP-300nm.

Table. 4.3. Indexes of the obtained samples and corresponding sintering conditions.

Sintering program	LATP-1.3 600 nm	LATP-1.3 300 nm	Sintering program	LATP-1.3 600 nm	LATP-1.3 300 nm
750 ℃ 0.5h	750-0.5-1	750-0.5-2	750 ℃ 6h	750-6-1	750-6-2
800 ℃ 0.5h	800-0.5-1	800-0.5-2	800 ℃ 6h	800-6-1	800-6-2
850 ℃ 0.5h	850-0.5-1	850-0.5-2	850 ℃ 6h	850-6-1	850-6-2
900 ℃ 0.5h	900-0.5-1	900-0.5-2	900 ℃ 6h	900-6-1	900-6-2
950 ℃ 0.5h	950-0.5-1	950-0.5-2	950 ℃ 6h	950-6-1	950-6-2
1000 ℃ 0.5h	1000-0.5-1	1000-0.5-2	1000 ℃ 6h	1000-6-1	1000-6-2
750 ℃ 2h	750-2-1	750-2-2	750 ℃ 10h	750-10-1	750-10-2
800 ℃ 2h	800-2-1	800-2-2	800 ℃ 10h	800-10-1	800-10-2
850 ℃ 2h	850-2-1	850-2-2	850 ℃ 10h	850-10-1	850-10-2
900 ℃ 2h	900-2-1	900-2-2	900 ℃ 10h	900-10-1	900-10-2
950 ℃ 2h	950-2-1	950-2-2	950 ℃ 10h	950-10-1	950-10-2
1000 ℃ 2h	1000-2-1	1000-2-2	1000 ℃ 10h	1000-10-1	1000-10-2

Figure. 4.54. showed the X-ray diffraction patterns of LATP-600nm and LATP-300nm samples obtained after sintering at different temperatures for sintering 6 and 10 hours. Characteristic reflections corresponding to $LiTi_2(PO_4)_3$ (PDF#35-0754) were observed from all samples, indicating that the original NASICON structure retained after sintering. The presence of impurity phases other than $AlPO_4$ (PDF #11-0500) present in the original LATP sample was not detected. It is noted that the intensity of the maximum corresponding to the $AlPO_4$ phase decreases with increasing temperature and time of sintering, which could be associated with the continuation of solid-state reaction.
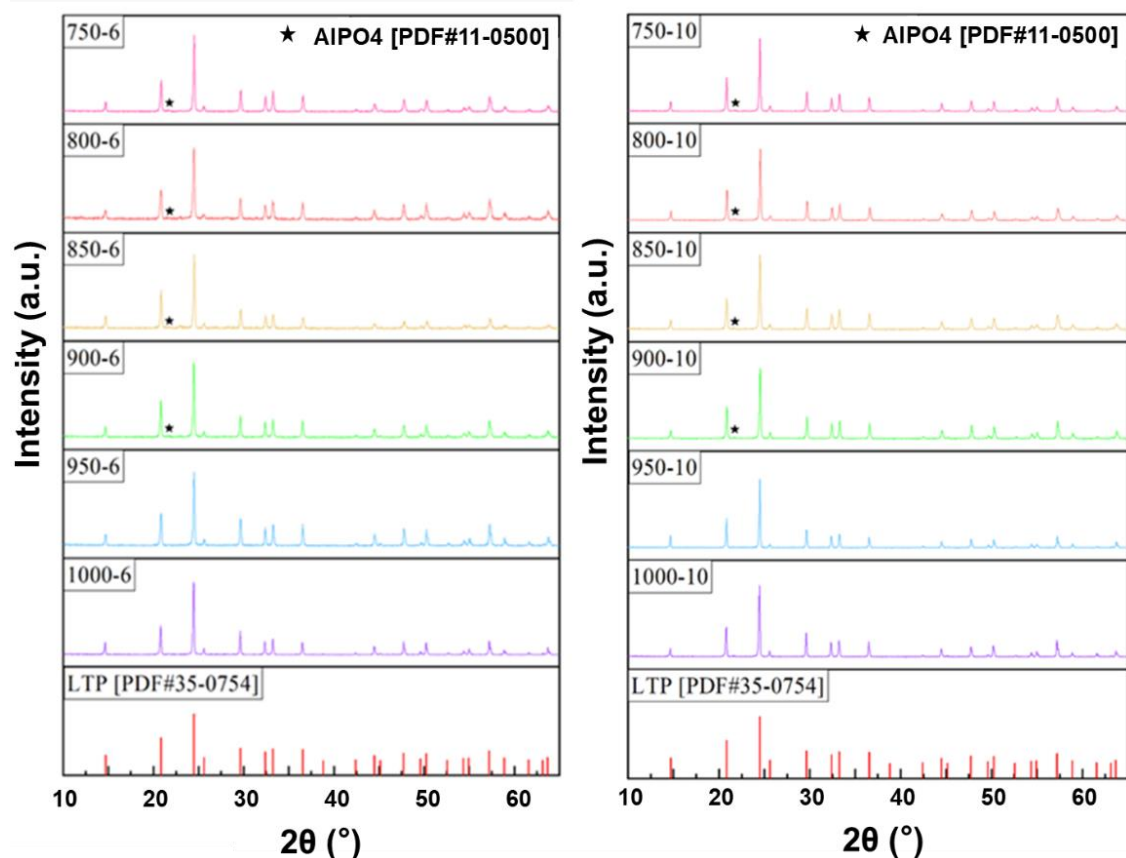
Figure. 4.54. X-ray diffraction patterns of LATP-600nm samples after sintering at different temperatures for 6 h (left) and 10 h (right), respectively.

The density after sintering is an important characteristic of the solid-state electrolyte ceramics. The closer the real density is to the theoretical X-ray density, the fewer pores are in the ceramic and the closer contact between the grains. Thus, a high relative density (ratio of real density to the theoretical X-ray density) is a necessary condition for good ionic conductivity in the solid-state electrolyte ceramic.

In Table. 4.4-5 and Figure. 4.55-56 shows the values of relative density before and after sintering under different conditions. Green body tablets made by LATP-600nm and LATP-300nm powders, sintered at 750°C, 800°C, 850, 900°C, 950°C and 1000°C for 0.5 h, 2 h, 6 h and 10 h.

Table. 4.4. Densities of solid-state electrolyte ceramic made by LATP-600nm powders, then sintered under different conditions.

Index	Before sintering process		After sintering process	
	Real density (g/cm^3)	Relative density (%)	Real density (g/cm^3)	Relative density (%)
750-0.5-1			2.02±0.07	69±2
800-0.5-1			2.23±0.05	76±2
850-0.5-1			2.45±0.05	83±2
900-0.5-1			2.50±0.04	85±2
950-0.5-1			2.53±0.03	86±1
1000-0.5-1			2.60±0.04	88±1
750-2-1			2.3±0.1	79±4
800-2-1			2.53±0.07	86±3
850-2-1			2.64±0.02	89.9±0.9
900-2-1			2.67±0.02	90.9±0.6
950-2-1			2.70±0.03	91.8±0.9
1000-2-1	1.63±0.05	56±2	2.67±0.03	91±1
750-6-1			2.5±0.1	84±4
800-6-1			2.7±0.1	91±5
850-6-1			2.78±0.02	94.5±0.6
900-6-1			2.78±0.01	94.5±0.5
950-6-1			2.80±0.04	95±2
1000-6-1			2.77±0.04	94±1
750-10-1			2.56±0.03	87±1
800-10-1			2.78±0.05	94±2
850-10-1			2.79±0.07	95±2
900-10-1			2.81±0.05	96±2
950-10-1			2.79±0.07	95±2
1000-10-1			2.78±0.03	94.7±0.9

Table. 4.5. Densities of solid-state electrolyte ceramic made by LATP-300nm powders, then sintered under different conditions.

Index	Before sintering process		After sintering process	
	Real density (g/cm³)	Relative density (%)	Real density (g/cm³)	Relative density (%)
750-0.5-2			2.16±0.09	73±3
800-0.5-2			2.4±0.1	81±4
850-0.5-2			2.48±0.04	84±1
900-0.5-2			2.54±0.05	86±2
950-0.5-2			2.58±0.04	88±1
1000-0.5-2			2.63±0.04	89±2
750-2-2			2.3±0.1	75±4
800-2-2			2.53±0.08	85±3
850-2-2			2.64±0.04	88±1
900-2-2			2.67±0.03	90±1
950-2-2			2.70±0.03	90.7±0.9
1000-2-2	1.66±0.05	56±2	2.67±0.02	91.2±0.6
750-6-2			2.49±0.06	85±2
800-6-2			2.6±0.1	88±4
850-6-2			2.76±0.06	94±2
900-6-2			2.76±0.04	94±1
950-6-2			2.72±0.03	92.4±0.9
1000-6-2			2.70±0.02	91.9±0.8
750-10-2			2.6±0.1	87±4
800-10-2			2.62±0.03	89.0±0.9
850-10-2			2.77±0.03	94.4±0.9
900-10-2			2.75±0.05	93±2
950-10-2			2.71±0.03	92.3±0.9
1000-10-2			2.70±0.03	92±1
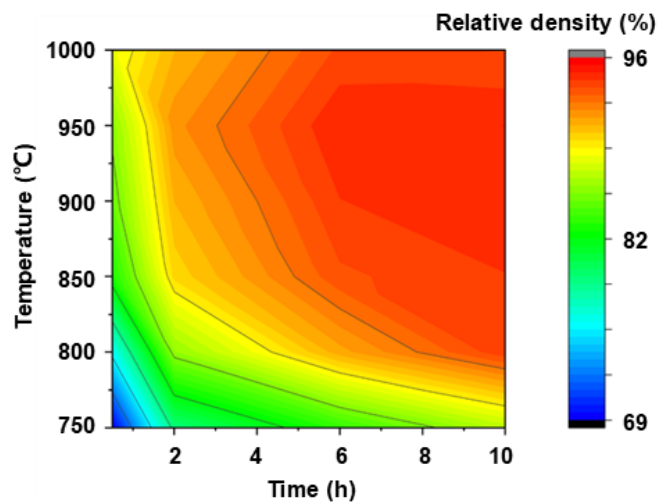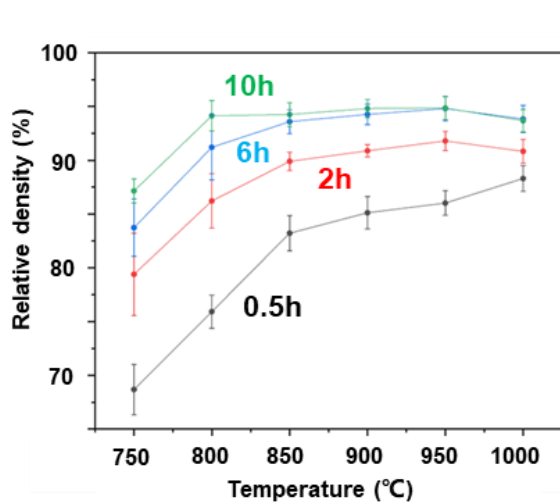
Figure. 4.55. Curves and 2D parametric map of the relative density of SSE ceramic made by LATP-600nm powder under different sintering conditions.
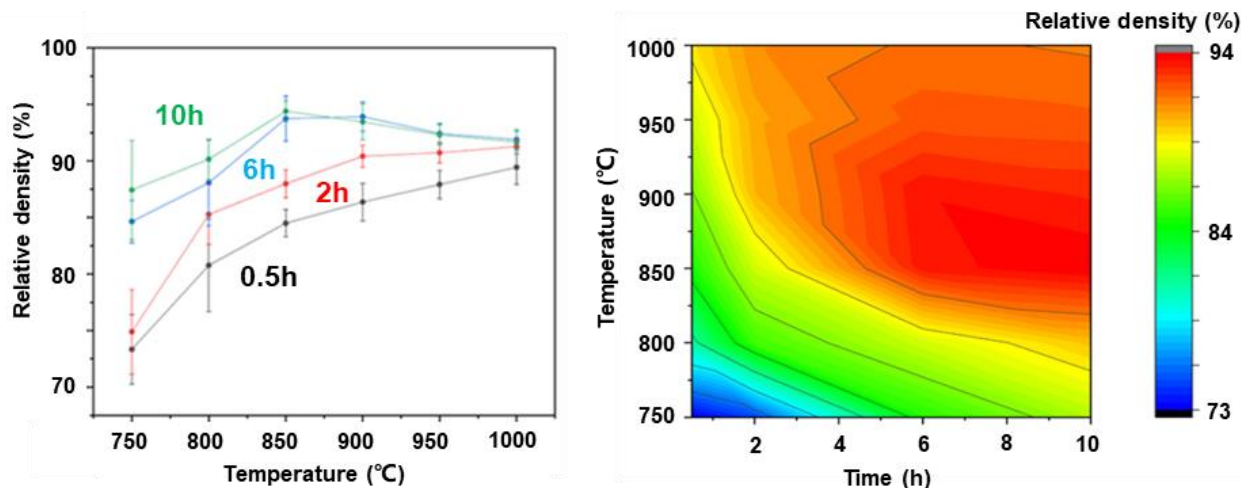
Figure. 4.56. Curves and 2D parametric map of the relative density of SSE ceramic made by LATP-300nm powder under different sintering conditions.

It has been established that for the green body tablet made by LATP-600nm powder, upon treatment for 0.5 h, the relative density increases with an increase in the sintering temperature. However, during treatment for 2 hours, 6 hours and 10 hours, the relative density of the green tablets tends to first increase (up to 950°C) and then decrease (above 950°C) with increasing sintering temperature. The maximum relative density (over 94%) of the LATP-600nm SSE ceramic was obtained by sintering between 850°C and 950°C for 6-10 h.

Figure. 4.56 shows similar trend for green body tablets made by LATP-300nm powder. The relative density of the samples during treatment for 0.5 h and 2 h increases with an increase in the sintering temperature. During treatment for 6 hours and 10 hours, the relative density first increased (up to 850°C), and then obviously decreased (above 950°C) with increasing sintering temperature. In the temperature range of 850-900°C, SSE tablets after sintering have a high relative density (more than 93%). This can be interpreted as the smaller particle size of LATP-300nm green body tablet compared to LATP-600nm increases the surface energy and reduces the optimum heat treatment temperature. The optimal sintering program for LATP-300nm green body tablet is treatment at temperatures from 850°C to 900°C for 6-10 hours.

In the supporting information shows the microstructure and the corresponding particle size distribution histograms for the green body tablets made by LATP-600nm and LATP-300nm powders, after sintering at different temperatures (750-1000°C) for different time (0.5-10 h), respectively.
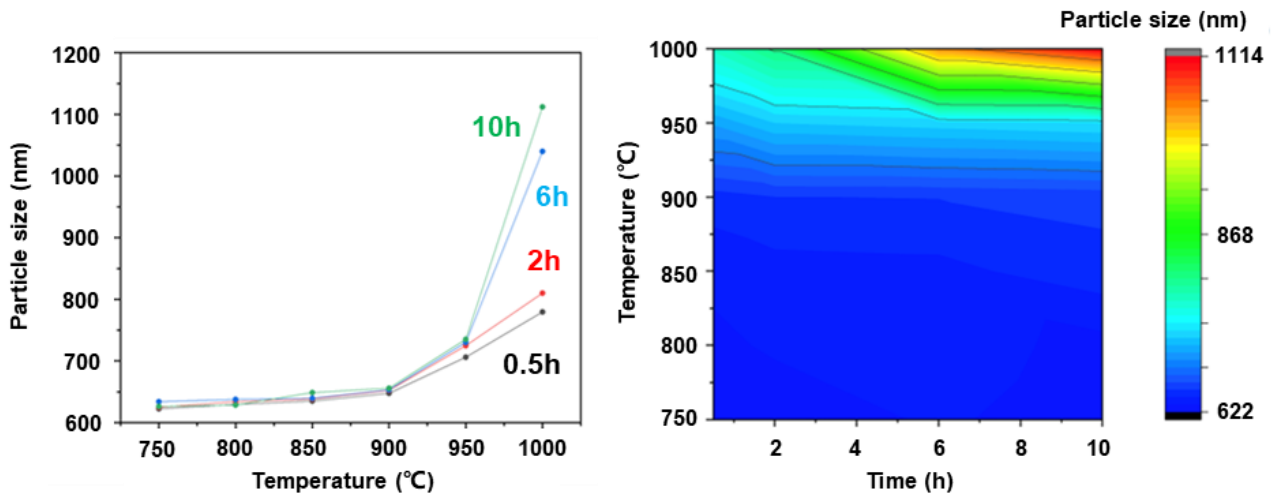
Figure. 4.57. Curves and 2D parametric map of the average particle size of green body tablets made by LATP-600nm powder after sintering in different programs.
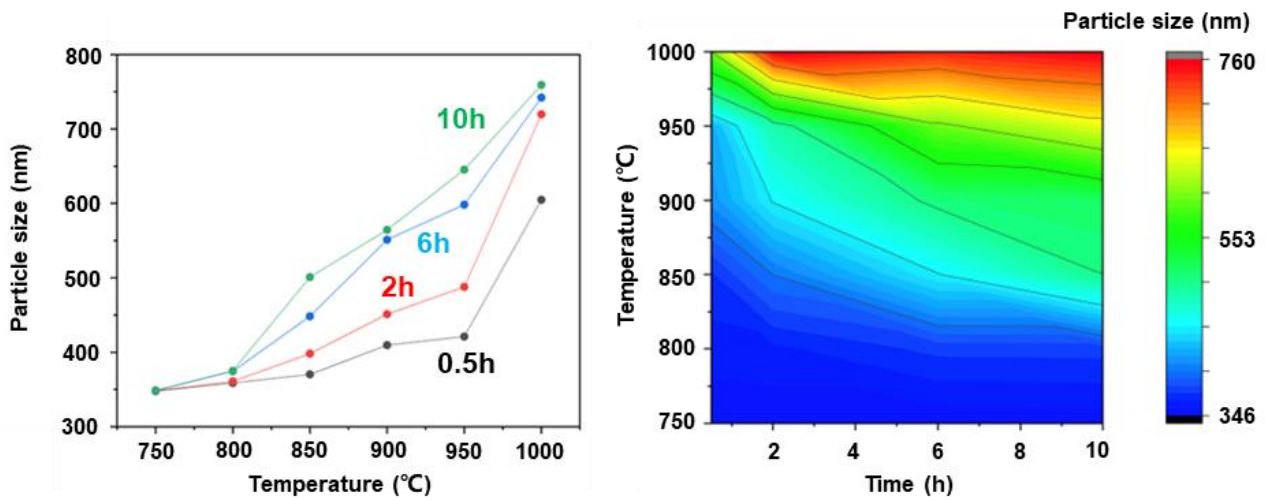
Figure. 4.58. Curves and 2D parametric map of the average particle size of green body tablets made by LATP-300nm powder after sintering in different programs.

As shown in Figure. 4.57-58, with increasing temperature and sintering time, the average particle size of green body tablets made by LATP-600nm and LATP-300nm powders after sintering also grew.

It is worth noting that when use some sintering programs, the phenomenon of abnormal grain growth (AGG) was also observed. As shown in Figure. 4.59-60, ultra-large grains were formed, which was much larger than the size of the grains during their normal growth when sintering (normal grain growth - NGG). The formation of large grains is accompanied by the formation of a large number of pores and defects in SSE ceramic, which are caused by the destruction of the original structure, such as the faster growth rate of AGG grains and the influence of their huge size on surrounding grains, etc. Here we only show several images to describe the abnormal grain growth (AGG) behavior that occurs during the green body sintering process.
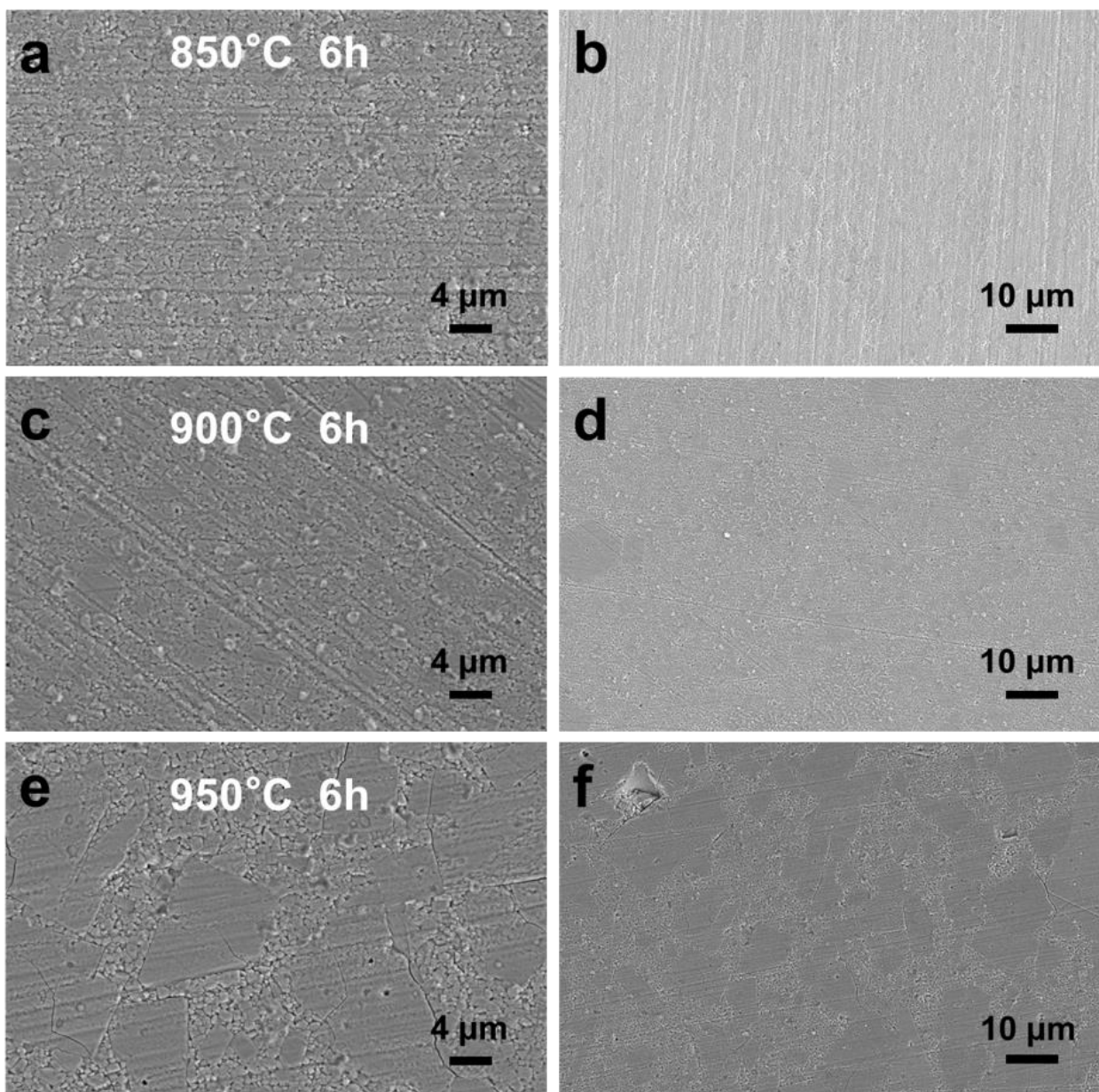
Figure. 4.59. Green body tablets made by LATP-600nm powder, after sintering at different temperatures (850-950°C) for 6 hours, respectively.

For SSE tablets made by LATP-600nm powder, the presence of large grains up to 10 μm and defects (pores and microcracks) could be observed in the SEM images, when using the following sintering programs: 1000°C for 0.5 h, 950°C for 2 h, 900°C for within 2-10 h. The presence of large grains up to 10-20 μm and a large number of defects could be observed in the SEM images, when using the following sintering programs: 1000°C for 2 h, 950°C for 6 h, and 950°C for 10 h. The presence of ultra-large grains with a size of more than 20 μm and a large number of defects could be observed in the SEM images, when using the following sintering programs: 1000°C for 6 h and 1000°C for 10 h. This phenomenon was more pronounced for SSE tablets made by LATP-300nm powder, which is associated with a smaller average particle size, which increases the surface energy and stimulates abnormal grain growth.
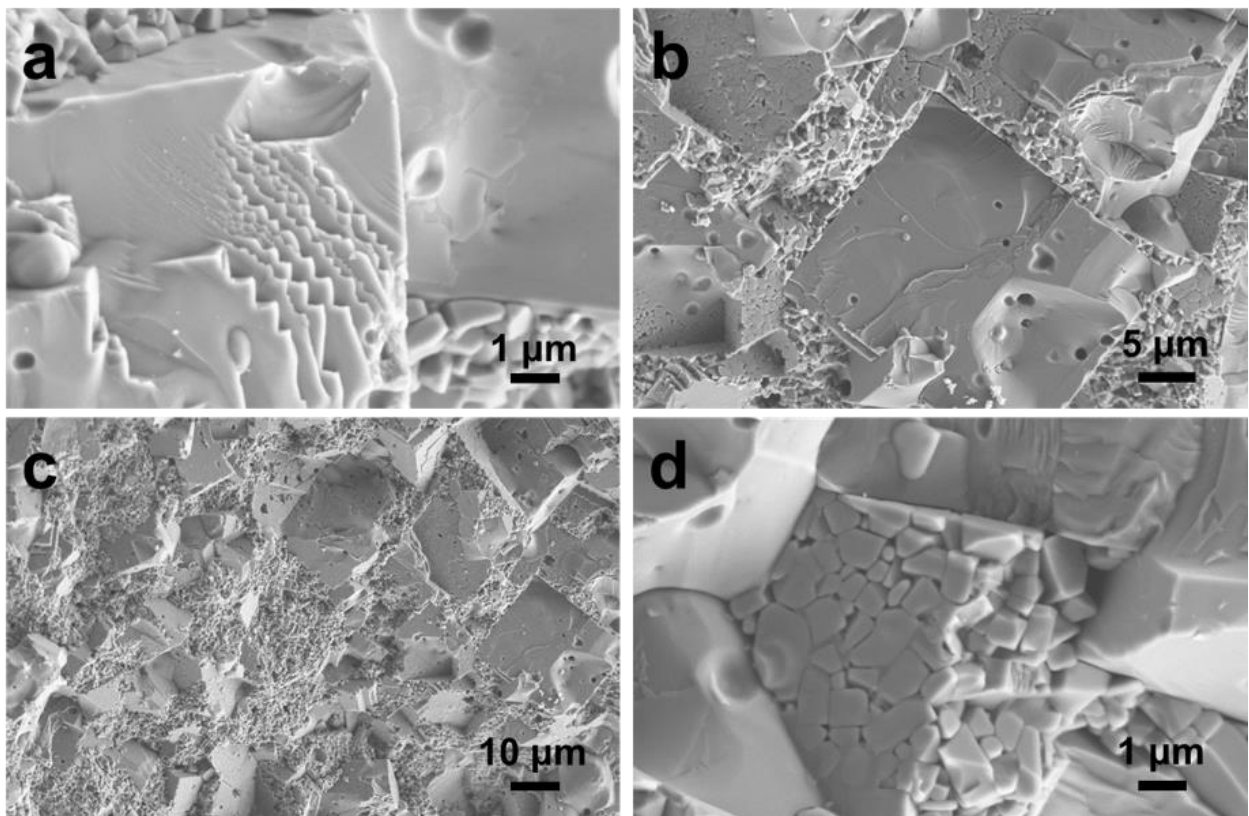
Figure. 4.60. SEM images of LATP-600nm sample with abnormal grain growth after sintering at 950°C for 6 h.

The SEM picture demonstrates typical abnormal grain growth phenomenon. Sintering of LATP green body tablet is a competing process of normal grain growth (NGG) with increased contact

between grains and abnormal grain growth (AGG) causing loss of contact between grains. Thus, increasing the sintering temperature as much as possible without abnormal grain growth and impurity phases to obtain better sintering quality is the challenge for phosphate-based ceramics due to its high thermal activity during densification.

Therefore, it is necessary to find a "balance" by selection of the optimal sintering program, which will achieve the most continuous and uniform grain growth, improve the contact between grains, as well as to suppress the number and size of large grains. Based on the data obtained, the optimal sintering programs, from the point of view of the microstructure, are:

1) Green body tablet made by LATP-600nm powder, better treated at 900°C for 6 h and 850°C for 10 h;

2) Green body tablet made by LATP-300nm powder, better treated at 850°C for 6 h and 800°C for 10 h.

4.3.2. Study of the SSE ceramic ionic conductivity from different sintering programs

Figure. 4.61-62 shows the impedance spectra in Nyquist coordinates at room temperature for a series of SSE tablets made by LATP-600nm powder after sintering at various temperatures (750-1000°C) and time (6 and 10 h). R_0 and R_1 in the equivalent circuit respectively correspond to the grain and boundary resistance.
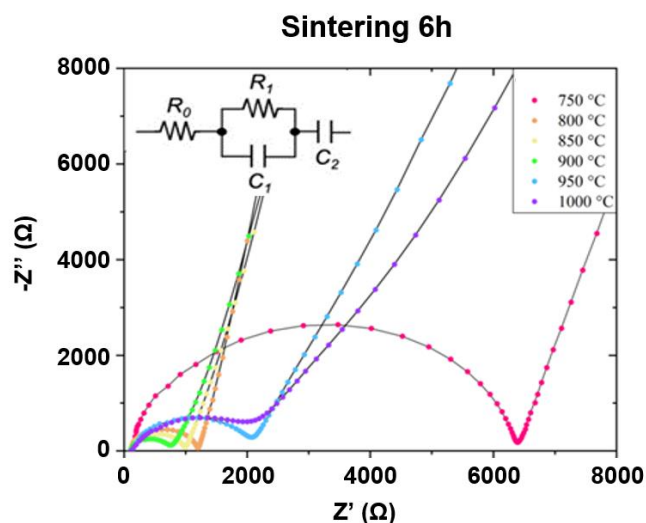
Figure. 4.61. Impedance spectra (in Nyquist coordinates) for SSE tablets made by LATP-600nm powder after sintering under different conditions.
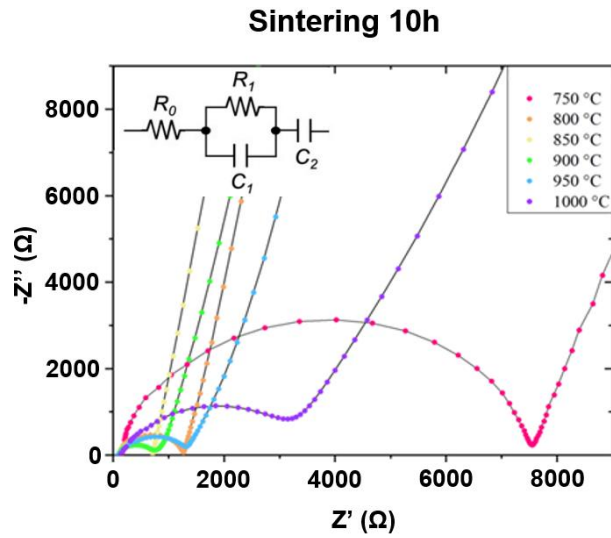
Sintering 10h

Figure. 4.62. Impedance spectra (in Nyquist coordinates) for SSE tablets made by LATP-600nm powder after sintering under different conditions.

The trend of change and the isolines of the total ionic conductivity are shown in Figure. 4.63-64.
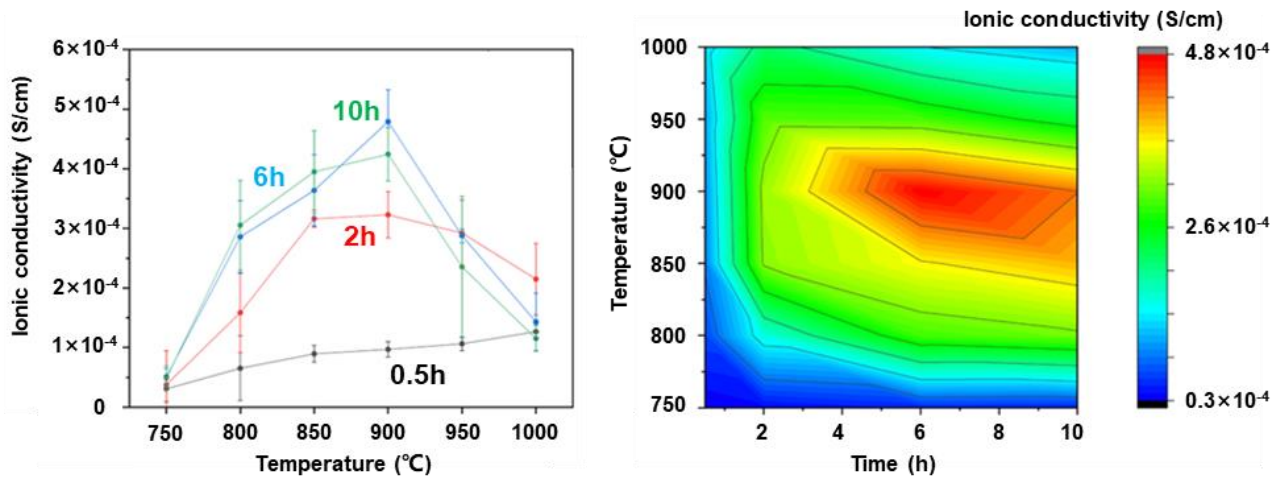
Figure. 4.63. Curves and 2D parametric map of the total ionic conductivity of SSE ceramic made by LATP-600nm powder after sintering in different programs.
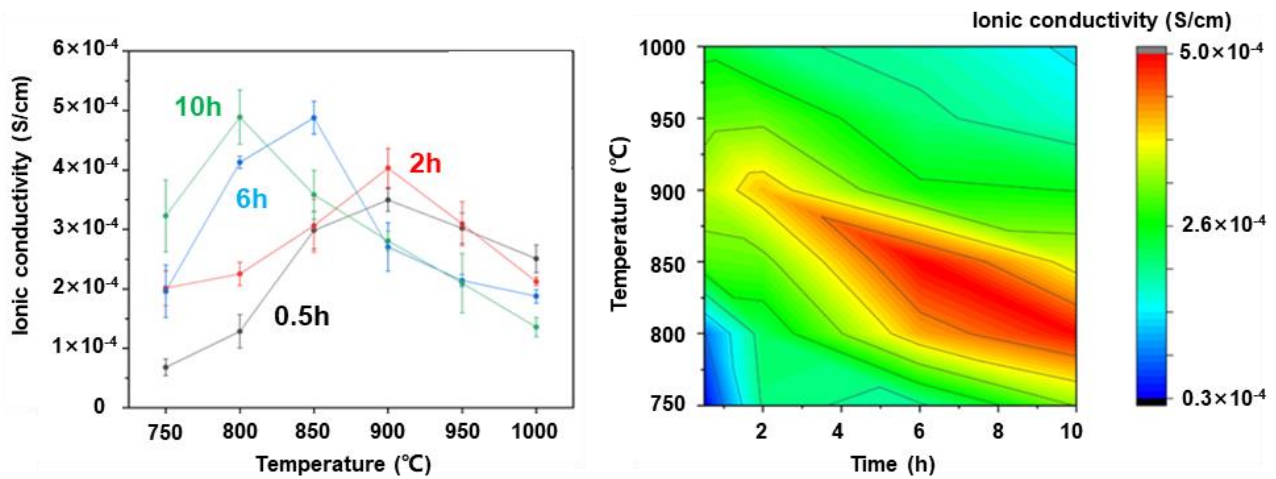
Figure. 4.64. Curves and 2D parametric map of the total ionic conductivity of SSE ceramic made by LATP-300nm powder after sintering in different programs.

For all SSE ceramic tablets after sintering, the σ_g have similar values regardless of the processing conditions. A significant change in σ_{gb} is associated with improved contact between grains during sintering process. Thus, the difference σ_t of all tablets are mainly related to the change of ionic conductivity along the grain boundaries.

SSE ceramic tablets made by LATP-600nm powder, with an increase in the sintering temperature from 750 to 1000°C for a sintering time of 0.5 h, the total ionic conductivity gradually increases, while the value of this parameter passes through maximum as the time increases to 2, 6, and 10 h. Thus, the SSE ceramic obtained by sintering green body tablet made by LATP-600nm at 900°C for 6 h demonstrates the highest total ionic conductivity $(4.8\pm0.5)\times10^{-4}$ S/cm. From the point of view of obtaining a high total ionic conductivity of the SSE ceramic, the optimal program is the sintering green body tablet made by LATP-600nm at 900°C for 6-10 h.

During sintering process of green tablets made by LATP-300nm powder with an increase in the sintering temperature, first increase and then decrease in the total ionic conductivity is observed. SSE ceramic obtained at 800°C for 10 h and 850°C for 6 h demonstrate high ionic conductivity $(4.9\pm0.3)\times10^{-4}$ S/cm and $(4.9\pm0.5)\times10^{-4}$ S/cm, respectively. From the point of view of obtaining a high total ionic conductivity of the SSE ceramic, the optimal program is the sintering green body tablet made by LATP-300nm at 800°C for 10 h or 850°C for 6 h.

4.3.3. Study of the SSE ceramic elastic modulus from different sintering programs
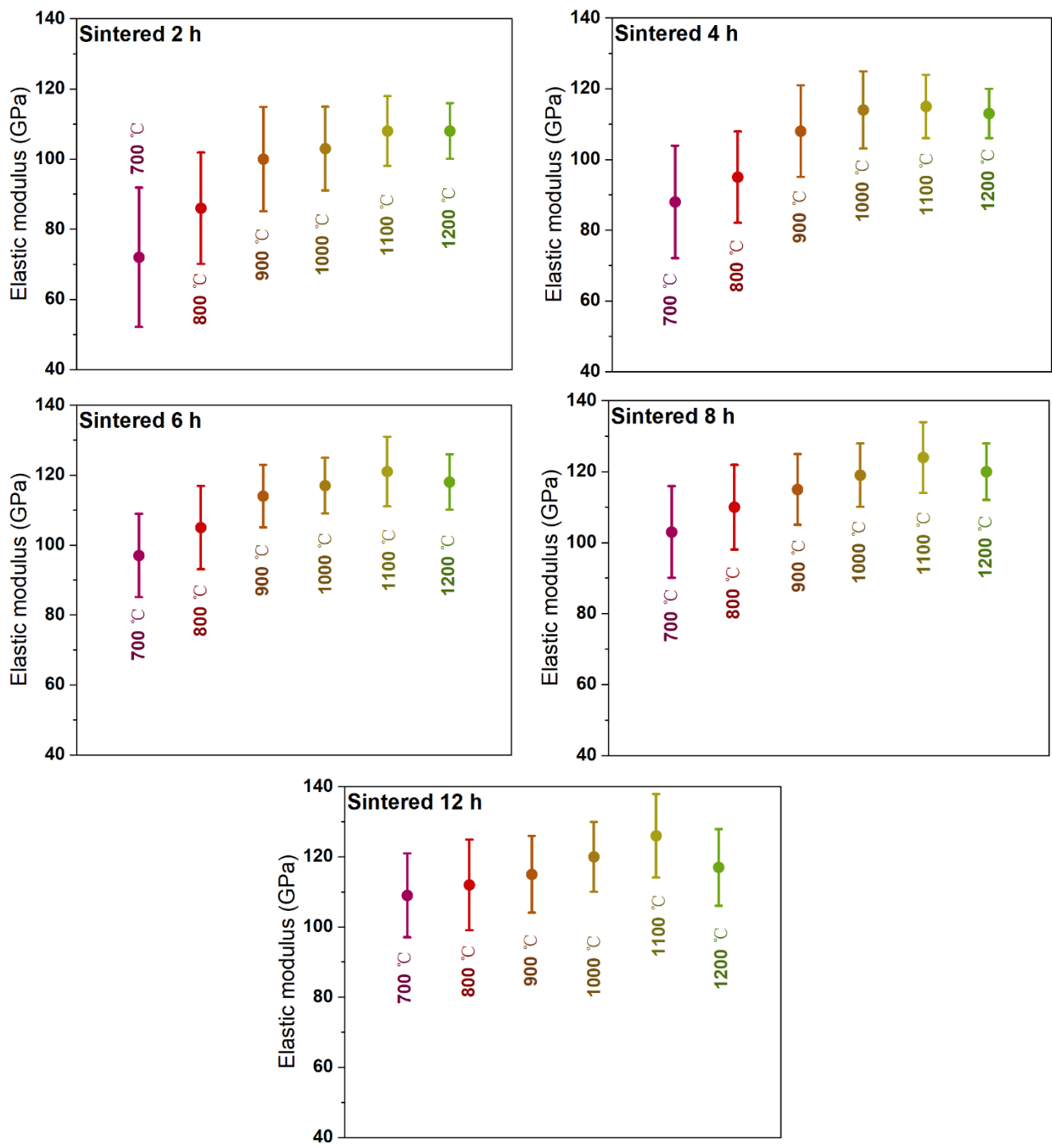
Figure. 4.65. Elastic modulus of LATP SSE obtained from different sintering programs depend on LATP-600nm powder. The load is 50mN.

Table. 4.6. Values of LATP SSE elastic modulus (GPa) obtained from different sintering programs depend on LATP-600nm powder.

Temperature	700°C	800°C	900°C	1000°C	1100°C	1200°C
Time						
2 h	72±20	86±16	100±15	103±12	108±10	108±8
4 h	88±16	95±13	108±13	114±11	115±9	113±7
6 h	97±12	105±12	114±9	117±8	121±10	118±8
8 h	103±13	110±12	115±10	119±9	124±10	120±8
12 h	109±12	112±13	115±11	120±10	126±12	117±11

In the sintering program of equal sintering time, the elastic modulus of LATP SSE ceramic always increases first with the increase of sintering temperature, and then decreases slightly after reaching the maximum value at 1000-1100°C. This can be attributed to the lower porosity at higher sintering temperature, since porosity reduces the elastic modulus of the material. As a comparison, the elastic modulus of the typical impurity phase $AlPO_4$ is about 77 GPa, which is one of the reasons for the different elastic modulus of LATP after sintering at different temperatures.
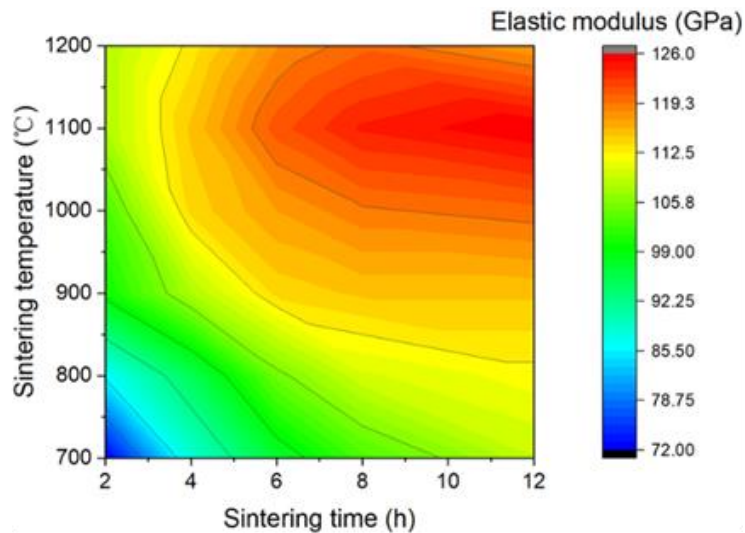
Figure. 4.66. 2D parametric maps of LATP SSE ceramic elastic modulus obtained from different sintering programs depend on LATP-600nm powder under 50mN loading.

When the loading is set to 50 mN, LATP SSE ceramics with an elastic modulus exceeding 115 GPa can be obtained after sintering at 900°C for 6-10h, at 1000°C for 4-10h, at 1100°C for 4-10h, and at 1200°C for 5-10h. The above sintering programs are the optimal selection interval for obtaining LATP SSE ceramics with high mechanical properties.

4.3.4. Selection of optimal sintering program for LATP

In summarizing all the experimental data obtained, key points should be highlighted:

1. For both 300nm and 600nm LATP powder the sintering temperature should be higher than 900°C to avoid the second phase of aluminum phosphate.

2. Focusing on the uniform microstructure (to minimize abnormal grain growth) and as a result the highest relative density of LATP ceramic, green body tablet made by LATP-600nm powder should be sintered between 850°C and 950°C for 6-10 h; green body tablet made by LATP-300nm powder, between 850°C and 900°C for 6-10 h, respectively.

4. Focusing on the highest total ionic conductivity, green body tablet made by LATP-600nm powder, should be treated at 900°C for 6-10 h; green body tablet made by LATP-300nm powder, should be treated at 800°C for 10 h or 850°C for 6 h.

5. Focusing on the highest elastic modulus, green body tablet made by LATP-600nm powder, should be treated at 900°C for 6-10h, at 1000°C for 4-10h, at 1100°C for 4-10h, and at 1200°C for 5-10h.

Based on our numerical simulations and experimental conclusions, we selected 600nm size LATP powder as the basic reference for all subsequent experiments, and selected hold 6 hours under 900°C as the standard sintering program. The core parameters under this selection are: relative density $94.5\pm0.5\%$, ionic conductivity $(4.8\pm0.5)\times10^{-4}$ S/cm, elastic modulus 114 ± 9 GPa under 50 mN stress loading.

4.4. Development of efficient approaches to densify ceramic materials of LATP

4.4.1. Fabrication of dense LATP ceramic SSE from bimodal powder precursor

4.4.1.1. Experimental data analysis
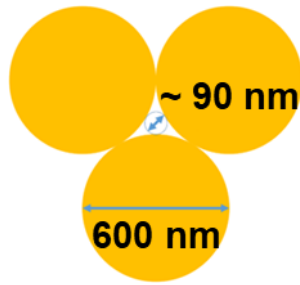
Figure. 4.67. Schematic illustration of pores in green body tablet made by LATP-600nm powder.

Based on discussions and conclusions in previous chapters, LATP-600nm powder was chosen as the benchmark system for subsequent tests. But based on the obvious geometric relationship, there are a large number of spaces with a size of at least 90nm between the particles of 600nm size in the green body tablet (Figure. 4.67). The corresponding density of green body will be shown later.
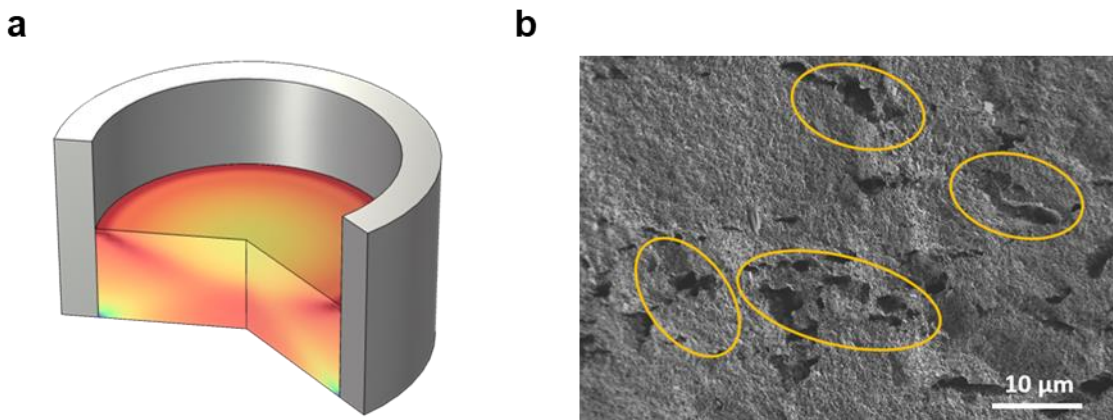
Figure. 4.68. (a) Stress distribution by numerical simulation in green body prepared by steel die. (b) Large defects in sintered LATP ceramic caused by stress.

Using a higher tableting pressure (>300 MPa) is an obvious way to increase the relative density of the green body tablet. However, based on the friction, the geometric relationship between the LATP particles, and the structure of the steel mold, excessive pressure will cause the uneven stress distribution in the green body affects the sintering process and produces large cracks (Figure. 4.68).
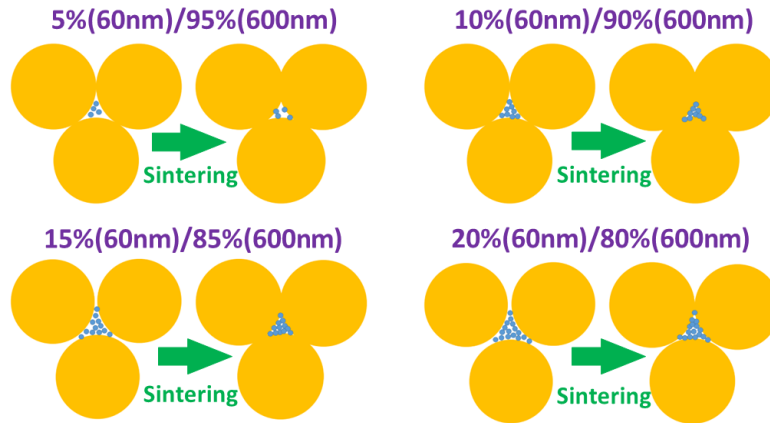
Figure. 4.69. Schematic illustration of fabricate dense LATP SSE ceramic from bimodal powder precursor.

Meanwhile, it seems very difficult to improve and achieve high ionic conductivity and high relative density at the same time simply by adjusting the sintering program. Therefore, a certain amount of LATP nanoparticles with the size of 60 nm was added into the matrix from the 600 nm size LATP. Powders with multimodal distribution of particle sizes are beneficial not only for sintering (Figure. 4.69) but, rather, to achieve higher green body density after uniaxial compaction in a steel die. In Table. 4.7, we showed relative density of 60 nm/600 nm LATP bimodal powder systems with mass ratios of 0%/100%, 5%/95%, 10%/90%, 15%/85%, 20%/80%, and 100%/0% after molding. With the introduction of 60nm particles, the relative density of green body gradually increased from 54.5±0.6% (only 600 nm particles were used) to 58.5±0.4% (the ratio of 60 nm particles was 15%), then gradually decreased and when use 60nm particle, the relative density of green body dropped down to 50.6±0.7%. It can be seen that adding an appropriate amount of small particle LATP can effectively improve the density of green body, but limited by the agglomeration effect between nanoparticles and the relative internal friction caused by an excessive relative surface area. Thus, an excessive admixture of small particles reduces the relative density of green body.

Table. 4.7. Relative density of 60 nm/600 nm LATP bimodal powder systems with weight fractions of 0%/100%, 5%/95%, 10%/90%, 15%/85%, 20%/80%, and 100%/0% after molding.

60 nm/600 nm samples	Relative density (%)
0%/100%	54.5±0.6
5%/95%	56.6±0.7
10%/90%	57.0±0.5
15%/85%	58.5±0.4
20%/80%	57.5±0.6
100%/0%	50.6±0.7
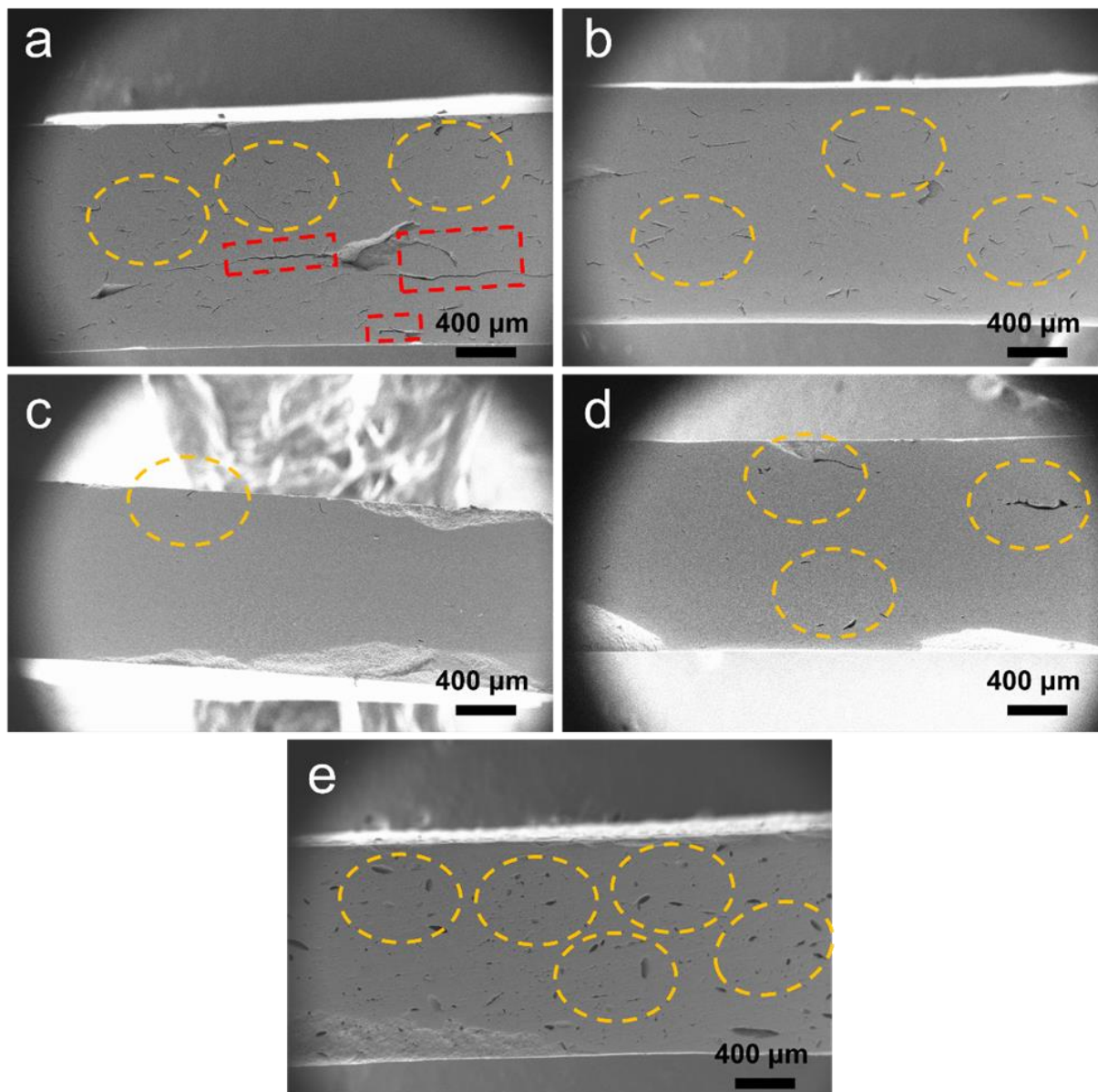
Figure. 4.70. Cross-section SEM images of LATP SSE ceramics from 60 nm/600 nm bimodal powders with the mass ratios of (a) 5%/95%, (b) 10%/90%, (c) 15%/85%, (d) 20%/80%, and (e) 100%/0% after sintering at 900°C for 6 hours. Defects from the sintering process are marked with yellow circles while the fractures surfaces from compaction are marked with red squares.

Figure. 4.70a-d show the cross-sectional SEM images of LATP SSE ceramics from 60nm/600nm composite powders with the ratio of 5%/95%, 10%/90%, 15%/85%, 20%/80%, which are sintered at 900°C for 6 h. The cracks in the areas marked with red rectangles mainly come from the fractures remaining in the green body due to the large friction force between the particles during the compaction (over pressing), and these cracks are retained in the solid-state electrolyte after sintering. The pores and defects in the areas marked with yellow circles are likely derived from the sintering process. With increasing the proportion of 60 nm powder from 5% to 15%, the cracks and porosity in the cross-section gradually decrease. However, when the proportion of 60 nm powder increases from 15% to 20%, the pores in the solid-state electrolyte begin to reappear, resulting in a decrease of density. By contrast, a significant number of pores and cracks obviously observed in the cross-section of pellets appears inside the solid electrolyte tablet with 100% 60 nm powder after sintering at 900°C for 6 h (Figure. 4.70e), which is caused by non-uniform grain growth of highly active nanoparticles during sintering.
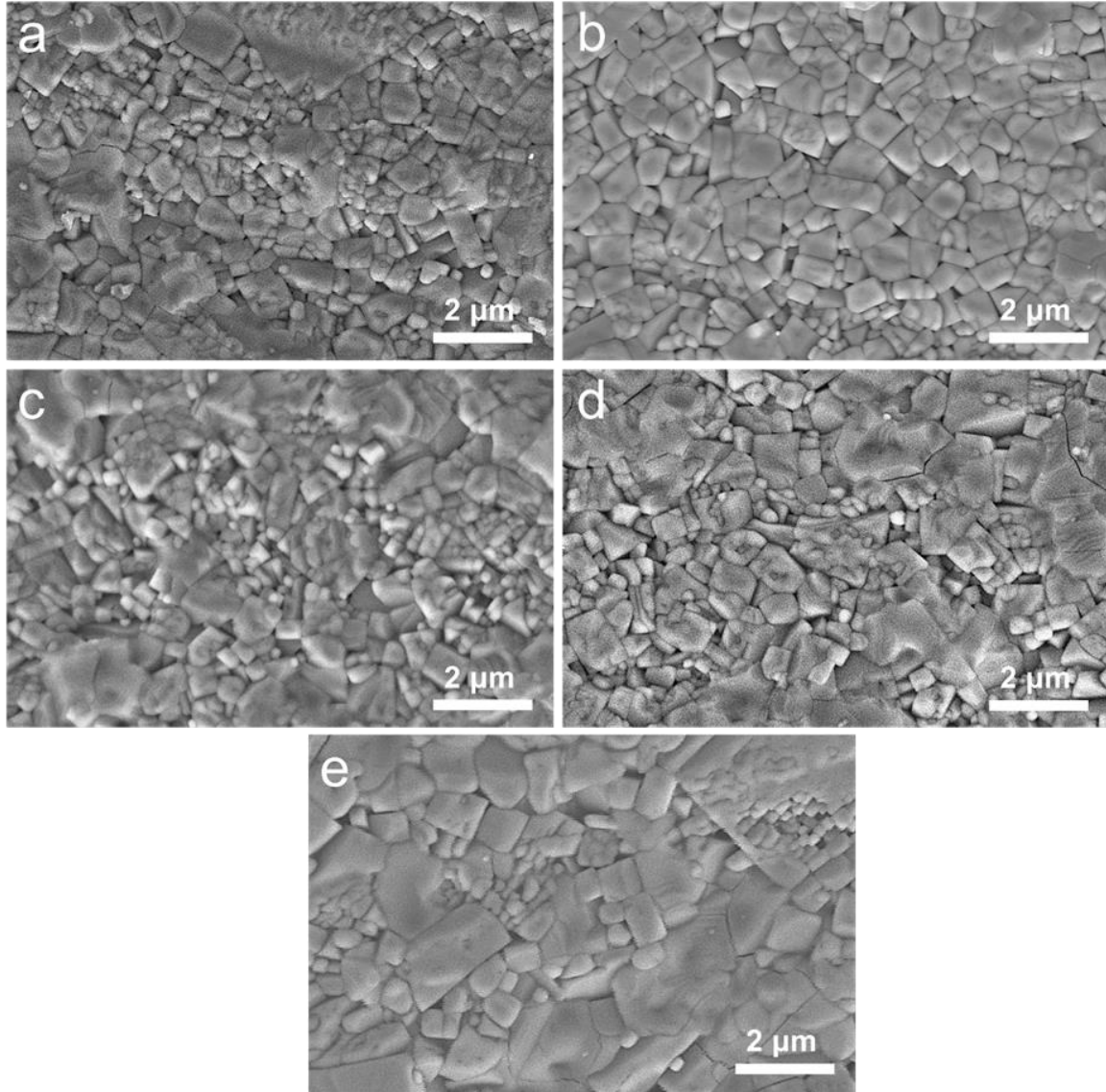
Figure. 4.71. SEM images of grain size distribution of LATP SSE ceramics from 60 nm/600 nm bimodal powder systems with the mass ratios of (a) 5%/95%, (b) 10%/90%, (c) 15%/85%, (d) 20%/80%, and (e) 100%/0% after sintering at 900°C for 6 h.

A comparison of micro-scale morphology of bimodal SSE is shown in Figure. 4.71. The SEM images display the morphology of 60 nm/600 nm LATP bimodal powder systems with different ratio of 5%/95%, 10%/90%, 15%/85%, 20%/80% and 100%/0% after sintering at 900°C for 6 h. For 60 nm/600 nm LATP powder with a ratio of 5%/95%, the insufficient amount of 60nm LATP particles can't completely fill the residual gaps after sintering of 600 nm LATP particles, resulting in obvious grain boundary defects and pores (Figure. 4.71a). Additionally, a part of the extra-large grains, presented inside the LATP SSE, is due to a high tendency to grain growth inherent to small particles.

For comparison, as the proportion of 60 nm LATP particles increases to 10%, the more regular shape of cubic grains appears in the solid-state electrolyte (Figure. 4.71b), while more and larger irregular grains and defects at grain boundaries are typical for SSEs with the ratios of 15%/85% and 20%/80%, of which the defects and pores are derived from the grain growth caused by sintering the excessive aggregates of 60 nm LATP. As shown in Figure. 4.71e, more obvious small particle agglomerates are observed by fusing with each other and overgrown through the sintering process.

Table. 4.8. Statistics of particle size (μm) distribution of bimodal system LATP after sintering

60 nm/600 nm samples	D_{10} (μm)	D_{50} (μm)	D_{90} (μm)	Average size (μm)
5%/95%	0.27	0.52	0.96	0.60
10%/90%	0.26	0.56	0.83	0.59
15%/85%	0.24	0.51	1.08	0.59
20%/80%	0.22	0.42	0.90	0.53
100%/0%	0.18	0.50	1.03	0.57
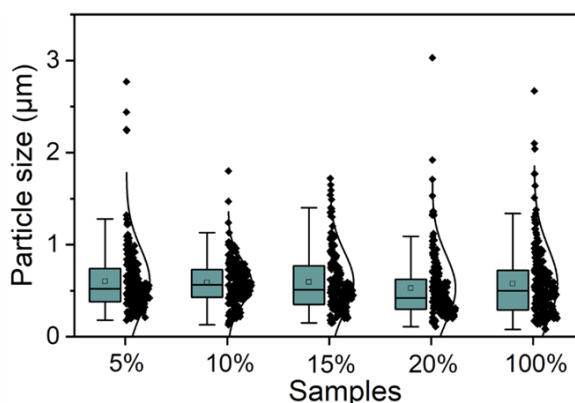
Figure. 4.72. Statistical diagram of grain size distribution of LATP SSE ceramic from 60 nm/600 nm composite powder systems with the mass ratios of 5%/95%, 10%/90%, 15%/85%, 20%/80%, and 100%/0% after sintering at 900°C for 6 hours.

Moreover, the size distribution of grains inside the electro-ceramic with ratio of 10%/90% is more uniform with the average particle size of 600 nm than with the ratio of 5%/95%, 15%/85%, 20%/80% and 100%/0% (Figure. 4.72). Meanwhile, the LATP SSE tablet with the ratio of 100%/0% after sintering exhibits lower density, and the average size of grains with about 10-fold changes than that before sintering, which is caused by the sintering of highly active small particles during sintering along

with fundamental feature of LATP consisted in of high mobility of grain boundaries compared to pores. The results indicate that the sintering procedure at 900°C for 6 h is not optimal for the tablet containing only 60 nm LATP particles. Extensive coarsening of grains and constrained sintering of the composite with rigid inclusions of secondary phases cause sintering stress resulting in low relative density. In Table. 4.8 statistics of particle size distribution of bimodal system LATP after sintering is given.
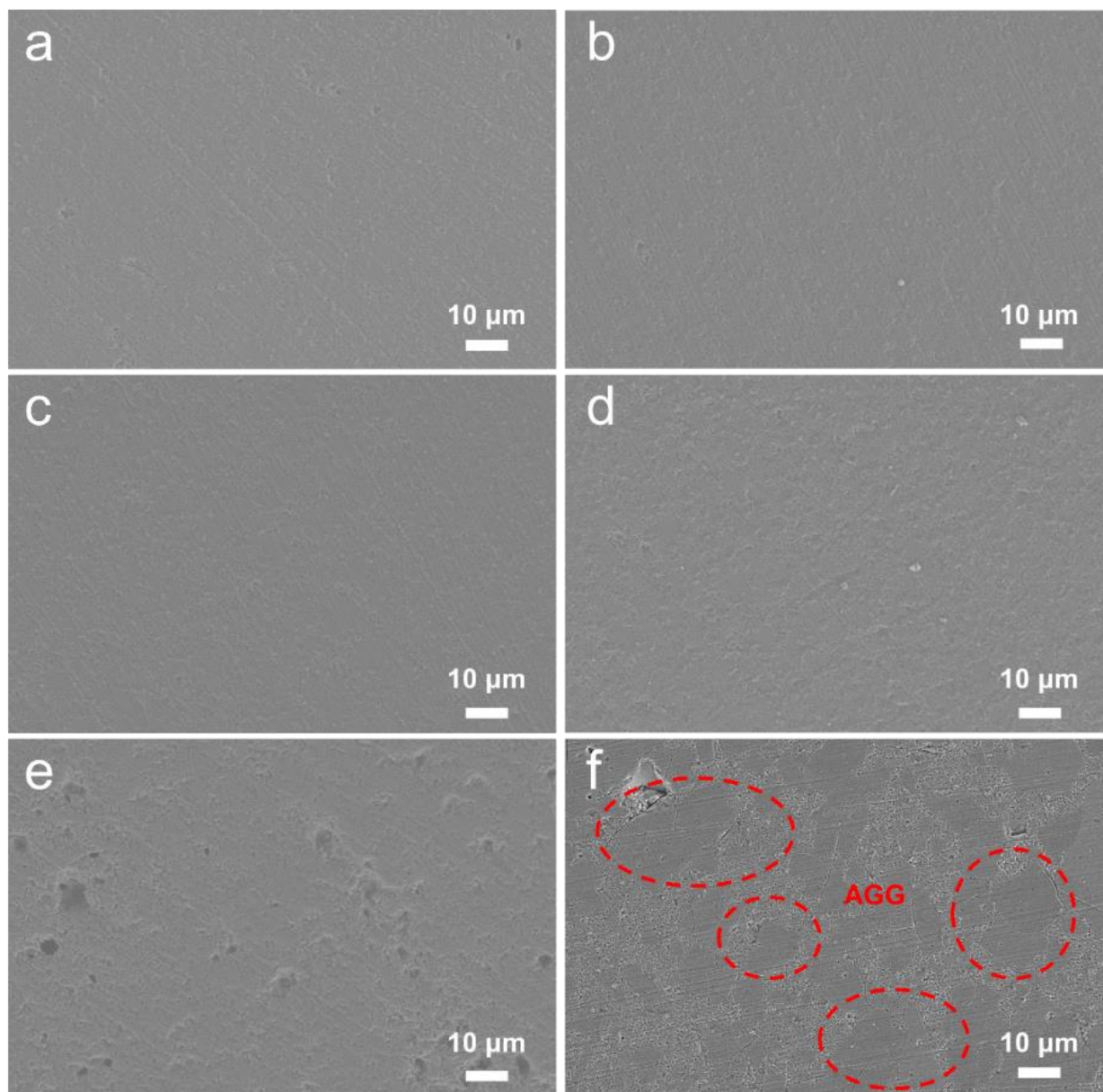
Figure. 4.73. a-e) SEM images of grain size distribution of LATP SSE ceramics from 60 nm/600 nm bimodal powder systems with the weight fractions of (a) 5%/95%, (b) 10%/90%, (c) 15%/85%, (d) 20%/80%, and (e) 100%/0% after sintering at 900°C for 6 h. (f) LATP SSE ceramic with typical AGG behavior made by LATP-600nm powder and sintered at 950°C for 6h.

Figure. 4.73a-e showed SEM images of grain size distribution of LATP SSE ceramics from 60 nm/600 nm bimodal powder systems with the mass ratios of 5%/95%, 10%/90%, 15%/85%, 20%/80%, and 100%/0% after sintering at 900°C for 6 h. Compared with the LATP SSE ceramic based on only LATP-600nm powder in Figure. 4.73f, it is very obvious that with the addition of 60nm size LATP nanoparticles, the AGG behavior is significantly suppressed, almost no obvious oversized grains (> 10 μm) appear.
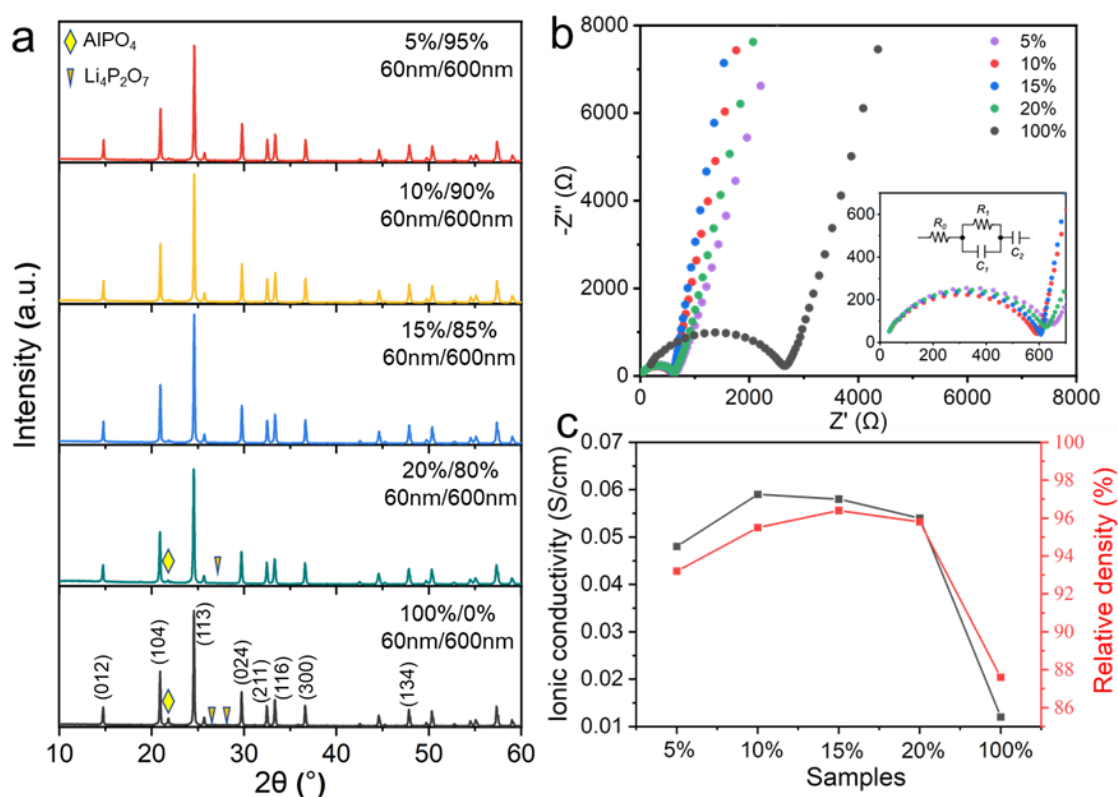
Figure. 4.74. (a) XRD, (b) Nyquist plots, (c) ionic conductivity and relative density of LATP SSE ceramics from 60 nm/600 nm bimodal powder systems with weight fractions of 5%/95%, 10%/90%, 15%/85%, 20%/80%, and 100%/0% after sintering at 900°C for 6 h.

Table. 4.9. Ionic conductivity (S/cm) and relative density (%) of 60 nm/600 nm LATP bimodal powders with mass ratios of 5%/95%, 10%/90%, 15%/85%, 20%/80%, and 100%/0% after sintering at 900°C for 6 h.

60 nm/600 nm systems	Bulk ionic conductivity	Boundary ionic conductivity	Total ionic conductivity	Relative density %
0%/100%	$(3.9\pm0.2)\times10^{-3}$	$(5.3\pm0.5)\times10^{-4}$	$(4.6\pm0.4)\times10^{-4}$	94 ± 1

5%/95%	$(3.7\pm0.2)\times10^{-3}$	$(5.5\pm0.5)\times10^{-4}$	$(4.8\pm0.5)\times10^{-4}$	93 ± 1
10%/90%	$(3.6\pm0.2)\times10^{-3}$	$(7.1\pm0.3)\times10^{-4}$	$(5.9\pm0.2)\times10^{-4}$	96 ± 1
15%/85%	$(3.4\pm0.2)\times10^{-3}$	$(7\pm0.3)\times10^{-4}$	$(5.9\pm0.3)\times10^{-4}$	96.4 ± 0.3
20%/80%	$(3.4\pm0.2)\times10^{-3}$	$(6.4\pm0.2)\times10^{-4}$	$(5.4\pm0.2)\times10^{-4}$	95.8 ± 0.4
100%/0%	$(1.6\pm0.1)\times10^{-3}$	$(1.3\pm0.1)\times10^{-4}$	$(1.2\pm0.2)\times10^{-4}$	87.6 ± 0.3

Figure. 4.74a show the XRD of LATP SSE ceramics from 60 nm/600 nm bimodal powder systems with mass ratios of 5%/95%, 10%/90%, 15%/85%, 20%/80%, and 100%/0% after sintering at 900°C for 6 hours, of which the secondary phases of aluminum phosphate and lithium pyrophosphate appear in the SSE tablets with the ratio of 20%/80% and 100%/0% after sintering and its corresponding content increases with the increasing proportion of 60 nm LATP particles. Appearance of the secondary phases was also indirectly demonstrated through the morphology changes for these samples and agrees with the SEM data. With the help of software "NOVA 2.1", the complex impedance curves of SSE tablets are shown in Figure. 4.74b. All plots have regular semicircle shapes. Figure 4.74c and Table. 4.9, SSE tablets with the ratios of 10%/90% and 15%/85% show the much higher total ionic conductivity than that with other ratios, which are $(5.9\pm0.2)\times10^{-4}$ S/cm and $(5.9\pm0.3)\times10^{-4}$ S/cm, respectively, and nearly 30% and 390% higher than only 600 nm powder $(4.6\pm0.3)\times10^{-4}$ S/cm and 60 nm powder $(1.2\pm0.2)\times10^{-4}$ S/cm under the same sintering conditions (Table. 4.9). Decrease in bulk ionic conductivity is mainly due to the change of crystal structure (evaporation of Li and precipitation of $AlPO_4$), and the degree of the drop of this value directly depends on the amount of admixed 60 nm particles. The grain boundary ionic conductivity is mainly affected by the relative density and the enrichment with the secondary phase at the grain boundary. According to the results shown, the boundary ionic conductivity can be predicted to rise first and then decrease, and reach a minimum value for 60nm system. The solid-state electrolyte obtained from bimodal powders containing 60 nm particles admixed to 600 nm particles with the ratio of 10-15%/90-85% displayed best key properties of SSE. Thus, the densities of LATP tablets with the ratio of 10%/90% and 15%/85% are higher (96 ± 1 and 96.4 ± 0.3) among all the solid-state electrolyte with other ratios. This is consistent with the SEM observation how the grains are interconnected and how pores are distributed in SSE tablets. At the same time, we compared our results with published data. Detailed information is presented in Table. 4.10. All earlier works are devoted to the utilizing additive based on another chemical compound in NASICON ceramic. In our view, the weak point of this approach is significant influence of the second

phase on the decrease of ionic conductivity of the grain boundary and the overall strength of the SSE. The approach developed in our experiment consists in regulating key SSE parameters from the perspective of chemical design without using artificial foreign phase additives. In the same time our SSE demonstrates a high value of ionic conductivity and relative density at room temperature competitive to earlier reported electro-ceramic compacted by utilizing the secondary phase. Based on the above results, these values can be efficiently improved by the proposed bimodal ceramic system, which is very promising for the solid-state battery. In addition, it could be easily transferred to the fabrication of the other SSEs.

Table. 4.10. Comparison with published data.

LATP system	Additive	Sintering method	Sintering temperature	Ionic Conductivity (S/cm)	Relative density (%)
$Li_{1.3}Al_{0.3}Ti_{1.7}(PO_4)_3$	None	Normal	1100°C	1.83×10^{-4}	92.8 ± 0.6
$Li_{1.3}Al_{0.3}Ti_{1.7}(PO_4)_3$	None	Normal	1080°C	3.8×10^{-4}	~90
$Li_{1.3}Al_{0.3}Ti_{1.7}(PO_4)_3$	None	Normal	900°C	$(5.9\pm0.2)\times10^{-4}$	96±1% (Our)
$Li_{1.5}Al_{0.5}Ti_{1.5}(PO_4)_3$	None	Normal	800°C	5.1×10^{-4}	~97
$Li_{1.5}Al_{0.5}Ti_{1.5}(PO_4)_3$	$Li_2B_4O_7$	Normal	900°C	6.4×10^{-4}	~95
$Li_{1.3}Al_{0.3}Ti_{1.7}(PO_4)_3$	$LiBF_4$	Normal	800°C	8.5×10^{-4}	~98
$Li_{1.3}Al_{0.3}Ti_{1.7}(PO_4)_3$	Li_2CO_3	Normal	875°C	6.5×10^{-4}	95.3
$Li_{1.3}Al_{0.3}Ti_{1.7}(PO_4)_3$	Li_3PO_4	Normal	800°C	2.0×10^{-4}	None
$Li_{1.3}Al_{0.3}Ti_{1.7}(PO_4)_3$	Li_2CO_3	Normal	850°C	3.0×10^{-4}	~95
$Li_{1.3}Al_{0.3}Ti_{1.7}(PO_4)_3$	$Li_2O+B_2O_3$	Normal	800°C	1.9×10^{-4}	~92.5
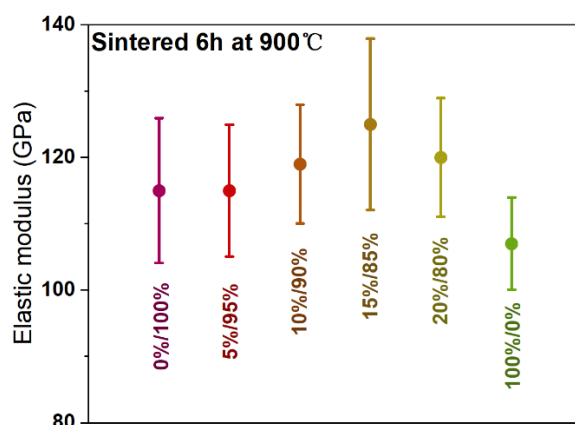
Figure. 4.75. Elastic modulus of LATP SSE ceramics from 60 nm/600 nm bimodal powder systems with mass ratios of 5%/95%, 10%/90%, 15%/85%, 20%/80%, and 100%/0% after sintering at 900°C for 6 h under 50 mN stress loading.

Table. 4.11. Values of LATP SSE ceramics elastic modulus (GPa) obtained from 60 nm/600 nm bimodal powder systems with mass ratios of 5%/95%, 10%/90%, 15%/85%, 20%/80%, and 100%/0% after sintering at 900°C for 6 h under 50 mN stress loading.

Samples	0%/100%	5%/95%	10%/90%	15%/85%	20%/80%	100%/0%
Elastic modulus (GPa)	115±11	115±10	119±9	125±13	120±9	107±7

It can be seen that with the introduction of 60nm LATP nanoparticles, the elastic modulus of LATP SSE ceramics is greater than that of the 0%/100% standard sample (115±11 GPa), showing a trend of first increasing and then slightly decreasing. The maximum value comes from the 15%/85% bimodal powder system after sintering at 900°C for 6 h, the elastic modulus of this sample is as high as 125±13 GPa, and the 10%/90% and 20%/80% also reach 119±9 GP and 120±9 GPa, respectively. These results match the SEM of the microstructure of LATP SSE ceramic and the relative density shown before.

4.4.1.2. Chapter conclusions

In summary, LATP SSE ceramic derived from bimodal powders containing 60 nm and 600 nm particles, have been successfully prepared by one-step isothermal sintering at 900°C for 6 h. SSE ceramic obtained from bimodal powders containing 60 nm particles admixed to 600 nm particles with the ratio of 10%/90% displays a high ionic conductivity of $(5.9\pm0.2)\times10^{-4}$ S/cm and relative density of 96±1% at room temperature. There is no AGG behavior in all bimodal SSE ceramic, and when the addition of nanoparticles is 10-20%, the elastic modulus is as high as ~ 120-125 GPa.

4.4.2. Fabrication of dense LATP SSE ceramic with LATP glass additive

In the bimodal powder system, the biggest challenge is that the optimal sintering temperature of 600nm size LATP powder does not match the optimal sintering temperature of 60nm size LATP powder. In the previous results, amount of 60nm size LATP powder was controlled and combined with long-term wet ball milling to mix the bimodal powder system, try to prevent the 60nm powder from

agglomerating in the green body tablet, thereby avoids leaving extra pores in the LATP SSE ceramic due to the lower sintering temperature of the nanoparticles.
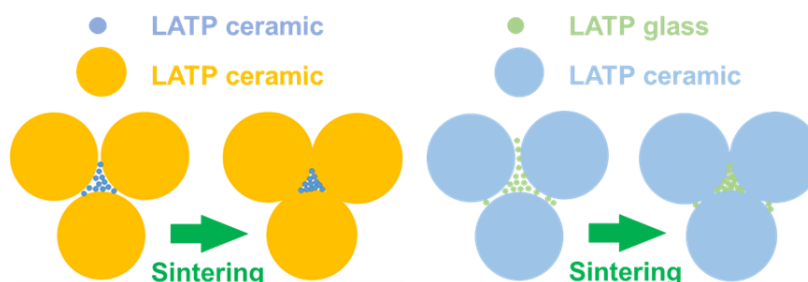
Figure. 4.76. Schematic illustration of the difference between a) bimodal powder system with LATP ceramic nanoparticle and b) composite powder system with LATP glass nanoparticle.

Based on the well-known facts, the amorphous LATP glass will undergo devitrification behavior during the heating process. With the continuation of the holding time, the LATP glass will gradually transform into LATP ceramics. Therefore, the nano-sized LATP powder was replaced in the bimodal system with LATP glass powder to further improve the relative density and other key indicators of LATP SSE.

4.4.2.1. Experimental data analysis of samples using one-step sintering program

To improve the relative density and ionic conductivity of SSE ceramic, a certain amount of 60nm LATP glass powder was mixed with 600nm LATP, of which the composited powder with bimodal distribution results to the increase of the green body density after uniaxial compaction in a steel die. Therefore, the glass/ceramic LATP composite powder systems have been prepared with weight fractions of 0%/100%, 1%/99%, 3%/97%, 5%/95%, 10%/90%, 15%/85% and 20%/80%. With the addition of LATP glass powder with an average particle size of 60nm, the relative density of the green tablets increases from ~ 54.5±0.6% (made by only 600nm LATP powder) to ~ 57.9±0.4% (the addition of glass powder is 5%), and then the density dropped to ~ 53.8±0.9% (the addition of glass powder is 20%), which was lower than that without LATP glass powder (Table. 4.12).

Table. 4.12. Relative density of glass/ceramic LATP composite powder with weight fractions of 0%/100%, 1%/99%, 3%/97%, 5%/95%, 10%/90%, 15%/85% and 20%/80% after molding.

Glass/Ceramic samples	Relative density (%)
0%/100%	54.5±0.6
1%/99%	55.9±0.8
3%/97%	56.4±0.5
5%/95%	57.4±0.5
10%/90%	57.9±0.4
15%/85%	55.3±0.5
20%/80%	53.8±0.9
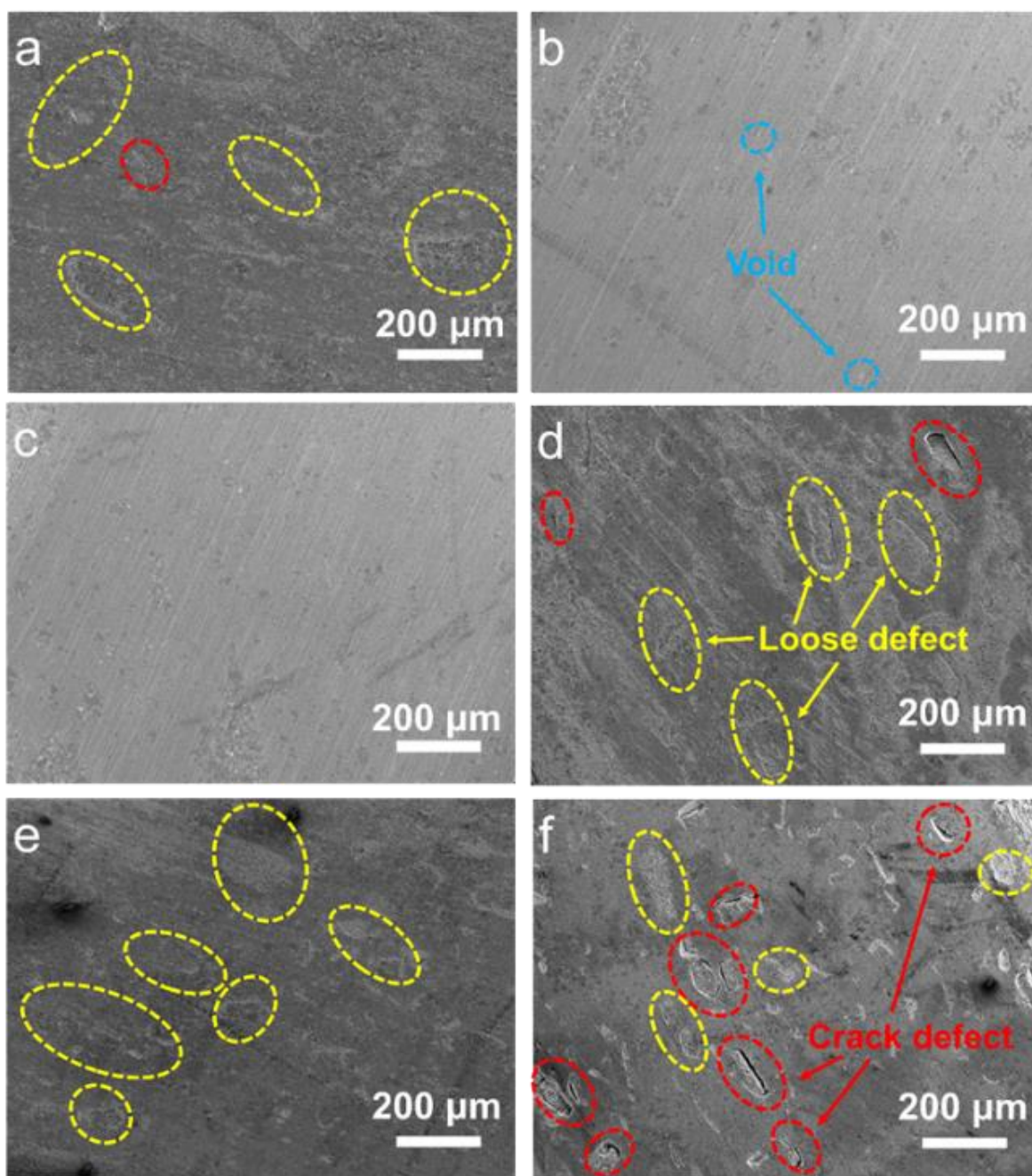
Figure. 4.77. Cross-section SEM images of LATP SSE ceramic from glass/ceramic composite powder systems with the mass ratios of 1%/99%, 3%/97%, 5%/95%, 10%/90%, 15%/85% and 20%/80% after sintering at 900°C for 6 hours, marked by 200μm scale. Crack defects (from the sintering process) are marked with red circles. Voids and high porosity areas are marked with blue and yellow circles, respectively.

Subsequently, the SSE green body tablets are sintered at 900°C for 6 h, and several obvious micro-scale coarse defected areas marked by yellow circles and cracks marked by red circles can be detected in the sintered LATP SSE with mass ratio of 20%/80% compared to other ratios (Figure. 4.77), which is derived from the sintering process.
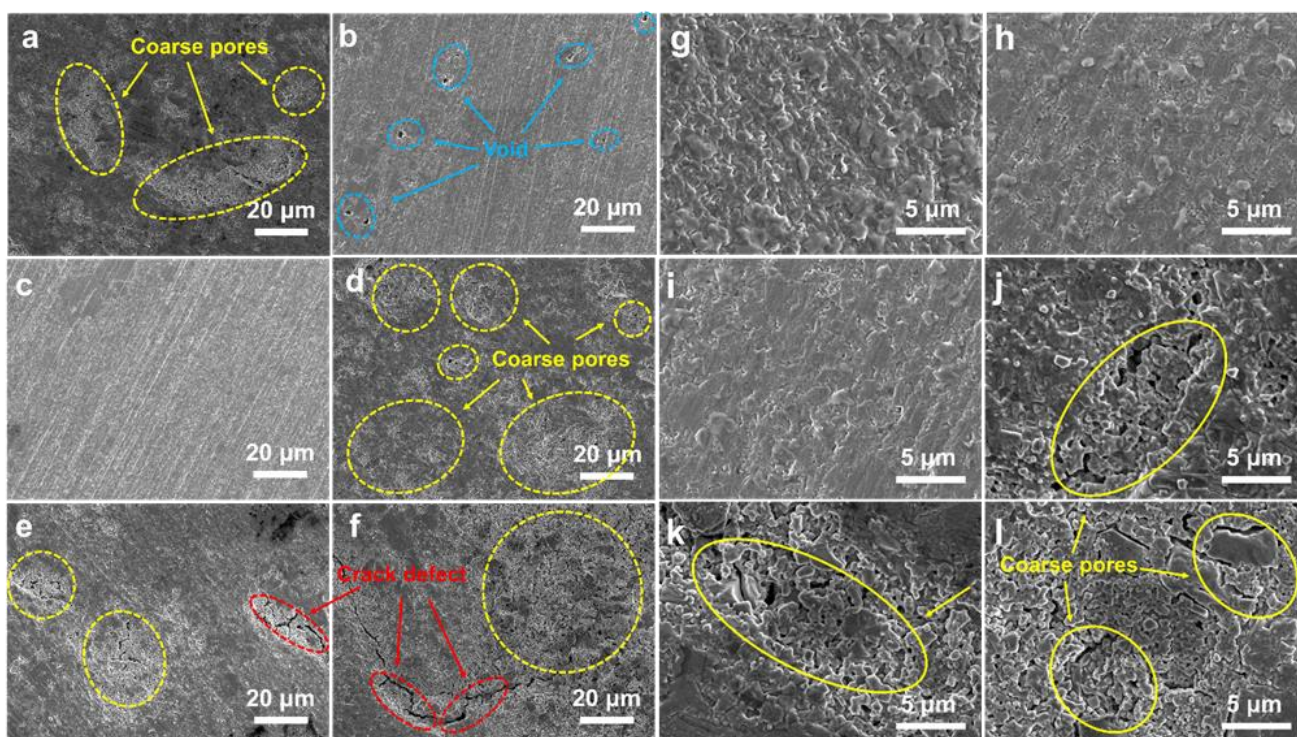
Figure. 4.78. Cross-section SEM images of LATP SSE ceramic from glass/ceramic composite powder systems with the mass ratios of 1%/99%, 3%/97%, 5%/95%, 10%/90%, 15%/85% and 20%/80% after sintering at 900°C for 6 hours, marked by 20μm scale (a-f) and 5μm scale (g-l), respectively. Crack defects (from the sintering process) are marked with red circles. Voids and high porosity areas are marked with blue and yellow circles, respectively.

Moreover, the small-scale SEM image shows a high-quality SSE ceramic without no obvious large-sized voids and crack defects (Figure. 4.78a-f) when the proportion of glass powder is up to 5%. As the fraction of glass powder continues to increase from 10% to 20%, micro-crack defects and coarse defects inside the SSE increase during the sintering process. For other ratios, some micro-scale areas

of high porosity appear inside the SSEs without obvious crack defects. The SSE ceramic with ratio of 5%/95% displays relatively dense morphology among others SEM images with scale bar of 5μm, while many coarse pores and crack defects appears in the SSE ceramic when the addition amount of glass powder exceeds 5% (Figure. 4.78g-l). This phenomenon can be explained by the relatively fast heating rate, so that the devitrification process of the glass powder has not yet fully proceeded while the powder has already entered the sintering process. When the glass powder is added less than 5%, the stress caused by the devitrification of the glass powder and its volume change during crystallization is less than the impact of the sintering stress in the glass/ceramic composite, thus a relatively dense solid electrolyte with almost no cracks and coarse pores can be obtained after sintering. When the amount of glass powder is 5-10%, the phase transition stress of glass powder due to crystallization and the sintering stress of powder act together to produce micron-sized cracks throughout the SSEs, and the coarse pore caused by excessive glass powder can be further reduced with the relative density of SSE tablets. When the amount of glass powder is over 10%, the devitrification process seriously affects the sintering of powder, and formation of crack defects and the coarse pores can be found everywhere in the SSE tablets. It also can be clearly observed that when the glass powder is introduced in an amount not exceeding 5%, the arrangement and contacts of the grains are better. As the amount of glass powder continues to increase, the quality of the SSE tablet deteriorates, and the appearance of many coarse pores and poor grain connections directly affect and reduce the relative density and ionic conductivity of the SSE tablets.
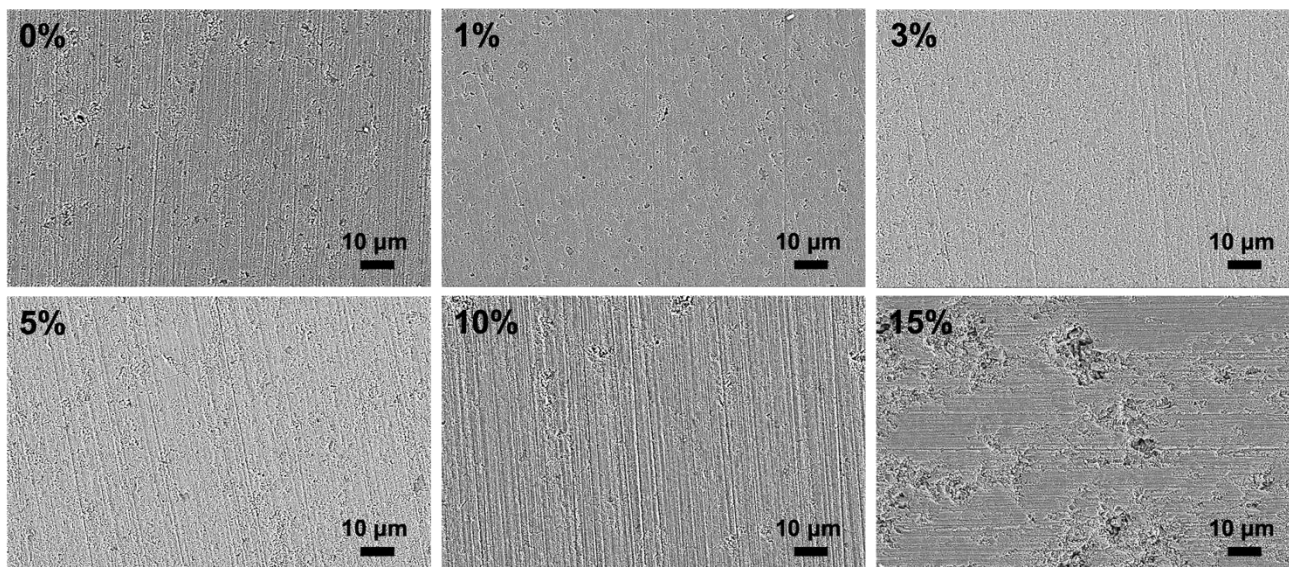
Figure. 4.79. Cross-section SEM images of LATP SSE ceramic from glass/ceramic composite powder systems with different weight fractions after sintering at 900°C for 6 hours.

Here we choose a relatively flat area with few defects to count the average grain size of different composite powder systems with glass additive after sintering and observe the AGG behavior. Obviously, with the increase of the relative content of the glass additive, the average grain size after sintering is slightly larger than that of the only LATP-600nm benchmark system. When 1% LATP glass is added to the composition, the number of defects decreases, the growth of abnormal grains stops, and controlled normal grain growth (NGG) proceeds. With the addition of 3-5% LATP glass, the densest inter-grain contact is observed in the samples and there are practically no defects. With the addition of >5% LATP glass, the number of defects increases and the intergranular contact deteriorates. However, abnormal grain growth (AGG) is still not observed in this case. With the addition of 10% LATP glass, the number of defects increases even more. The addition of 15% LATP glass leads to the formation of many defects and many nanoparticles with a size of about 100 nm formed between large grains depend on the crystallization of the LATP glass, which contribute to the loss of contact between grain. For samples with a ratio of more than 20% LATP glass, it is almost impossible to find a relatively complete area, and large cracks and small defects are everywhere, so we do not show the corresponding SEM here.

The addition of LATP glass to the initial composition ensures controlled normal grain growth (NGG) during sintering and obtaining particles of similar size, which is since the process of crystallization of glass occupying the space between the initial grains takes time and slows down the mass transfer process. However, the excess content of the LATP glass (more than 5 wt.%) leads to its crystallization between the initial grains with the formation of many nanoparticles, which destroy the overall structure due to the anisotropy of their formation. The addition of 3-5% LATP glass powder is the most optimal and provides the most effective contact between grains, while reducing the number of defects.
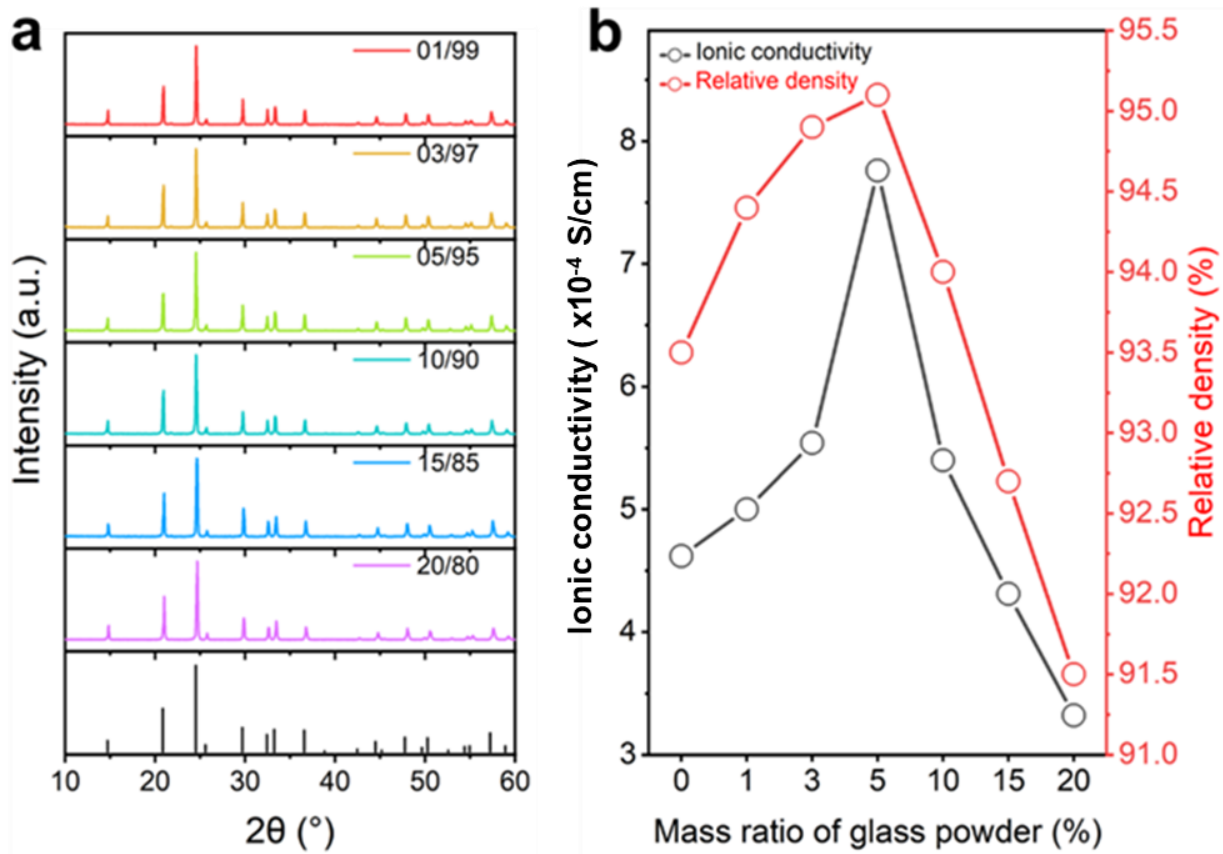
Figure. 4.80. (a) XRD patterns with $LiTi_2(PO_4)_3$ standard card (black color) and (b) corresponding ionic conductivity and density of LATP SSE ceramics from glass/ceramic composite powder systems with the weight fractions of 1%/99%, 3%/97%, 5%/95%, 10%/90%, 15%/85% and 20%/80%, after sintering at 900°C for 6 hours.
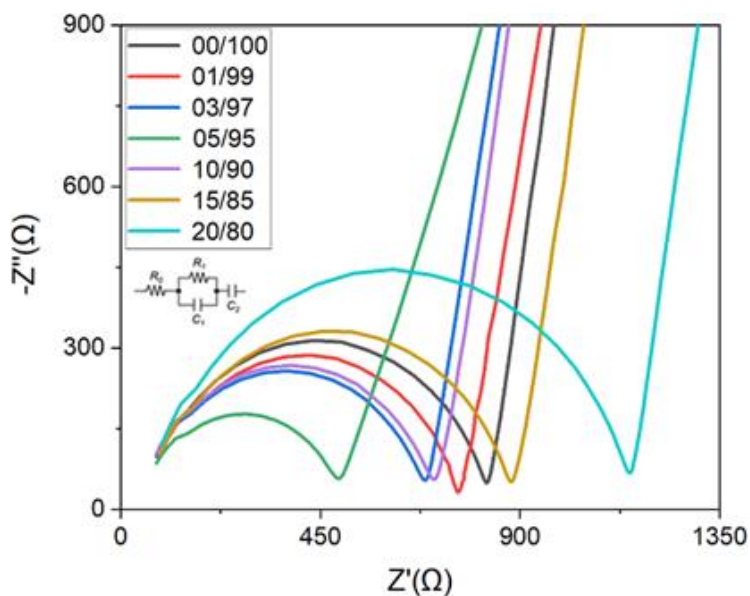
Figure. 4.81. Nyquist plots of LATP SSE ceramics from glass/ceramic composite powder systems with mass ratios of 0%/100%, 1%/99%, 3%/97%, 5%/95%, 10%/90%, 15%/85% and 20%/80% after sintering at 900°C for 6 hours.

Table. 4.13. Relative density and ionic conductivity of LATP SSE ceramics from glass/ceramic composite powder systems with weight fractions of 0%/100%, 1%/99%, 3%/97%, 5%/95%, 10%/90%, 15%/85% and 20%/80% after sintering at 900°C for 6 hours.

Glass/Ceramics	Total ionic conductivity (S/cm)	Relative density (%)
0%/100%	$(4.6\pm0.4)\times10^{-4}$	94 ± 1
1%/99%	$(5.0\pm0.2)\times10^{-4}$	94.4 ± 0.9
3%/97%	$(5.5\pm0.2)\times10^{-4}$	94.9 ± 0.5
5%/95%	$(7.8\pm0.2)\times10^{-4}$	95.1 ± 0.3
10%/90%	$(5.4\pm0.3)\times10^{-4}$	94.0 ± 0.6
15%/85%	$(4.3\pm0.4)\times10^{-4}$	93 ± 1
20%/80%	$(3.3\pm0.6)\times10^{-4}$	92 ± 1

In order to investigate the structure of the LATP SSE tablets during the sintering, X-Ray powder diffraction (XRD) was employed in the 2θ ranging from 10° to 60° with a speed of 5°/min. As shown in Figure. 4.80a, no glass and foreign phases appear inside SSEs after sintering at 900°C for 6 hours, and all the peaks of each LATP SSE ceramics match with that of $LiTi_2(PO_4)_3$. Additionally, LATP SSE ceramic exhibits the highest ionic and relative density of $(7.8\pm0.2)\times10^{-4}$ S/cm and $95.1\pm0.3\%$ when the amount of glass powder is 5% (Figure. 4.80b, Figure. 4.81 and Table. 4.13), which is only based on the program of sintering at 900°C for 6h.

4.4.2.2. Study on thermal behavior of LATP glass

To optimize consolidation processing to produce dense, highly ionic conductive SSE, thermal behavior of LATP glass were analyzed.
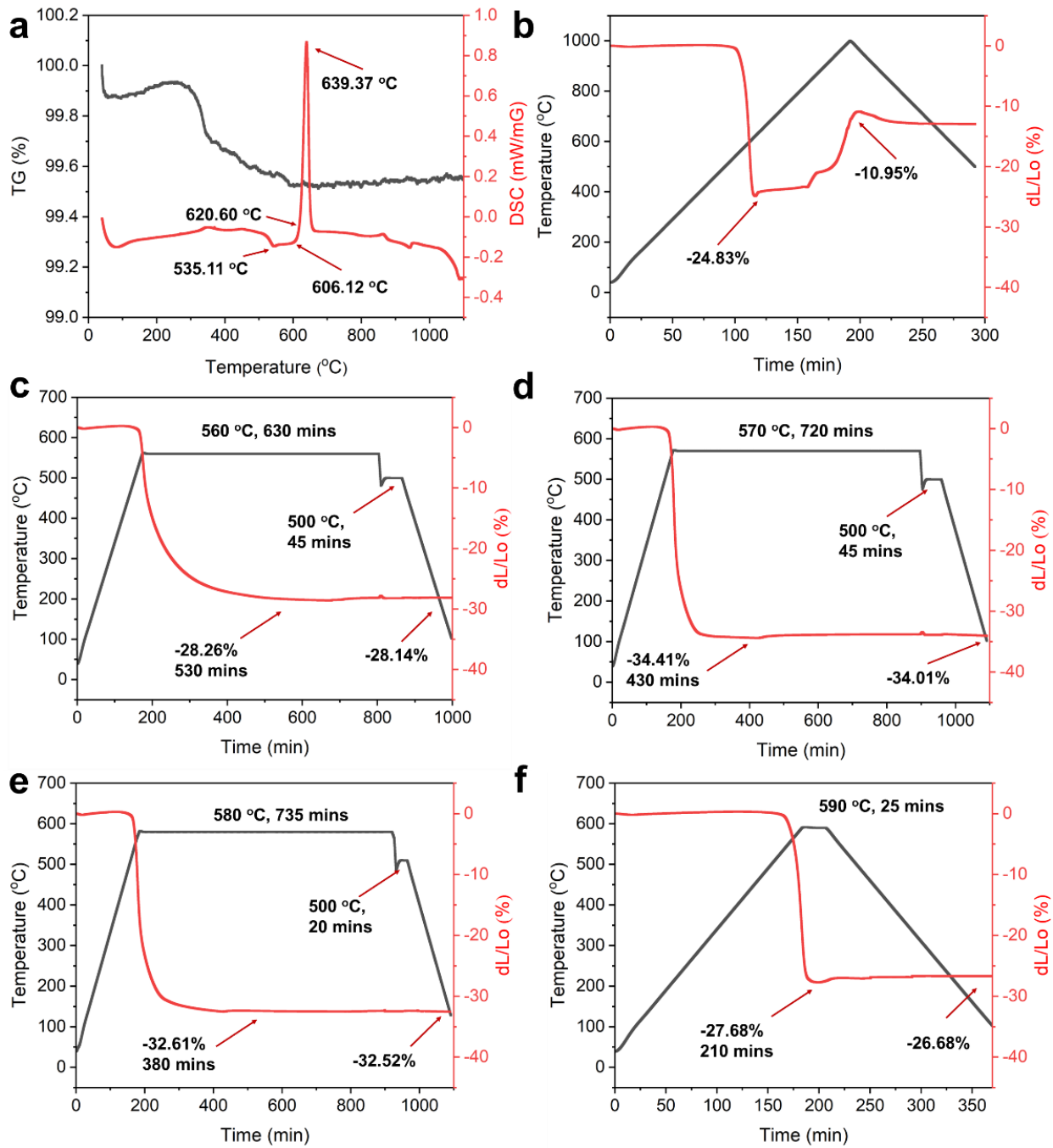
Figure. 4.82. (a) TGA-DSC curves of the LATP glass, (b-f) dilatometry analyzes of LATP glass under different heating programs (heat up to 1000°C at a speed of 5°C/min, and then cool at a uniform speed; heat up to 560°C, 570°C, 580°C, and 590°C at a speed of 3°C/min, and keep a short residence time hold at 500°C then cool down at a uniform speed, respectively).
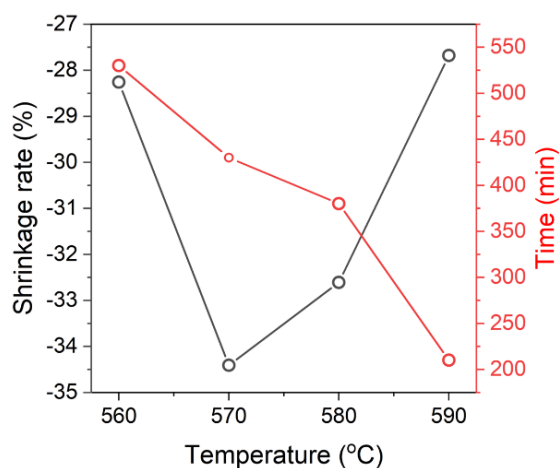
Figure. 4.83. The corresponding shrinkage rate and time of the LATP glass green body tablet at different heating programs.

As shown in Figure. 4.82a, the TGA-DSC curves of pure LATP glass powder show a small step at 535°C, which is assigned to the glass heating transition temperature (T_g). The predominant exothermic peak at 639°C is corresponding to the crystallization of the glassy phase (T_c). Some crystallization process occurs even before T_c, while the glassy matrix quickly crystallizes once the temperature reaches to T_c. Moreover, only one sharp peak at 639.4°C is observed in the TGA-DSC curves of LATP glass powder and almost no weight changes during the heating process of the glass powder, indicating the formation of a single crystalline phase. Figure. 4.82b-f shows in-situ checking processes of volume change of LATP glass during heating. Subsequently, the LATP tablet made by 100% glass powder was heated to 1000°C at a speed of 5°C/min, and then cool at a uniform speed (Figure. 4.82b), of which a rapid densification process (the beginning of viscous flow) occurs at 535°C inside the green tablet of glass powder, and corresponds to a shrinkage of -5%, which is observed from dilatometer. The maximum shrinkage ratio under this heating program is -24.83% at about 570°C, and then the shrinkage ratio begins to decrease with a further increase in temperature, which is associated with spontaneous nucleation and anisotropic growth of nanocrystals inside the LATP glass. Due to the anisotropic nucleation and growth of nanograins inside the sample, stresses are generated that break the initial compaction.

The results indicate that shrinkage of the LATP glass green body tablet during heating program mainly depends on the softening and bonding process of the glass powder. Since the maximum shrinkage occurs around 570°C, four different heating programs, such as 560°C, 570°C, 580°C and

590°C for holding 343 mins, 240 mins, 186 mins and 20 mins (without the heating time), were employed to explore the densification time and shrinkage of LATP glass green body tablets. As shown in Figure. 4.82c-g, the LATP glass tablet treated at 570°C for holding 240 mins display the highest shrinkage rate of -34.41% than that with other heating programs (-28.26%, -32.61% and -27.68%), which means that the program of holding 570 °C for 6 h is enough to realize the maximum densification process of green tablets. The results can be explained that the higher holding temperature accelerates the softening of the glass powder and the connection process between ceramic particles through glass component, while the potential crystallization process could impede the further densification of the SSE tablets.

4.4.2.3. Experimental data analysis of samples using two-steps sintering program

Consistent with the experiments in the previous chapters, we prepared LATP green body tablets from glass/ceramic composite powder systems with mass ratios of 0%/100%, 1%/99%, 3%/97%, 5%/95%, 10%/90%, 15%/85% and 20%/80%, and measured the relative density after preheating at 560-590°C for 6 hours to verify our conjecture.

Table. 4.14. The relative density of LATP green body tablets from glass/ceramic composite powder systems with mass ratios of 0%/100%, 1%/99%, 3%/97%, 5%/95%, 10%/90%, 15%/85% and 20%/80% after heating at 560°C, 570°C, 580°C, 590°C for 6 hours, respectively.

Glass/Ceramic samples	Green tablet density (%)	After heat at 560°C for 6h	After heat at 570°C for 6h	After heat at 580°C for 6h	After heat at 590°C for 6h
0%/100%	54.5±0.6	54.6±0.8	54.7±0.7	54.8±0.6	54.7±0.7
1%/99%	55.9±0.8	56.1±0.6	56.3±0.5	56.4±0.6	56.6±0.7
3%/97%	56.4±0.5	56.8±0.6	56.9±0.7	57.0±0.8	57.2±0.9
5%/95%	57.4±0.5	58.2±0.8	58.4±0.6	58.3±0.7	58.3±0.8
10%/90%	57.9±0.4	58.6±0.7	58.6±0.9	58.5±0.8	58.8±0.7
15%/85%	55.3±0.5	59.1±0.9	59±1	59.6±0.9	60±1
20%/80%	53.8±0.9	60±1	60±1	60±2	60±2

	560℃	570℃	580℃	590℃
0%	+0.1%	+0.2%	+0.3%	+0.2%
1%	+0.2%	+0.4%	+0.5%	+0.7%
3%	+0.4%	+0.5%	+0.6%	+0.8%
5%	+0.8%	+1.0%	+0.9%	+0.9%
10%	+0.7%	+0.7%	+0.6%	+0.9%
15%	+3.8%	+4.1%	+4.3%	+4.4%
20%	+5.7%	+6.0%	+6.1%	+6.5%

Figure. 4.84. The increased ratio of LATP green body tablets relative density from glass/ceramic composite powder systems with mass ratios of 0%/100%, 1%/99%, 3%/97%, 5%/95%, 10%/90%, 15%/85% and 20%/80% after preliminary heating at 560℃, 570℃, 580℃, 590℃ for 6 hours, respectively, compared with green tablets made by LATP-600nm powder without this step of heating treatment.

From Figure. 4.84 and Table. 4.14, it is obvious that compared with the green body tablets prepared only from LATP-600nm powder without heating treatment, all samples after heating at 560-590℃ for 6 hours, all the green body tablets have a higher relative density. In the 0%/100% glass/ceramic composite powder system, the increase is about 0.1-0.3 %, which is based on the loss of moisture absorbed in the powder. The increase in the relative density of the green body tablets in the 1-20%/99-80% glass/ceramic composite powder systems are mainly due to the softening of the glass powder and the connection between glass and crystal powder reduces the relative distance between particles, thereby increasing the green body relative density.
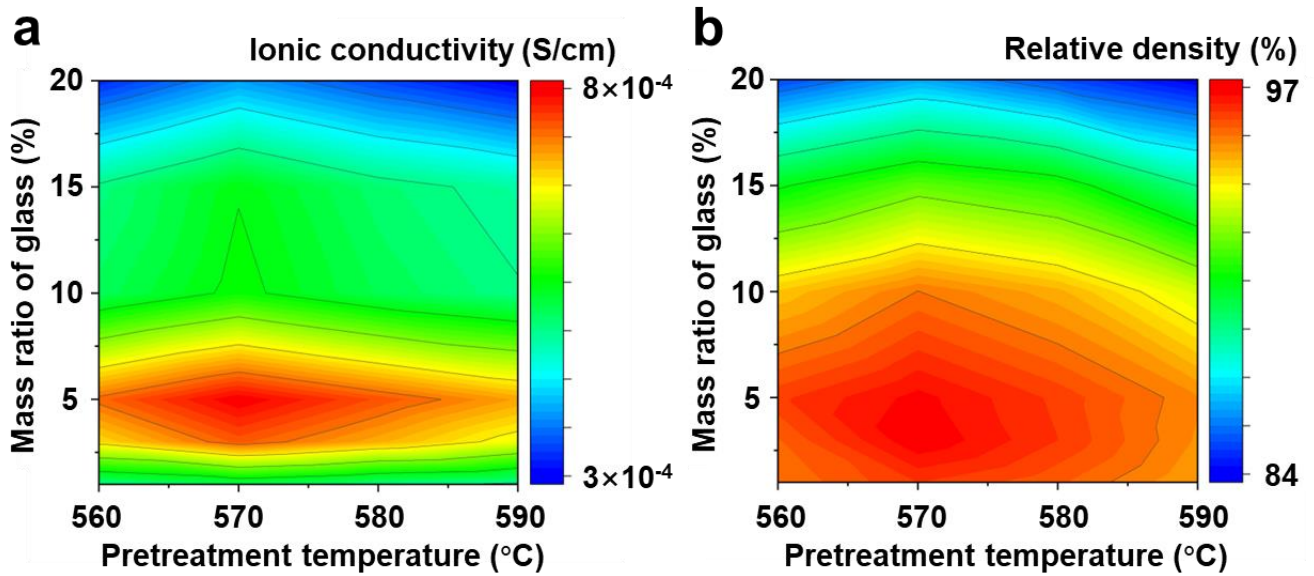
Figure. 4.85. 2D parametric maps for the ionic conductivity and the relative density of different ratio glass/ceramic LATP composite powder sintered at different pretreatment program (560°C for 6 h and 900°C for 6 h; 570°C for 6 h and 900°C for 6 h; 580°C for 6 h and 900°C for 6 h; 590°C for 6 h and 900°C for 6 h).

Table. 4.15. Ionic conductivity and relative density of glass/ceramic LATP composite powder with mass ratios of 0%/100%, 1%/99%, 3%/97%,5%/95%, 10%/90%, 15%/85% and 20%/80% after sintering at 560°C for 6 h then 900°C for 6 h.

Glass/Ceramic	Total ionic conductivity (S/cm)	Relative density (%)
0%/100%	$(4.6\pm0.3)\times10^{-4}$	93.4 ± 0.8
1%/99%	$(4.9\pm0.2)\times10^{-4}$	94.5 ± 0.3
3%/97%	$(6.9\pm0.2)\times10^{-4}$	94.8 ± 0.3
5%/95%	$(7.5\pm0.2)\times10^{-4}$	95.4 ± 0.4
10%/90%	$(5.1\pm0.3)\times10^{-4}$	93.2 ± 0.5
15%/85%	$(5\pm0.4)\times10^{-4}$	88 ± 2
20%/80%	$(3.3\pm0.6)\times10^{-4}$	82 ± 2

Table. 4.16. Ionic conductivity and relative density of glass/ceramic LATP composite powder with mass ratios of 0%/100%, 1%/99%, 3%/97%,5%/95%, 10%/90%, 15%/85% and 20%/80% after sintering at 570°C for 6 h then 900°C for 6 h.

Glass/Ceramic	Total ionic conductivity (S/cm)	Relative density (%)
0%/100%	$(4.7\pm0.3)\times10^{-4}$	93.5 ± 0.8
1%/99%	$(5.2\pm0.1)\times10^{-4}$	95.5 ± 0.4
3%/97%	$(7.5\pm0.1)\times10^{-4}$	96.5 ± 0.3
5%/95%	$(8\pm0.2)\times10^{-4}$	96.3 ± 0.2
10%/90%	$(5.6\pm0.3)\times10^{-4}$	94.5 ± 0.8
15%/85%	$(5.5\pm0.4)\times10^{-4}$	90 ± 2
20%/80%	$(3.8\pm0.6)\times10^{-4}$	83 ± 2

Table. 4.17. Ionic conductivity and relative density of glass/ceramic LATP composite powder with mass ratios of 0%/100%, 1%/99%, 3%/97%,5%/95%, 10%/90%, 15%/85% and 20%/80% after sintering at 580°C for 6 h then 900°C for 6 h.

Glass/Ceramic	Total ionic conductivity (S/cm)	Relative density (%)
0%/100%	$(4.7\pm0.3)\times10^{-4}$	93.4 ± 0.7
1%/99%	$(5\pm0.2)\times10^{-4}$	94.9 ± 0.4
3%/97%	$(7.1\pm0.2\times10^{-4}$	95.5 ± 0.4
5%/95%	$(7.6\pm0.2)\times10^{-4}$	95.4 ± 0.3
10%/90%	$(5.2\pm0.3)\times10^{-4}$	93.6 ± 0.5
15%/85%	$(5\pm0.4)\times10^{-4}$	89 ± 2
20%/80%	$(3.4\pm0.5)\times10^{-4}$	82 ± 2

Table. 4.18. Ionic conductivity and relative density of glass/ceramic LATP composite powder with mass ratios of 0%/100%, 1%/99%, 3%/97%,5%/95%, 10%/90%, 15%/85% and 20%/80% after sintering at 590°C for 6 h then 900°C for 6 h.

Glass/Ceramics	Total ionic conductivity (S/cm)	Relative density (%)
0%/100%	$(4.7\pm0.3)\times10^{-4}$	93.6 ± 0.7
1%/99%	$(4.8\pm0.1)\times10^{-4}$	93.8 ± 0.2
3%/97%	$(6.6\pm0.2)\times10^{-4}$	94.1 ± 0.2

5%/95%	$(7.2\pm0.2)\times10^{-4}$	94.2 ± 0.3
10%/90%	$(4.9\pm0.3)\times10^{-4}$	91.7 ± 0.9
15%/85%	$(4.8\pm0.4)\times10^{-4}$	86 ± 2
20%/80%	$(3\pm0.6)\times10^{-4}$	80 ± 2

Therefore, a new two-step sintering program was proposed to heat the glass/ceramic composite SSE green tablets by using a heating rate of 2°C/min to 560°C, 570°C, 580°C and 590°C, respectively. After 6 hours of heat preservation, the SSE green tablets were heated to 900°C at a heating rate of 2°C/min, and then cooled naturally with the furnace after 6 hours of heat preservation. The ionic conductivity at room temperature was measured after sputtering 30 nm of platinum on both sides of tablet after two-step sintering. As shown in Figure. 4.85 and Table. 4.15-18, the SSE tablets prepared by using glass/ceramic powders with the mass ratio of 5% shows the best ionic conductivity and relative density than that with other ratios at all different heating programs.
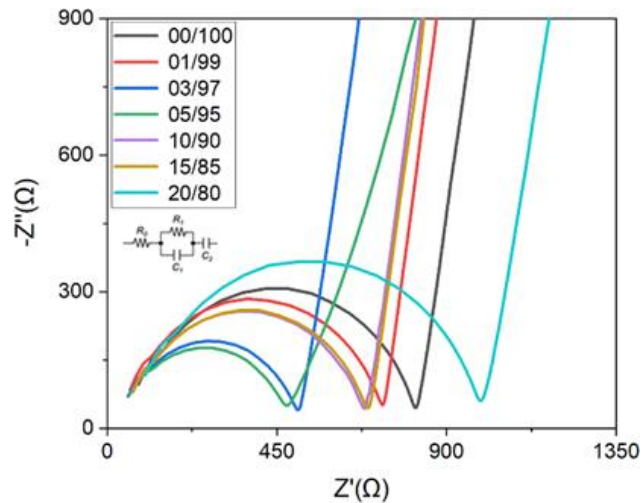
Figure. 4.86. Nyquist plots from glass/ceramic powders with the mass ratios of 1%/99%, 3%/97%, 5%/95%, 10%/90%, 15%/85%, 20%/80%, and 100%/0% after pretreatment at 570°C for 6 hours then sintered at 900 °C for 6 hours.

Moreover, among all the different heating programs, the SSE tablet prepared by using glass/ceramic powders with the mass ratio of 5% shows the best ionic conductivity of $(8\pm0.2)\times10^{-4}$ S/m than that with other ratios, while its relative density (96.3±0.2%) is also very high near to the best

ratio of 3% (96.5±0.3) after pretreatment at 570°C for 6 hours then sintered at 900°C for 6 hours. This can be explained by the fact that the pretreatment temperature of 570°C with duration of 6h for glass softening is long enough, so that the 60nm size glass powder could build a three-dimensional framework surrounding the 600nm LATP powder in the SSE green tablet (the degree of continuity depends on the amount of the added glass powder). Therefore, the addition of LATP glass powder additive, combined with a specially designed sintering procedure, helps to obtain LATP tablets with higher relative density and ionic conductivity.
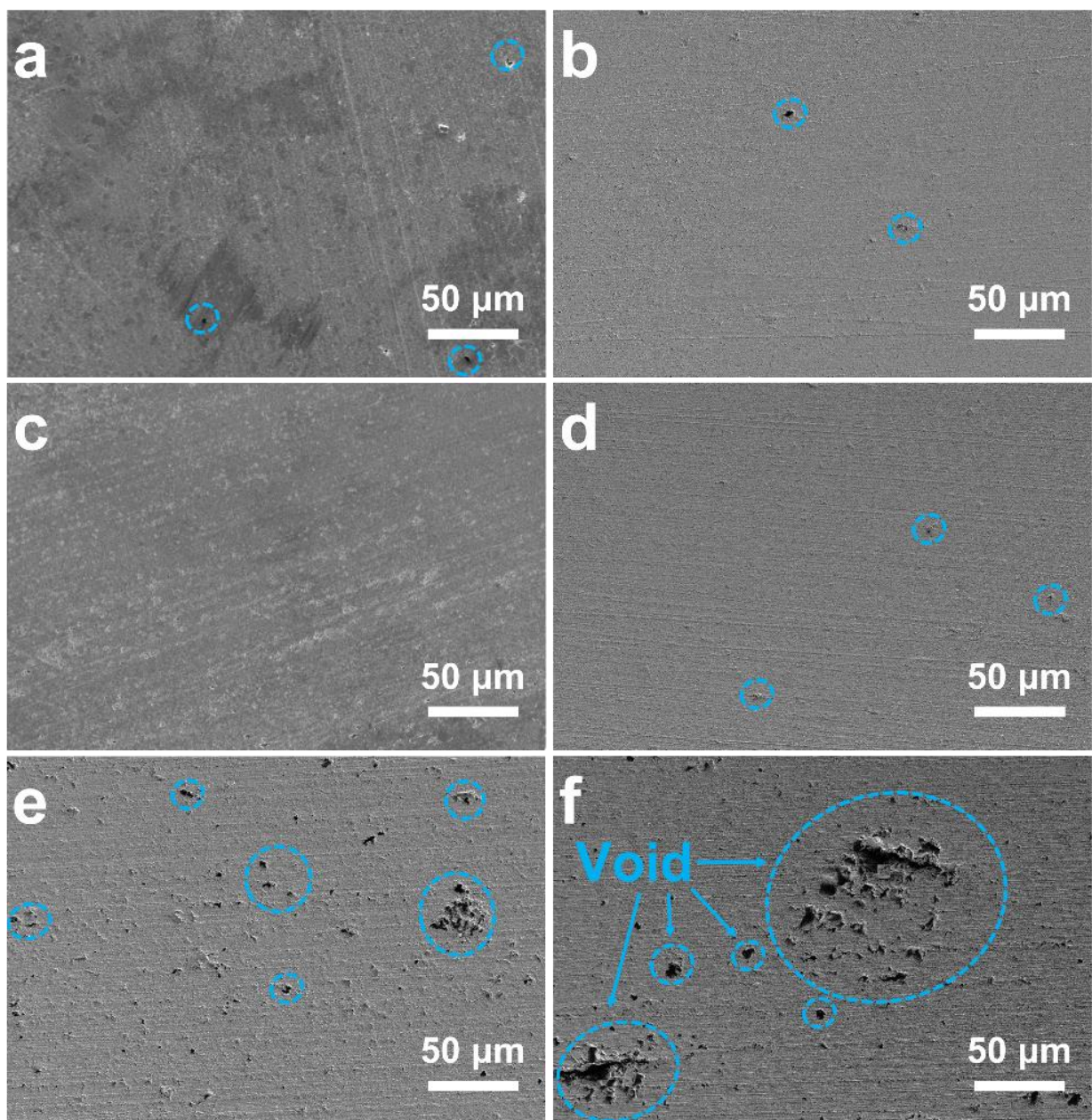
Figure. 4.87. Large-scale cross-section SEM images of SSE tablets from glass/ceramic powders with the mass ratios of (a) 1%/99%, (b) 3%/97%, (c) 5%/95%, (d) 10%/90%, (e) 15%/85% and (f) 20%/80% after pretreatment at 570°C for 6 hours then sintered at 900°C for 6 hours. Void defects from the sintering process are marked with blue circles.
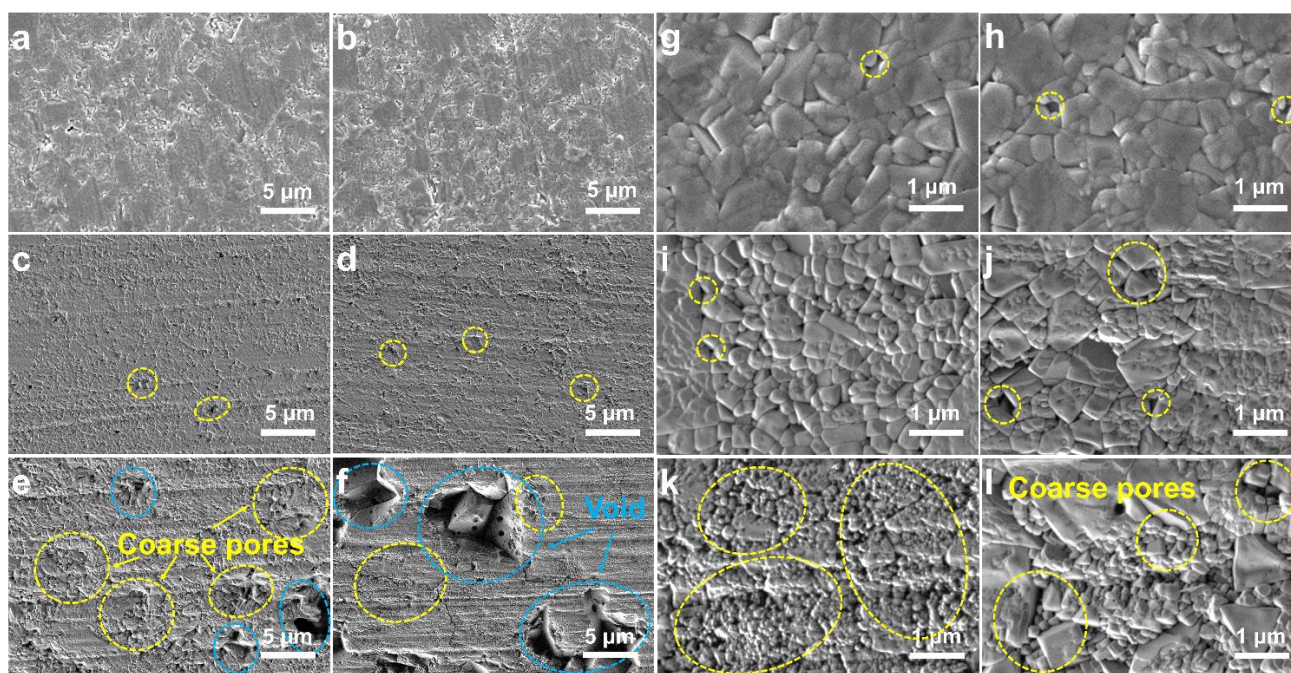
Figure. 4.88. Cross-section SEM images of SSE tablets from glass/ceramic powders with the mass ratios of 1%/99%, 3%/97%, 5%/95%, 10%/90%, 15%/85% and 20%/80% after pretreatment at 900°C for 6 hours then sintered at 900°C for 6 hours, marked by 5μm scale (a-f) and 1μm scale (g-l), respectively. Void defects and coarse pores from the sintering process are marked with blue and yellow circles, respectively.

To observe the morphology of the LATP SSE ceramics after two-step sintering program (after pretreatment at 570°C for 6 hours then sintered at 900°C for 6 hours), the cross-section SEM images of LATP tablets were measured by using glass/ceramic composite powder systems with weight fractions of 1%/99%, 3%/97%, 5%/95%, 10%/90%, 15%/85% and 20%/80%. As shown in Figure. 4.87 and Figure. 4.88a-f, when the amount of glass powder introduced is less than 10%, there are almost no defects except for a small number of small voids in the large and micro-scale cross-section SEM images, while many observable void defects and coarse pores appear inside the SSE tablets when the amount of glass powder introduced exceeds 10%. Detailly, when the addition of glass powder is

less than 10%, the SSE tablets show a higher relative density (Figure. 4.88g-j). Moreover, the SSE ceramics display better sintering quality with a relatively uniform size and without obvious large number of grain boundary defects when the addition of glass powder is less than 5%. With the increasing glass powder to 15%, the average size of grains decreased to nm-scale and SSE tablet shows a lower degree of densification (Figure. 4.88k). However, when the added glass powder admixed with LATP ceramic particles with the ratio of 20%/80%, the excess of thermally active nano-LATP particles formed during crystallization of glass demonstrate extensive coarsening of grains (Figure. 4.88l). Constrained sintering of the composite with formed coarse defects results in low relative density. The results indicate that the developed sintering procedure is not optimal for the tablet containing more than 10% of LATP glass additive.
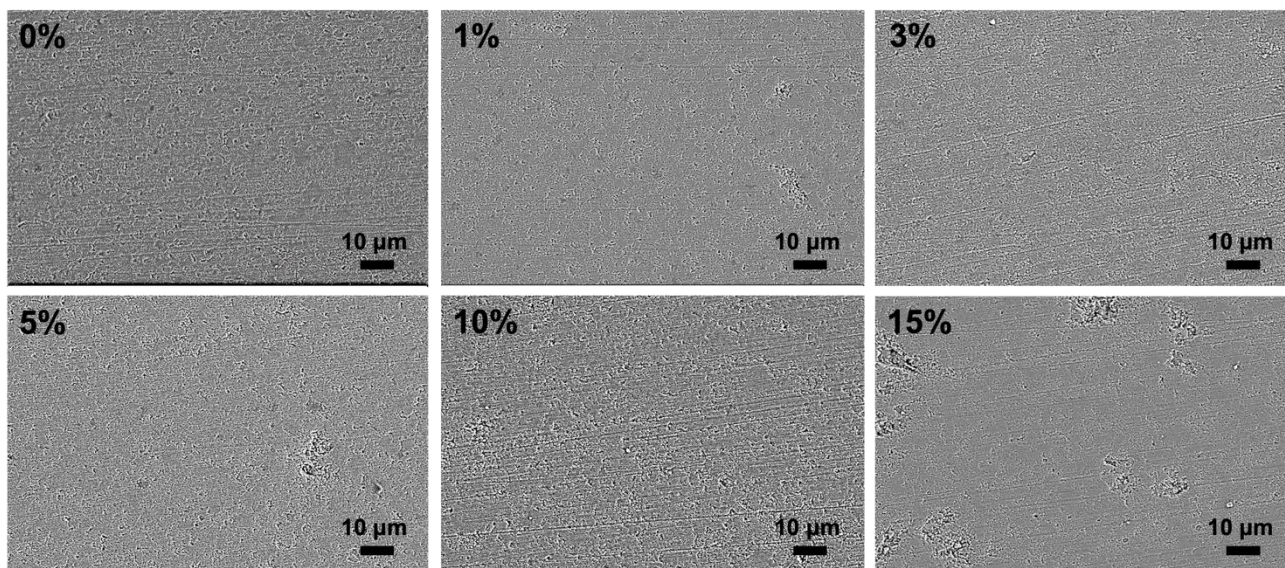
Figure. 4.89. Cross-section SEM images of LATP SSE ceramic from glass/ceramic composite powder systems with different ratio after sintering at 570°C for 6 hours then 900°C for 6 hours.

Here we again choose a relatively flat area with few defects to count the average grain size of different composite powder systems with glass additive after 2-steps sintering and observe the AGG behavior. Obviously, with the increase of the relative content of the glass additive, no typical AGG behavior. The average grain size after sintering is slightly larger than that of the only LATP-600nm benchmark system. With an increase in the relative content of the LATP glass, the particle size also increased. But the particle size of 2-setps method samples slightly exceeding the particle size of 1-step

method with the same ratio of LATP glass additive. The increase in average grain size for 2-steps method compared to 1-step method is due to the additional process of glass compaction, the nanograins formed as a result of crystallization of the LATP glass have closer contact with the original grains and contribute to their growth. All other trends in 2-steps method are like those in 1-step method shown before. All in all, the additional glass densification process in the 2-steps method in the first sintering stage provides better results compared to 1-step method.

Additionally, the XRD patterns of the LATP SSE tablets with different ratios of glass/ceramic powder treated by two-step sintering program shows the similar trend with that of using common sintering program, which matches well with the standard card of $LiTi_2(PO_4)_3$ as predominant phase with neglible amount of $AlPO_4$ without any second phase in all samples after sintering (Figure. 4.90).
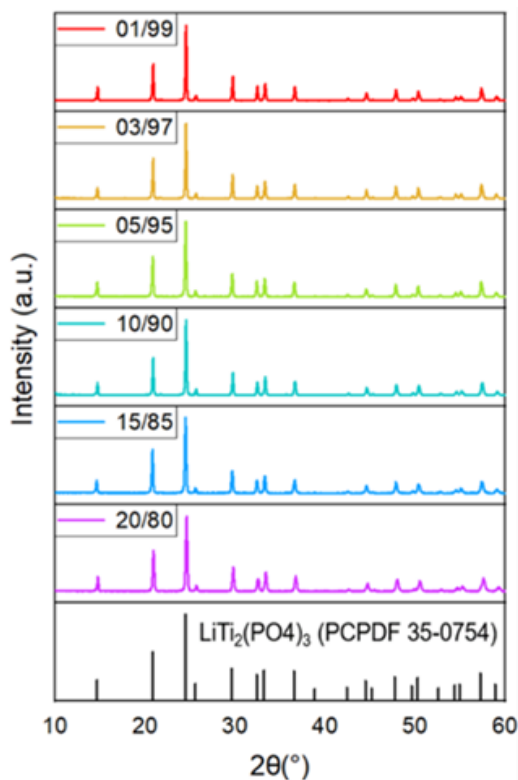
Figure. 4.90. XRD patterns of LATP SSE ceramics from glass/ceramic composite powder systems with the weight fractions of 1%/99%, 3%/97%, 5%/95%, 10%/90%, 15%/85% and 20%/80%, after pretreatment at 560-590°C for 6 hours then sintered at 900°C for 6 hours.
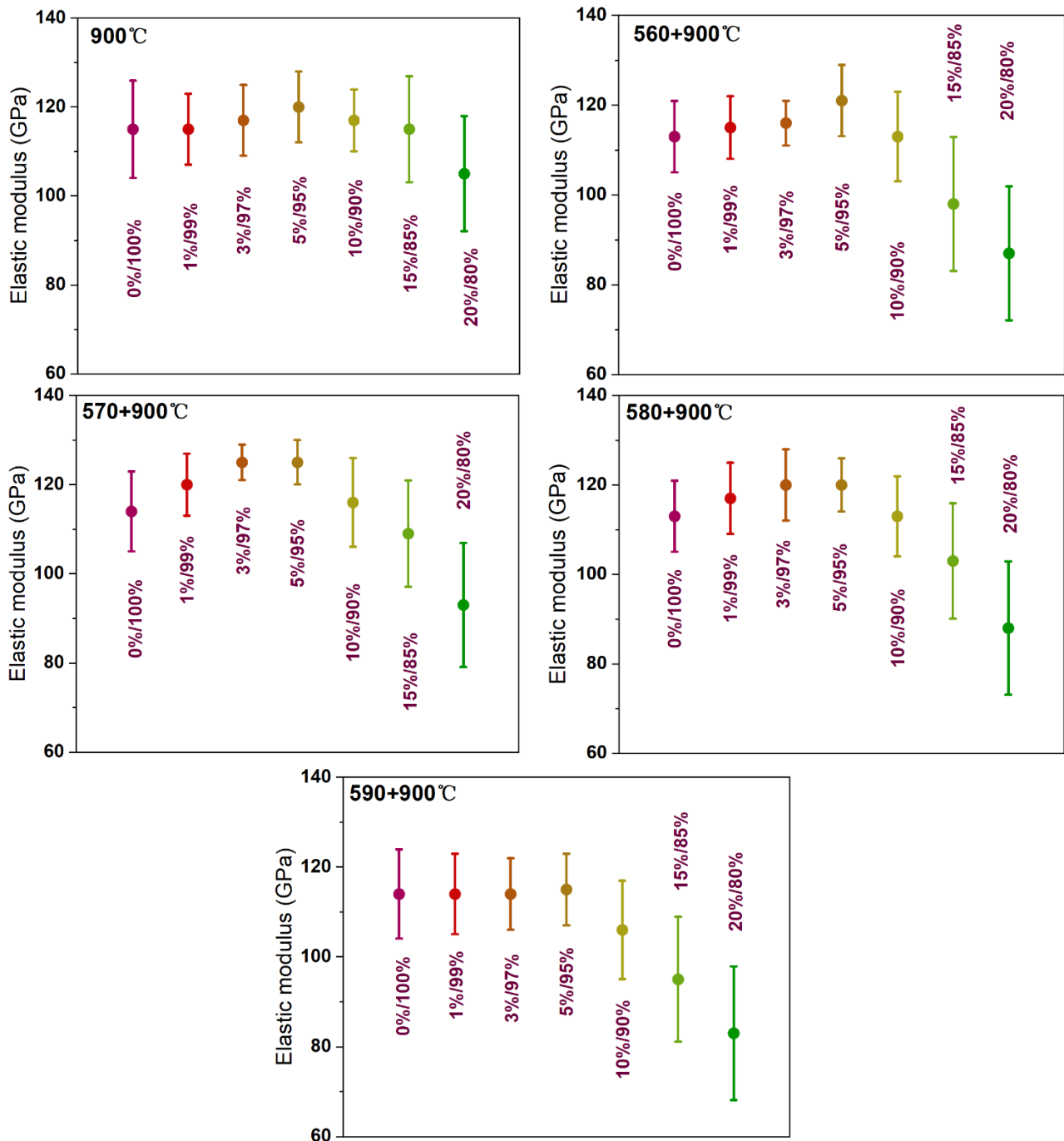
Figure. 4.91. Elastic modulus of LATP SSE ceramics from glass/ceramic composite powder systems with the weight fractions of 1%/99%, 3%/97%, 5%/95%, 10%/90%, 15%/85% and 20%/80%, compared with each other after pretreatment at 560°C, 570°C, 580°C, 590°C for 6 hours then sintered at 900°C for 6 hours under 50 mN loading, respectively.

In Figure. 4.91, we show that when 0-20% glass powder additives are introduced, the LATP SSE ceramics use 1-step method (900°C for 6 hours) and 2-steps method (wherein the first step is 560°C, 570°C, 580°C, 590°C for 6 hours, respectively; the second step is 900°C for 6 hours) distribution and change trend of elastic modulus under 50 mN loads after sintering. It can be clearly observed that in

all sintering programs, with the increase of the LATP glass powder, the elastic modulus always presents a slight increase at first, and then a relatively obvious decrease. The maximum value of elastic modulus comes from LATP SSE ceramics containing 3-10% glass, especially 3-5%. This matches the data shown in the SEM, where high relative density and a relatively homogeneous and defect-free microstructure are necessary conditions for the LATP SSE ceramic to have a high elastic modulus.
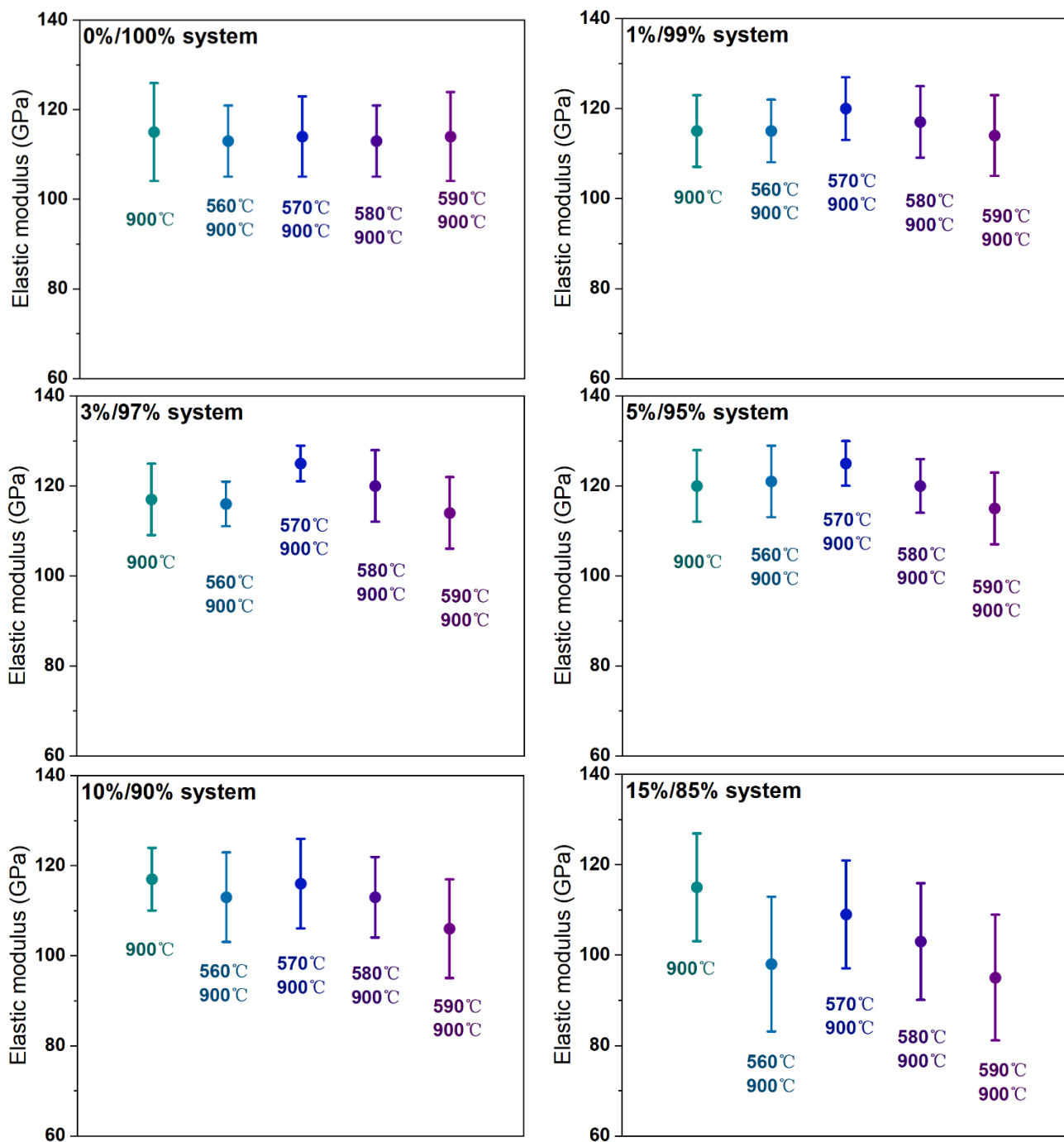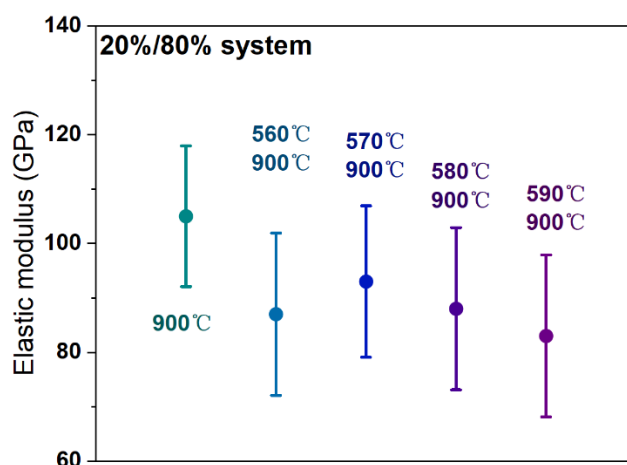
Figure. 4.92. Elastic modulus of LATP SSE ceramics after pretreatment at 560°C, 570°C, 580°C, 590°C for 6 hours then sintered at 900 °C for 6 hours, compared with each other from glass/ceramic composite powder systems with the weight fractions of 1%/99%, 3%/97%, 5%/95%, 10%/90%, 15%/85% and 20%/80% under 50 mN loading, respectively.

In order to compare the effect of the sintering program on the elastic modulus of the LATP SSE ceramic more clearly, we organized the data in another version. In Figure. 4.92, we can clearly see that the elastic modulus of the SSE ceramics after sintering without glass powder additives are not affected by the sintering program. With the addition of glass powder, the influence of different sintering programs on ceramics began to appear. When the addition amount of glass powder is 1%, 3% and 5%, the elastic modulus difference of the SSE ceramics using 1-step method and 2-steps method (560°C) is small. But there is a significant increase in the elastic modulus of the SSE ceramics by 2-steps method (570°C), and a significant stepwise decrease in the elastic modulus for the 2-steps (580°C and 590°C) SSE ceramics. When the addition of glass powder is 10%, 15% and 20%, using any 2-steps sintering programs will cause a significant decrease in the elastic modulus of the SSE ceramics. These conclusions also match the microscopic morphology shown in SEM. Thus, the largest elastic modulus derived from LATP SSE ceramics containing 3-5% glass powder additives, processed under the 2-step sintering program (570°C), can reach values of 125±4 GPa and 125±5 GPa, respectively, under a load of 50 mN. Detailed data are presented in the tables below.

Table. 4.19. Values of LATP SSE ceramics elastic modulus (GPa) obtained from glass/ceramic LATP composite powder system with mass ratios of 0%/100%, 1%/99%, 3%/97%,5%/95%, 10%/90%, 15%/85% and 20%/80% after sintering at different programs under 50 mN loading.

Temperature	0%/100%	1%/99%	3%/97%	5%/95%	10%/90%	15%/85%	20%/80%
900°C	115±11	115±8	117±8	120±8	117±7	115±12	105±13
560+900°C	113±8	115±7	116±5	121±8	113±10	98±15	87±15
570+900°C	114±9	120±7	125±4	125±5	116±10	109±12	93±14
580+900°C	113±8	117±8	120±8	120±6	113±9	103±13	88±15
590+900°C	114±10	114±9	114±8	115±8	106±11	95±14	83±15

4.4.2.4. Chapter conclusions

In summary, LATP SSE ceramics were successfully fabricated by adding different amount of LATP glass powder into LATP crystal powder, and then treated by improved 2-steps sintering program (pretreated at 560-590°C for 6 hours and sintered at 900°C for 6 hours). Moreover, the LATP SSE tablet containing 60 nm LATP glass powder and 600 nm LATP crystal powder with the ratio of 5%/95% shows the best ionic conductivity of $(8\pm0.2)\times10^{-4}$ S/m than that with other ratios, while its relative density (96.3 ± 0.2)% is also very high near to the best ratio of 3% (96.5 ± 0.3)% after pretreatment at 570°C for 6 hours then sintered at 900°C for 6 hours and without the typical AGG behavior.

4.5. Fabrication of LATP SSE membranes
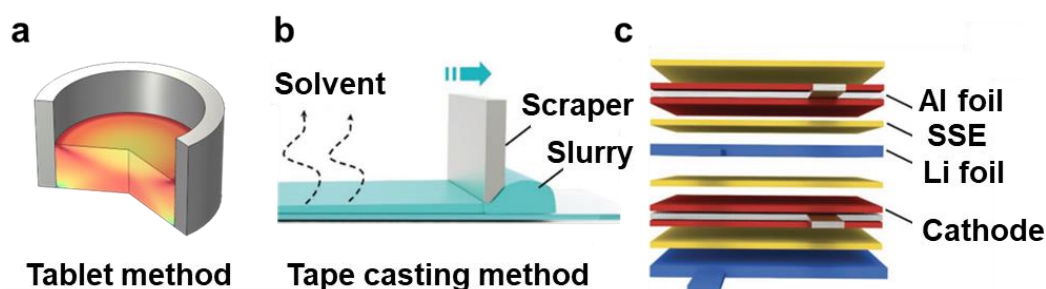
Figure. 4.93. Schematic images of a) tableting method (uneven stress distribution causes potential cracks), b) Tape-casting method, c) structure of solid-state pouch cell.

Tape casting is a promising method for the large-scale production of ultrathin freestanding ceramic electrolyte films. Easy scale-up fabrication of oxide ceramic electrolyte by tape-casting

method for all-solid-state batteries has been successfully demonstrated in the frame of current work.
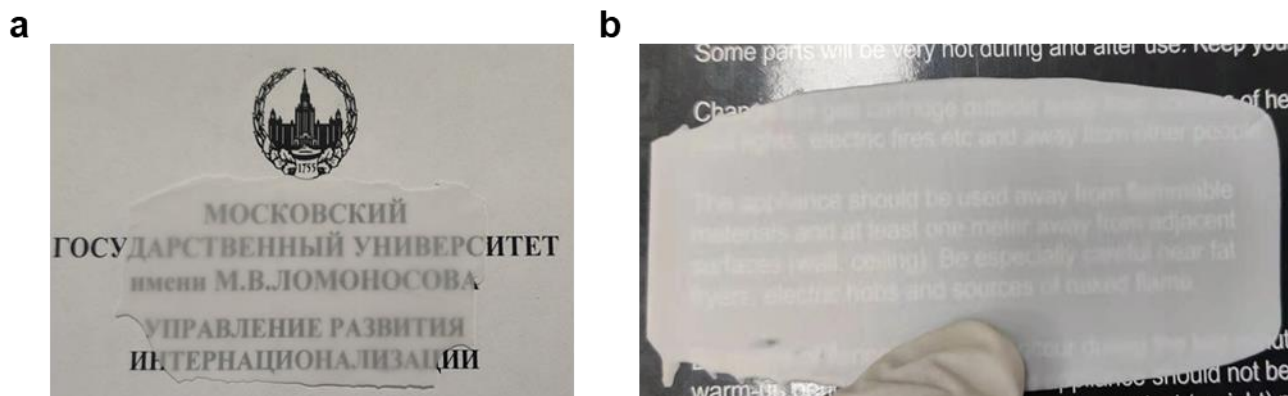
Figure. 4.94. (a) ~60 μm thickness, (b) ~200-220 μm thickness SSE film after sintering.
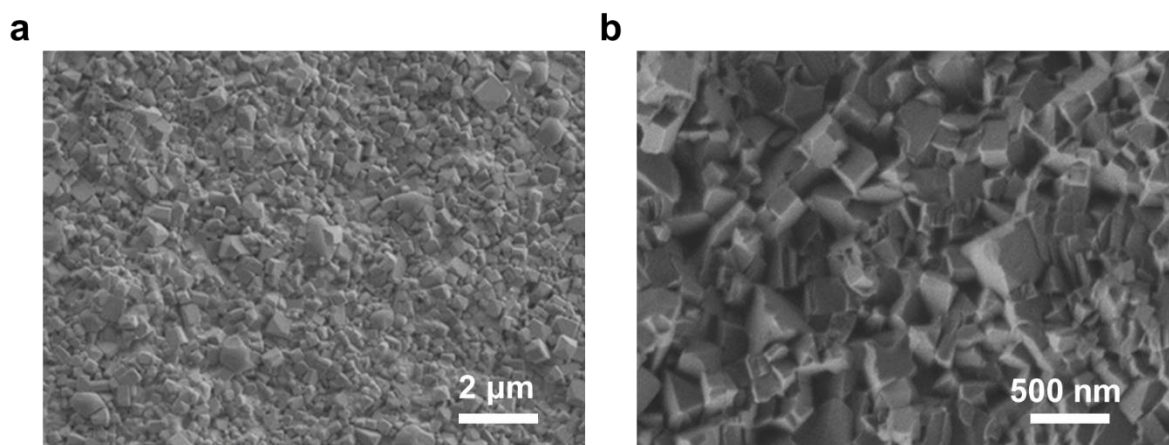
Figure. 4.95. SEM images of LATP SSE film surface morphology.
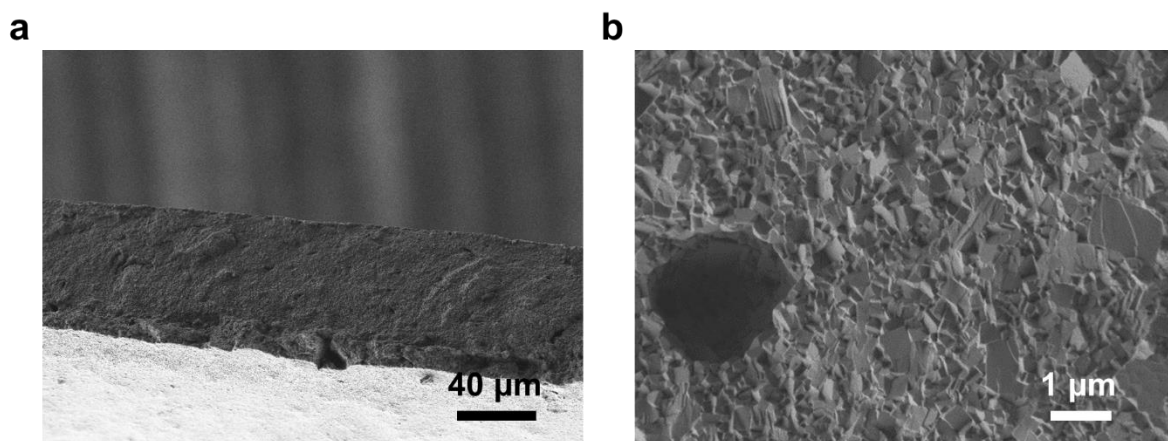
Figure. 4.96. SEM images of LATP SSE film cross-section morphology.

After sintering, solid-state electrolyte film with a thickness as low as 60 μm and a maximum size of 100×100 μm was obtained, and the edge of the ceramic film was flat, which is suitable for the

assembly of all-solid-state electrolyte batteries. Based on our previously explored optimal sintering program for LATP, the SEM of the solid-state electrolyte film revealed good sintering quality and uniform grain size after sintering. A small number of micron-scale pores in the cross-section come from the air bubbles mixed in the slurry mixing process, which remain in the polymer-based precursor film after photocuring. Therefore, in the follow-up exploration, how to further improve the relative density of the solid-state electrolyte film (~ 92-93%) is the main direction.

The mechanical properties of LATP films with a thickness of 60 μm have been measured. The total measurement area is 80×80 μm, and the area of a single measurement area is 4×4 μm (the small square area in Figure. 4.97).
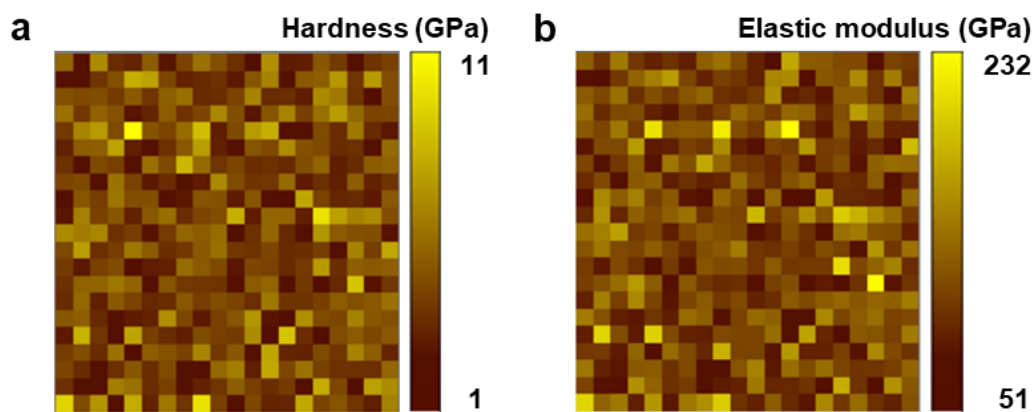
Figure. 4.97. 2D parametric maps of: (a) hardness and (b) elastic modulus.
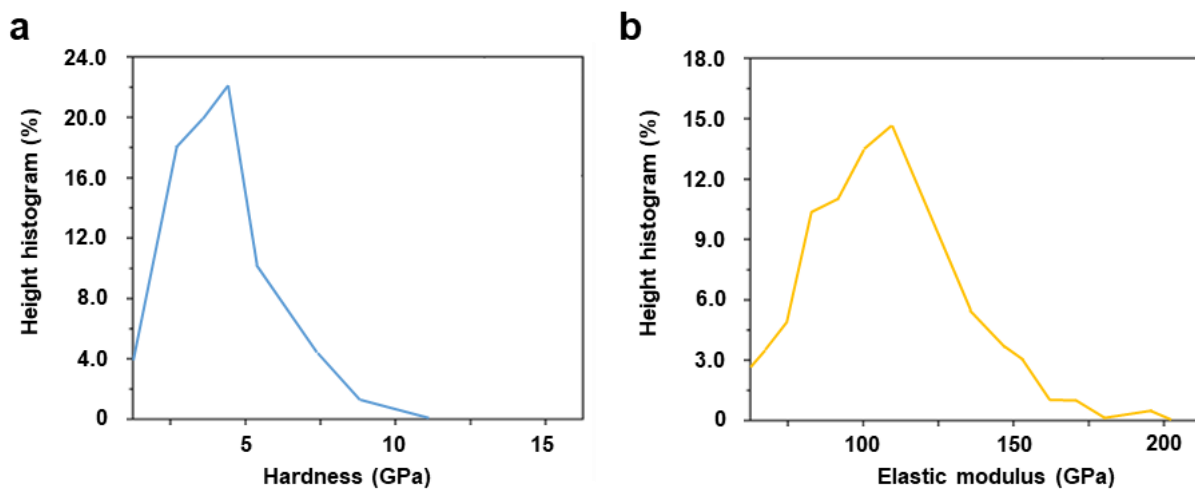
Figure. 4.98. Histogram of the distribution of hardness (a) and modulus of elasticity (b) on the sample based on the results of processing a series of 441 injections.

Non-Gaussian distributions in the values of hardness and modulus of elasticity indicate the effect of roughness on the average value of these mechanical characteristics. The hardness of the sample is 4.6±1.6 GPa, the elastic modulus is 114±31 GPa, and the fracture toughness is 3.2±1.0 Mpa·$m^{0.5}$.

4.6. Electrochemical testing of cells using obtained LATP SSE ceramic

4.6.1. LATP solid-state electrolyte ceramics from bimodal powder precursor
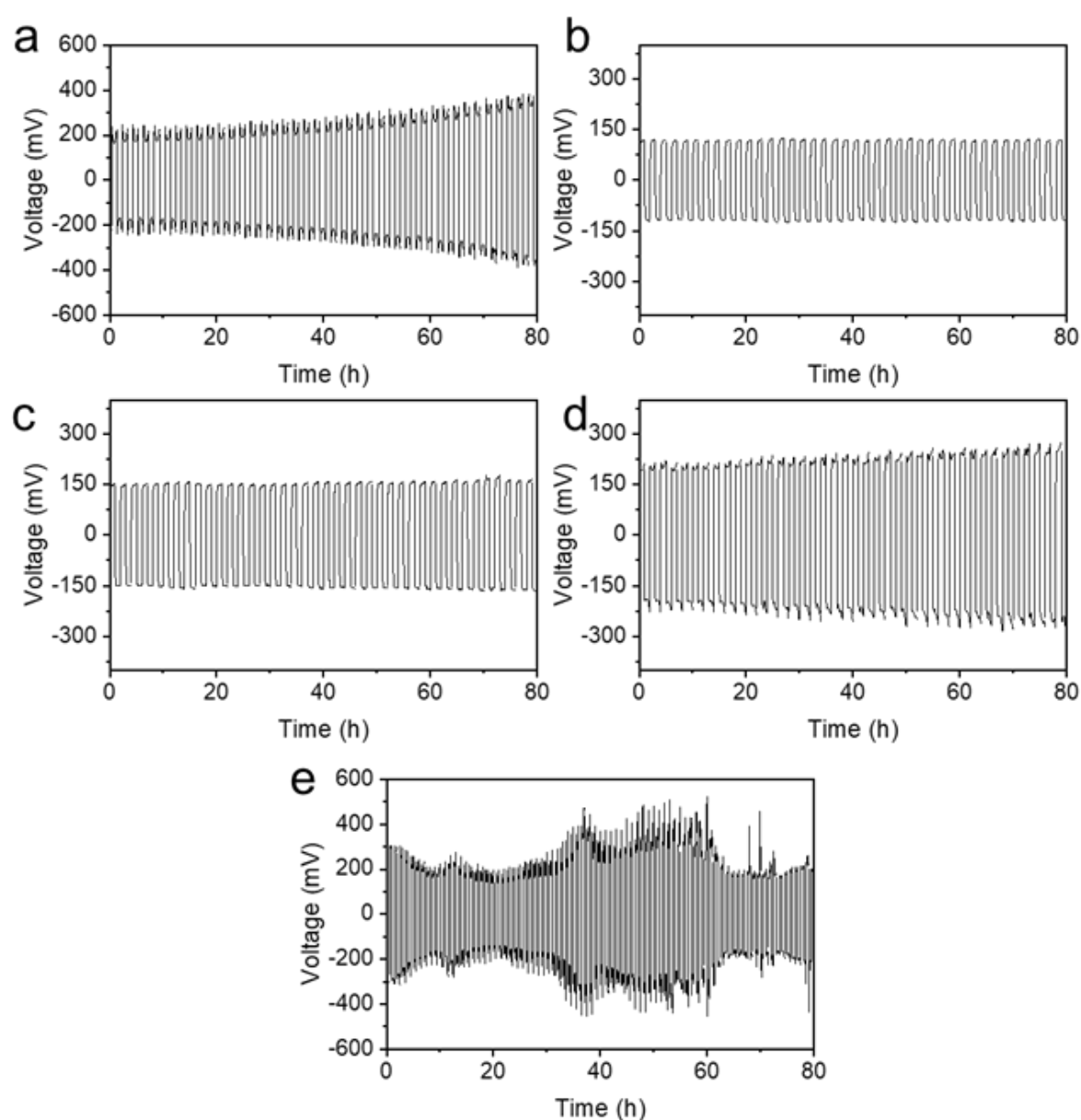
Figure. 4.99. The voltage profiles of the Li||LATP||Li symmetric cells, 60 nm/600 nm bimodal powder with mass ratios of 5%/95%, 10%/90%, 15%/85%, 20%/80%, and 100%/0% tested at a current density of 0.1 mA/cm^2 with a

stripping/plating period of 1 h at room temperature.

The Li‖LATP‖Li symmetric cell with the ratio of 100%/0% shows extremely unstable voltage during the Li plating/stripping. This is attributed to the interface failure caused by the continuous side reaction of the solid electrolyte (reduction of tetravalent titanium) with the lithium metal anode during cycling. The rough lithium metal/solid electrolyte interface indirectly increases the relative area where side reactions occur, and there is a large number of mechanically unstable microstructures on the surface of the rough interface extremely proned to fracture during the reaction. The existence of internal pores and defects will also relatively reduce the comprehensive mechanical properties of solid electrolytes. As the lithium dendrites expand along the surface damage area to the interior of the solid electrolyte, the cracks will penetrate each other between the pores and defects, resulting in a violent oscillation of the polarization potential. As shown in Figure. 4.99a and Figure. 4.99d, in the 5%/95% and 20%/80% systems, the higher relative density and ionic conductivity make the polarization potential relatively small, and the initial potentials are 190.2 mV and 208.5 mV respectively. However, as the cycling process progresses, the lithium gradually destroyed the electrode/solid-state electrolyte interface and extend to the interior of the solid electrolyte with the help of internal cracks and defects, which also leads to a continuous increase in its subsequent polarization potential (showing a horn shape). In Figure. 4.99b, the Li‖LATP‖Li symmetric cell with the ratio of 10%/90% demonstrates the best cyclic stability with the steady polarization voltage of 121.2 mV than that with other ratios. It should be also noted that 150 mV polarization potential recorded for the sample 15%/85% (Fig. 4.99c) can be regarded as a promising result. Therefore, improving the ionic conductivity and density of ceramic electrolyte is beneficial to maintain the cycling stability of the battery either.

4.6.2. LATP SSE ceramics from composite powder system with LATP glass additive
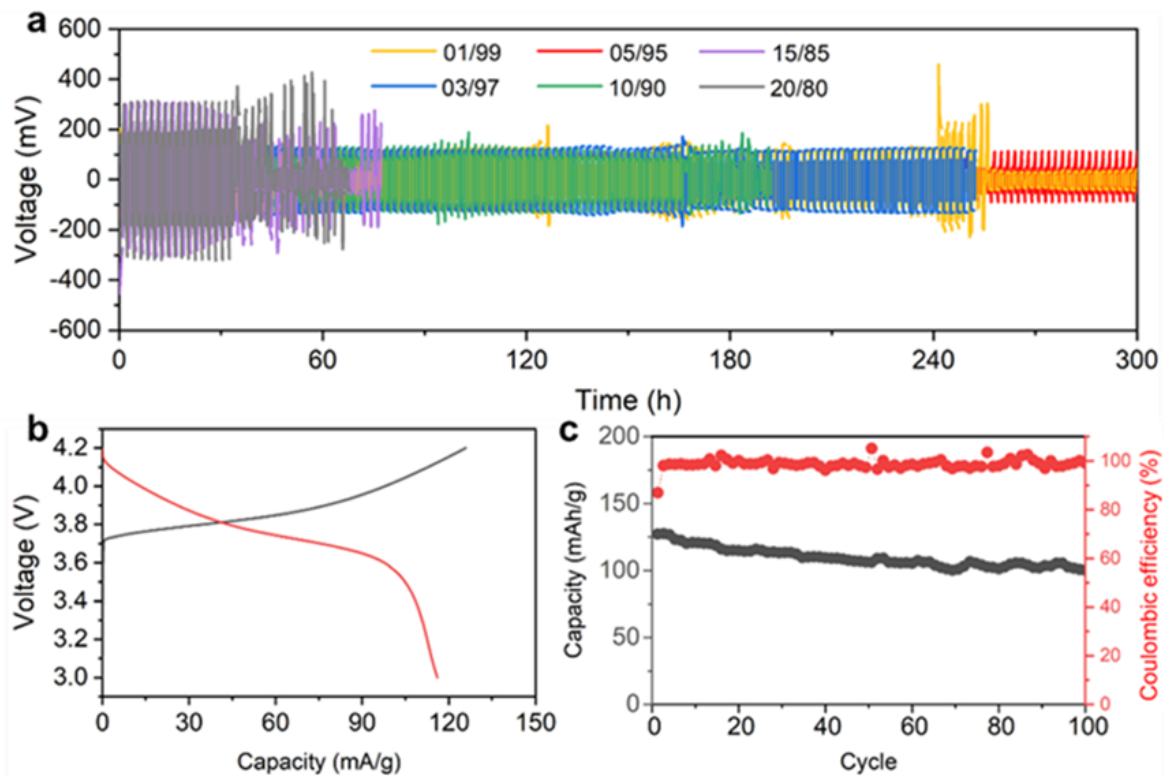
Figure. 4.100. (a) The voltage profiles of the Li‖LATP‖Li symmetric cells of LATP SSE tablets from glass/ceramic composite powder systems with the different mass ratios after pretreatment at 570°C for 6 hours then sintered at 900°C for 6 hours. (b-c) The charge/discharge voltage profiles and cycle performance of Li‖LATP‖NCM111 full cell with the LATP SSE ceramic from glass/ceramic powder system with the mass ratios 5%/95% after pretreatment at 570°C for 6 hours then sintered at 900°C for 6 hours at a current density of 0.1 mA/cm^2.

The Li‖LATP‖Li symmetric cell using LATP SSE tablet with the mass ratio of 5%/95% exhibits the best stable voltages for 300 h than that with other ratios. Moreover, the symmetric cells using LATP SSE tablets with the ratio of 1%/99%, 3%/99%, and 10%/90% could display good stable voltages for 240h, 260h and 200h, respectively, which indicates that the LATP SSE tablets with high relative density and ionic conductivity can promote the electrochemical stability during cycling. Moreover, the Li‖LATP‖NCM111 full cell was tested at 0.1 C with the voltage range of 3.0-4.2 V. LATP SSE tablet from glass/ceramic powder system with the mass ratios 5%/95% after pretreatment at 570°C for 6 hours then sintered at 900°C for 6 hours, which exhibits excellent cycling performance over 100 cycles with capacity of 100.3 mAh/g (capacity retention of 79.1%). The results can be explained that the developed SSE with good mechanical property, high relative density and ionic conductivity are

beneficial to maintain the structural stability of the electrolyte, which could mitigate the generation and aggravation of the cracks inside the SSE during cycling and could accelerate its development in the industrialization of all-state lithium metal battery.

5. Conclusions

1. It was established during modeling by the phase field method and visualization of the processes of lithium protrusions formation in the solid-state electrolyte that, with an overall fixed porosity, the presence of a large number of smaller diameter pores accelerates the process of electrolyte destruction during the growth of lithium protrusions. It was revealed that high values of grain boundary destruction energy suppress the propagation of lithium protrusions in the solid-state electrolyte, while the grain size factor makes a smaller contribution.

2. An original version method for the synthesis of $Li_{1.3}Al_{0.3}Ti_{1.7}(PO_4)_3$ particles with the NASICON structure using polymerized matrices has been developed. It has been established that the concentration of reagents, as well as the process temperature are the main factors allowing to achieve a controlled average particle size in the range from 25 to 600 nm. The solid-state method makes it possible to obtain $Li_{1.3}Al_{0.3}Ti_{1.7}(PO_4)_3$ particles with a controlled average size in the range from 300 to 2400 nm. The optimal sintering conditions for the resulting powders were determined, including sintering at 800°C and 900°C for 6 hours, respectively.

3. It has been demonstrated that the transition from a unimodal distribution of $Li_{1.3}Al_{0.3}Ti_{1.7}(PO_4)_3$ particles to a bimodal distribution with 10 wt.% nano (~ 60 nm) and 90 wt.% submicron particles (~ 600 nm) makes it possible to obtain a ceramic solid-state electrolyte with improved values of relative density of 96±1%, ionic conductivity of $(5.9\pm0.2)\times10^{-4}$ S/cm and elastic modulus of 119±9 GPa compared to the values of relative density of 94±1%, ionic conductivity of $(4.8\pm0.5)\times10^{-4}$ S/cm and elastic modulus of 114±9 GPa of ceramics made from the powder precursor without added nanoparticles.

4. A method for the producing of ceramic solid-state electrolyte using composites based on crystalline and glassy phases of the $Li_{1.3}Al_{0.3}Ti_{1.7}(PO_4)_3$ has been proposed. This approach makes it possible to avoid the process of abnormal grain growth during sintering and improve the functional properties of the solid-state electrolyte, including increasing ionic conductivity up to $(7.8\pm0.2)\times10^{-4}$ S/cm, relative density up to 95.1±0.3% and elastic modulus up to 120±8 GPa. The optimal mass ratio of the crystalline and glassy phases

was established as 95%:5%. Based on the dilatometry data, a 2-steps sintering mode (570°C, 6h; 900°C, 6h) of composites based on $Li_{1.3}Al_{0.3}Ti_{1.7}(PO_4)_3$ has been developed, which allows to achieve maximum ionic conductivity values of $(8\pm0.2)\times10^{-4}$ S/cm, relative density of $96.3\pm0.2\%$ and elastic modulus of 125 ± 5 GPa.

5. An approach has been developed to forming synthesized powders in the form of thin membranes with the thickness from 60 to 250 μm. The approach is based on thin-film tape casting of a photocurable multicomponent polymer mixture containing the target powder precursor of $Li_{1.3}Al_{0.3}Ti_{1.7}(PO_4)_3$ followed by 2× stage heat treatment to remove polymer components and consolidate the ceramics. The proposed concept allows to assemble working prototypes of solid-state power supplies with improved specific characteristics by reducing the thickness of the solid-state electrolyte.

6. It has been shown that solid-state electrolytes with both a bimodal particle distribution and ceramics obtained using glassy components demonstrate high stability during electrochemical cycling of $Li||Li_{1.3}Al_{0.3}Ti_{1.7}(PO_4)_3||Li$ symmetric cells. The magnitude of the overvoltage correlates with the ionic conductivity and relative density and is 121 mV for the solid-state electrolyte with bimodal particle distribution, and down to 100 mV for the ceramics based on glassy components, respectively. The prototype battery with Li metal anode and NCM111 cathode using the developed $Li_{1.3}Al_{0.3}Ti_{1.7}(PO_4)_3$ solid-state electrolyte demonstrated high performance characteristics: high cyclic stability over 100 cycles while maintaining a specific capacity of 79.1% (100.3 mAh/g) at the discharge/charge rate of 0.1 mA/cm^2 in the voltage range of 3.0-4.2 V.

References

[1] Reddy, M. V., Mauger, A., Julien, C. M., Paolella, A., & Zaghib, K. (2020). Brief history of early lithium-battery development. *Materials*, *13*(8), 1884.

[2] Scrosati, B. (2011). History of lithium batteries. *Journal of solid-state electrochemistry*, *15*(7), 1623-1630.

[3] Li, H. (2019). Practical evaluation of Li-ion batteries. *Joule*, *3*(4), 911-914.

[4] Braeuer K, Moyes K R. High energy density battery: U. S. Patent 3, 514, 337[P]. 1970.05.26.

[5] Whittingham, M. S. (2004). Lithium batteries and cathode materials. *Chemical reviews*, *104*(10), 4271-4302.

[6] Staprans, A., McCune, E., & Ruetz, J. A. (1973). High-power linear-beam tubes. *Proceedings of the IEEE*, *61*(3), 299-330.

[7] Peled, E. (1983). Film forming reaction at the lithium/electrolyte interface. *Journal of Power Sources*, *9*(3), 253-266.

[8] Mizushima, K. J. P. C., Jones, P. C., Wiseman, P. J., & Goodenough, J. B. (1980). Li_xCoO_2 (0< x<-1): A new cathode material for batteries of high energy density. *Materials Research Bulletin*, *15*(6), 783-789.

[9] Yoshinari, T., Koerver, R., Hofmann, P., Uchimoto, Y., Zeier, W. G., & Janek, J. (2019). Interfacial stability of phosphate-NASICON solid electrolytes in Ni-rich NCM cathode-based solid-state batteries. *ACS applied materials & interfaces*, *11*(26), 23244-23253.

[10] Cooke, P. (2020). Gigafactory logistics in space and time: Tesla's fourth gigafactory and its rivals. *Sustainability*, *12*(5), 2044.

[11] Yu, W., Guo, Y., Shang, Z., Zhang, Y., & Xu, S. (2022). A review on comprehensive recycling of spent power lithium-ion battery in China. *eTransportation*, 100155.

[12] Liu, B., Jia, Y., Yuan, C., Wang, L., Gao, X., Yin, S., & Xu, J. (2020). Safety issues and mechanisms of lithium-ion battery cell upon mechanical abusive loading: A review. *Energy Storage Materials*, *24*, 85-112.

[13] Pan, H., Zhang, S., Chen, J., Gao, M., Liu, Y., Zhu, T., & Jiang, Y. (2018). Li-and Mn-rich layered oxide cathode materials for lithium-ion batteries: a review from fundamentals to research progress

and applications. *Molecular Systems Design & Engineering*, *3*(5), 748-803.

[14] Zhang, W., Sun, X., Tang, Y., Xia, H., Zeng, Y., Qiao, L., ... & Chen, X. (2019). Lowering charge transfer barrier of $LiMn_2O_4$ via nickel surface doping to enhance Li+ intercalation kinetics at subzero temperatures. *Journal of the American Chemical Society*, *141*(36), 14038-14042.

[15] Huang, W., Wang, G., Luo, C., Xu, Y., Xu, Y., Eckstein, B. J., ... & Marks, T. J. (2019). Controllable growth of $LiMn_2O_4$ by carbohydrate-assisted combustion synthesis for high performance Li-ion batteries. *Nano Energy*, *64*, 103936.

[16] Lyu, Y., Wu, X., Wang, K., Feng, Z., Cheng, T., Liu, Y., ... & Guo, B. (2021). An overview on the advances of $LiCoO_2$ cathodes for lithium-ion batteries. *Advanced Energy Materials*, *11*(2), 2000982.

[17] Wang, Y., Zhang, Q., Xue, Z. C., Yang, L., Wang, J., Meng, F., ... & Li, H. (2020). An in situ formed surface coating layer enabling $LiCoO_2$ with stable 4.6 V high-voltage cycle performances. *Advanced Energy Materials*, *10*(28), 2001413.

[18] Zhang, J., Hu, J., Liu, Y., Jing, Q., Yang, C., Chen, Y., & Wang, C. (2019). Sustainable and facile method for the selective recovery of lithium from cathode scrap of spent $LiFePO_4$ batteries. *ACS Sustainable Chemistry & Engineering*, *7*(6), 5626-5631.

[19] Wang, X., Feng, Z., Huang, J., Deng, W., Li, X., Zhang, H., & Wen, Z. (2018). Graphene-decorated carbon-coated $LiFePO_4$ nanospheres as a high-performance cathode material for lithium-ion batteries. *Carbon*, *127*, 149-157.

[20] Chen, C., Yao, W., He, Q., Ashuri, M., Kaduk, J., Liu, Y., & Shaw, L. (2019). Tunable $LiAlO_2/Al_2O_3$ coating through a wet-chemical method to improve cycle stability of nano-$LiCoO_2$. *ACS Applied Energy Materials*, *2*(5), 3098-3113.

[21] Zhao, Y., Li, J., & Dahn, J. R. (2017). Interdiffusion of cations from metal oxide surface coatings into $LiCoO_2$ during sintering. *Chemistry of Materials*, *29*(12), 5239-5248.

[22] Ramkumar, B., Yuvaraj, S., Surendran, S., Pandi, K., Ramasamy, H. V., Lee, Y. S., & Selvan, R. K. (2018). Synthesis and characterization of carbon coated $LiCo_{1/3}Ni_{1/3}Mn_{1/3}O_2$ and bio-mass derived graphene like porous carbon electrodes for aqueous Li-ion hybrid supercapacitor. *Journal of Physics and Chemistry of Solids*, *112*, 270-279.

[23] Wang, X., Feng, Z., Hou, X., Liu, L., He, M., He, X., ... & Wen, Z. (2020). Fluorine doped carbon coating of $LiFePO_4$ as a cathode material for lithium-ion batteries. *Chemical Engineering*

Journal, *379*, 122371.

[24] Eftekhari, A. (2017). LiFePO₄/C nanocomposites for lithium-ion batteries. *Journal of Power Sources*, *343*, 395-411.

[25] Meng, Y., Li, Y., Xia, J., Hu, Q., Ke, X., Ren, G., & Zhu, F. (2019). F-doped LiFePO₄@ N/B/F-doped carbon as high-performance cathode materials for Li-ion batteries. *Applied Surface Science*, *476*, 761-768.

[26] Shi, S., Liu, L., Ouyang, C., Wang, D. S., Wang, Z., Chen, L., & Huang, X. (2003). Enhancement of electronic conductivity of LiFePO₄ by Cr doping and its identification by first-principles calculations. *Physical Review B*, *68*(19), 195108.

[27] Ouyang, C., Shi, S., Wang, Z., Huang, X., & Chen, L. (2004). First-principles study of Li ion diffusion in LiFePO₄. *Physical Review B*, *69*(10), 104303.

[28] Cheng, H., Shapter, J. G., Li, Y., & Gao, G. (2021). Recent progress of advanced anode materials of lithium-ion batteries. *Journal of Energy Chemistry*, *57*, 451-468.

[29] Luo, J., Wu, C. E., Su, L. Y., Huang, S. S., Fang, C. C., Wu, Y. S., ... & Wu, N. L. (2018). A proof-of-concept graphite anode with a lithium dendrite suppressing polymer coating. *Journal of Power Sources*, *406*, 63-69.

[30] Periyasamy, S., & Muthuchamy, M. (2018). Electrochemical oxidation of paracetamol in water by graphite anode: effect of pH, electrolyte concentration and current density. *Journal of environmental chemical engineering*, *6*(6), 7358-7367.

[31] Cui, X., Tang, F., Li, C., Zhang, Y., Wang, P., Li, S., & Ye, X. (2017). Pretreatment of Graphite Anodes with Lithium Sulfate to Improve the Cycle Performance of Lithium-Ion Batteries. *Energy Technology*, *5*(4), 549-556.

[32] An, W., Gao, B., Mei, S., Xiang, B., Fu, J., Wang, L., ... & Huo, K. (2019). Scalable synthesis of ant-nest-like bulk porous silicon for high-performance lithium-ion battery anodes. *Nature communications*, *10*(1), 1-11.

[33] Yan, Z., Jin, H., & Guo, J. (2019). Low-temperature synthesis of graphitic carbon-coated silicon anode materials. *Carbon Energy*, *1*(2), 246-252.

[34] Wang, F., Chen, G., Zhang, N., Liu, X., & Ma, R. (2019). Engineering of carbon and other protective coating layers for stabilizing silicon anode materials. *Carbon Energy*, *1*(2), 219-245.

[35] Liu, N., Wu, H., McDowell, M. T., Yao, Y., Wang, C., & Cui, Y. (2012). A yolk-shell design for

stabilized and scalable Li-ion battery alloy anodes. *Nano letters*, *12*(6), 3315-3321.

[36] Jow, T. R., Xu, K., Borodin, O., & Ue, M. (Eds.). (2014). *Electrolytes for lithium and lithium-ion batteries* (Vol. 58, pp. 18-476). New York: Springer.

[37] Jia, H., Billmann, B., Onishi, H., Smiatek, J., Roeser, S., Wiemers-Meyer, S., ... & Cekic-Laskovic, I. (2019). LiPF6 stabilizer and transition-metal cation scavenger: a bifunctional bipyridine-based ligand for lithium-ion battery application. *Chemistry of materials*, *31*(11), 4025-4033.

[38] Ming, J., Cao, Z., Wu, Y., Wahyudi, W., Wang, W., Guo, X., ... & Alshareef, H. N. (2019). New insight on the role of electrolyte additives in rechargeable lithium-ion batteries. *ACS Energy Letters*, *4*(11), 2613-2622.

[39] Francis, C. F., Kyratzis, I. L., & Best, A. S. (2020). Lithium-ion battery separators for ionic-liquid electrolytes: a review. *Advanced Materials*, *32*(18), 1904205.

[40] Song, Y. Z., Zhang, Y., Yuan, J. J., Lin, C. E., Yin, X., Sun, C. C., ... & Zhu, L. P. (2018). Fast assemble of polyphenol derived coatings on polypropylene separator for high performance lithium-ion batteries. *Journal of Electroanalytical Chemistry*, *808*, 252-258.

[41] Jin, S. Y., Manuel, J., Zhao, X., Park, W. H., & Ahn, J. H. (2017). Surface-modified polyethylene separator via oxygen plasma treatment for lithium-ion battery. *Journal of Industrial and Engineering Chemistry*, *45*, 15-21.

[42] Ryou, M. H., Lee, Y. M., Park, J. K., & Choi, J. W. (2011). Mussel-inspired polydopamine-treated polyethylene separators for high-power Li-ion batteries. *Advanced materials*, *23*(27), 3066-3070.

[43] Zheng, H., Wang, Z., Shi, L., Zhao, Y., & Yuan, S. (2019). Enhanced thermal stability and lithium-ion conductivity of polyethylene separator by coating colloidal SiO_2 nanoparticles with porous shell. *Journal of colloid and interface science*, *554*, 29-38.

[44] Li, L., Liu, P., Fu, Q. S., Gong, Y., Zhang, S. R., He, H. J., & Chen, J. (2019). Study on preparation of polyacrylonitrile/polyimide composite lithium-ion battery separator by electrospinning. *Journal of Materials Research*, *34*(4), 642-651.

[45] He, M., Zhang, X., Jiang, K., Wang, J., & Wang, Y. (2015). Pure inorganic separator for lithium-ion batteries. *ACS applied materials & interfaces*, *7*(1), 738-742.

[46] Cho, T. H., Tanaka, M., Ohnishi, H., Kondo, Y., Yoshikazu, M., Nakamura, T., & Sakai, T. (2010). Composite nonwoven separator for lithium-ion battery: Development and characterization. *Journal of Power Sources*, *195*(13), 4272-4277.

[47] Chen, R., Li, Q., Yu, X., Chen, L., & Li, H. (2019). Approaching practically accessible solid-state batteries: stability issues related to solid electrolytes and interfaces. *Chemical reviews*, *120*(14), 6820-6877.

[48] Turcheniuk, K., Bondarev, D., Singhal, V., & Yushin, G. (2018). Ten years left to redesign lithium-ion batteries.

[49] Luo, X., Wang, J., Dooner, M., & Clarke, J. (2015). Overview of current development in electrical energy storage technologies and the application potential in power system operation. *Applied energy*, *137*, 511-536.

[50] Fan, X., & Wang, C. (2021). High-voltage liquid electrolytes for Li batteries: progress and perspectives. *Chemical Society Reviews*.

[51] Zhao, Q., Stalin, S., Zhao, C. Z., & Archer, L. A. (2020). Designing solid-state electrolytes for safe, energy-dense batteries. Nature Reviews Materials, 5(3), 229-252.

[52] Wang, L., Menakath, A., Han, F., Wang, Y., Zavalij, P. Y., Gaskell, K. J., ... & Eichhorn, B. W. (2019). Identifying the components of the solid–electrolyte interphase in Li-ion batteries. *Nature chemistry*, *11*(9), 789-796.

[53] Jana, A., Woo, S. I., Vikrant, K. S. N., & García, R. E. (2019). Electrochemomechanics of lithium dendrite growth. *Energy & Environmental Science*, *12*(12), 3595-3607.

[54] He, J., & Manthiram, A. (2020). Long-life, high-rate lithium–sulfur cells with a carbon-free VN host as an efficient polysulfide adsorbent and lithium dendrite inhibitor. *Advanced Energy Materials*, *10*(3), 1903241.

[55] Hong, Z., & Viswanathan, V. (2019). Prospect of thermal shock induced healing of lithium dendrite. *ACS Energy Letters*, *4*(5), 1012-1019.

[56] Han, F., Westover, A. S., Yue, J., Fan, X., Wang, F., Chi, M., ... & Wang, C. (2019). High electronic conductivity as the origin of lithium dendrite formation within solid electrolytes. *Nature Energy*, *4*(3), 187-196.

[57] Patra, S., BR, V. K., Chakravarty, S., & Murugan, R. (2019). Microstructural engineering in lithium garnets by hot isostatic press to cordon lithium dendrite growth and negate interfacial resistance for all solid-state battery applications. *Electrochimica Acta*, *312*, 320-328.

[58] Su, Y., Rong, X., Gao, A., Liu, Y., Li, J., Mao, M., ... & Hu, Y. S. (2022). Rational design of a topological polymeric solid electrolyte for high-performance all-solid-state alkali metal

batteries. *Nature communications*, *13*(1), 1-15.

[59] Oh, D. Y., Kim, K. T., Jung, S. H., Kim, D. H., Jun, S., Jeoung, S., ... & Jung, Y. S. (2022). Tactical hybrids of Li$^+$-conductive dry polymer electrolytes with sulfide solid electrolytes: Toward practical all-solid-state batteries with wider temperature operability. *Materials Today*, *53*, 7-15.

[60] Mozaffari, K., Liu, L., & Sharma, P. (2022). Theory of soft solid electrolytes: Overall properties of composite electrolytes, effect of deformation and microstructural design for enhanced ionic conductivity. *Journal of the Mechanics and Physics of Solids*, *158*, 104621.

[61] Wang, H., Sheng, L., Yasin, G., Wang, L., Xu, H., & He, X. (2020). Reviewing the current status and development of polymer electrolytes for solid-state lithium batteries. *Energy Storage Materials*, *33*, 188-215.

[62] Płcharski, J., & Weiczorek, W. (1988). PEO based composite solid electrolyte containing nasicon. *Solid State Ionics*, *28*, 979-982.

[63] Liu, Q., Liu, Y., Jiao, X., Song, Z., Sadd, M., Xu, X., ... & Song, J. (2019). Enhanced ionic conductivity and interface stability of hybrid solid-state polymer electrolyte for rechargeable lithium metal batteries. *Energy Storage Materials*, *23*, 105-111.

[64] Tsutsumi, H., Yamamoto, M., Morita, M., Matsuda, Y., Nakamura, T., & Asai, H. (1993). Single- and double-ion type cross-linked polysiloxane solid electrolytes for lithium cells. *Journal of power sources*, *41*(3), 291-298.

[65] Commarieu, B., Paolella, A., Collin-Martin, S., Gagnon, C., Vijh, A., Guerfi, A., & Zaghib, K. (2019). Solid-to-liquid transition of polycarbonate solid electrolytes in Li-metal batteries. *Journal of Power Sources*, *436*, 226852.

[66] Wu, Y., Li, Y., Wang, Y., Liu, Q., Chen, Q., & Chen, M. (2022). Advances and prospects of PVDF based polymer electrolytes. *Journal of Energy Chemistry*, *64*, 62-84.

[67] Zheng, Y., Yao, Y., Ou, J., Li, M., Luo, D., Dou, H., ... & Chen, Z. (2020). A review of composite solid-state electrolytes for lithium batteries: fundamentals, key materials and advanced structures. *Chemical Society Reviews*, *49*(23), 8790-8839.

[68] Forsyth, M., Porcarelli, L., Wang, X., Goujon, N., & Mecerreyes, D. (2019). Innovative electrolytes based on ionic liquids and polymers for next-generation solid-state batteries. *Accounts of chemical research*, *52*(3), 686-694.

[69] Cao, C., Li, Z. B., Wang, X. L., Zhao, X. B., & Han, W. Q. (2014). Recent advances in inorganic

solid electrolytes for lithium batteries. *Frontiers in energy research*, *2*, 25.

[70] Famprikis, T., Canepa, P., Dawson, J. A., Islam, M. S., & Masquelier, C. (2019). Fundamentals of inorganic solid-state electrolytes for batteries. *Nature materials*, *18*(12), 1278-1291.

[71] Zhang, T., He, W., Zhang, W., Wang, T., Li, P., Sun, Z., & Yu, X. (2020). Designing composite solid-state electrolytes for high performance lithium ion or lithium metal batteries. Chemical Science, 11(33), 8686-8707.

[72] DeWees, R., & Wang, H. (2019). Synthesis and properties of NaSICON-type LATP and LAGP solid electrolytes. *ChemSusChem*, *12*(16), 3713-3725.

[73] Ishado, Y., Inoishi, A., & Okada, S. (2020). Exploring Factors Limiting Three-Na^+ Extraction from $Na_3V_2(PO_4)_3$. *Electrochemistry*, 20-00080.

[74] Yang, Y., Chen, W., & Lu, X. (2022). Coordination Li diffusion chemistry in NASICON $Li_{1.5}Al_{0.5}Ge_{1.5}(PO_4)_3$ solid electrolyte. *Solid State Ionics*, *381*, 115947.

[75] Wang, C., Fu, K., Kammampata, S. P., McOwen, D. W., Samson, A. J., Zhang, L., ... & Hu, L. (2020). Garnet-type solid-state electrolytes: materials, interfaces, and batteries. *Chemical reviews*, *120*(10), 4257-4300.

[76] Yeandel, S. R., Chapman, B. J., Slater, P. R., & Goddard, P. (2018). Structure and lithium-ion dynamics in fluoride-doped cubic $Li_7La_3Zr_2O_{12}$ (LLZO) garnet for Li solid-state battery applications. *The Journal of Physical Chemistry C*, *122*(49), 27811-27819.

[77] Raju, M. M., Altayran, F., Johnson, M., Wang, D., & Zhang, Q. (2021). Crystal structure and preparation of $Li_7La_3Zr_2O_{12}$ (LLZO) solid-state electrolyte and doping impacts on the conductivity: An overview. *Electrochem*, *2*(3), 390-414.

[78] Li, Y., Han, J. T., Wang, C. A., Xie, H., & Goodenough, J. B. (2012). Optimizing Li+ conductivity in a garnet framework. Journal of Materials Chemistry, 22(30), 15357-15361.

[79] Krauskopf, T., Dippel, R., Hartmann, H., Peppler, K., Mogwitz, B., Richter, F. H., ... & Janek, J. (2019). Lithium-metal growth kinetics on LLZO garnet-type solid electrolytes. *Joule*, *3*(8), 2030-2049.

[80] Kanno, R., & Murayama, M. (2001). Lithium ionic conductor thio-LISICON: the Li_2S-GeS_2-P_2S_5 system. *Journal of the electrochemical society*, *148*(7), A742.

[81] Bruce, P. G., & West, A. R. (1982). Ionic conductivity of LISICON solid solutions, $Li_{2+2x}Zn_{1-x}GeO_4$. *Journal of Solid-State Chemistry*, *44*(3), 354-365.

[82] Murayama, M., Kanno, R., Irie, M., Ito, S., Hata, T., Sonoyama, N., & Kawamoto, Y. (2002). Synthesis of new lithium ionic conductor thio-LISICON-lithium silicon sulfides system. *Journal of Solid-State Chemistry*, *168*(1), 140-148.

[83] Kamaya, N., Homma, K., Yamakawa, Y., Hirayama, M., Kanno, R., Yonemura, M., ... & Mitsui, A. (2011). A lithium superionic conductor. *Nature materials*, *10*(9), 682-686.

[84] Reddy, M. V., Julien, C. M., Mauger, A., & Zaghib, K. (2020). Sulfide and oxide inorganic solid electrolytes for all-solid-state Li batteries: a review. *Nanomaterials*, *10*(8), 1606.

[85] Bonanos, N., Knight, K. S., & Ellis, B. (1995). Perovskite solid electrolytes: structure, transport properties and fuel cell applications. *Solid State Ionics*, *79*, 161-170.

[86] Lu, J., & Li, Y. (2021). Perovskite-type Li-ion solid electrolytes: a review. *Journal of Materials Science: Materials in Electronics*, *32*(8), 9736-9754.

[87] Zhang, L., Zhang, X., Tian, G., Zhang, Q., Knapp, M., Ehrenberg, H., ... & Du, F. (2020). Lithium lanthanum titanate perovskite as an anode for lithium-ion batteries. *Nature communications*, *11*(1), 1-8.

[88] Dawson, J. A., Attari, T. S., Chen, H., Emge, S. P., Johnston, K. E., & Islam, M. S. (2018). Elucidating lithium-ion and proton dynamics in anti-perovskite solid electrolytes. *Energy & Environmental Science*, *11*(10), 2993-3002.

[89] Yin, L., Murphy, M., Kim, K., Hu, L., Cabana, J., Siegel, D. J., & Lapidus, S. H. (2020). Synthesis of antiperovskite solid electrolytes: comparing Li_3SI, Na_3SI, and Ag_3SI. *Inorganic Chemistry*, *59*(16), 11244-11247.

[90] Xia, W., Zhao, Y., Zhao, F., Adair, K., Zhao, R., Li, S., ... & Sun, X. (2022). Antiperovskite Electrolytes for Solid-State Batteries. *Chemical Reviews*, *122*(3), 3763-3819.

[91] Kozen, A. C., Pearse, A. J., Lin, C. F., Noked, M., & Rubloff, G. W. (2015). Atomic layer deposition of the solid electrolyte LiPON. *Chemistry of Materials*, *27*(15), 5324-5331.

[92] Senevirathne, K., Day, C. S., Gross, M. D., Lachgar, A., & Holzwarth, N. A. W. (2013). A new crystalline LiPON electrolyte: Synthesis, properties, and electronic structure. *Solid State Ionics*, *233*, 95-101.

[93] Hamon, Y., Douard, A., Sabary, F., Marcel, C., Vinatier, P., Pecquenard, B., & Levasseur, A. (2006). Influence of sputtering conditions on ionic conductivity of LiPON thin films. *Solid State Ionics*, *177*(3-4), 257-261.

[94] Lacivita, V., Artrith, N., & Ceder, G. (2018). Structural and compositional factors that control the li-ion conductivity in LiPON electrolytes. *Chemistry of Materials*, *30*(20), 7077-7090.

[95] Hayashi, A., Fukuda, T., Hama, S., Yamashita, H., Morimoto, H., Minami, T., & Tatsumisago, M. (2004). Lithium Ion Conducting Glasses and Glass-Ceramics in the Systems Li_2S-M_xS_y (M= Al, Si and P) Prepared by Mechanical Milling. In *Journal of the Ceramic Society of Japan, Supplement Journal of the Ceramic Society of Japan, Supplement 112-1, PacRim5 Special Issue* (pp. S695-S699). The Ceramic Society of Japan.

[96] Chen, X., Guan, Z., Chu, F., Xue, Z., Wu, F., & Yu, Y. (2022). Air-stable inorganic solid-state electrolytes for high energy density lithium batteries: Challenges, strategies, and prospects. *InfoMat*, *4*(1), e12248.

[97] Khorassani, A., Izquierdo, G., & West, A. R. (1981). The solid electrolyte system, Li_3PO_4-Li_4SiO_4. *Materials Research Bulletin*, *16*(12), 1561-1567.

[98] Zheng, F., Kotobuki, M., Song, S., Lai, M. O., & Lu, L. (2018). Review on solid electrolytes for all-solid-state lithium-ion batteries. Journal of Power Sources, 389, 198-213.

[99] Sun, Y. Y., Zhang, Q., Yan, L., Wang, T. B., & Hou, P. Y. (2022). A review of interfaces within solid-state electrolytes: fundamentals, issues and advancements. Chemical Engineering Journal, 437, 135179.

[100] Xu, H., Yu, Y., Wang, Z., & Shao, G. (2019). First principal material genome approach for all solid-state batteries. *Energy & Environmental Materials*, *2*(4), 234-250.

[101] Yu, T., Yang, X., Yang, R., Bai, X., Xu, G., Zhao, S., ... & Wang, J. (2021). Progress and perspectives on typical inorganic solid-state electrolytes. *Journal of Alloys and Compounds*, *885*, 161013.

[102] Ravdel, B., Abraham, K. M., Gitzendanner, R., DiCarlo, J., Lucht, B., & Campion, C. (2003). Thermal stability of lithium-ion battery electrolytes. Journal of Power Sources, 119, 805-810.

[103] Yan, G. (2020). *Mechanical behavior of solid electrolyte materials for lithium-ion batteries* (No. RWTH-2020-04421). Lehrstuhl für Werkstofftechnik der Metalle und Institut für Eisenhüttenkunde.

[104] Balaish, M., Gonzalez-Rosillo, J. C., Kim, K. J., Zhu, Y., Hood, Z. D., & Rupp, J. L. (2021). Processing thin but robust electrolytes for solid-state batteries. *Nature Energy*, *6*(3), 227-239.

[105] Key, B., Schroeder, D. J., Ingram, B. J., & Vaughey, J. T. (2012). Solution-based synthesis and

characterization of lithium-ion conducting phosphate ceramics for lithium metal batteries. *Chemistry of materials*, *24*(2), 287-293.

[106] Mariappan, C. R., Yada, C., Rosciano, F., & Roling, B. (2011). Correlation between micro-structural properties and ionic conductivity of $Li_{1.5}Al_{0.5}Ge_{1.5}(PO_4)_3$ ceramics. *Journal of Power Sources*, *196*(15), 6456-6464.

[107] Thokchom, J. S., & Kumar, B. (2010). The effects of crystallization parameters on the ionic conductivity of a lithium aluminum germanium phosphate glass-ceramic. *Journal of Power Sources*, *195*(9), 2870-2876.

[108] Yang, J., Huang, Z., Huang, B., Zhou, J., & Xu, X. (2015). Influence of phosphorus sources on lithium ion conducting performance in the system of $Li_2O\text{-}Al_2O_3\text{-}GeO_2\text{-}P_2O_5$ glass-ceramics. *Solid State Ionics*, *270*, 61-65.

[109] Cui, Y., Mahmoud, M. M., Rohde, M., Ziebert, C., & Seifert, H. J. (2016). Thermal and ionic conductivity studies of lithium aluminum germanium phosphate solid-state electrolyte. *Solid State Ionics*, *289*, 125-132.

[110] Jiménez, R., del Campo, A., Calzada, M. L., Sanz, J., Kobylianska, S. D., Liniova, B. O., ... & Ragulya, A. V. (2018). Improved conductivity in tape casted Li-NASICON supported thick films: Effect of temperature treatments and lamination. *Journal of the European Ceramic Society*, *38*(4), 1679-1687.

[111] Yoon, Y., Kim, J., Park, C., & Shin, D. (2013). The relationship of structural and electrochemical properties of NASICON structure $Li_{1.3}Al_{0.3}Ti_{1.7}(PO_4)_3$ electrolytes by a sol-gel method. *Journal of Ceramic Processing Research*, *14*(4).

[112] Bitzer, M., Van Gestel, T., & Uhlenbruck, S. (2016). Sol-gel synthesis of thin solid $Li_7La_3Zr_2O_{12}$ electrolyte films for Li-ion batteries. *Thin Solid Films*, *615*, 128-134.

[113] Ma, Q., Xu, Q., Tsai, C. L., Tietz, F., & Guillon, O. (2016). A Novel Sol-Gel Method for Large-Scale Production of Nanopowders: Preparation of $Li_{1.5}Al_{0.5}Ti_{1.5}(PO_4)_3$ as an Example. *Journal of the American Ceramic Society*, *99*(2), 410-414.

[114] Lu, X., Wang, R., Zhang, F., & Li, J. (2020). The influence of phosphorous source on the properties of NASICON lithium-ion conductor $Li_{1.3}Al_{0.3}Ti_{1.7}(PO_4)_3$. *Solid State Ionics*, *354*, 115417.

[115] Yi, E. J., Yoon, K. Y., Jung, H. A., Nakayama, T., Ji, M. J., & Hwang, H. (2019). Fabrication

and electrochemical properties of $Li_{1.3}Al_{0.3}Ti_{1.7}(PO_4)_3$ solid electrolytes by sol-gel method. Applied Surface Science, 473, 622-626.

[116] Liu, X., Tan, J., Fu, J., Yuan, R., Wen, H., & Zhang, C. (2017). Facile synthesis of nanosized lithium-ion-conducting solid electrolyte $Li_{1.4}Al_{0.4}Ti_{1.6}(PO_4)_3$ and its mechanical nanocomposites with $LiMn_2O_4$ for enhanced cyclic performance in lithium-ion batteries. *ACS Applied Materials & Interfaces*, *9*(13), 11696-11703.

[117] Zhao, E., Ma, F., Jin, Y., & Kanamura, K. (2016). Pechini synthesis of high ionic conductivity $Li_{1.3}Al_{0.3}Ti_{1.7}(PO_4)_3$ solid electrolytes: The effect of dispersant. *Journal of Alloys and Compounds*, *680*, 646-653.

[118] Huang, L., Wen, Z., Wu, M., Wu, X., Liu, Y., & Wang, X. (2011). Electrochemical properties of $Li_{1.4}Al_{0.4}Ti_{1.6}(PO_4)_3$ synthesized by a co-precipitation method. *Journal of Power Sources*, *196*(16), 6943-6946.

[119] Wang, X., & Yushin, G. (2015). Chemical vapor deposition and atomic layer deposition for advanced lithium-ion batteries and supercapacitors. *Energy & Environmental Science*, *8*(7), 1889-1904.

[120] Pearse, A., Schmitt, T., Sahadeo, E., Stewart, D. M., Kozen, A., Gerasopoulos, K., ... & Gregorczyk, K. E. (2018). Three-dimensional solid-state lithium-ion batteries fabricated by conformal vapor-phase chemistry. *ACS nano*, *12*(5), 4286-4294.

[121] Rosenberger, A., Gao, Y., & Stanciu, L. (2015). Field-assisted sintering of $Li_{1.3}Al_{0.3}Ti_{1.7}(PO_4)_3$ solid-state electrolyte. *Solid State Ionics*, *278*, 217-221.

[122] Liu, Y., Sun, Q., Wang, D., Adair, K., Liang, J., & Sun, X. (2018). Development of the cold sintering process and its application in solid-state lithium batteries. *Journal of Power Sources*, *393*, 193-203.

[123] Lee, W., Lyon, C. K., Seo, J. H., Lopez-Hallman, R., Leng, Y., Wang, C. Y., ... & Gomez, E. D. (2019). Ceramic–salt composite electrolytes from cold sintering. *Advanced Functional Materials*, *29*(20), 1807872.

[124] Chang, C. M., Lee, Y. I., Hong, S. H., & Park, H. M. (2005). Spark plasma sintering of LiTi2 (PO4) 3-based solid electrolytes. *Journal of the American Ceramic Society*, *88*(7), 1803-1807.

[125] Waetzig, K., Rost, A., Langklotz, U., Matthey, B., & Schilm, J. (2016). An explanation of the microcrack formation in $Li_{1.3}Al_{0.3}Ti_{1.7}(PO_4)_3$ ceramics. *Journal of the European Ceramic*

Society, *36*(8), 1995-2001.

[126]   Kubanska, A., Castro, L., Tortet, L., Schäf, O., Dollé, M., & Bouchet, R. (2014). Elaboration of controlled size $Li_{1.5}Al_{0.5}Ge_{1.5}(PO_4)_3$ crystallites from glass-ceramics. *Solid State Ionics*, *266*, 44-50.

[127]   Levit, O., Xu, P., Shvartsev, B., Avioz Cohen, G., Stanciu, L., Tsur, Y., & Ein-Eli, Y. (2020). Interphases Formation and Analysis at the Lithium-Aluminum-Titanium-Phosphate (LATP) and Lithium-Manganese Oxide Spinel (LMO) Interface during High-Temperature Bonding. Energy Technology, 8(12), 2000634.

[128]   Hallopeau, L., Bregiroux, D., Rousse, G., Portehault, D., Stevens, P., Toussaint, G., & Laberty-Robert, C. (2018). Microwave-assisted reactive sintering and lithium-ion conductivity of $Li_{1.3}Al_{0.3}Ti_{1.7}(PO_4)_3$ solid electrolyte. *Journal of Power Sources*, *378*, 48-52.

[129]   Davis III, C., & Nino, J. C. (2015). Microwave Processing for Improved Ionic Conductivity in Li_2O-Al_2O_3-TiO_2-P_2O_5 Glass-Ceramics. *Journal of the American Ceramic Society*, *98*(8), 2422-2427.

[130]   Munir, Z. A., Anselmi-Tamburini, U., & Ohyanagi, M. (2006). The effect of electric field and pressure on the synthesis and consolidation of materials: A review of the spark plasma sintering method. *Journal of materials science*, *41*(3), 763-777.

[131]   Omori, M. (2000). Sintering, consolidation, reaction and crystal growth by the spark plasma system (SPS). *Materials Science and Engineering: A*, *287*(2), 183-188.

[132]   Croquesel, J., Bouvard, D., Chaix, J. M., Carry, C. P., Saunier, S., & Marinel, S. (2016). Direct microwave sintering of pure alumina in a single mode cavity: Grain size and phase transformation effects. *Acta Materialia*, *116*, 53-62.

[133]   Davis III, C. G., & Nino, J. C. (2014, April). Enhanced Ionic Conductivity of Microwave Processed Li_2O-Al_2O_3-TiO_2-P_2O_5 Glass Ceramics. In Electrochemical Society Meeting Abstracts 225 (No. 2, pp. 298-298). The Electrochemical Society, Inc.

[134]   Yao, Y., Huang, Z., Xie, P., Lacey, S. D., Jacob, R. J., Xie, H., ... & Hu, L. (2018). Carbothermal shock synthesis of high-entropy-alloy nanoparticles. *Science*, *359*(6383), 1489-1494.

[135]   Li, T., Yao, Y., Huang, Z., Xie, P., Liu, Z., Yang, M., ... & Hu, L. (2021). Denary oxide nanoparticles as highly stable catalysts for methane combustion. *Nature Catalysis*, *4*(1), 62-70.

[136]   Wang, C., Ping, W., Bai, Q., Cui, H., Hensleigh, R., Wang, R., ... & Hu, L. (2020). A general method to synthesize and sinter bulk ceramics in seconds. *Science*, *368*(6490), 521-526.

[137]   Qiao, H., Wang, X., Dong, Q., Zheng, H., Chen, G., Hong, M., ... & Hu, L. (2021). A high-entropy phosphate catalyst for oxygen evolution reaction. *Nano Energy*, *86*, 106029.

[138]   Abdelhafiz, A., Wang, B., Harutyunyan, A. R., & Li, J. (2022). Carbothermal shock synthesis of high entropy oxide catalysts: dynamic structural and chemical reconstruction boosting the catalytic activity and stability toward oxygen evolution reaction. Advanced Energy Materials, 12(35), 2200742.

[139]   Song, J. Y., Kim, C., Kim, M., Cho, K. M., Gereige, I., Jung, W. B., ... & Jung, H. T. (2021). Generation of high-density nanoparticles in the carbothermal shock method. Science Advances, 7(48), eabk2984.

[140]   Monroe, C., & Newman, J. (2005). The impact of elastic deformation on deposition kinetics at lithium/polymer interfaces. *Journal of The Electrochemical Society*, *152*(2), A396.

[141]   Ni, J. E., Case, E. D., Sakamoto, J. S., Rangasamy, E., & Wolfenstine, J. B. (2012). Room temperature elastic moduli and Vickers hardness of hot-pressed LLZO cubic garnet. *Journal of Materials Science*, *47*(23), 7978-7985.

[142]   Jackman, S. D., & Cutler, R. A. (2012). Effect of microcracking on ionic conductivity in LATP. *Journal of Power Sources*, *218*, 65-72.

[143]   Lan, W., Fan, H., Lau, V. W. H., Zhang, J., Zhang, J., Zhao, R., & Chen, H. (2020). Realizing $Li_7La_3Zr_2O_{12}$ garnets with high Li^+ conductivity and dense microstructures by Ga/Nb dual substitution for lithium solid-state battery applications. *Sustainable Energy & Fuels*, *4*(4), 1812-1821.

[144]   Zhang, L., Yang, K., Mi, J., Lu, L., Zhao, L., Wang, L., ... & Zeng, H. (2015). Na3PSe4: A novel chalcogenide solid electrolyte with high ionic conductivity. *Advanced Energy Materials*, *5*(24), 1501294.

[145]   Wang, D., Zhu, C., Fu, Y., Sun, X., & Yang, Y. (2020). Interfaces in garnet-based all-solid-state lithium batteries. *Advanced Energy Materials*, *10*(39), 2001318.

[146]   Yuan, C., Gao, X., Jia, Y., Zhang, W., Wu, Q., & Xu, J. (2021). Coupled crack propagation and dendrite growth in solid electrolyte of all-solid-state battery. *Nano Energy*, *86*, 106057.

[147]   Hao, S., Daemi, S. R., Heenan, T. M., Du, W., Tan, C., Storm, M., ... & Shearing, P. R. (2021).

Tracking lithium penetration in solid electrolytes in 3D by in-situ synchrotron X-ray computed tomography. *Nano Energy*, *82*, 105744.

[148]   Porz, L., Swamy, T., Sheldon, B. W., Rettenwander, D., Frömling, T., Thaman, H. L., ... & Chiang, Y. M. (2017). Mechanism of lithium metal penetration through inorganic solid electrolytes. *Advanced Energy Materials*, *7*(20), 1701003.

[149]   Cao, D., Sun, X., Li, Q., Natan, A., Xiang, P., & Zhu, H. (2020). Lithium dendrite in all-solid-state batteries: growth mechanisms, suppression strategies, and characterizations. Matter, 3(1), 57-94.

[150]   Zhu, J., Zhao, J., Xiang, Y., Lin, M., Wang, H., Zheng, B., ... & Yang, Y. (2020). Chemomechanical failure mechanism study in NASICON-type $Li_{1.3}Al_{0.3}Ti_{1.7}(PO_4)_3$ solid-state lithium batteries. *Chemistry of Materials*, *32*(12), 4998-5008.

[151]   Fincher, C. D., Ojeda, D., Zhang, Y., Pharr, G. M., & Pharr, M. (2020). Mechanical properties of metallic lithium: from nano to bulk scales. *Acta Materialia*, *186*, 215-222.

[152]   Chen, Z., Kim, G. T., Kim, J. K., Zarrabeitia, M., Kuenzel, M., Liang, H. P., ... & Passerini, S. (2021). Highly Stable Quasi-Solid-State Lithium Metal Batteries: Reinforced $Li_{1.3}Al_{0.3}Ti_{1.7}(PO_4)_3$/Li Interface by a Protection Interlayer. *Advanced Energy Materials*, *11*(30), 2101339.

[153]   Qi, Y., Ban, C., & Harris, S. J. (2020). A new general paradigm for understanding and preventing Li metal penetration through solid electrolytes. Joule, 4(12), 2599-2608.

[154]   Nagao, M., Hayashi, A., Tatsumisago, M., Kanetsuku, T., Tsuda, T., & Kuwabata, S. (2013). In situ SEM study of a lithium deposition and dissolution mechanism in a bulk-type solid-state cell with a Li_2S-P_2S_5 solid electrolyte. *Physical Chemistry Chemical Physics*, *15*(42), 18600-18606.

[155]   Cheng, E. J., Sharafi, A., & Sakamoto, J. (2017). Intergranular Li metal propagation through polycrystalline $Li_{6.25}Al_{0.25}La_3Zr_2O_{12}$ ceramic electrolyte. *Electrochimica Acta*, *223*, 85-91.

[156]   Shi, T., Zhang, Y. Q., Tu, Q., Wang, Y., Scott, M. C., & Ceder, G. (2020). Characterization of mechanical degradation in an all-solid-state battery cathode. *Journal of Materials Chemistry A*, *8*(34), 17399-17404.

[157]   Kazyak, E., Garcia-Mendez, R., LePage, W. S., Sharafi, A., Davis, A. L., Sanchez, A. J., ... & Dasgupta, N. P. (2020). Li penetration in ceramic solid electrolytes: operando microscopy analysis

of morphology, propagation, and reversibility. *Matter*, *2*(4), 1025-1048.

[158]   Zhang, L., Yang, T., Du, C., Liu, Q., Tang, Y., Zhao, J., ... & Huang, J. (2020). Lithium whisker growth and stress generation in an in situ atomic force microscope–environmental transmission electron microscope set-up. *Nature nanotechnology*, *15*(2), 94-98.

[159]   Vishnugopi, B. S., Dixit, M. B., Hao, F., Shyam, B., Cook, J. B., Hatzell, K. B., & Mukherjee, P. P. (2022). Mesoscale interrogation reveals mechanistic origins of lithium filaments along grain boundaries in inorganic solid electrolytes. Advanced Energy Materials, 12(3), 2102825.

[160]   Shishvan, S. S., Fleck, N. A., McMeeking, R. M., & Deshpande, V. S. (2020). Growth rate of lithium filaments in ceramic electrolytes. *Acta Materialia*, *196*, 444-455.

[161]   Song, X., Lu, Y., Wang, F., Zhao, X., & Chen, H. (2020). A coupled electro-chemo-mechanical model for all-solid-state thin film Li-ion batteries: The effects of bending on battery performances. *Journal of Power Sources*, *452*, 227803.

[162]   Tantratian, K., Yan, H., Ellwood, K., Harrison, E. T., & Chen, L. (2021). Unraveling the Li penetration mechanism in polycrystalline solid electrolytes. *Advanced Energy Materials*, *11*(13), 2003417.

[163]   Tian, H. K., Liu, Z., Ji, Y., Chen, L. Q., & Qi, Y. (2019). Interfacial electronic properties dictate Li dendrite growth in solid electrolytes. *Chemistry of Materials*, *31*(18), 7351-7359.

[164]   Verma, A., Kawakami, H., Wada, H., Hirowatari, A., Ikeda, N., Mizuno, Y., ... & Mukherjee, P. P. (2021). Microstructure and pressure-driven electrodeposition stability in solid-state batteries. *Cell Reports Physical Science*, *2*(1), 100301.

[165]   Tu, Q., Barroso-Luque, L., Shi, T., & Ceder, G. (2020). Electrodeposition and mechanical stability at lithium-solid electrolyte interface during plating in solid-state batteries. *Cell Reports Physical Science*, *1*(7), 100106.

[166]   Wang, X., Zeng, W., Hong, L., Xu, W., Yang, H., Wang, F., ... & Jiang, H. (2018). Stress-driven lithium dendrite growth mechanism and dendrite mitigation by electroplating on soft substrates. *Nature Energy*, *3*(3), 227-235.

[167]   Fu, K., Gong, Y., Liu, B., Zhu, Y., Xu, S., Yao, Y., ... & Hu, L. (2017). Toward garnet electrolyte–based Li metal batteries: An ultrathin, highly effective, artificial solid-state electrolyte/metallic Li interface. *Science Advances*, *3*(4), e1601659.

[168]   Li, H. Y., Huang, B., Huang, Z., & Wang, C. A. (2019). Enhanced mechanical strength and

ionic conductivity of LLZO solid electrolytes by oscillatory pressure sintering. *Ceramics International*, *45*(14), 18115-18118.

[169]   Yu, S., & Siegel, D. J. (2018). Grain boundary softening: a potential mechanism for lithium metal penetration through stiff solid electrolytes. ACS applied materials & interfaces, 10(44), 38151-38158.

[170]   Zangina, T., Hassan, J., Matori, K. A., Ahmadu, U., & See, A. (2016). Sintering behavior, ac conductivity and dielectric relaxation of $Li_{1.3}Ti_{1.7}Al_{0.3}(PO_4)_3$ NASICON compound. Results in physics, 6, 719-725.

[171]   Zhong, Y., Luo, J., Shang, F., & Chen, G. (2022). Preparation, microstructure and ionic conductivity of $Li_{1.3}Al_{0.3}Ti_{1.7}(PO_4)_3/50Li_2O-50P_2O_5$ glass ceramic electrolytes. Journal of Materials Science: Materials in Electronics, 33(10), 7869-7882.

[172]   Narváez-Semanate, J. L., & Rodrigues, A. C. M. (2010). Microstructure and ionic conductivity of $Li_{1+x}Al_xTi_{2-x}(PO_4)_3$ NASICON glass-ceramics. Solid State Ionics, 181(25-26), 1197-1204.

[173]   Soman, S., Sonigra, D., & Kulkarni, A. R. (2016). Isothermal crystallization and effect of soak time on phase evolution, microstructure and ionic conductivity of $Li_2O-Al_2O_3-TiO_2-P_2O_5$ glass–ceramic. Journal of Non-Crystalline Solids, 439, 38-45.

[174]   Сапрыкова З.А. Физико-химические методы исследования координационных соединений в растворах. (2002).

[175]   Яцимирский, К. Б., & Васильев, В. П. (1959). Константы нестойкости комплексных соединений.

[176]   Либерман Н.Р. Спектроскопические методы в химии комплексных соединении.

[177]   Ashton, T. E., Baker, P. J., Shakespeare, Y. S., Commandeur, D., & Darr, J. A. (2022). Phase Evolution and Li Diffusion in LATP Solid-State Electrolyte Synthesized via a Direct Heat-Cycling Method. Advanced Energy and Sustainability Research, 3(8), 2200017.

[178]   Giarola, M., Sanson, A., Tietz, F., Pristat, S., Dashjav, E., Rettenwander, D., ... & Mariotto, G. (2017). Structure and vibrational dynamics of NASICON-type $LiTi_2(PO_4)_3$. The Journal of Physical Chemistry C, 121(7), 3697-3706.

[179]   Jiménez, R., Sobrados, I., Martínez-Chaparro, S., del Campo, A. A., Calzada, M. L., Sanz, J., ... & Kežionis, A. (2019). Preparation and characterization of large area Li-NASICON

electrolyte thick films. Inorganics, 7(9), 107.

[180]   Kuz'micheva, G. M., Savinkina, E. V., Obolenskaya, L. N., Belogorokhova, L. I., Mavrin, B. N., Chernobrovkin, M. G., & Belogorokhov, A. I. (2010). Synthesis, characterization, and properties of nanoscale titanium dioxide modifications with anatase and η-TiO$_2$ structures. Crystallography Reports, 55, 866-871.

[181]   Etacheri, V., Seery, M. K., Hinder, S. J., & Pillai, S. C. (2011). Oxygen rich titania: A dopant free, high temperature stable, and visible-light active anatase photocatalyst. Advanced Functional Materials, 21(19), 3744-3752.

[182]   Cho, S. G., Johnson, P. F., & Condrate, R. A. (1990). Thermal decomposition of (Sr, Ti) organic precursors during the Pechini process. Journal of Materials Science, 25, 4738-4744.

[183]   Li, T., Tian, B., Zhang, J., Dong, R., Wang, T., & Yang, F. (2013). Facile tailoring of anatase TiO2 morphology by use of H2O2: From microflowers with dominant {101} facets to microspheres with exposed {001} facets. Industrial & Engineering Chemistry Research, 52(20), 6704-6712.

[184]   Savinkina, E. V., Obolenskaya, L. N., Kuzmicheva, G. M., Kabachkov, E. N., Gainanova, A. A., Zubavichus, Y. V., ... & Sadovskaya, N. V. (2015). Introduction of peroxo groups into titania: Preparation, characterization and properties of the new peroxo-containing phase. CrystEngComm, 17(37), 7113-7123.

[185]   Wu, J. Y., & Chen, Y. W. (2020). Preparation of WO$_3$-modified TiO$_2$ thin film by peroxo sol-gel method and its photocatalytic activity in degradation of methylene blue. Research on Chemical Intermediates, 46, 4627-4643.

[186]   Bordiga, S., Damin, A., Bonino, F., Ricchiardi, G., Lamberti, C., & Zecchina, A. (2002). The Structure of the Peroxo Species in the TS-1 Catalyst as Investigated by Resonant Raman Spectroscopy. Angewandte Chemie International Edition, 41(24), 4734-4737.

[187]   Irvine, J. T., Sinclair, D. C., & West, A. R. (1990). Electroceramics: characterization by impedance spectroscopy. Advanced materials, 2(3), 132-138.

[188]   Dickinson, E. J., & Wain, A. J. (2020). The Butler-Volmer equation in electrochemical theory: Origins, value, and practical application. Journal of Electroanalytical Chemistry, 872, 114145.

[189]   Fabre, S. D., Guy-Bouyssou, D., Bouillon, P., Le Cras, F., & Delacourt, C. (2011). Charge/discharge simulation of an all-solid-state thin-film battery using a one-dimensional model.

Journal of The Electrochemical Society, 159(2), A104.

[190] Ferrese, A., & Newman, J. (2014). Mechanical deformation of a lithium-metal anode due to a very stiff separator. Journal of The Electrochemical Society, 161(9), A1350.

[191] Monroe, C., & Newman, J. (2004). The effect of interfacial deformation on electrodeposition kinetics. Journal of The Electrochemical Society, 151(6), A880.

[192] Ghosh, S., & Mallett, R. L. (1994). Voronoi cell finite elements. Computers & Structures, 50(1), 33-46.

[193] Mollon, G., & Zhao, J. (2012). Fourier–Voronoi-based generation of realistic samples for discrete modelling of granular materials. Granular matter, 14, 621-638.

[194] Decker, L., & Jeulin, D. (2000). Simulation 3D de matériaux aléatoires polycristallins. Revue de Métallurgie, 97(2), 271-175.

[195] Me´ric, L., Poubanne, P., & Cailletaud, G. (1991). Single crystal modeling for structural calculations: part 1-model presentation.

[196] Cailletaud, G. (1992). A micromechanical approach to inelastic behaviour of metals. International Journal of Plasticity, 8(1), 55-73.

[197] Tashman, L., Masad, E., Little, D., & Zbib, H. (2005). A microstructure-based viscoplastic model for asphalt concrete. International Journal of Plasticity, 21(9), 1659-1685.

[198] Masad, E., Tashman, L., Little, D., & Zbib, H. (2005). Viscoplastic modeling of asphalt mixes with the effects of anisotropy, damage and aggregate characteristics. Mechanics of Materials, 37(12), 1242-1256.

[199] Musienko, A., & Cailletaud, G. (2009). Simulation of inter-and transgranular crack propagation in polycrystalline aggregates due to stress corrosion cracking. Acta materialia, 57(13), 3840-3855.

[200] Onck, P., & van der Giessen, E. (1997). Microstructurally-based modelling of intergranular creep fracture using grain elements. Mechanics of Materials, 26(2), 109-126.

[201] Lemaitre, J. (2012). A course on damage mechanics. Springer Science & Business Media.

[202] Liu, X., Garcia-Mendez, R., Lupini, A. R., Cheng, Y., Hood, Z. D., Han, F., ... & Chi, M. (2021). Local electronic structure variation resulting in Li filament formation within solid electrolytes. Nature Materials, 20(11), 1485-1490.

[203] К.М. Кевролева. Структура и некоторые свойства кристаллогидратов.

[204]   He, Y., Li, B., Duan, H., Wang, S., Yin, S., Hao, Y., ... & Wu, K. (2020). Nano-grass like AlOOH as an Al source for synthesis of $Li_{1.3}Al_{0.3}Ti_{1.7}(PO_4)_3$ solid electrolytes with high ionic conductivity. Ceramics International, 46(9), 14143-14149.

[205]   Van Dyke, J. D., & Kasperski, K. L. (1993). Thermogravimetric study of polyacrylamide with evolved gas analysis. Journal of Polymer Science Part A: Polymer Chemistry, 31(7), 1807-1823.

[206]   Ohsaka, T., Izumi, F., & Fujiki, Y. (1978). Raman spectrum of anatase, TiO2. Journal of Raman spectroscopy, 7(6), 321-324.

[207]   Zhang, M., Huang, Z., Cheng, J., Yamamoto, O., Imanishi, N., Chi, B., ... & Li, J. (2014). Solid state lithium ionic conducting thin film $Li_{1.4}Al_{0.4}Ge_{1.6}(PO_4)_3$ prepared by tape casting. Journal of Alloys and Compounds, 590.

[208]   Ramaraghavulu, R., Buddhudu, S., & Kumar, G. B. (2011). Analysis of structural and thermal properties of Li_2TiO_3 ceramic powders. Ceramics International, 37(4), 1245-1249.

[209]   Sun, Z., Shi, J. R., Tay, B. K., & Lau, S. P. (2000). UV Raman characteristics of nanocrystalline diamond films with different grain size. Diamond and related materials, 9(12), 1979-1983.

[210]   He, S., Xu, Y., Zhang, B., Sun, X., Chen, Y., & Jin, Y. (2018). Unique rhombus-like precursor for synthesis of $Li_{1.3}Al_{0.3}Ti_{1.7}(PO_4)_3$ solid electrolyte with high ionic conductivity. Chemical engineering journal, 345, 483-491.

Acknowledgements

The author expresses his sincere gratitude to the scientific and pedagogical staff of the Faculty of Chemistry and the Faculty of Materials Sciences of Lomonosov Moscow State University for the invaluable experience gained during training and scientific work and also the author would like to express his deep gratitude to the China Scholarship Council for financial support during his postgraduate studies.

The author is grateful to supervisors Dr. Kapitanova O.O. and corresponding member of RAS, Dr. Goodilin E.A. for scientific guidance.

The author expresses deep gratitude to the staff of the biomaterials group of Laboratory of Inorganic Materials Science in the Faculty of Chemistry, in particular, prof. Putlayev V.I. and Dr. Evdokimov P.V. for fruitful cooperation, valuable recommendations and discussions on the work on the synthesis and characterization of ceramic materials.

The author is sincerely grateful to prof. Veselova I.A. for the opportunity to work in the laboratory of bioanalytical methods and optical sensor systems in the Faculty of Chemistry.

The author expresses special gratitude to the group led by prof. Song Zhongxiao from Xi'an Jiaotong University (China) and group led by prof. Aleksandar Matic from Chalmers University of Technology (Sweden), in particular, Dr. Xiong Shizhao, Dr. Wang Yongjing, Dr. Liu Yangyang, Dr. Jiao Xingxing for fruitful cooperation, valuable recommendations and discussion of work in the field of modeling work.

The author thanks for assistance in conducting studies of samples using the AFM method - prof. Gallyamov M.O., XRD measurement - Philipova T.V., electrochemical testing - Dr. Krivchenko V.A., SEM measurement - Dr. Zimbovsky D.S., measurements of mechanical properties - PhD. student Wang Xuyang, for contribution to experimental work in the field of synthesis of ceramic materials – master student Kirianova A.V. (synthesis using polymerized matrices), PhD. student Yakovlev I.I. (solid-state synthesis), PhD. student Zhou Diancheng (composite system with glass additive).

The author expresses gratitude to opponents prof. Almjasheva O.V., prof. Sorokin P.B. and Dr. Sokolov P.S. for valuable comments during the review of PhD work.

The author expresses gratitude all members of the commission for their attention to work.

The author expresses his sincere gratitude to his family and friends for their invaluable help and moral support.

Supporting information

Chapter 1. Study of the chemical composition and stability of the titanium (IV) peroxo complex

The chemical composition and stability constant of the titanium (IV) peroxo complex were studied by spectrophotometry using a UVmini-1240 spectrometer, Shimadzu (Japan). The maximum optical density was observed at a wavelength of $\lambda \sim 420$ nm. To obtain highly reproducible results, the determination of the composition was carried out by Isomolar series method, Asmus straight-line method and Harvey-Manning slope ratio method, respectively. Study of each method is based on various variations in the concentrations and volumes of precursors, which affects the final composition and concentration of the complex.

Thus, the Isomolar series method assumes that only one complex is formed, so the optical density of the solution is directly proportional to its concentration according to the Bouguer-Beer-Lambert law:

$$A = C_{complex} \cdot \varepsilon \cdot l$$

where A is the optical density, $C_{complex}$ is the concentration of the complex, ε is the molar coefficient of light absorption, and l is the thickness of the solution layer. Then, at the same concentration of precursors ($C_{Ti}^0 = C_{H2O2}^0$) and a constant total volume of the solution of their mixture ($V_{Ti} + V_{H2O2} = const$), the maximum of the optical density curve depending on the added volume of one of the reagents corresponds to the value that determines the coordination number of the complex:

$$n = \frac{C_{H_2O_2}^{max}}{C_{Ti}^{max}} = \frac{V_{H_2O_2}^{max}}{V_{Ti}^{max}}$$

where n is the coordination number, $C_{H_2O_2}^{max}$ and C_{Ti}^{max} are the concentrations of hydrogen peroxide and Ti^{4+} in the solution corresponding to the maximum optical density, $V_{H_2O_2}^{max}$ and V_{Ti}^{max}

are the volumes of added precursors that make up the solution with maximum optical density. Also, the Isomolar series method makes it possible to determine the stability constant of a given complex as a result of its dissociation. In theory, the maximum optical density of the solution of the complex is the point of intersection of two straight lines, which are described by the Bouguer-Lambert-Beer law with a decrease in the concentration of the complex in the process of changing the volumes of the added precursors. However, the dissociation of the complex also reduces its concentration, which leads to the deviation of the $A(V_{H2O2})$ function from a linear dependence. The difference between the theoretical and practical values of the maximum optical density determines the stability constant of the complex according to the following formula:

$$\beta = \frac{(A_{theo}^{max} - A_{prac}^{max})(C_{H_2O_2}^0 \cdot A_{theo}^{max} - nC_{Ti}^0 \cdot A_{prac}^{max})^n}{A_{theo}^{max} \cdot A_{prac}^{max \, n}}$$

where β is the stability constant, A_{theo}^{max} and A_{prac}^{max} are the maximum theoretical and practical optical density, respectively, $C_{H_2O_2}^0$ and C_{Ti}^0 are the concentrations of precursors, n is the coordination number of the complex.

Sample preparation (Table. 3.1) for the Isomolar series method consisted in preliminary preparation of 25 ml solutions of hydrogen peroxide and Ti^{4+} with a concentration of 0.01 M in 8 M nitric acid, which is required to dissolve titanium (IV) butoxide. Prepare solutions of corresponding concentrations in quartz cuvettes, and the solution in each cuvette is 6 ml. To establish equilibrium, spectrophotometric measurements were carried out 2 hours after mixing. The reference solution was 8M nitric acid.

Another way to study the chemical composition of the titanium (IV) peroxo complex was the Asmus straight line method. It is also assumed that there is only one complex. As a result of its dissociation, saturation is not achieved at an excessive concentration of the ligand. In this case, the following equation is valid:

$$\frac{1}{V_{H_2O_2}^n} = \frac{B}{\beta} \cdot \frac{l}{A} - \frac{C}{\beta}$$

where V_{H2O2} is the volume of the hydrogen peroxide solution, n is the coordination number, A is the optical density, l is the thickness of the solution layer, β is the stability constant, B and C are constants for a series of experiments. As a result, the plot constructed in the coordinates $1/\ V_{H_2O_2}^n$ versus l/A will be linear only for n, which truly corresponds to the coordination number of the complex under study. In practice, to measure the Asmus straight line, it was necessary to preliminarily prepare 25 ml of solutions of hydrogen peroxide and Ti^{4+} with a concentration of 0.01M in 8M nitric acid. Then, in volumetric flasks, a series of mixtures of precursors with different excesses of hydrogen peroxide was prepared according to Table. 3.1. The volumes of all obtained solutions were adjusted to 2 ml with 8 M nitric acid to obtain the same concentration of hydrogen peroxide. Optical density measurements were taken after 2 hours to establish equilibrium. The reference solution was 8M nitric acid. The third spectrophotometric method for determining the coordination composition of the titanium (IV) peroxo complex was the Harvey-Manning slope ratio method. It consists in measuring two series: equilibrium shift for the metal (C_{H2O2} = const) and for the ligand (C_{Ti} = const). Since the dependence of the optical density of the solution on the concentration of the complex is determined by the linear Bouguer-Beer-Lambert law, the slope of this straight line shows the rate of change in the concentration of the complex when the concentration of only one of the reagents changes. As a result, the ratio of the tangents of the inclination angles of both series allows us to determine the coordination number:

$$n = \frac{tg\alpha_{Ti}}{tg\alpha_{H_2O_2}}$$

where $tg\alpha_{Ti}$ and $tg\alpha_{H_2O_2}$ are the tangents of the slopes of the straight lines for a series of equilibrium shifts for the metal and for the ligand, respectively.

In practice, it was necessary to preliminarily prepare 25 ml solutions of hydrogen peroxide and Ti^{4+} with a concentration of 0.01M in 8M nitric acid. Mixtures of solutions of precursors with a constant concentration of Ti^{4+} were prepared in volumetric flasks according to Table. 3.1. The volumes of the resulting solutions were adjusted to 2 ml with 8 M nitric acid. Spectrophotometric measurements were carried out after two hours. Further, the obtained results were approximated by a linear function to determine the slope tangents.

## Chapter 2. Synergistic effect of multiple interfacial defects
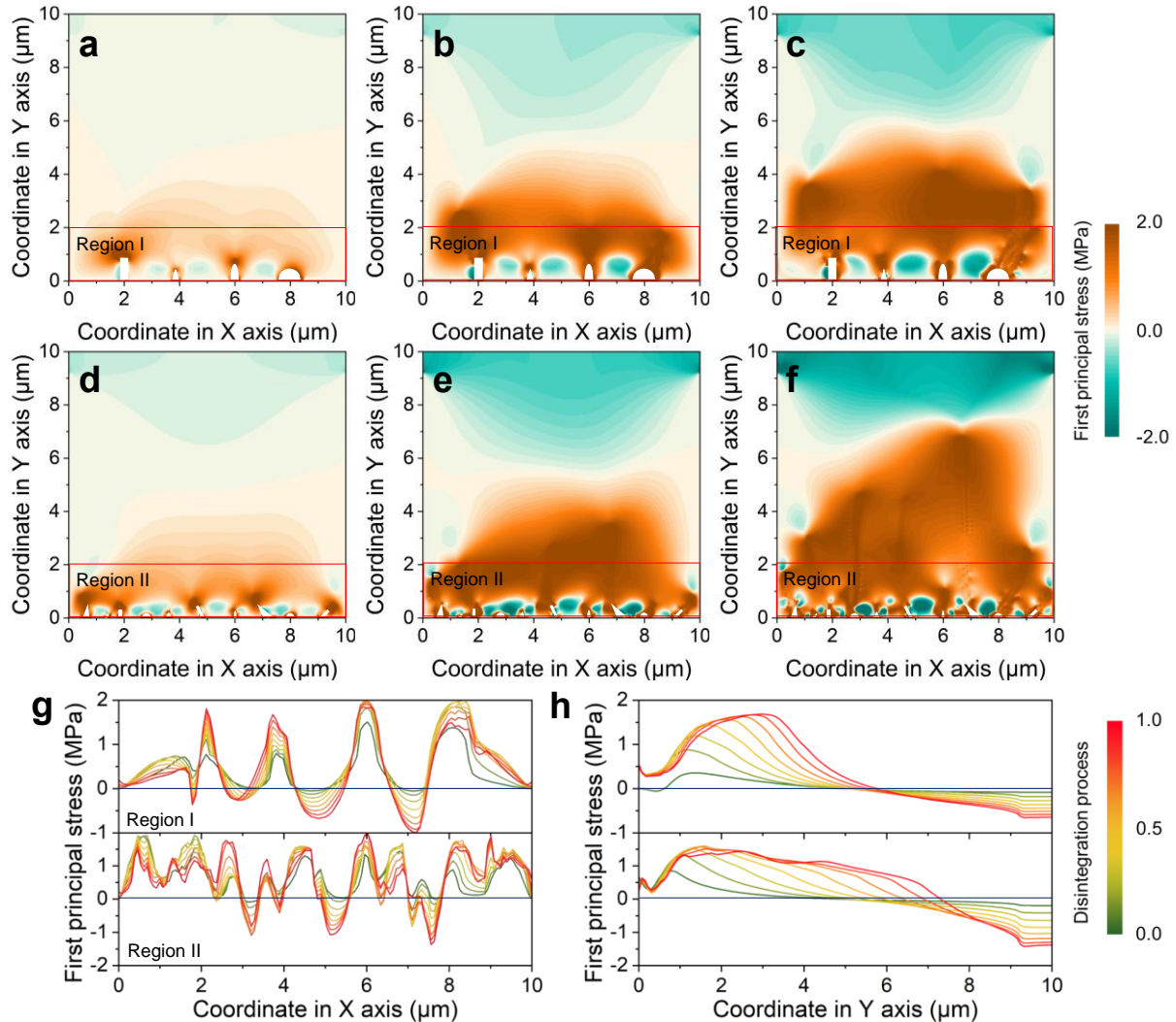
Figure. S1. Evolution of stress field inside solid-state electrolyte caused by the interfacial defects. a-c) Distribution of first principal stress inside the solid-state electrolyte with 4 interface defects at failure time of (a) 0.5 s, (b) 2.0 s and (c) 4.0 s. d-f) Distribution of first principal stress inside the solid-state electrolyte with 10 random interface defects at failure time of (d) 0.5 s, (e) 2.0 s and (f) 4.0 s. g-h) Variation of first principal stress (g) at the interface (marked with red square in Figures 1a-f) and (h) along orientation from the interface to bulk of electrolyte during electrodeposition of Li metal. White geometries represent the interface defects.

To discuss the synergy of multi-interfacial defects and the effect of Li metal's deposition on the solid-state electrolyte was investigated with the series time of 0.5 s, 2.0 s and 4.0 s. As shown in Figure. S1a-c, the distribution of the first principal stress inside the solid-state electrolyte with four interfacial defects mainly comes from the compression of electrodeposition of Li metal against the interfacial

defects inward to the bulk of electrolyte, which seriously increases to 5 μm in Y axis when failure time is up to 4 s. Moreover, when the random interfacial defects are up to ten, the distribution of the first principal stress becomes more serious than that with four interfacial defects at the same time. Solid-state electrolyte with ten random interfacial defects displays severe stress distribution to 7 μm in Y axis when the failure time reaches 4 s. In addition, the variation of the first principal stress in X axis was statistically summarized from the marked region with red square in Figure. S1a-f during electrodeposition of Li metal. As shown in Figure. S1g, the solid-state electrolyte with different interfacial defects in X axis shows much higher positive first principal stress than that with other parts, while other parts between the two defects present the lowest negative first principal stress inside the electrolyte, which demonstrate that the region above interfacial defects witness compressive stress and that between defects witness tensile stress. In comparation, the solid-state electrolyte with ten random interfacial defects exhibits similar behavior of the stress, of which the stress is much stronger than that with four different interfacial defects. Figure. S1h shows the first principal stress inside the electrolyte along orientation from the interface to bulk of electrolyte during electrodeposition of Li metal, which demonstrates that the region of the stress with ten random interfacial defects (0 to 7.7 μm) is larger than that with four defects (0 to 5.6 μm). ***The results indicate that the stress inside the electrolyte increases significantly with the increase of interfacial defects, which displays a large compressive stress around and above the interfacial defects, and a strong tensile stress between any two defects, predicting the interfacial failure of the solid-state electrolyte.***
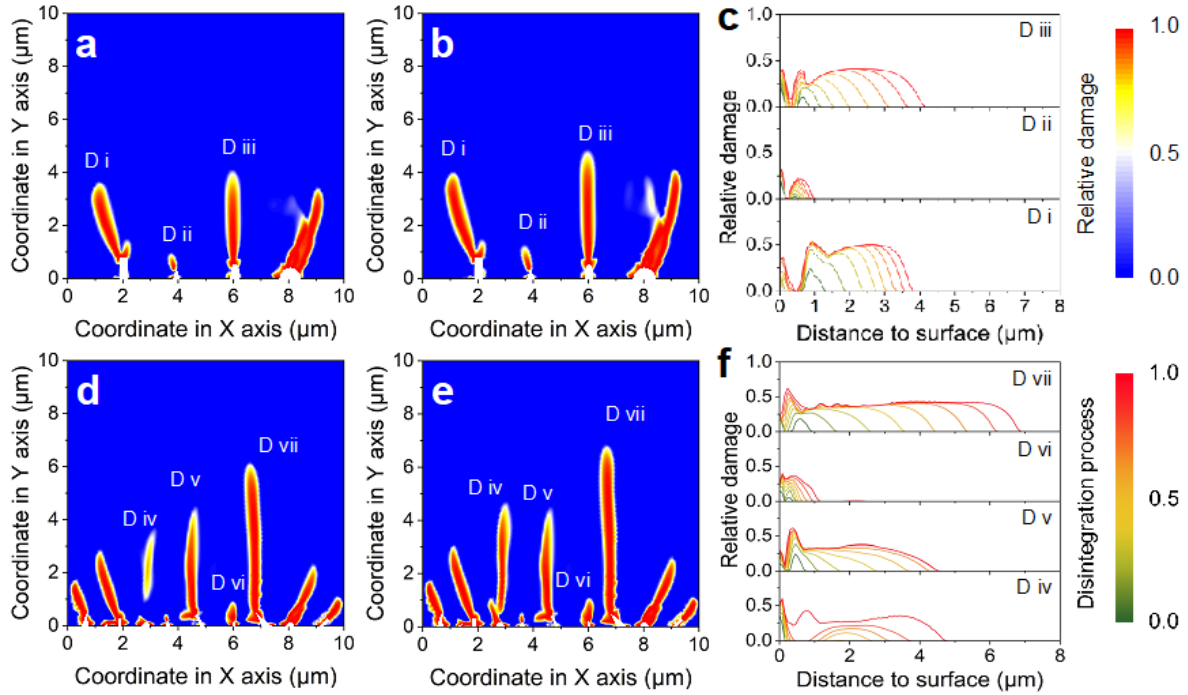
Figure. S2. Development of damage inside solid-state electrolytes with interfacial defects. a-b) Visualization of the damage regions inside the solid-state electrolyte with four interfacial defects at failure time of (a) 3.5 s and (b) 4.0 s. (c) Development of represented damage regions during the mechanical failure process of solid-state electrolyte with four interfacial defects. d-e) Visualization of the damage regions inside the solid-state electrolyte with ten random interfacial defects at failure time of (d) 3.5 s and (e) 4.0 s. (f) Development of represented damage regions during the mechanical failure process of solid-state electrolyte with ten random interfacial defects. D represents damage region and roman numerals represent corresponding numbers of the interfacial defects. White geometries represent the interface defects.

As shown in Figure. S2a-b, the solid-state electrolyte with cubic and semi-elliptical interfacial defects shows similar damage behavior with clubbed shape from the bottom to the inside electrolyte named Di and Diii, while the region Dii between cubic and semi-elliptical interface defects presents a tiny teardrop-shaped damage. Furthermore, Figure. S2c displays the development of represented damage regions during the mechanical failure process of solid-state electrolyte with four interface defects. It can be obviously found that cubic and semi-elliptical interfacial defects could cause the relative damage around 4 μm from the bottom of the electrolyte, whereas damage region between cubic and semi-elliptical interfacial defects only reaches 1 μm. In addition, the relative damages inside the solid-state electrolyte with cubic and semi-elliptical interfacial defects (around 0.5) are much stronger

than that between cubic and semi-elliptical interfacial defects (0.25), indicating that the development of relative damage with pyramidal defect Dii between two giant damage regions are suppressed obviously. As shown in Figure. S2d-e, the solid-state electrolyte with ten random interface defects shows the similar behavior of the development of represented damage regions with that containing four interfacial defects during the mechanical failure process, of which the interfacial defects could arouse the clubbed damage toward the electrolyte and the region of Dvi with small damage is restricted by the defects on both sides. Obviously, the damage in the Div region inside the solid-state electrolyte appears at the position without defects above the semi-sphere interfacial defect, indicating that the position without defect inside the solid-state electrolyte also can be affected by the damage caused by the interface defect to generate the internal damage, which is because the damage that has been formed will cause the stress to transfer to other parts of the electrolyte to squeeze around the position without defects and form damage. Paying more attention, the development of damage region Dv can be recognized in two orthogonal directions, horizontal with interface and vertical to interface, with different developing rates. Additionally, the relative damage in the region of Dvii reaches 6.9 μm from the bottom of the electrolyte, which is much larger than other regions and the damage in Dvi between the defects on both sides can only increase to 1.2 μm (Figure. S2f). The damage over the defect in the region of Div pops up at 2.5 s and can be attached to the damage caused by the defect from the bottom at 4 s. Consequently, the cracks originated from the tips of each interfacial defects grow straightly inward solid-state electrolyte from defected interface, which is severer with greater interfacial defects. Therefore, we suggest that the damage caused by the electrodeposition of Li metal at the defected interface propagates inward the solid-state electrolyte while it can nucleate spontaneously inside the solid-state electrolyte as well. And the internal failure can be accepted as the source of the short of solid-state electrolyte.
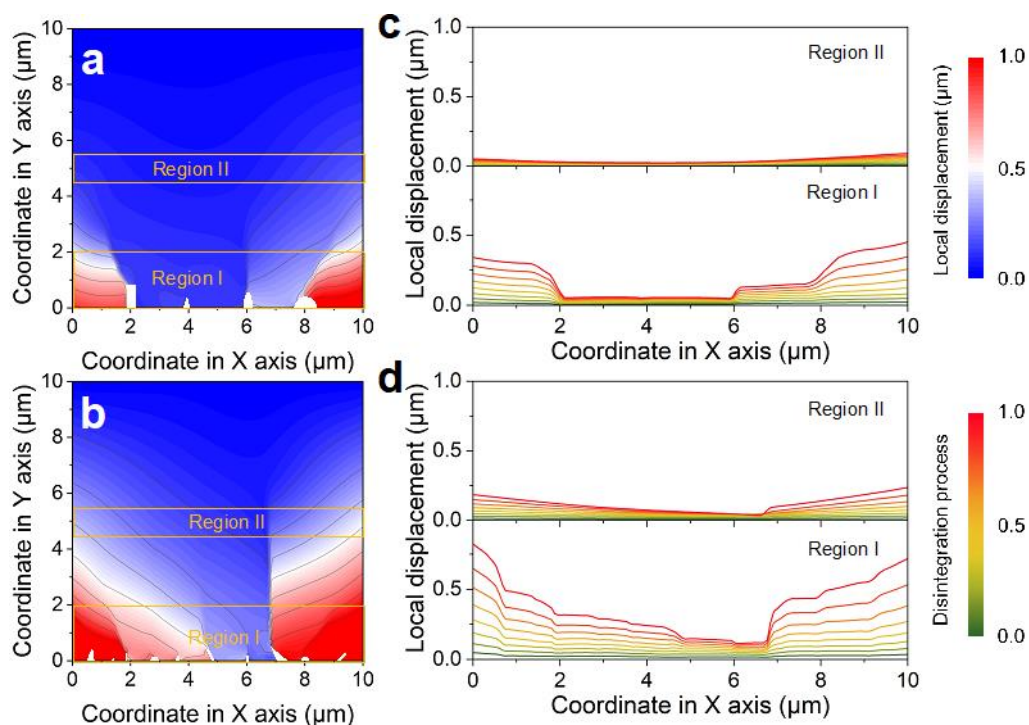
Figure S3. Disintegration of solid-state electrolytes caused by the interfacial defects. a-b) Visualization of local displacement inside solid-state electrolytes with (a) four interfacial defects and (b) ten random interface defects. c-d) Variation of displacement of the interface (marked with yellow rectangles in Figure. S9a-b named as Region I) and middle region of solid-state electrolyte (marked with yellow rectangles in Figure. S9a-b named as Region II) of the solid-state electrolytes with (c) four interfacial defects and (d) ten random interface defects. Calculation time is 4.5 s. White geometries represent the interface defects.

Furthermore, the visualization of local displacement inside interfacial-defected solid-state electrolytes was carried out to reveal the interfacial disintegration of solid-state electrolytes caused the electrodeposition of Li metal at defected interface. As shown in Figure. S3a-b, the center interface between two side of defects displays much lower local displacement compared with other parts, demonstrating that the edges of the defected interface will be "pushed" out of the integrity of solid-state electrolyte. When the interfacial defects change to greater, the local displacement inside electrolyte in both of X and Y axis is obviously rising, which shows that larger chunks will dissociate off. In addition, the local displacements in the Region I and Region II have been statistically counted to unburied the disintegration process of the solid-state electrolyte with different defected interface and distance to the surface during the electrodeposition of Li metal in Figure. S3c-d. In the Region I from 0 to 2 μm in Y axis that is intimate to surface, the solid-state electrolyte with ten random defects

shows much higher local displacement (maximum value of 0.8) than that with four interfacial defects (maximum value of 0.3). Moreover, the region from 2 μm to 6 μm in X axis shows almost no local displacement during the electrodeposition of Li metal, which is caused by the restriction effect. In Region II from 4.5 to 5.5 μm in Y axis, the local displacement is relatively low during whole disintegration process, of which the solid-state electrolyte with ten random defects exhibits slightly higher local displacement than that with four defects. Therefore, the interfacial failure of solid-state electrolyte is identified well due to giant difference in the local displacements of the regions near surface and inside the solid-state electrolyte. ***Moreover, the solid-state electrolyte with the defect between the two side defects shows very small structural destruction and the solid-state electrolyte with more interfacial defects can cause more serious disintegration.***

## Chapter 3. Effects of voids inside of SSE (Effect on the longitudinal-section)
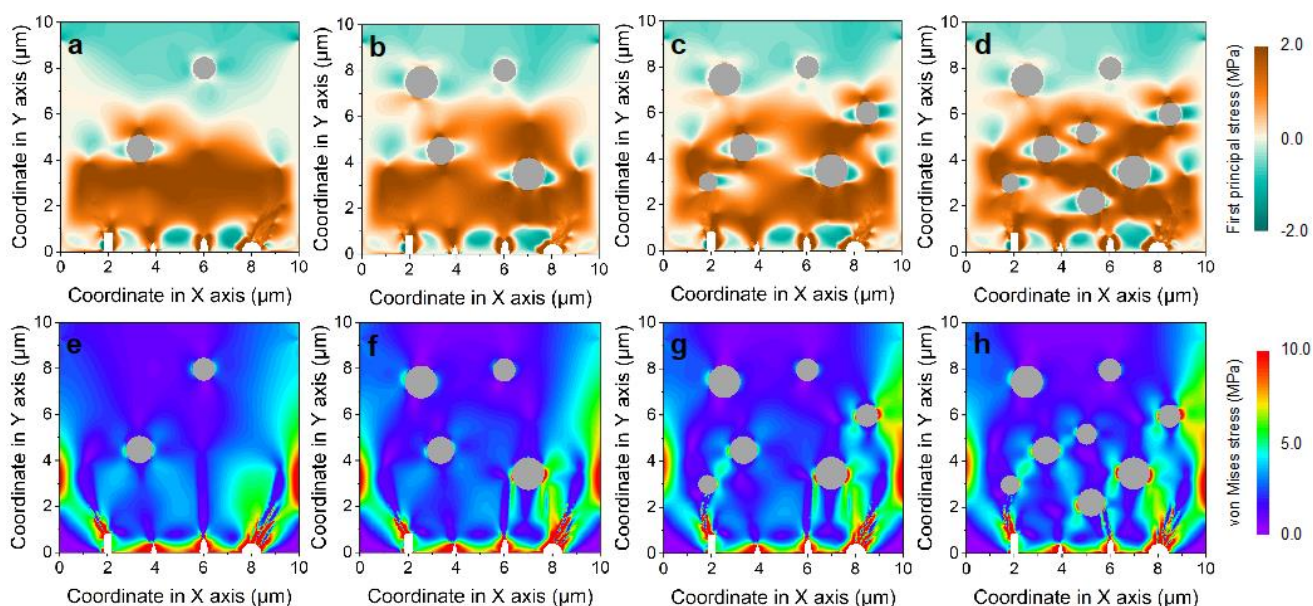
Figure. S4. Stress field inside solid-state electrolytes with interfacial and internal defects. a-b) Distribution of first principal stress inside the solid-state electrolyte with (a) two, (b) four, (c) six and (d) eight internal voids. e-h) Distribution of von Mises stress inside the solid-state electrolyte with (e) two, (f) four, (g) six and (h) eight internal voids. White geometries represent the interface defects. Gray circles represent the internal voids.

Besides the interfacial defects, the existence of internal defects inside the solid-state electrolyte, voids from sintering, is unavoidable, which are predicted to play a great impact on the structural

stability of the electrolyte. Therefore, two, four, six and eight internal voids were introduced into the solid-state electrolyte with defected interface to investigate the effect of the internal defects on the electrolyte. As shown in Figure. S4a-d, it can be distinguished that the regions surrounding the interfacial defects show obvious compressive stress against the solid-state electrolyte during the electrodeposition of Li metal processing, which is similar to that without internal voids. Whereas, the regions surrounding the internal voids witness different distribution of stress, where he top and bottom side of internal voids show compressive stress while the double side of internal voids displays tensile stress. In general, with increasing number of the internal voids, the distribution of the first principal stress displays obvious concentration of stress from interfacial defects to about 7 μm in Y axis, which indicates that the deposition of Li has a significant extrusion on the solid electrolyte below 7 μm in Y axis and little effect on the solid electrolyte in the region from 7 to 10 μm in Y axis. Same to the distribution of first principal stress inside solid-state electrolyte, considerable stress concentration arises inside the region surrounding the interfacial defects. While, compared the negligible stress at top and bottom side of internal voids, higher stress distributes at double sides of internal voids (Figure. S4e-f). ***Through the description with the first principal stress and von Mises stress, considerable compressive stress and tensile stresses distribute surrounding the interfacial defects and double side of internal voids, respectively, demonstrating that the existence of internal voids reforms the spread of stress from the electrodeposition of Li metal.***
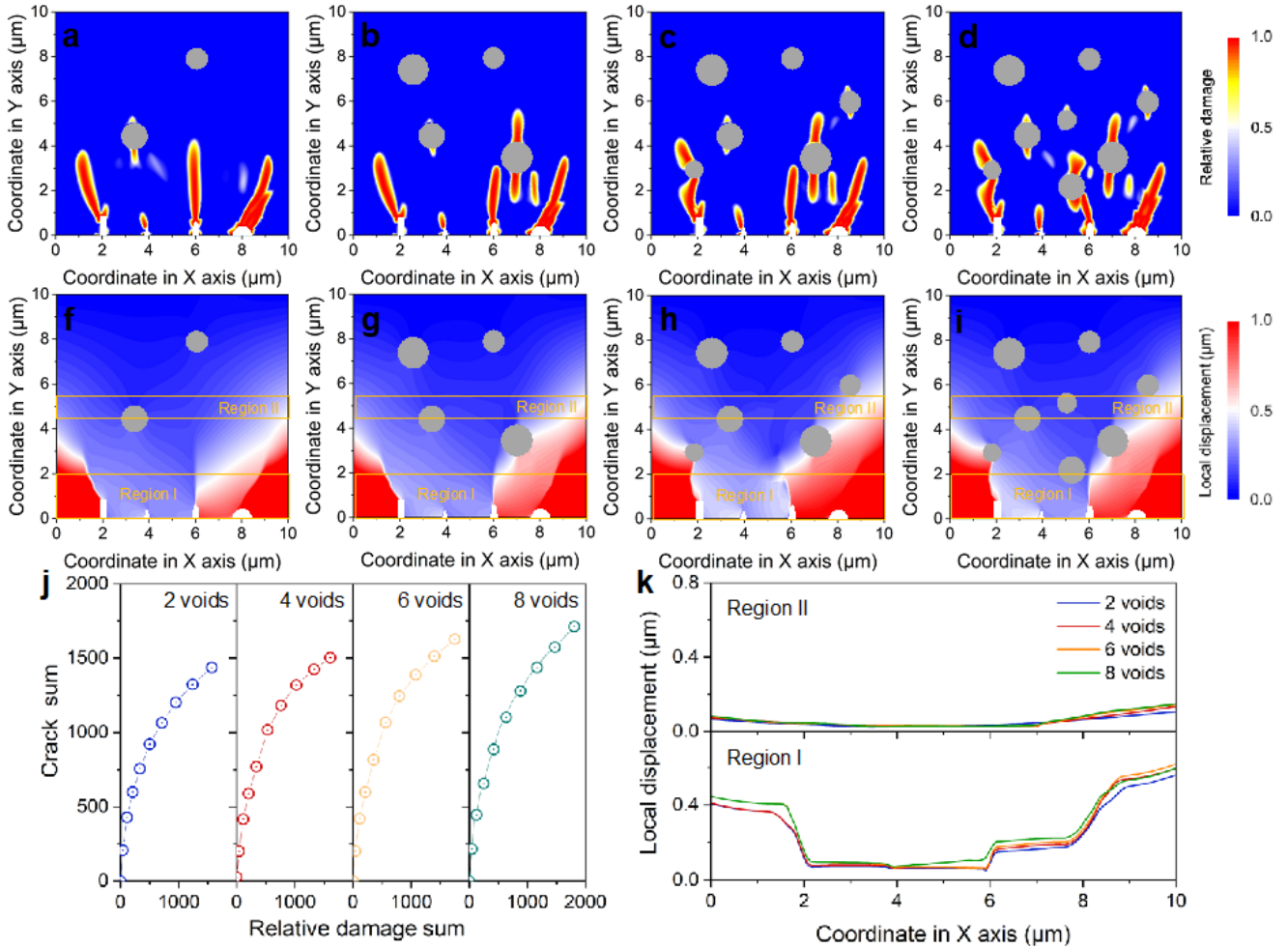
Figure. S5. Mechanical failure of solid-state electrolyte with interface and internal defects. a-b) Relative damage of solid-state electrolytes with (a) two, (b) four, (c) six and (d) eight internal voids. f-i) Displacement of solid-state electrolytes with (f) two, (g) four, (h) six and (i) eight internal voids. (j) The relationship between relative damage sum and generated crack inside the solid-state electrolyte with different internal voids. Variation of displacement of the interface (marked with yellow rectangular named as Region I) and middle region of solid-state electrolyte (marked with yellow rectangular named as Region II) of the solid-state electrolytes. Calculation time is set as 12 s. White geometries represent the interface defects. Gray circles represent the internal defects.

As shown in Figure. S5a-d, the relative damage inside interface-defected solid-state electrolyte with different amount of internal voids exhibits similar failure process with rod-like shape, which are mainly initiated and propagated along the interfacial defects to the inside solid-state electrolyte. Specially, the damage developing inward the solid-state electrolytes will cause the generation of damage around the internal voids, which are propagating oppositely, named reverse-tearing behavior. Some can meet with each other to form a straight damage region from interfacial defect to internal

voids, while some develops to form two parallel damage regions. Along with the development of damage originated from internal voids to the interface solid-state electrolyte, the damage nucleates at the opposite site of internal voids and develops inward the solid-state electrolyte as well. During the development of damage inside the solid-state electrolyte from both of interfacial defects and internal voids, the perfect region between two damage regions will witness the nucleation of damage. This reverse-tearing behavior shifts to more distinguished with the increase of the number of internal voids. Eventually, the generation of the rod-like shape inside solid-state electrolyte means that the solid-state electrolytes are seriously damaged after the electrodeposition of Li metal inside the interfacial defects. Furthermore, with the increasing number of internal defects, the relative damage is aggravated from 4 μm to 7 μm in Y axis, which mainly focuses around the internal voids below 5 μm in Y axis inside the solid-state electrolyte. When the internal voids inside the solid-state electrolyte are over 5 μm in Y axis, the process of Li metal's deposition shows no obvious damage inside the electrolyte. Consequently, the crack develops from the tips of interfacial defects and from the opposite side of internal voids as well. And the maximum crack inside the interfacial-defected solid-state electrolyte grows up slightly from 9.7 to 11.3 μm with the increase of number of internal voids from 2 to 8.

As mentioned above, the interfacial and internal defects can arouse severe cracks and damages inside the solid-state electrolyte during the deposition of Li metal at the same time, which directly affect the integrity of the electrolyte structure. As shown in Figure. S5f-i, the similar regions with different number of the internal voids show significant displacement in X axis from 0 to 2 μm and 6 μm to 10 μm, of which the regions inside the solid-state electrolyte have suffered very huge displacement and exfoliated from electrolyte. Moreover, the region and degree of displacement have been enhanced with the increasing number of the internal voids, which are surrounded by the internal voids lower 5 μm in Y axis. ***The results indicate that the internal voids below 5 μm in Y axis can accelerate mechanical failure of solid-state electrolytes during the deposition of Li metal.***

To reveal the effect of interfacial and internal defects inside the solid-state electrolyte on its mechanical failure, the relationship between relative damage sum and generated crack inside the solid-state electrolyte with different internal voids has been summarized with a series of failure time from 0 to 12 s. As shown in Figure. S5j, the crack sum inside the solid-state electrolyte with different number of internal voids shows similar behavior with a sharp upward trend during the deposition of Li metal. Moreover, the crack sum inside the solid-state electrolyte with eight voids is largest among that with

other number of internal voids. In addition, with the increasing number of internal voids, the solid-state electrolyte with eight internal voids displays the greatest crack sum during the plating of Li metal. Apparently, the local displacement of solid-state electrolyte with different internal voids displays the similar behavior in Region I (0 μm to 2 μm in Y axis) and Region II (4.5 μm to 5.5 μm in Y axis), which mainly happens at the interface of solid-state electrolyte. And the regions from 2 μm to 6 μm in X axis between the both side defects show a very small local displacement, which can be attributed to that the damage caused by the defects on both sides can prevent breakage of the medial area between them (Figure. S5k). Combining the visualization of local displacement and the development of damage inside, it can be distinguished that catastrophically interfacial disintegration of solid-state electrolyte with interfacial defects happens during the electrodeposition of Li metal inside the inner space of interfacial defect. Moreover, the inside damage with the associated cracks appears as well.

Chapter 4. SEM images of LATP solid-state electrolyte sintering behavior
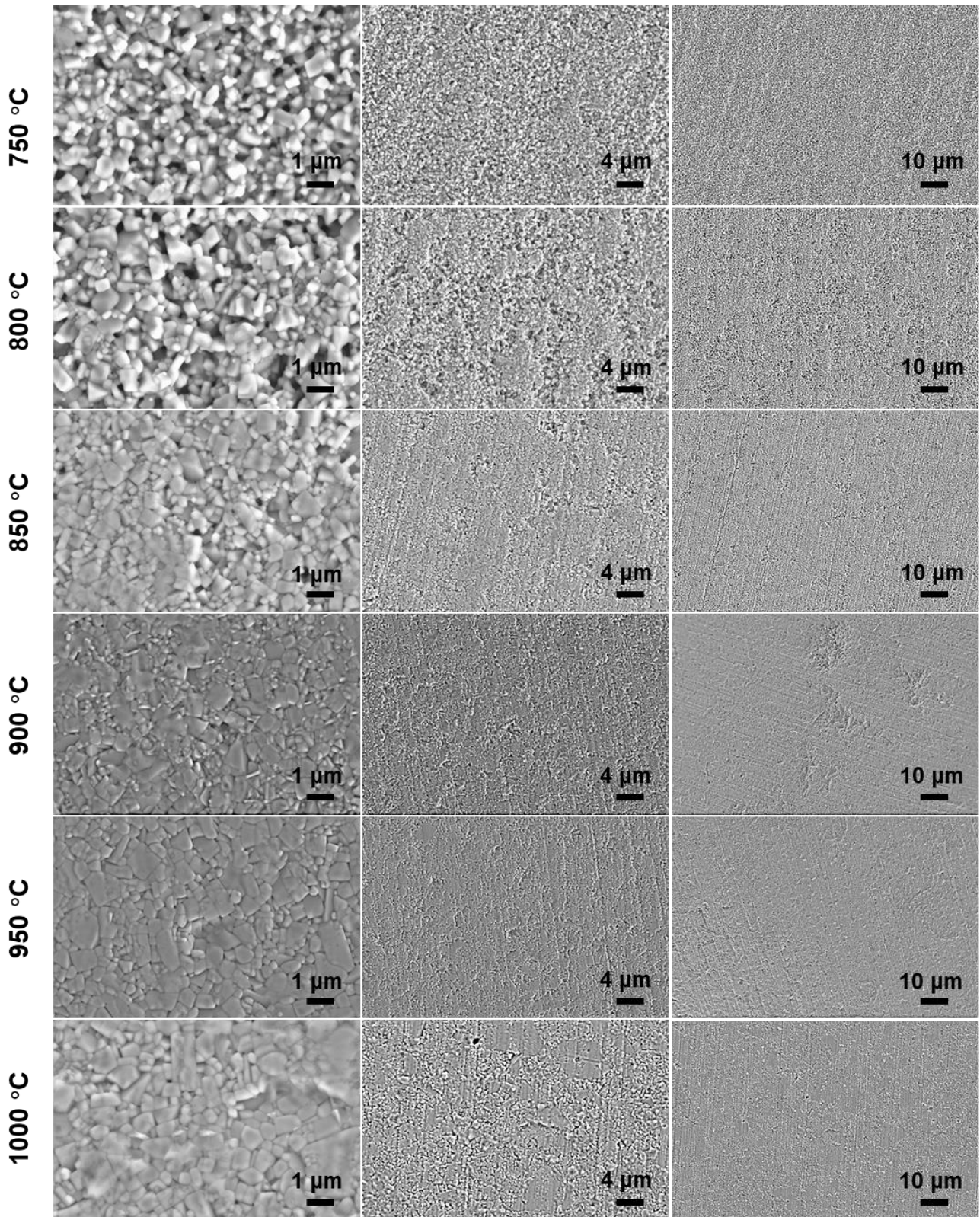
Figure. S6. SEM images of the microstructure of green body tablets made by LATP-600nm powder after sintering at various temperatures for 0.5 h.
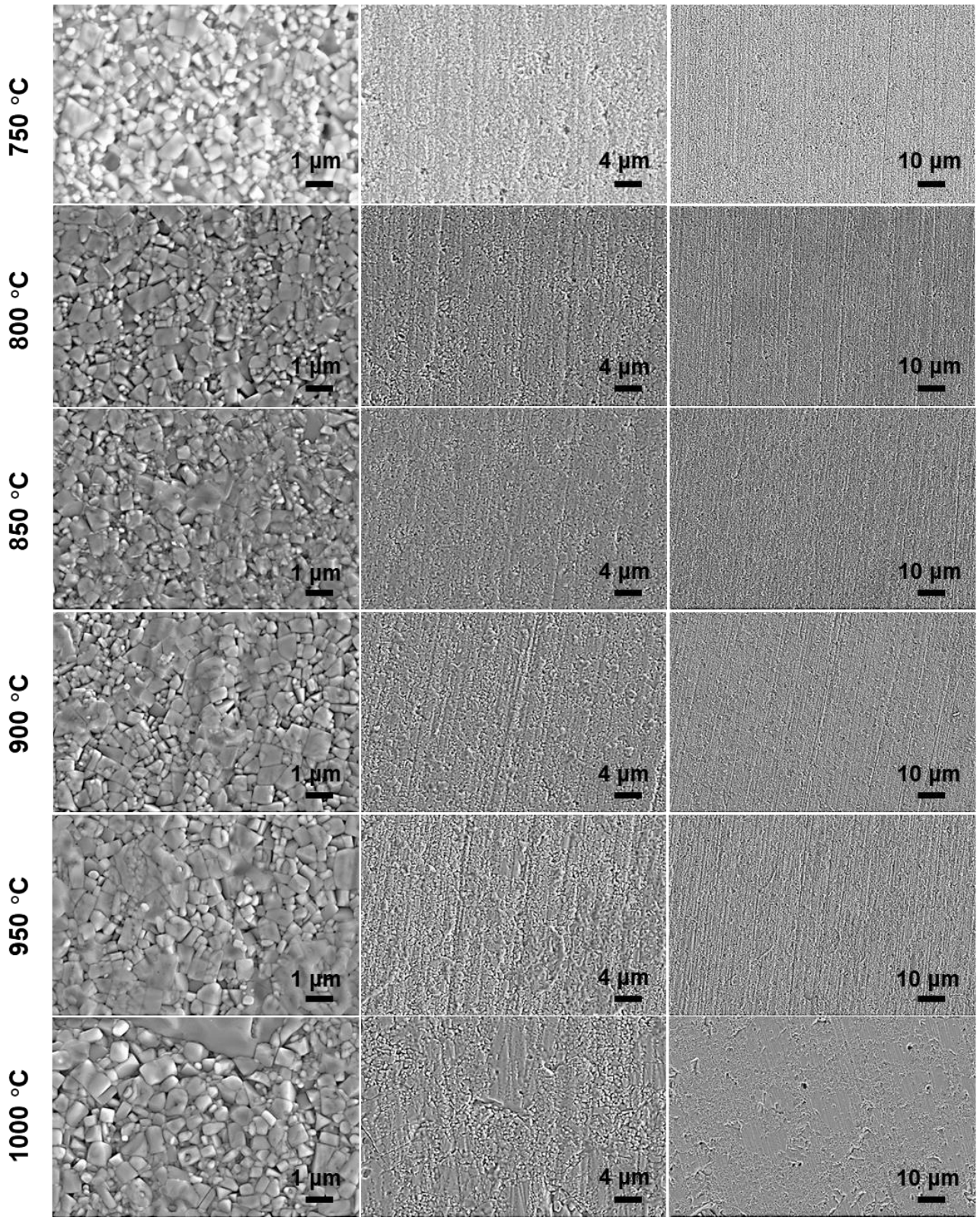
Figure. S7. SEM images of the microstructure of green body tablets made by LATP-600nm powder after sintering at various temperatures for 2 h.
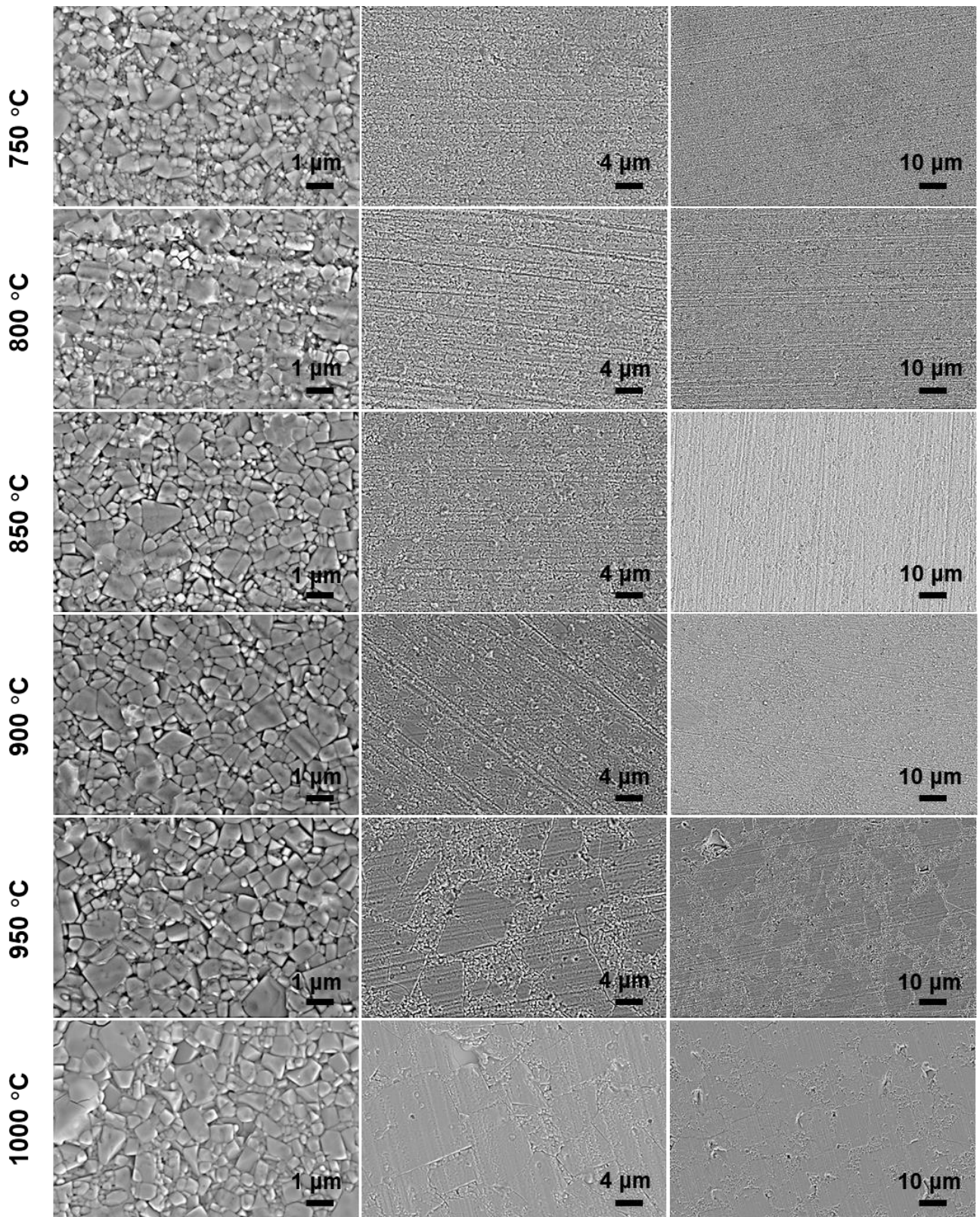
Figure. S8. SEM images of the microstructure of green body tablets made by LATP-600nm powder after sintering at various temperatures for 6 h.
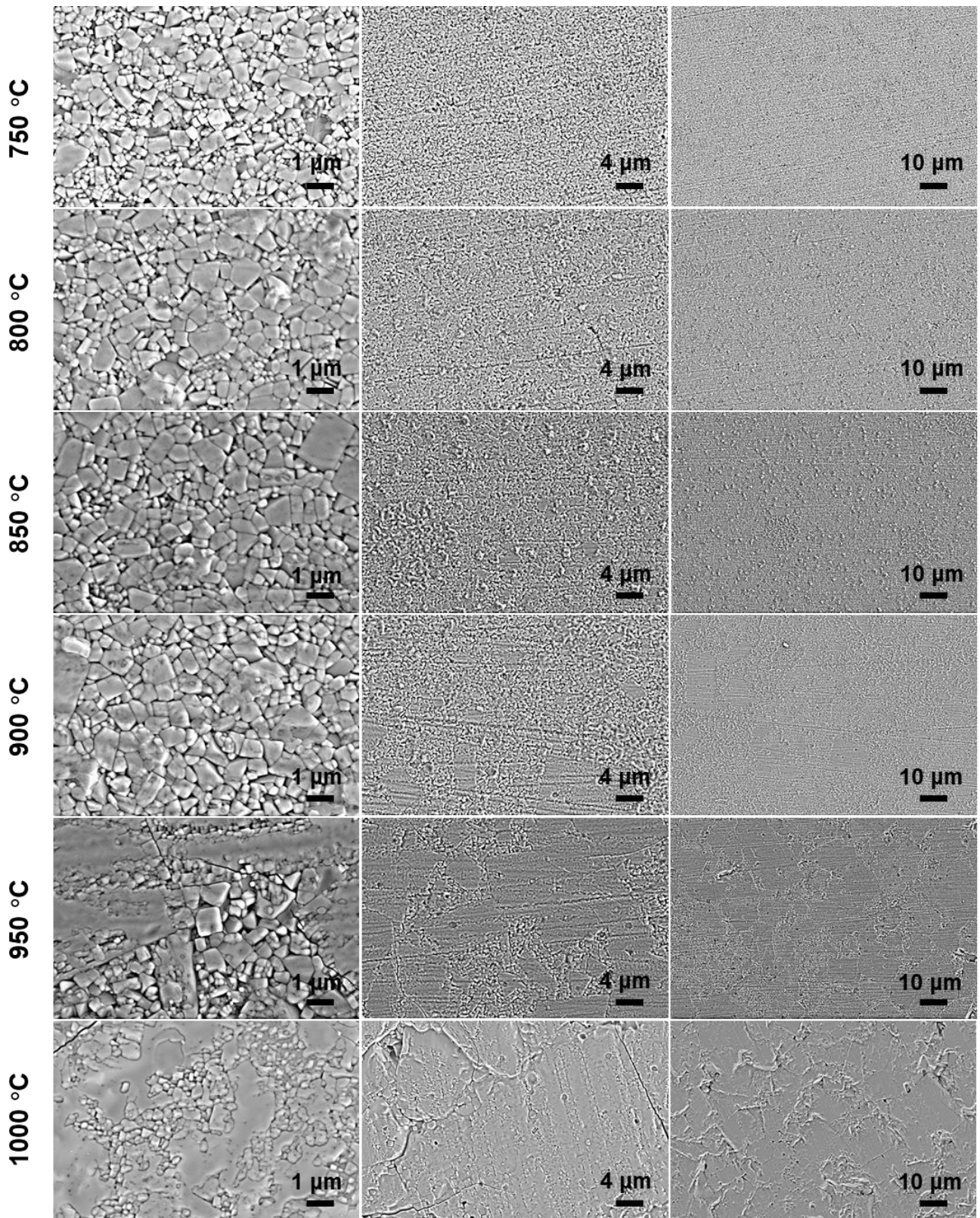
Figure. S9. SEM images of the microstructure of green body tablets made by LATP-600nm powder after sintering at various temperatures for 10 h.
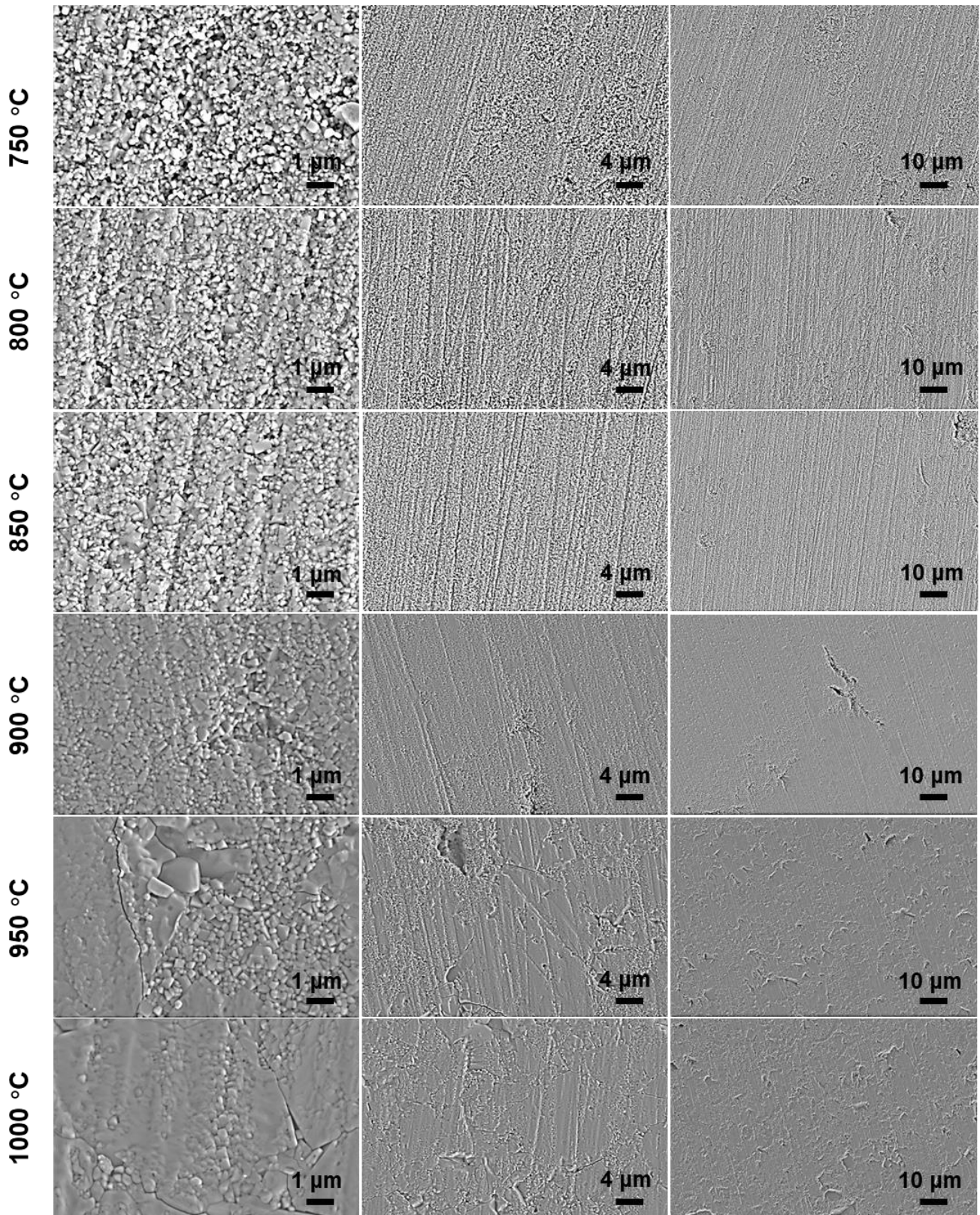
Figure. S10. SEM images of the microstructure of green body tablets made by LATP-300nm powder after sintering at various temperatures for 0.5 h.
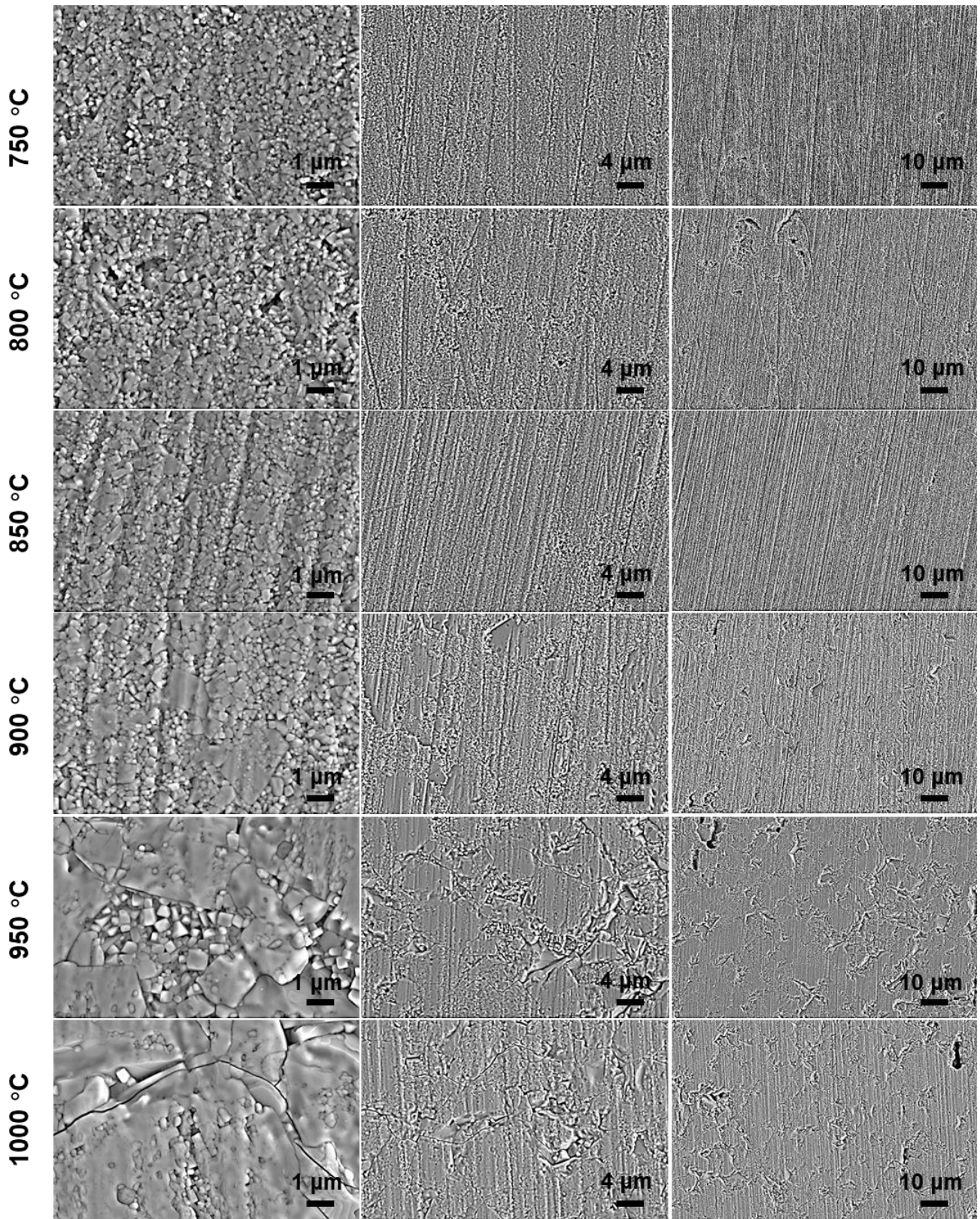
Figure. S11. SEM images of the microstructure of green body tablets made by LATP-300nm powder after sintering at various temperatures for 2 h.
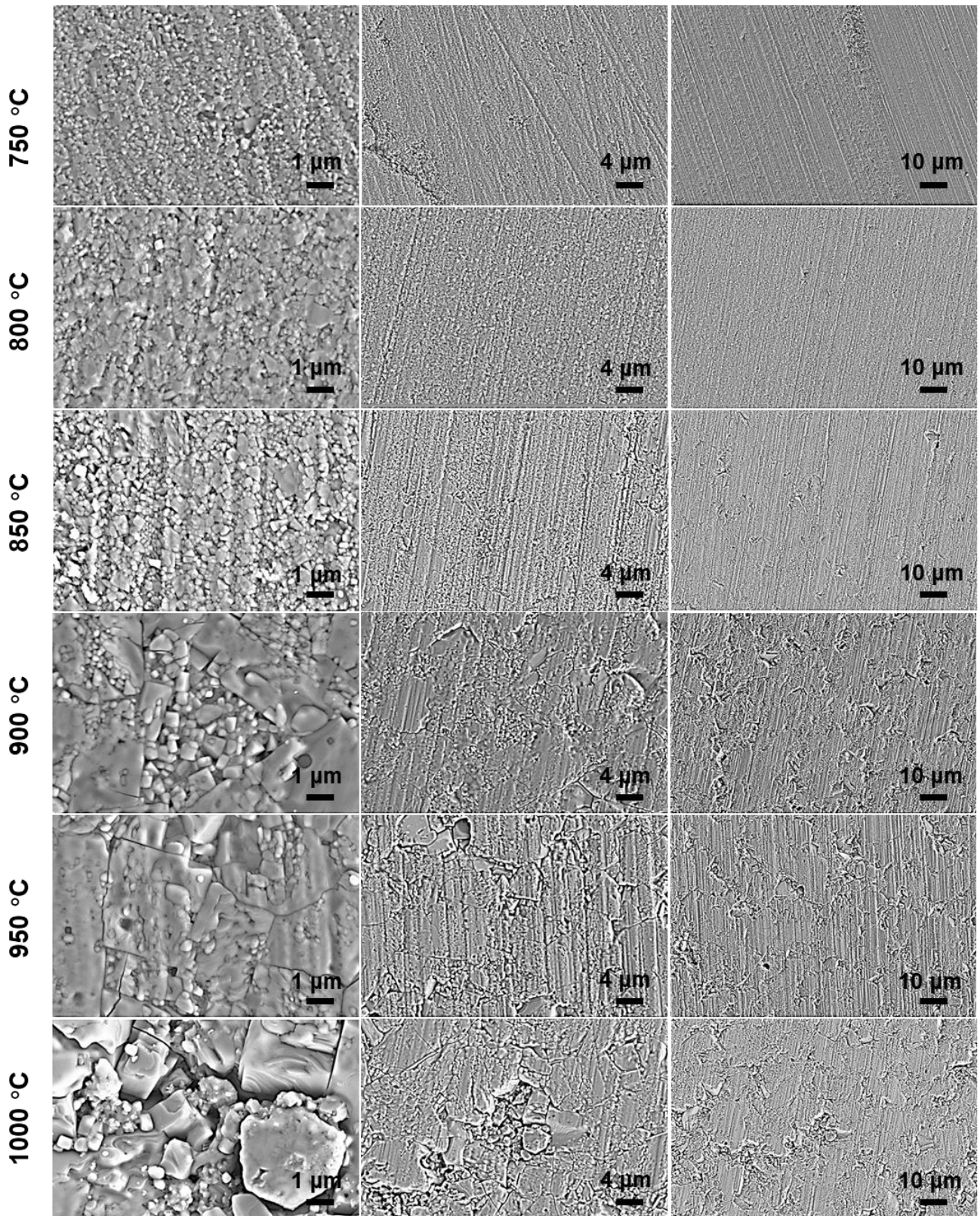
Figure. S12. SEM images of the microstructure of green body tablets made by LATP-300nm powder after sintering at various temperatures for 6 h.
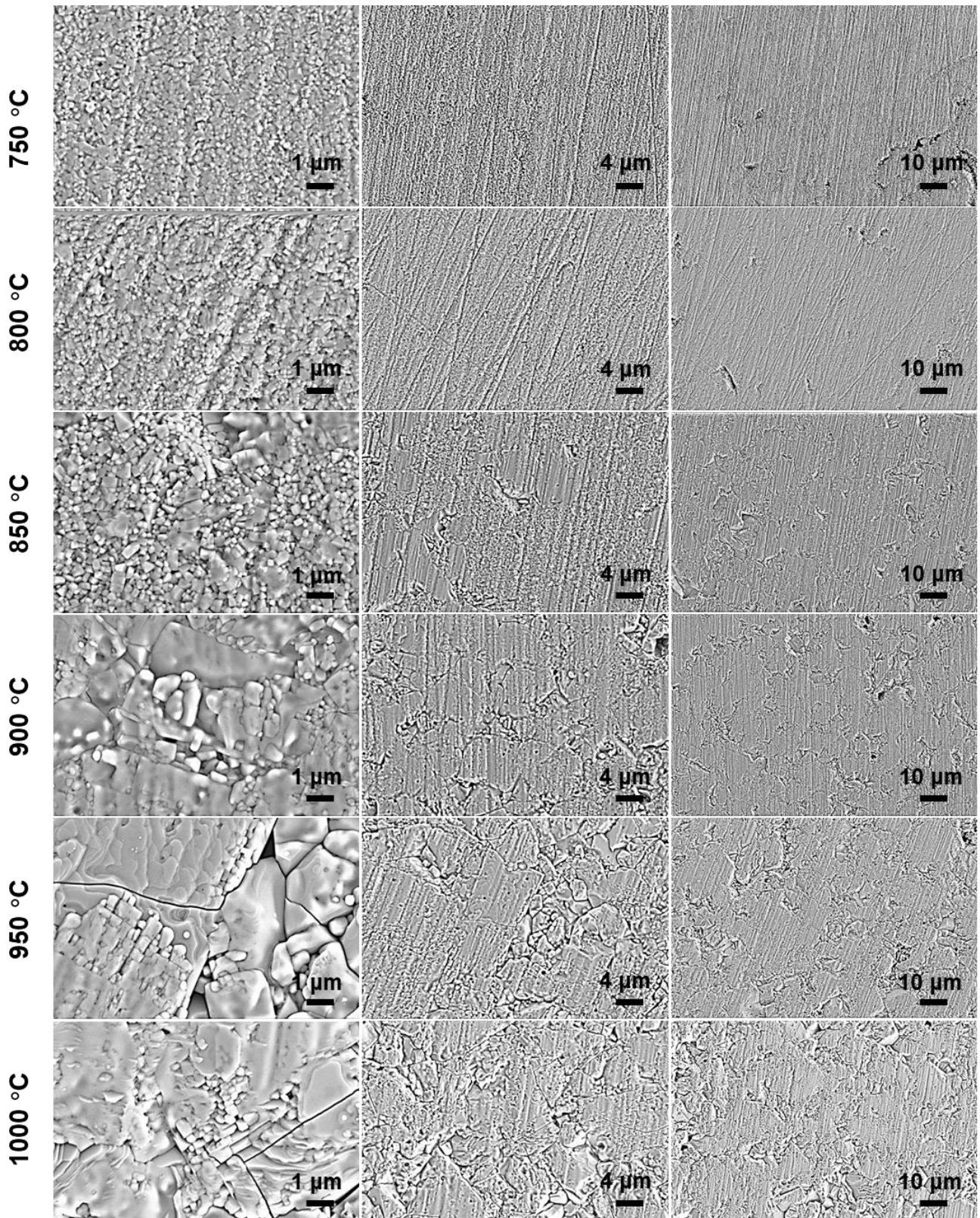
Figure. S13. SEM images of the microstructure of green body tablets made by LATP-300nm powder after sintering at various temperatures for 10 h.

## Chapter 5. AGG behavior of LATP ceramic from glass/ceramic composite systems
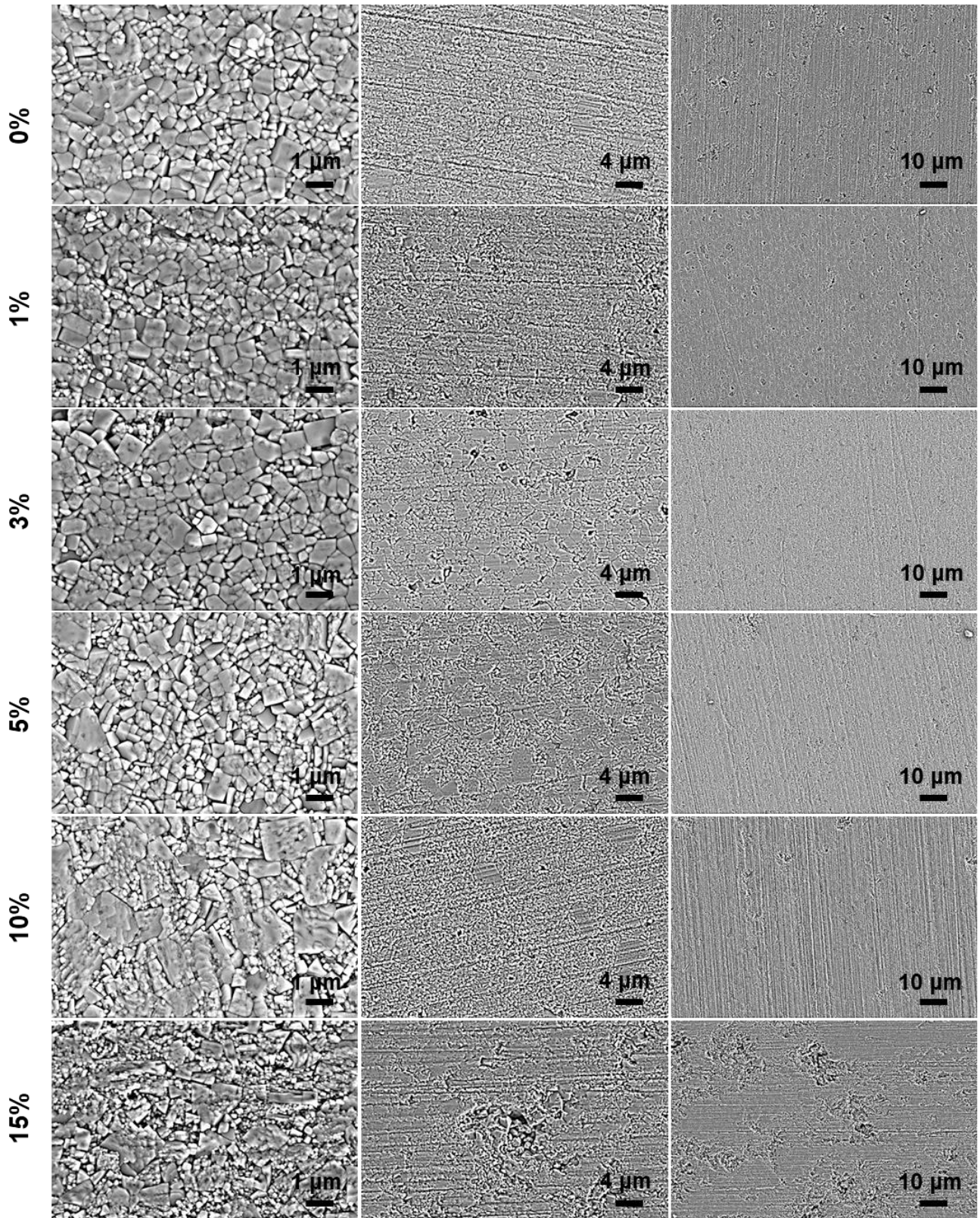
Figure. S14. Cross-section SEM images of LATP SSE ceramic from glass/ceramic composite powder systems with the mass ratios of 1%/99%, 3%/97%, 5%/95%, 10%/90% and 15%/85% after sintering at 900°C for 6 hours (1-step method), marked by 1-10 μm scale to observe AGG behavior, respectively.
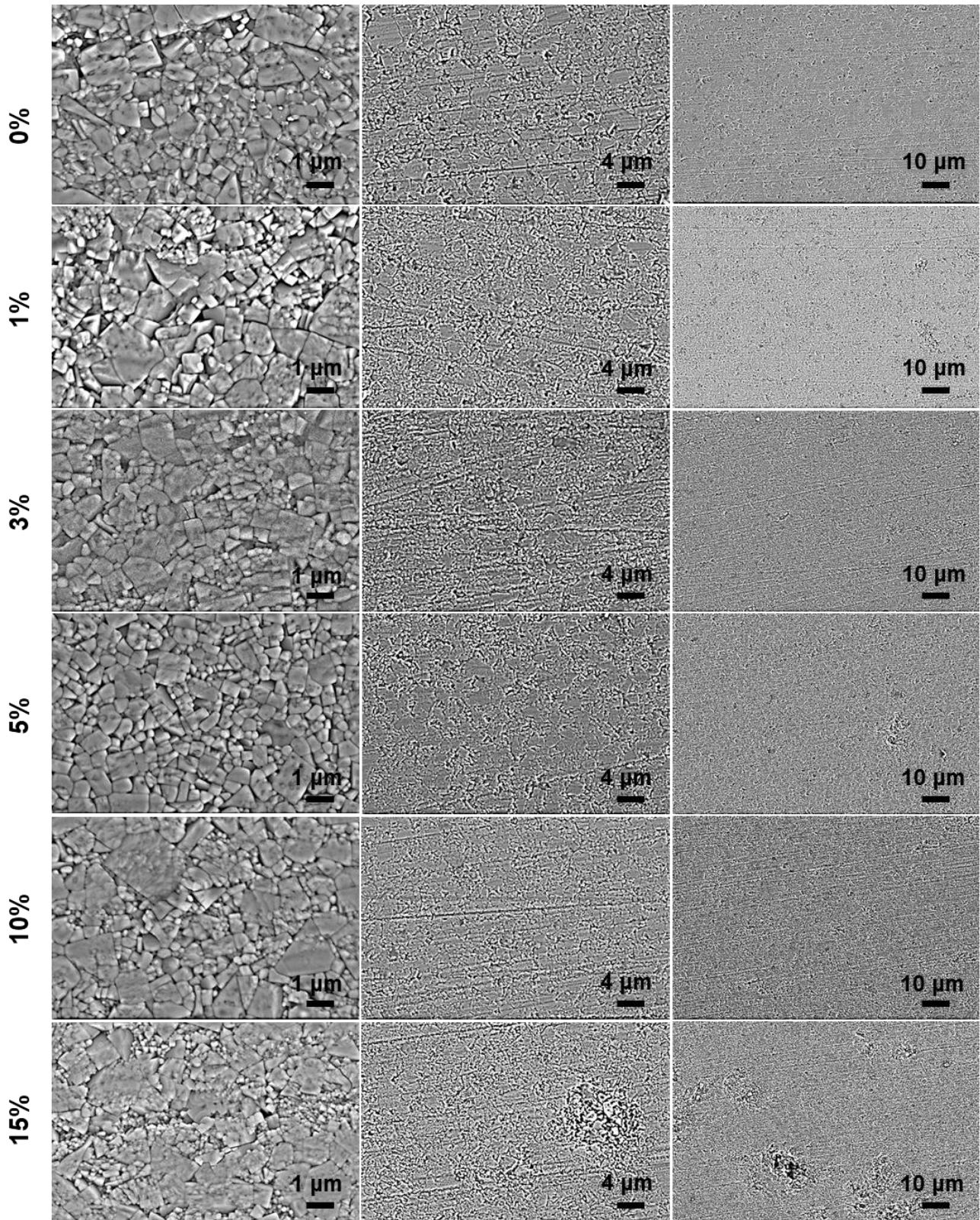
Figure. S15. Cross-section SEM images of LATP SSE ceramic from glass/ceramic composite powder systems with the mass ratios of 1%/99%, 3%/97%, 5%/95%, 10%/90% and 15%/85% after pretreatment at 570 °C for 6 hours then sintered at 900°C for 6 hours (2-steps method), marked by 1-10 μm scale to observe AGG behavior, respectively.